U.S. Department
of Transportation
**Federal Railroad
Administration**

Estimation of Actual Residual Stresses Due to Braking and Contact Loading of Rail Vehicle Wheels

Office of Research and
Development
Washington, DC 20590

Research and Special Programs Administration
John A. Volpe National Transportation Systems Center
Cambridge, MA 02142-1093

DOT/FRA/ORD-96/02
DOT-VNTSC-FRA-95-13

Final Report
March 1996

REPORT DOCUMENTATION PAGE

Form Approved
OMB No. 0704-0188

1. AGENCY USE ONLY (Leave blank)	2. REPORT DATE	3. REPORT TYPE AND DATES COVERED
	March 1996	Final Report February 1993 - July 1995

4. TITLE AND SUBTITLE
Estimation of Actual Residual Stresses Due to Braking and Contact Loading of Rail Vehicle Wheels

5. FUNDING NUMBERS
R-3026/RR-328
R-4005/RR-428
R-5005/RR-528

6. AUTHOR(S)
M. Holowinski and E. S. Bobrov

7. PERFORMING ORGANIZATION NAME(S) AND ADDRESS(ES)
Massachusetts Institute of Technology*
Francis Bitter National Magnet Laboratory
Cambridge, MA 02139

8. PERFORMING ORGANIZATION REPORT NUMBER
DOT-VNTSC-FRA-95-13

9. SPONSORING/MONITORING AGENCY NAME(S) AND ADDRESS(ES)
U.S. Department of Transportation
Federal Railroad Administration
Office of Research and Development
Washington, DC 20590

10. SPONSORING/MONITORING AGENCY REPORT NUMBER
DOT/FRA/ORD-96/02

11. SUPPLEMENTARY NOTES
*under contract to: U.S. Department of Transportation
Research and Special Programs Administration
Volpe National Transportation Systems Center
Cambridge, MA 02142

12a. DISTRIBUTION/AVAILABILITY STATEMENT
This document is available to the public through the National Technical Information Service, Springfield, VA 22161

12b. DISTRIBUTION CODE

13. ABSTRACT (Maximum 200 words)

A finite element formulation for shakedown stress analysis of rail vehicle wheels is presented, based on a hypothesis that the shakedown state is axisymmetric. The method can be used to estimate shakedown stresses in wheels subjected to combined mechanical (wheel/rail contact) and thermal (temperature gradients and thermal stress due to braking) loads. The formulation includes provisions for initial manufacturing stress, shifting contact locations, and temperature-dependent material properties. Validation results and demonstration example analyses of an actual wheel design are presented.

14. SUBJECT TERMS
Finite element; Rail vehicle wheels;
Residual stress; Shakedown; Thermal stress

15. NUMBER OF PAGES
154

16. PRICE CODE

17. SECURITY CLASSIFICATION OF REPORT	18. SECURITY CLASSIFICATION OF THIS PAGE	19. SECURITY CLASSIFICATION OF ABSTRACT	20. LIMITATION OF ABSTRACT
Unclassified	Unclassified	Unclassified	Unlimited

PREFACE

This report is the seventh of a series on the effects of service loads on railroad vehicle wheels. The study began in 1991, in response to a request from the Federal Railroad Administration (FRA) Office of Safety for technical support from the FRA Office of Research and Development. The wheels on three similar fleets of multiple unit (MU) power cars used in commuter service had been found to have unusually high rates of cracking. The purpose of the requested technical support was to assist the FRA Office of Safety in monitoring the affected fleets. At the same time, the FRA Office of Research and Development undertook a wheel performance research project to identify and evaluate options for long-term solutions.

The first five reports in the series cover the work done to evaluate the immediate actions which were taken to assure operational safety. Additionally, one fleet which had been equipped with straight tread brakes was to be upgraded to a blended brake system as a part of a scheduled program to replace the existing DC motors with AC motors. The effects of alternative blended brake options on wheel rim temperature were studied and summarized in the sixth report. Completion of this work coincided with closeout of the special monitoring program by the FRA Office of Safety. In the second phase, now underway, the effort is focused on wheel performance research.

Rim temperature attained during braking is widely recognized as a significant factor affecting wheel performance, i.e., the potential for thermal cracking. The crack formation mechanism is generally understood, in qualitative terms, to be the result of residual stress reversal in the rim. Modern railroad vehicle wheels are manufactured so as to enter service with compressive residual hoop stress in the outer part of the rim, and this compression acts as a barrier to crack progression. In service, the temperature gradient periodically set up in the rim during tread braking imposes thermal stresses, and if excessive demands are made upon the wheel, the thermal stresses can be large enough to cause plastic deformation and permanent change of the outer rim hoop stress from compression to a neutral or tensile state. Under such circumstances, surface cracks that would normally be prevented from growing until removed by natural wear can progress into the rim, becoming thermal cracks which pose the risk of wheel fracture.

The goal of the wheel performance research project is to develop a method of analysis which can be pro-actively applied to estimate the point at which the demand upon a wheel could lead to adverse residual stress in the outer rim. Conventional numerical analyses suffice for the prediction of initial manufacturing stresses, but it has been necessary to develop a special method for estimation of service effects, based on the hypothesis that the residual stresses reach a stable state after sufficient repetition of the mechanical and thermal loads in service.

This report summarizes the development and partial validation of the special method. It originated as a concept for prediction of rail residual stress, a development which was carried out under the FRA Track Safety Research Program. The foundations of the method are well documented in the track research literature and, therefore, are only briefly mentioned here. Most of this report focuses on the development of essential modifications to the rail analysis method to provide for the analysis of wheels which undergo changes in mechanical properties at the elevated temperatures associated with tread braking. The modifications involve significant extensions, which have been individually validated by comparison of calculated results with available independent solutions to simplified test problems. These comparisons are presented and discussed to document the validation, and also, to convey an idea of the level of modeling detail required to obtain results of

acceptable quality. This part of the report (sections 2 and 3) will be of interest mainly to researchers and applications engineers specializing in numerical stress analysis methods.

Section 3 of the report documents several example analyses of the MU wheel and, therefore, will also be of some interest to engineers and officers of railroad mechanical departments. The examples have been intentionally simplified in order to highlight effects of individual service factors. The results are encouraging because they produce expected trends and magnitudes.

One essential validation step still remains to be taken, namely: comparison of model predictions with field experience for actual cases. The experience gained in the first phase is to be used for this step. Differences in vehicle characteristics and operations were associated with different types of cracking that were observed in each of the three MU fleets. These characteristics are to be used as input to the wheel residual stress model, and the model predictions are to be compared with the actual fleet experience in each case. A report on this validation step is expected in the summer of 1996.

METRIC/ENGLISH CONVERSION FACTORS

ENGLISH TO METRIC

LENGTH (APPROXIMATE)

1 inch (in)	=	2.5 centimeters (cm)
1 foot (ft)	=	30 centimeters (cm)
1 yard (yd)	=	0.9 meter (m)
1 mile (mi)	=	1.6 kilometers (km)

AREA (APPROXIMATE)

1 square inch (sq in, in^2)	=	6.5 square centimeters (cm^2)
1 square foot (sq ft, ft^2)	=	0.09 square meter (m^2)
1 square yard (sq yd, yd^2)	=	0.8 square meter (m^2)
1 square mile (sq mi, mi^2)	=	2.6 square kilometers (km^2)
1 acre = 0.4 hectare (he)	=	4,000 square meters (m^2)

MASS - WEIGHT (APPROXIMATE)

1 ounce (oz)	=	28 grams (gm)
1 pound (lb)	=	0.45 kilogram (kg)
1 short ton = 2,000 pounds (lb)	=	0.9 tonne (t)

VOLUME (APPROXIMATE)

1 teaspoon (tsp)	=	5 milliliters (ml)
1 tablespoon (tbsp)	=	15 milliliters (ml)
1 fluid ounce (fl oz)	=	30 milliliters (ml)
1 cup (c)	=	0.24 liter (l)
1 pint (pt)	=	0.47 liter (l)
1 quart (qt)	=	0.96 liter (l)
1 gallon (gal)	=	3.8 liters (l)
1 cubic foot (cu ft, ft^3)	=	0.03 cubic meter (m^3)
1 cubic yard (cu yd, yd^3)	=	0.76 cubic meter (m^3)

TEMPERATURE (EXACT)

[(x-32)(5/9)] °F = y °C

METRIC TO ENGLISH

LENGTH (APPROXIMATE)

1 millimeter (mm)	=	0.04 inch (in)
1 centimeter (cm)	=	0.4 inch (in)
1 meter (m)	=	3.3 feet (ft)
1 meter (m)	=	1.1 yards (yd)
1 kilometer (km)	=	0.6 mile (mi)

AREA (APPROXIMATE)

1 square centimeter (cm^2)	=	0.16 square inch (sq in, in^2)
1 square meter (m^2)	=	1.2 square yards (sq yd, yd^2)
1 square kilometer (km^2)	=	0.4 square mile (sq mi, mi^2)
10,000 square meters (m^2)	=	1 hectare (ha) = 2.5 acres

MASS - WEIGHT (APPROXIMATE)

1 gram (gm)	=	0.036 ounce (oz)
1 kilogram (kg)	=	2.2 pounds (lb)
1 tonne (t) = 1,000 kilograms (kg)	=	1.1 short tons

VOLUME (APPROXIMATE)

1 milliliter (ml)	=	0.03 fluid ounce (fl oz)
1 liter (l)	=	2.1 pints (pt)
1 liter (l)	=	1.06 quarts (qt)
1 liter (l)	=	0.26 gallon (gal)
1 cubic meter (m^3)	=	36 cubic feet (cu ft, ft^3)
1 cubic meter (m^3)	=	1.3 cubic yards (cu yd, yd^3)

TEMPERATURE (EXACT)

[(9/5) y + 32] °C = x °F

QUICK INCH - CENTIMETER LENGTH CONVERSION

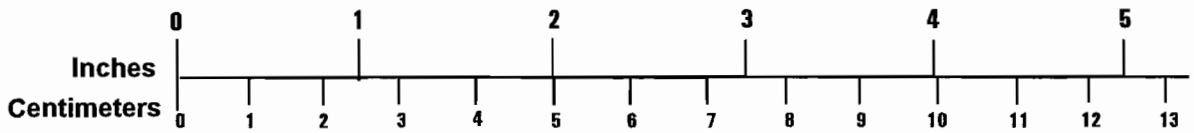

QUICK FAHRENHEIT - CELSIUS TEMPERATURE CONVERSION

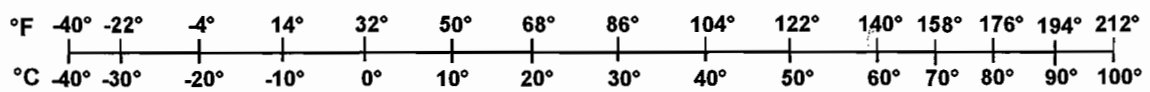

For more exact and or other conversion factors, see NIST Miscellaneous Publication 286, Units of Weights and Measures. Price $2.50 SD Catalog No. C13 10286

Updated 1/23/95

TABLE OF CONTENTS

LIST OF ILLUSTRATIONS

LIST OF ILLUSTRATIONS (cont'd)

LIST OF ILLUSTRATIONS (cont'd)

LIST OF ILLUSTRATIONS (cont'd)

LIST OF ILLUSTRATIONS (cont'd)

LIST OF ILLUSTRATIONS (cont'd)

LIST OF ILLUSTRATIONS (cont'd)

LIST OF ILLUSTRATIONS (cont'd)

LIST OF TABLES

EXECUTIVE SUMMARY

This report summarizes the development of specialized finite element software for estimation of residual stresses in rail vehicle wheels subjected to combinations of mechanical stresses from wheel/rail contact and thermal stresses from frictional heating by tread brakes. The work reported here is part of an ongoing research project on wheel performance sponsored by the Federal Railroad Administration (FRA) Office of Research and Development and carried out by the Volpe National Transportation Systems Center. This project grew out of a quick reaction task, in which the FRA Office of Research and Development and the Volpe Center provided technical support to the FRA Office of Safety to evaluate immediate actions taken to deal with episodes of thermal cracking in the wheels of three similar fleets of multiple unit (MU) power cars, operated in commuter service in the Greater New York Area, and to assess options for reconfiguration of the braking system on one of the fleets. The technical support effort is documented in six earlier reports.

The development of a residual stress estimation model is a key element of long-term FRA research. The goals are a means of predicting wheel performance in service and, via application of the model, guidelines for improving product quality.

Prior research by the Association of American Railroads (AAR) has shown that residual hoop tension in a freight car wheel rim promotes the formation and progression of thermal cracks. Modern freight car wheels enter service with residual compression, which acts as a barrier to thermal cracking, due to a rim quenching heat treatment during fabrication. The rim normally retains the compression for its entire service life, but excessive heating from abnormal grade braking conditions can reverse the stress to tension.

In those MU car wheels that experienced thermal cracking, the cause was found to be excessive concentration of heat during stop braking. Experimental work showed that the MU car wheels also entered service with hoop compression, but that the effect of stop braking was to relieve or reverse the stress in a shallow layer of the outer rim, and in most cases the thermal cracks tended not to progress into the underlying region. Nevertheless, the circumstances are not desirable because safety considerations lead to frequent inspection, removal of the thermally cracked layer, and consequent shortening of wheel service life.

Taken together the above cases highlight rim residual stress as the key factor affecting wheel performance in service, as regards resistance to thermal cracking. It is thus useful to have a model capable of estimating rim residual stress based on practical specification of the service environment in terms of vehicle weight, maximum operating speed, and profile of tread braking effort as a function of speed. The finite element model described in this report was developed for this purpose.

The wheel rim stress model is an extension of a model originally developed to estimate residual stress in rails. The approach is based on a hypothesis that, in either case, the residual stress attains a stable state as long as the service conditions remain generally the same. The stable state is then sought directly, as a so-called shakedown state, under a simplifying assumption that the material strain hardening during plastic deformation can be neglected. In fact both rail and wheel steels do exhibit strain hardening, but the assumption can be justified on the grounds that any plastic deformation is confined by surrounding material and, therefore, that the magnitude of the plastic strain is low. The shakedown state is estimated by means of a mathematical optimization technique that searches among all the possible states (those satisfying the appropriate equilibrium conditions) to find the one state that also keeps the sum of residual and live stresses

within the material elastic limit. This approach leads to several important advantages in the numerical computations:

- Only elastic representations of the live stresses are needed. This considerably simplifies the task of calculating live mechanical stresses from wheel/rail contact and live thermal stresses due to temperature gradients during braking.

- The hypothesized shakedown state can be assumed to possess certain symmetry that allows reduction of the finite element model from three to two dimensions. The hypothesized state is axially symmetric for a wheel, and the finite element mesh is defined for the typical radial plane. The two-dimensional character of the model dramatically reduces the number of unknowns, computer memory required, and time needed for the numerical solution.

- If the search criterion is satisfied for the live stresses corresponding to the greatest magnitude of any given service load type (e.g., wheel/rail contact centered at a particular lateral position on the tread), then it follows that the criterion is also satisfied for any smaller load of the same type. Thus, the live stresses need to be calculated only for the envelope of greatest load magnitudes (one for each type) expected in service.

- A shakedown state is by definition independent of the details of the sequence of loads by which the state is reached. Thus, there is no need to attempt to specify a detailed history of service loading, such as would be required for the estimation of a residual stress state by conventional means.

- In practice, the service loading consists of different load types that occur at different times. For example, the position of the wheel/rail contact load is expected to shift laterally across the tread as a wheel encounters tangent and curve track. Such conditions are easily treated with the shakedown model simply by finding a solution for the first load type, using the solution as an initial stress condition for the second load type, and so on. The solution thus obtained after the last load type is considered as a candidate shakedown state. The candidate state is then used as an initial stress state for a second series of analyses in reverse order. If the solution finally obtained after returning to the first load type is the same, then the candidate solution is accepted as a good estimate of the actual residual stress state. Although the foregoing procedure appears to be cumbersome, it is easy to execute, and the required computational effort is still one or two orders of magnitude less than would be needed to obtain a comparable solution by conventional means.

In the original rail shakedown stress model, calculations of elastic wheel/rail contact stresses were limited to representation of contact pressure based on an approximation of the Hertz theory used by track design engineers. This approach was justified by arguments that the model was intended to represent lubricated contact at some distance from the rail gage corner. Under such conditions, forces tangent to the rail surface can be neglected in comparison with the contact pressure, and theoretical expressions representing internal stresses due to pressure can be directly programmed, provided one is willing to neglect effects due to the slight curvature of the surface near the rail crown.

Conversely, neither of the foregoing assumptions is justified for calculation of internal contact stresses in wheels. It is essential to be able to account for longitudinal tangent forces due to braking and inclined tangent forces due to flange contact, as well as lateral

tangent forces due to creep. Also, it is important to be able to represent contact near the flange throat, where the surface is so highly curved that the theoretical expressions are not valid. Consequently, a numerical approach (see section 2) was adopted in place of the simplified approach from the original model.

Unlike the hypothesized residual stress state, the contact stresses are not axisymmetric because the wheel/rail contact pressure is concentrated on a small area and any tangent loads are generally asymmetric. In principle, a model with three-dimensional finite elements could have been used to compute the contact stresses, but in practice such an approach would require either too much computational effort to attain sufficient mesh detail or too much bookkeeping (with chances for error) to grade the mesh from refined near the contact zone to coarse elsewhere.

Therefore, a Fourier harmonic finite element formulation and the corresponding software were developed for the contact stress computations. Any arbitrary load distribution around the circumference of an axisymmetric body can be represented as a Fourier series consisting of a zeroth (axisymmetric) harmonic and additional harmonics expressed in terms of sine and cosine functions. The series coefficients, which are determined by a given load distribution, play the role of driving forces in the finite element analysis. Corresponding to the set of zeroth harmonic force coefficients is the conventional axisymmetric finite element. Stiffnesses corresponding to the higher harmonics are derived from the same sine and cosine functions. For computation of elastic stresses, linear superposition can be used to decouple the formulation, i.e., the force coefficients and element stiffnesses can be used to determine stress coefficients for each harmonic. The full stress solution is then expressed as Fourier series in the solution coefficients and corresponding harmonic distribution functions.

The Fourier harmonic software was validated by comparison with results obtained from conventional 2D finite element software. The validation examples were limited to problems with simple geometry: a circular disc in plane stress loaded by surface forces concentrated on 1/24 of the circumference, and a thick-walled cylinder axisymmetrically loaded by internal pressure varying along the longitudinal axis. Both pressure and tangent forces were treated in the disc example. The harmonic software was tested with four uniform meshes, doubling the grid density in each succeeding case, to demonstrate convergence to the conventionally obtained solution.

In theory the Fourier series contains an infinite number of terms, but only a finite number can be included in a practical numerical analysis. One of the objectives of the validation was to determine the minimum number required for good results. The disc test examples were run with about 25% more harmonics than actually needed to obtain accurate solutions. Examination of the results revealed two important points. First, the highest harmonic that must be included should have 4 to 6 wavelengths in the circumferential width of the contact zone. Second, adding still higher harmonics does not improve the quality of the solution if the finite element mesh is too coarse.

The validation was continued with an example analysis of contact stresses in the MU wheel. Since it was not possible to obtain good quality results from a conventional 3D finite element analysis, the finite element mesh was repeatedly refined in the region near the contact zone until convergence could be inferred from agreement of results from the two most dense grids. Convergence was demonstrated with five levels of mesh refinement, of which the coarsest was a slight modification of the mesh the Volpe Center used in a heat transfer model to calculate MU wheel temperatures during stop braking (see the second report in this series). The two most dense grids consisted of 1495 and 1621 finite elements, respectively. Examples of contact pressure alone and contact pressure (P) combined with

longitudinal tangent forces (L) in the ratio $L/P = 0.2$ were executed. The first example required 1189 harmonics, based on the criterion of at least 6 wavelengths per contact zone width; the second example required twice as many because anti-symmetric as well as symmetric harmonic modes were required to represent the tangent force effects.

The original software for estimation of rail shakedown stress states had to be modified for adaptation to wheel analysis. The finite element had been formulated in cartesian geometry to include four stress components: normal stress parallel to the rail axis, lateral and vertical normal stresses, and the shear stress in the transverse plane. The modified element was reformulated in cylindrical geometry in a manner similar to a conventional axisymmetric element, but all six stress components (three normal stresses and three shears) had to be included in order to represent the antisymmetric effects of longitudinal tangent forces as well as the axisymmetric effects of pressure and thermal stresses.

Two example analyses were carried out and compared with results obtained from conventional 2D finite element software. In each case, the material was assumed to be elastic-perfectly plastic (no strain hardening), and only one load type was considered. Under these conditions, only one cycle of loading and unloading is needed to attain the shakedown residual stress state, and the conventional approach of incremental elastic-plastic analysis can be applied.

The first case involved the same thick-walled cylinder that was used in the validation of the elastic contact stress software. Convergence to agreement with the conventional solution was demonstrated by means of the same mesh refinement technique. The results for this case suggested that the quality of the residual stress solution was influenced by the elastic contact stress solution, as well as by grid density.

In the second case, the MU wheel model was subjected to a cycle of temperature gradients and thermal stresses representing a stop from 128 km/h (80 mph) at 0.091 g (2 mph/s) with 154.6 kN (17.4 ton) axle load. The time histories of the temperature and elastic thermal stress were supplied by the Volpe Center. Since there were no contact forces involved in this example, the medium-density finite element grid was used in order to allow the conventional analysis to be run.

Since the material properties depend on temperature, the yield strength is a function of both time and location in the wheel cross section, as well as the elastic thermal stress. The simplest way to carry out a shakedown analysis under such conditions is to consider only the maximum magnitude of the thermal stresses, an approach that would be fully justified if the yield strength were constant. To obtain accurate results, however, it was found necessary to treat the thermal stresses at a number of discrete times as different load types and to apply a modification of the heuristic procedure outlined earlier for dealing with shifting contact locations. The main purpose of this test was to validate this extension and to determine the number of such load types needed for acceptable solution quality. In the modified procedure, the elastic thermal stress solution was first used to determine the discrete times at which the first and last occurrences of yielding would be expected; the period between these times was then divided into equal intervals, and the thermal stresses at the ends of the intervals were used as the load types. Solutions with 8 and 15 load types agreed reasonably well with the conventional finite element results, and the two shakedown solutions also agreed closely, indicating the achievement of convergence.

Several additional example analyses of shakedown stresses in MU wheels were carried out in order to demonstrate the software capabilities. In most cases, the load environment factors

were considered either individually or in pairs in order to illustrate their interactions. The results led to the following observations:

- Wheel/rail contact loading with or without shifting of the contact location gave results that were qualitatively similar to the solutions for rail residual stress. For example, both hoop stress in the wheel and axial stress in the rail consisted of a tension zone underlying a compression zone just below the tread surface.

- Lateral shifting of the contact location broadens the residual stress patterns and also causes some increase in the hoop stress magnitude.

- When the contact loading includes longitudinal tangent forces, antisymmetric residual shear stresses occur, and their magnitudes are on the order of 10 to 30% of the normal stress magnitudes. The magnitude of the axisymmetric shear stress component is also increased by about 20%, relative to its magnitude when the contact loading is limited to pressure. However, longitudinal tangent forces of the amount studied ($L/P = 0.2$) have no significant effect on the magnitude of residual hoop stress.

- In order to obtain accurate results when longitudinal tangent forces are included, it is necessary to define a number of wheel cross section planes at intervals through the contact zone, to treat the elastic contact stresses in each plane as the results of an individual load type, and to apply a heuristic procedure similar to the one described above for the thermal stresses. Close agreement was obtained from cases in which 9 and 17 load types were so defined. In contrast, a shakedown analysis with only pressure loading requires only one load type (the stresses in the cross section plane containing the center of contact).

- Loading due to the thermal stress cycle only, as was used in the validation example, can also be viewed as a simulation of a wheel subjected to inductive heating or dynamometer drag braking. The resulting shakedown state includes, as expected, quite large tensile residual hoop stresses in the outer rim region.

- When contact loads without shifting and thermal stresses due to stop braking are considered in combination, the compressive hoop residual stress layer just below the tread surface is decreased in magnitude under the contact zone and reversed to tension on either side of the contact zone.

- Thermal stresses due to stop braking were also considered in combination with initial manufacturing stresses. The initial stresses, obtained from a Volpe Center simulation of a rim quenching heat treatment, exhibited a deep layer of hoop compression in the rim. The computed stresses, representing the effect of repeated inductive heating or dynamometer drag braking, included a reversal to residual hoop tension in the outer rim region.

The foregoing results lead to the following general conclusions. First, the wheel shakedown stress software has been validated as far as regards its basic logic and the quality of stress solutions obtained under the given assumptions. Second, the extra computational effort required to consider tangent as well as pressure loads is not justified for low load ratios (L/P not exceeding 0.2) in view of the lack of significant effect on the stress of most concern, but

such effort will likely be needed to evaluate high tractive effort wheels ($0.3 < L/P < 0.4$). Third, the predicted effects and interactions appear to be consistent with expectations based on field experience.

A final step in the validation process still remains to be taken, namely: detailed comparison of the model predictions with field experience. Work on this step is now in progress, based on the MU field experience, and will be the subject of a later report. In view of the results already demonstrated, it appears reasonable to expect that this last step will provide the practical key to interpretation of the model results, namely: the level at which predicted hoop stress reduction or reversal should be considered to indicate loss of resistance to thermal cracking.

1. INTRODUCTION

This report is the seventh of a series on the results of an engineering study of the effects of service loads on railroad vehicle wheels. The study began in September 1991, in response to a request for assessment of contributing factors and corrective actions taken regarding high rates of crack occurrence in certain multiple unit (MU) power cars used in commuter service. The ultimate goal of the study is the evaluation of safe limits on performance demand (weight carried per wheel, maximum speed, vehicle braking rate) as a function of wheel design, material selection, and manufacture, as well as percentage of braking effort absorbed through the wheel tread. The models developed in the study are intended to provide the capability for similar engineering design analyses of other railroad vehicle wheels besides the types used on MU cars.

1.1 BACKGROUND

Special inspections of commuter rail vehicles conducted by the Federal Railroad Administration (FRA) Office of Safety in 1991 revealed chronic problems of cracking in the wheels of MU cars operated by three railroads serving the Greater New York area. The car design types are similar, but the vehicle characteristics and wheel cracking features were found to have significant differences.

The highest rate of cracking was found in the wheels of moderate weight vehicles, operated at moderate speeds, and equipped with blended dynamic braking to supplement the wheel tread brakes. The wheel cracks in this fleet, predominantly of thermal origin at the front rim edge, were attributed to maintenance problems: (1) dispatching of vehicles with inoperative traction motors, and thus also inoperative dynamic braking; and (2) inadequate tread brake unit refurbishment, leading to brake shoes riding over the front rim edge.

A comparable rate of cracking was found in the wheels of moderate weight vehicles, operated at high speed (100 mph), and equipped solely with tread brakes. The wheel cracks in this fleet, of thermal origin in the center tread position, were attributed to the demand for heat absorption through the tread imposed by high-speed operation without auxiliary brakes.

A lower rate of cracking with mixed thermal and mechanical origins was found in the third fleet. This fleet consists of heavy vehicles, operated at moderate speeds, and equipped with blended dynamic braking to supplement the tread brakes. Vehicle weight, heat input to the wheel tread, and occasional maintenance problems were identified as the factors contributing to wheel cracks in this case.

The FRA Office of Safety took immediate action to address identified maintenance problems, set requirements for daily inspection of wheels in service, and required re-profiling of wheels found to have cracks before returning them to service. Each affected railroad also started to take longer term actions and develop options for lasting solutions. Actions already taken include upgrade of material properties and adoption of an advanced plate design in the specifications for new wheel orders and, for those MU cars not so equipped, retrofit of new motors with dynamic braking capability.

1.2 PRELIMINARY STUDIES

Preliminary studies undertaken from September 1991 through September 1992 included reviews of wheel maintenance records, fluorescent magnetic particle inspections of wheels removed from service to locate and measure cracks, saw cutting of a new wheel and one

removed from service for estimation of residual stresses in the rim, metallographic examinations, hardness testing, fractography, laboratory simulation of the combined high temperature and rapid plastic compression experienced by wheel rims in service, and heat transfer calculations with an approximate model. The results of the preliminary studies suggested that cracks of thermal origin are the main concern, and that a process of shallow stress reversal is responsible for the formation of such cracks in the wheels of the MU cars [1].

Stress reversal (from hoop compression to tension) is a well known cause of thermal cracking and fracture in freight car wheels which have been subjected to repeated drag braking for long periods of time at low power, but in such cases the stress is usually reversed in the bulk of the rim, most of which is heated to high temperature. Conversely, typical stop-braking profiles involve high power for short periods of time and tend to flash-heat the outer rim region to temperatures much higher than those in the bulk of the rim. The thermal stresses, which are induced by temperature gradients, then concentrate in the outer rim region. Thus, wheel thermal response to stop-braking is not necessarily indicated by its response to drag-braking. Also, any subsequent drag-braking can apparently cause rapid propagation of thermal cracks which have formed under less severe conditions.

Based on these findings, the decision was made to develop a set of detailed finite element models which could be used to evaluate the potential for different types of wheels to resist cracking under various combinations of service conditions. The approach, relation between models, and relation of models to validation tests are outlined in the following section.

1.3 DETAILED ENGINEERING STUDIES

The wheels of a typical MU car experience on the order of 10^4 stop-braking events and 10^7 wheel/rail contact cycles in a year of service. Many stops and contact cycles are thus involved, even if rim stress is reversed in just a few days or weeks. The performance demand (weight carried per wheel, maximum speed, vehicle braking rate) may either modify or reverse the residual hoop stress in the rim. These outcomes can be distinguished by assuming that the modified or reversed stresses are stable, i.e., they are not changed simply by further repetition of the same performance demands after some period of service has elapsed. Such states, referred to as shakedown stresses, can be calculated from the known initial conditions (residual stress from manufacture) and descriptions of the loads imposed by repeated performance demands.

A recently developed method for estimating shakedown stresses in a body requires only that each load be described in terms of the stress magnitudes it would cause in the body, assuming purely elastic behavior [2]. This task is easily accomplished by means of elastic finite element stress analysis models. The method has been successfully applied to the problem of estimating shakedown stresses in rails [3], including cases in which initial conditions must be accounted for [4], [5]. This method can also be used to estimate wheel shakedown stresses, with both mechanical (weight per wheel) and thermal (braking) loads as inputs. The method is also computationally efficient because one can assume the sought shakedown state to be axially symmetric, based on the logical hypothesis that, for each location in the wheel profile, every material point around the circumference should experience substantially the same history of live stresses.

The block diagram in figure 1.1 illustrates the organization of models and tests required to develop a realistic procedure for estimating wheel shakedown stresses. The shaded blocks denote items covered in this report.

The dashed box encloses those items which constitute the inputs and output of the wheel shakedown stress model. The other blocks in figure 1.1 represent the tasks required to prepare the inputs for the shakedown stress model.

The theoretical paths are emphasized because the models can produce complete descriptions of input stresses which also conform to the laws of mechanical equilibrium. Completeness and conformity are necessary to avoid propagation and amplification of numerical errors in the shakedown stress calculations. Conversely, experimental stress analyses usually cover only part of the body, and the results often contain equilibrium errors when measurements are made on complex bodies such as wheels or rails. In spite of these limitations, experiments are still essential for checking the realism of the models.

Axisymmetric heat transfer and elastic stress finite element models have been used to compute the temperature and thermal stress distributions representing a variety of MU stop-braking events and braking systems configurations. The validation of and results obtained from these models were documented earlier (see bibliography of reports in this series). A thermal stress history for a moderate weight MU car braked at 2 mph/s from 80 mph to a full stop, as computed by these models, is used as an illustrative case for the thermal stress envelope in the work reported here.

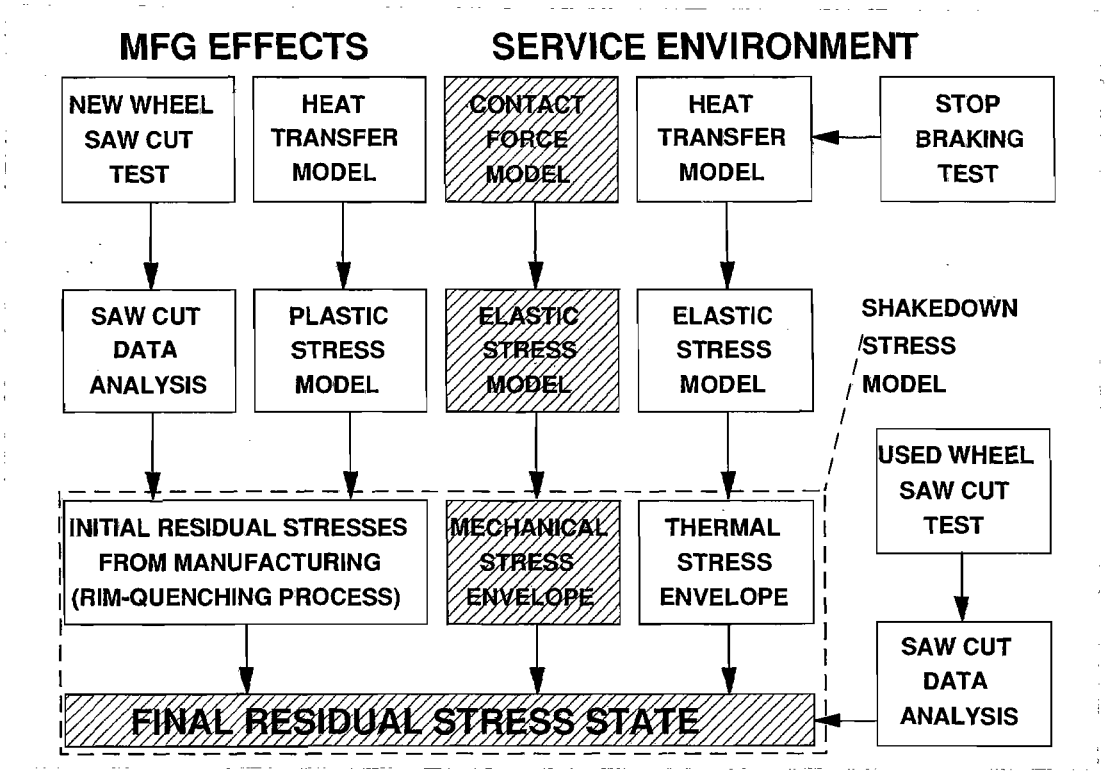

Figure 1.1 Model and Test Relationships

Estimation of the initial manufacturing stresses also requires experimental validation of models, activities which are still in progress. Axisymmetric heat transfer and elastic-plastic stress finite element models are being used to estimate the manufacturing stresses. Preliminary results in reasonable agreement with the available experimental data have been obtained [6] and are used for illustrative purposes as the initial manufacturing stress input in the work reported here.

This report describes the development and validation of modifications to the rail software [4] for the purpose of estimating shakedown stresses in wheels. The modifications include a change from cartesian to axisymmetric geometry, allowance for thermal as well as mechanical live stresses, wheel/rail contact areas of any specified shape and size, traction forces as well as axle loading, and temperature-dependent material properties.

The general treatment of wheel/rail contact loading requires a numerical approach to the computation of live mechanical stresses. These loads and stresses are not axisymmetric, but the stress computations can be dealt with in the format of an axisymmetric model by means of the Fourier harmonic method. Section 2 explains the formulation and summarizes the validation of this part of the model by reference to independently derived solutions of problems with simplified geometry.

The addition of temperature dependence to the material properties in the shakedown estimation model is also validated by reference to independently derived solutions, including one simplified example of a wheel assumed to be subjected only to thermal stress cycles. In such cases the shakedown state is the same as would be obtained from an incremental plasticity analysis of a single cycle, and the independent solution was thus computed with a well established commercial software package. This part of the validation and the results of several illustrative examples of wheel shakedown stress estimation are presented in section 3.

2. ELASTIC MODEL FOR ANALYSIS OF CONTACT STRESSES

This section covers all the matters associated with the development of an elastic model for analysis of contact stresses in railroad car wheels. Section 2.1 contains some introductory remarks dealing with possible ways of such analysis. Sections 2.2 and 2.3 describe the mechanical and numerical models, respectively. The above models have been implemented in two computer programs described in section 2.4. The approach has been validated by means of test problems formulated for a circular disk and a thick-walled cylinder. The results of these tests and their discussion are presented in section 2.5. Finally, the model has been applied to the evaluation of elastic contact stresses in a railroad car wheel subject to both normal and tangent tractions (section 2.6).

2.1 INTRODUCTORY SECTION

The subject of this section is analysis of elastic stresses in a selected class of axisymmetric bodies subject to contact loading. The purpose of the work is to formulate a reliable method of analysis of such stresses in railroad car wheels under normal and tangent tractions.

In general, there are two approaches to the problem of analysis of elastic contact stresses. The first one is mainly based on analytical formulae and certain experimental observations. The second approach takes advantage of numerical methods, especially of the finite element method.

As far as the first approach is concerned, the engineering design of rail and wheel profiles is traditionally based on the simplified application of the Hertz contact theory [7]. Both the rail and the wheel are modelled as circular cylinders crossing at right angles. The cylinder radii are defined as the design crown radius of the rail and the design nominal rolling radius of the wheel, respectively. The normal load pressing the cylinders together is defined as equal to the design static load supported by the wheel. The contact area is an ellipse with semi-major axis A and semi-minor axis B computed by means of the Hertz formulae. The normal pressure distribution over the contact zone is given by

$$p(X,Y) = p_0\sqrt{1-\left(\frac{X}{A}\right)^2-\left(\frac{Y}{B}\right)^2} \tag{2.1}$$

with respect to tangent-plane coordinates (X,Y) and with the origin at the center of the contact zone. The peak pressure p_0 is also computed using the Hertz formulae. The main task in the next step of this approach is to compute the corresponding stresses. This is usually done by means of integration of the classical Boussinesq influence functions [7] for stresses due to a unit normal force acting at a surface point on an unbounded half space. In this case the pressure distribution determined from the Hertz formulae plays the role of a weighting function. A similar approach may be applied in case of a tangent load using the classical Cerruti influence functions [7] for stresses due to a unit tangent force acting at a surface point on an unbounded half space.

The main disadvantage of this approach is quite restrictive assumptions concerning the shape of the surfaces in contact. As for the shape of the contact zone and the distribution of the surface tractions, they can be modified quite easily in order to take into account real conditions, e.g., to deal with offset contacts (by introducing local radii, including the third radius representing the wheel profile curvature) or to comply with experimental observations. On the contrary, the application of simplified formulae for stress distributions may result in significant violation of the equilibrium equations and the static boundary conditions.

As regards the second approach, numerical methods seem to be the most powerful methods of analysis of contact problems. They allow not only to take into account the real geometry of the bodies in contact and their material properties but also to model the contact phenomenon including all accompanying effects. The problem could be solved using one of the widespread finite element analysis programs. However, their practical applications in the case under consideration are limited, especially when one takes into account the fact that the problem is fully three-dimensional, the shapes of the wheel and rail are quite complex, and the size of the contact zone is very small. It implies application of meshes that consist of a huge number of finite elements. The analysis becomes extremely memory- and time-consuming, not to mention all the problems connected with mesh generation.

In this work, the main purpose of the elastic analysis of contact stresses is to provide essential input data for the elastic-plastic analysis of residual stresses. The elastic analysis usually has to be performed repeatedly, especially when multiple loading paths are considered. That is why it has been decided to apply a simplified approach to the problem. Both the shape and size of the contact zone and the surface tractions as well are treated as known data, usually but not necessarily obtained by means of the Hertz formulae. The approach also allows one to eliminate the rail from the analysis and to take advantage of the axisymmetric shape of the wheel. The key point in this approach is that the external loads can be expanded in the Fourier series and the complete analysis can be performed by superimposing the response due to the symmetric and antisymmetric load contributions. The problem is still three-dimensional but only a selected radial plane has to be discretized. This allows one to reduce significantly the total number of unknown variables and consequently the required amount of computer memory, unfortunately at the expense of central processor time. This approach is described in section 2.3.

2.2 MECHANICAL MODEL

Let a body be in a state of static equilibrium under the action of body forces $\overline{F}_i(\mathbf{x})$ in V, surface tractions $\overline{T}_i(\mathbf{x})$ on ∂V_σ, and displacements $\overline{u}_i(\mathbf{x})$ on ∂V_u, where V is the volume occupied by the body, ∂V_σ and ∂V_u are parts of the boundary surface ∂V, $\mathbf{x}$ represents a point of the body, and $i = 1, 2, 3$.

It has been assumed that both the stress-strain and strain-displacement relations are linear. These assumptions, usually considered to be very restrictive in analysis of contact stresses, are consistent with the assumptions underlying the model for analysis of residual stresses (section 3) where elastic stresses are used as input data.

Thus, the problem of analysis of elastic stresses is the classical boundary value problem of linear elasticity and may be solved using the minimum total potential energy principle [8]. This principle may be stated in the form of the following optimization problem:

Find the minimum of the total potential energy functional

$$\Pi = \int_V \frac{1}{2}\varepsilon_{ij} E_{ijkl} \varepsilon_{kl}\, dV - \int_V u_i \overline{F}_i\, dV - \int_{\partial V_\sigma} u_i \overline{T}_i\, dS \tag{2.2}$$

with respect to the displacement field $u_i(\mathbf{x})$ satisfying the kinematical boundary conditions

$$u_i = \overline{u}_i \qquad \text{on } \partial V_u, \tag{2.3}$$

where $\varepsilon_{ij}(\mathbf{x})$ is the strain field related to the displacement field $u_i(\mathbf{x})$ by

$$\varepsilon_{ij} = \frac{1}{2}\left(\frac{\partial u_i}{\partial x_j} + \frac{\partial u_j}{\partial x_i}\right) \tag{2.4}$$

and E_{ijkl} is the tensor of elasticity coefficients that relates the stress field $\sigma_{ij}(\mathbf{x})$ to the strain field $\varepsilon_{ij}(\mathbf{x})$ in generalized Hooke's law

$$\sigma_{ij} = E_{ijkl}\varepsilon_{kl}. \tag{2.5}$$

For proof of the minimum total potential energy principle, the reader is referred to [8].

2.3 NUMERICAL MODEL

This section describes the numerical model applied to the analysis of elastic stresses. It has been divided into three parts. The first part presents some basics of the finite element method, its concepts and notation. The second and third parts deal with the detailed description of the finite element that has been implemented in the computer programs worked out for the problem under consideration.

2.3.1 Finite-Element Formulation

The numerical model applied to the analysis of elastic stresses is the displacement model of the finite element method. It may be derived from the minimum total potential energy principle (see the previous section). The region of the body V is divided into a finite number N_e disjoint subregions V_n (finite elements) and the functional (2.2) is written (using matrix notation) in the form

$$\Pi = \sum_{n=1}^{N_e} \pi_n \tag{2.6}$$

in which

$$\pi_n = \int_{V_n} \frac{1}{2}\boldsymbol{\varepsilon}^T \mathbf{E}\boldsymbol{\varepsilon}\, dV - \int_{V_n} \mathbf{u}^T \overline{\mathbf{F}}\, dV - \int_{(\partial V_\sigma)_n} \mathbf{u}^T \overline{\mathbf{T}}\, dS, \tag{2.7}$$

where $(\partial V_\sigma)_n$ denotes the part of ∂V_σ that belongs to the nth element.

For each finite element, the displacements $\mathbf{u}$ are represented in the following form

$$\mathbf{u} = \mathbf{N}\mathbf{q}_n \tag{2.8}$$

where $\mathbf{N}$ is the displacement interpolation matrix and $\mathbf{q}_n$ is the vector of generalized displacements defined at a finite number of nodal points of the element. The corresponding strains $\boldsymbol{\varepsilon}$, related to the displacements $\mathbf{u}$ by (2.4), and stresses $\boldsymbol{\sigma}$, related to the strains $\boldsymbol{\varepsilon}$ by (2.5), can also be expressed in terms of the generalized displacements $\mathbf{q}_n$, that is

$$\boldsymbol{\varepsilon} = \mathbf{L}\mathbf{u} = \mathbf{L}\mathbf{N}\mathbf{q}_n = \mathbf{B}\mathbf{q}_n, \tag{2.9}$$

$$\boldsymbol{\sigma} = \mathbf{E}\boldsymbol{\varepsilon} = \mathbf{E}\mathbf{B}\mathbf{q}_n \tag{2.10}$$

where $\mathbf{L}$ is the matrix of differential operators and $\mathbf{B}$ is the strain interpolation matrix.

The substitution of (2.8) and (2.9) into (2.7) results in

$$\pi_n = \frac{1}{2}\mathbf{q}_n^T \mathbf{k}_n \mathbf{q}_n - \mathbf{q}_n^T \mathbf{Q}_n \tag{2.11}$$

in which

$$\mathbf{k}_n = \int_{V_n} \mathbf{B}^T \mathbf{E} \mathbf{B}\, dV \tag{2.12}$$

and

$$\mathbf{Q}_n = \int_{V_n} \mathbf{N}^T \overline{\mathbf{F}}\, dV + \int_{(\partial V_\sigma)_n} \mathbf{N}^T \overline{\mathbf{T}}\, dS \tag{2.13}$$

are, respectively, the element stiffness matrix and the vector of generalized forces due to loads acting on the element.

Finally, the substitution of (2.11) into (2.6) yields

$$\Pi = \sum_{n=1}^{N_e} \left(\frac{1}{2}\mathbf{q}_n^T \mathbf{k}_n \mathbf{q}_n - \mathbf{q}_n^T \mathbf{Q}_n \right) \tag{2.14}$$

which may be written in the following short form

$$\Pi = \frac{1}{2}\mathbf{q}^T \mathbf{K} \mathbf{q} - \mathbf{q}^T \mathbf{Q}, \tag{2.15}$$

where $\mathbf{K}$ is the stiffness matrix of the whole domain, $\mathbf{q}$ is the vector of total generalized displacements, and $\mathbf{Q}$ is the vector of total generalized forces. The total generalized displacements $\mathbf{q}$ can be found as such values that satisfy the kinematical boundary conditions (2.3) and minimize the total potential energy of the body (2.15). After they have been determined, the corresponding strains $\boldsymbol{\varepsilon}$ and stresses $\boldsymbol{\sigma}$ can be evaluated using formulae (2.9) and (2.10). For more extensive description of the finite element method and its techniques, the reader is referred to [9], [10], [11].

2.3.2 Axisymmetric Element with Non-Symmetric Deformation

The subject of analysis is an axisymmetric body subject to non-symmetric external loads. It has been assumed that the loads can be represented by means of the Fourier series. Taking into account the well-known orthogonality properties of these series and assuming that the material of the body is linear elastic, uncoupling between the Fourier modes occurs and the analysis can be performed by superimposing the response of the body due to the symmetric and antisymmetric load contributions. Thus, the description of the finite element can be simplified significantly [9], [11].

In the case under consideration, it is convenient to describe the problem in the system of cylindrical coordinates (r, φ, z). Some of the relations just presented can be rewritten almost automatically and it will be done without any extensive comment. The other relations, especially those connected with the strain interpolation matrix and element

stiffness matrix, will be discussed in detail to provide assistance in case the computer programs have to be modified.

The first goal of the analysis is to describe the external loads and their Fourier representation. The vector of surface tractions $\overline{\mathbf{T}}$ can be written in the following form

$$\overline{\mathbf{T}}^T(\varphi,s) = \left\{ \overline{T}_r(\varphi,s) \quad \overline{T}_\varphi(\varphi,s) \quad \overline{T}_z(\varphi,s) \right\} \tag{2.16}$$

in which

$$\begin{aligned}
\overline{T}_r(\varphi,s) &= \sum_{l=0}^{L} \left[\overline{T}^s_{rl}(s)\cos l\varphi + \overline{T}^a_{rl}(s)\sin l\varphi \right], \\
\overline{T}_\varphi(\varphi,s) &= \sum_{l=0}^{L} \left[\overline{T}^s_{\varphi l}(s)\sin l\varphi + \overline{T}^a_{\varphi l}(s)\cos l\varphi \right], \\
\overline{T}_z(\varphi,s) &= \sum_{l=0}^{L} \left[\overline{T}^s_{zl}(s)\cos l\varphi + \overline{T}^a_{zl}(s)\sin l\varphi \right]
\end{aligned} \tag{2.17}$$

where the indices s and a denote the symmetric and antisymmetric load contributions, respectively. Almost identical expansions can also be written for body forces, boundary conditions, etc. The coordinate s represents any local coordinate that allows one to describe the surface tractions uniquely for all points of the boundary surface. Usually, it is identified with the axial coordinate z except for flat vertical parts of the boundary surface where the radial coordinate r is used instead.

In order to simplify the notation, further considerations will be restricted to the symmetric load contributions and only the lth Fourier mode will be taken into account (consequently, the indices s, a, and l will be omitted). For the antisymmetric loading, the sine function should be replaced by the cosine function and vice versa. When derivatives are calculated (matrix $\mathbf{B}$), such replacement is sometimes accompanied by the change in the sign.

The vector of displacements $\mathbf{u}$, the vector of generalized displacements $\mathbf{q}_n$, and the displacement interpolation matrix $\mathbf{N}$ defined in (2.9) can be written in the system of cylindrical coordinates as follows

$$\mathbf{u}^T(r,\varphi,z) = \left\{ u_r(r,\varphi,z) \quad u_\varphi(r,\varphi,z) \quad u_z(r,\varphi,z) \right\}, \tag{2.18}$$

$$\mathbf{q}_n^T = \left\{ \mathbf{q}_1^T \quad \dots \quad \mathbf{q}_k^T \right\}, \tag{2.19}$$

$$\mathbf{N}(r,\varphi,z) = \left[\mathbf{N}_1(r,\varphi,z) \quad \dots \quad \mathbf{N}_k(r,\varphi,z) \right] \tag{2.20}$$

in which

$$\mathbf{q}_i^T = \left\{ q_{ri} \quad q_{\varphi i} \quad q_{zi} \right\}, \qquad i = 1, \dots, k, \tag{2.21}$$

$$\mathbf{N}_i(r,\varphi,z) = \begin{bmatrix} N_i(r,z)\cos l\varphi & 0 & 0 \\ 0 & N_i(r,z)\sin l\varphi & 0 \\ 0 & 0 & N_i(r,z)\cos l\varphi \end{bmatrix} \tag{2.22}$$

where k is equal to the number of nodal points of the element, $\mathbf{q}_i$ is the vector of generalized nodal displacements at the ith node of the element, and N_i is the shape function associated

with this node. Such assemblage of different parameters connected with nodal points of finite elements will be used quite frequently. It corresponds to the structure of the computer programs. There also exists an opposite approach where the information of the same type is grouped for the whole element or even for the whole structure. In spite of the fact that it usually allows one to describe the problem much more concisely, it is rarely implemented in computer codes.

Further analysis requires the relations (2.9) and (2.10) also to be specified in the system of cylindrical coordinates. The stress $\boldsymbol{\sigma}$ and strain $\boldsymbol{\varepsilon}$ vectors, and the matrix of differential operators $\mathbf{L}$ can be written as follows

$$\boldsymbol{\varepsilon}^T = \left\{ \varepsilon_{rr} \quad \varepsilon_{\varphi\varphi} \quad \varepsilon_{zz} \quad \gamma_{r\varphi} \quad \gamma_{\varphi z} \quad \gamma_{rz} \right\}, \tag{2.23}$$

$$\boldsymbol{\sigma}^T = \left\{ \sigma_{rr} \quad \sigma_{\varphi\varphi} \quad \sigma_{zz} \quad \tau_{r\varphi} \quad \tau_{\varphi z} \quad \tau_{rz} \right\}, \tag{2.24}$$

$$\mathbf{L} = \begin{bmatrix} \dfrac{\partial}{\partial r} & 0 & 0 \\ \dfrac{1}{r} & \dfrac{1}{r}\dfrac{\partial}{\partial \varphi} & 0 \\ 0 & 0 & \dfrac{\partial}{\partial z} \\ \dfrac{1}{r}\dfrac{\partial}{\partial \varphi} & \dfrac{\partial}{\partial r} - \dfrac{1}{r} & 0 \\ 0 & \dfrac{\partial}{\partial z} & \dfrac{1}{r}\dfrac{\partial}{\partial \varphi} \\ \dfrac{\partial}{\partial z} & 0 & \dfrac{\partial}{\partial r} \end{bmatrix}. \tag{2.25}$$

The form of the matrix of elasticity coefficients $\mathbf{E}$ does not depend on the system of coordinates, that is

$$\mathbf{E} = \frac{E}{(1+\nu)(1-2\nu)} \begin{bmatrix} 1-\nu & \nu & \nu & 0 & 0 & 0 \\ & 1-\nu & \nu & 0 & 0 & 0 \\ & & 1-\nu & 0 & 0 & 0 \\ & & & \dfrac{1-2\nu}{2} & 0 & 0 \\ & \text{sym} & & & \dfrac{1-2\nu}{2} & 0 \\ & & & & & \dfrac{1-2\nu}{2} \end{bmatrix} \tag{2.26}$$

where E is Young's modulus and ν is Poisson's ratio.

Before the strain interpolation matrix $\mathbf{B}$ is derived, it is convenient, as it was done in (2.19) and (2.20), to divide it into submatrices that are associated with the nodal points of the element

$$\mathbf{B} = [\,\mathbf{B}_1 \quad \dots \quad \mathbf{B}_k\,]. \tag{2.27}$$

The substitution of (2.27), (2.25), (2.20), and (2.22) into (2.9) results in

$$\mathbf{B}_i = \begin{bmatrix} \dfrac{\partial N_i}{\partial r}\cos l\varphi & 0 & 0 \\ \dfrac{N_i}{r}\cos l\varphi & l\dfrac{N_i}{r}\cos l\varphi & 0 \\ 0 & 0 & \dfrac{\partial N_i}{\partial z}\cos l\varphi \\ -l\dfrac{N_i}{r}\sin l\varphi & \left(\dfrac{\partial N_i}{\partial r} - \dfrac{N_i}{r}\right)\sin l\varphi & 0 \\ 0 & \dfrac{\partial N_i}{\partial z}\sin l\varphi & -l\dfrac{N_i}{r}\sin l\varphi \\ \dfrac{\partial N_i}{\partial z}\cos l\varphi & 0 & \dfrac{\partial N_i}{\partial r}\cos l\varphi \end{bmatrix}. \tag{2.28}$$

Consequently, before the element stiffness matrix $\mathbf{k}_n$ is computed, the integrand in (2.12) should be decomposed, to yield

$$\mathbf{B}^T\mathbf{E}\mathbf{B} = \begin{bmatrix} \mathbf{B}_1^T \\ \vdots \\ \mathbf{B}_k^T \end{bmatrix} \mathbf{E}\,[\,\mathbf{B}_1 \quad \dots \quad \mathbf{B}_k\,] = \begin{bmatrix} \mathbf{B}_1^T\mathbf{E}\mathbf{B}_1 & \dots & \mathbf{B}_1^T\mathbf{E}\mathbf{B}_k \\ & \ddots & \vdots \\ \text{sym} & & \mathbf{B}_k^T\mathbf{E}\mathbf{B}_k \end{bmatrix} \tag{2.29}$$

in which

$$\mathbf{B}_i^T\mathbf{E}\mathbf{B}_j = \frac{E}{(1+\nu)(1-2\nu)} \begin{bmatrix} k_{11} & k_{12} & k_{13} \\ & k_{22} & k_{23} \\ **\text{sym}** & & k_{33} \end{bmatrix}. \tag{2.30}$$

It should be stressed that the matrix in (2.30) is not symmetric. The abbreviation **sym** is used to point out that the components of the lower triangular part of the matrix may be computed using the expressions for the corresponding symmetric components of the upper part but at the same time the indices i and j have to be exchanged i.e.

$$k_{mn}(i,j) = k_{nm}(j,i). \tag{2.31}$$

The substitution of (2.28) with the appropriate indices and (2.26) into the left-hand side of (2.30) results in the following expressions for the components of the matrix on the

right-hand side of (2.30)

$$k_{11} = (1-\nu)\frac{\partial N_i}{\partial r}\frac{\partial N_j}{\partial r}\cos^2 l\varphi + \nu\frac{\partial N_i}{\partial r}\frac{N_j}{r}\cos^2 l\varphi + \nu\frac{N_i}{r}\frac{\partial N_j}{\partial r}\cos^2 l\varphi + \left[(1-\nu)\cos^2 l\varphi + \frac{1-2\nu}{2}l^2\sin^2 l\varphi\right]\frac{N_i}{r}\frac{N_j}{r} + \frac{1-2\nu}{2}\frac{\partial N_i}{\partial z}\frac{\partial N_j}{\partial z}\cos^2 l\varphi, \tag{2.32a}$$

$$k_{12} = \nu l\frac{\partial N_i}{\partial r}\frac{N_j}{r}\cos^2 l\varphi - \frac{1-2\nu}{2}l\frac{N_i}{r}\frac{\partial N_j}{\partial r} + \left[(1-\nu)\cos^2 l\varphi + \frac{1-2\nu}{2}\sin^2 l\varphi\right]l\frac{N_i}{r}\frac{N_j}{r}, \tag{2.32b}$$

$$k_{13} = \nu\frac{\partial N_i}{\partial r}\frac{\partial N_j}{\partial z}\cos^2 l\varphi + \frac{1-2\nu}{2}\frac{\partial N_i}{\partial z}\frac{\partial N_j}{\partial r}\cos^2 l\varphi + \nu\frac{N_i}{r}\frac{\partial N_j}{\partial z}\cos^2 l\varphi, \tag{2.32c}$$

$$k_{22} = \frac{1-2\nu}{2}\frac{\partial N_i}{\partial r}\frac{\partial N_j}{\partial r}\sin^2 l\varphi - \frac{1-2\nu}{2}\frac{\partial N_i}{\partial r}\frac{N_j}{r}\sin^2 l\varphi - \frac{1-2\nu}{2}\frac{N_i}{r}\frac{\partial N_j}{\partial r}\sin^2 l\varphi + \left[(1-\nu)l^2\cos^2 l\varphi + \frac{1-2\nu}{2}\sin^2 l\varphi\right]\frac{N_i}{r}\frac{N_j}{r} + \frac{1-2\nu}{2}\frac{\partial N_i}{\partial z}\frac{\partial N_j}{\partial z}\sin^2 l\varphi, \tag{2.32d}$$

$$k_{23} = \nu l\frac{N_i}{r}\frac{\partial N_j}{\partial z}\cos^2 l\varphi - \frac{1-2\nu}{2}l\frac{\partial N_i}{\partial z}\frac{N_j}{r}\sin^2 l\varphi, \tag{2.32e}$$

$$k_{33} = \frac{1-2\nu}{2}\frac{\partial N_i}{\partial r}\frac{\partial N_j}{\partial r}\cos^2 l\varphi + \frac{1-2\nu}{2}l^2\frac{N_i}{r}\frac{N_j}{r}\sin^2 l\varphi + (1-\nu)\frac{\partial N_i}{\partial z}\frac{\partial N_j}{\partial z}\cos^2 l\varphi. \tag{2.32f}$$

Finally, the integrand in the second term of (2.13) should be found (in case of the body forces the procedure is identical). Using the same approach as before, it can be written as follows

$$\mathbf{N}^T\overline{\mathbf{T}} = \begin{bmatrix}\mathbf{N}_1^T\\ \vdots \\ \mathbf{N}_k^T\end{bmatrix}\overline{\mathbf{T}} = \begin{bmatrix}\mathbf{N}_1^T\overline{\mathbf{T}}\\ \vdots \\ \mathbf{N}_k^T\overline{\mathbf{T}}\end{bmatrix} \tag{2.33}$$

in which

$$\mathbf{N}_i^T\overline{\mathbf{T}} = \begin{Bmatrix} N_i\overline{T}_r\cos^2 l\varphi \\ N_i\overline{T}_\varphi\sin^2 l\varphi \\ N_i\overline{T}_z\cos^2 l\varphi\end{Bmatrix}. \tag{2.34}$$

This way, the most important formulae that allow one to compute the element stiffness matrix $\mathbf{k}_n$ and the vector of the generalized forces $\mathbf{Q}_n$, defined respectively in (2.12) and

(2.13), have been derived. After the displacement interpolation matrix **N** has been assumed, the appropriate integration (usually numerical) can be performed and both the matrices can be assembled. The integration should be carried out in the system of cylindrical coordinates, that is

$$\int_{V_n} f(x,y,z)\,dV = \int_0^{2\pi}\int_{A_n} f(r,\varphi,z)\,r\,dr\,d\varphi\,dz, \tag{2.35a}$$

$$\int_{(\partial V_\sigma)_n} f(x,y,z)\,dS = \int_0^{2\pi}\int_{s_n} f(r,\varphi,z)\,r\,ds\,d\varphi \tag{2.35b}$$

where A_n is the area of the nth element and s_n denotes the side of the element that belongs to $(\partial V_\sigma)_n$. In the above finite-element formulae, the only functions that depend on φ are the trigonometric functions, so the integration along the circumference may be carried out separately. Additionally, taking into account the following integrals

$$\int_0^{2\pi} \cos^2 l\varphi\,d\varphi = \begin{cases} 2\pi, & \text{if } l = 0 \\ \pi, & \text{if } l = 1, 2, \ldots \end{cases}, \tag{2.36a}$$

$$\int_0^{2\pi} \sin^2 l\varphi\,d\varphi = \begin{cases} 0, & \text{if } l = 0 \\ \pi, & \text{if } l = 1, 2, \ldots \end{cases} \tag{2.36b}$$

the formulae can be simplified significantly.

2.3.3 Quadrilateral Finite Element

The finite element applied to the analysis of elastic stresses is the isoparametric four-node element with the bilinear interpolation of the displacement field. It corresponds to the element that is used for the analysis of residual stresses in order to simplify the process of data preparation.

All the elements are described in the system of global coordinates (r,z) defined on a selected radial plane. In general, they are irregular quadrilateral elements (figure 2.1a) and that is why it is convenient first to transform them into squares (figure 2.1b) and then to construct the interpolation functions only for one typical element. For the case under consideration, the transformation can be written as follows

$$\begin{aligned} r &= \sum_{i=1}^{4} f_i(\xi,\eta) r_i, \\ z &= \sum_{i=1}^{4} f_i(\xi,\eta) z_i \end{aligned} \tag{2.37}$$

in which

$$f_i(\xi,\eta) = \frac{1}{4}(1+\xi\xi_i)(1+\eta\eta_i) \tag{2.38}$$

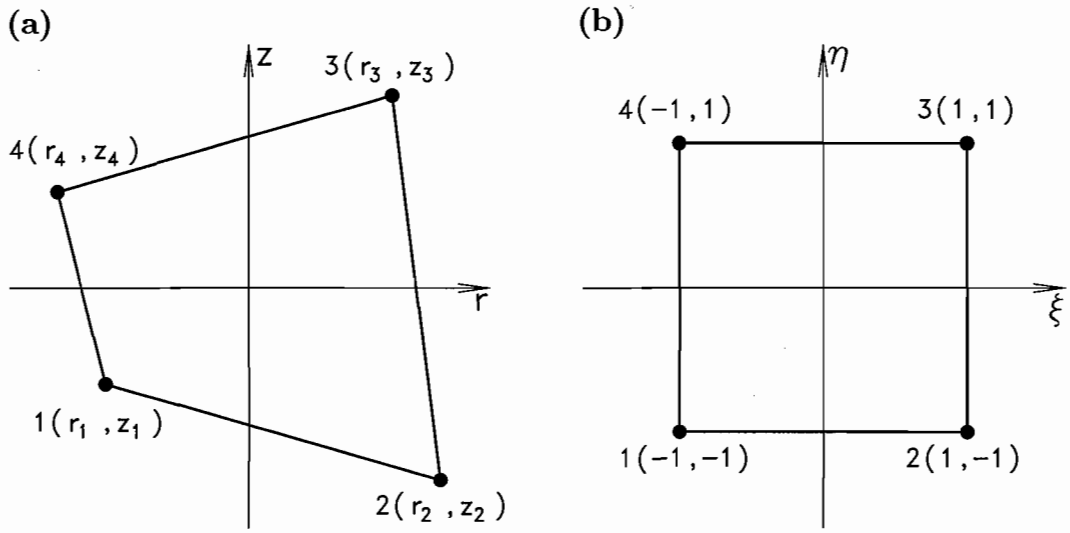

Figure 2.1 Quadrilateral Finite Element

where (r_i, z_i) and (ξ_i, η_i) are the coordinates of the nodes in the systems of global and local coordinates, respectively.

The computation of the basic finite-element matrices requires the differentiation and integration in the system of global coordinates (r, z). However, both these operations can also be carried out in the system of local coordinates (ξ, η) using the following relations

$$\begin{Bmatrix} \dfrac{\partial}{\partial r} \\ \dfrac{\partial}{\partial z} \end{Bmatrix} = \mathbf{J}^{-1} \begin{Bmatrix} \dfrac{\partial}{\partial \xi} \\ \dfrac{\partial}{\partial \eta} \end{Bmatrix}, \tag{2.39}$$

$$\int_{A_n} g(r,z)\, dr\, dz = \int_{-1}^{1}\int_{-1}^{1} g(\xi,\eta)\, |\det \mathbf{J}|\, d\xi\, d\eta \tag{2.40}$$

where

$$\mathbf{J} \equiv \begin{bmatrix} \dfrac{\partial r}{\partial \xi} & \dfrac{\partial z}{\partial \xi} \\ \dfrac{\partial r}{\partial \eta} & \dfrac{\partial z}{\partial \eta} \end{bmatrix} \tag{2.41}$$

is the Jacobian matrix (operator) relating the global coordinate derivatives to the local coordinate derivatives and

$$\det \mathbf{J} \equiv \frac{\partial r}{\partial \xi}\frac{\partial z}{\partial \eta} - \frac{\partial r}{\partial \eta}\frac{\partial z}{\partial \xi} \tag{2.42}$$

is the determinant of the Jacobian matrix. The substitution of (2.37) and (2.38) into (2.41) and (2.42) results in

$$\mathbf{J} = \begin{bmatrix} a_1 + a_3\eta & b_1 + b_3\eta \\ a_2 + a_3\xi & b_2 + b_3\xi \end{bmatrix}, \tag{2.43}$$

$$\det \mathbf{J} = a_1 b_2 - a_2 b_1 + (a_1 b_3 - a_3 b_1)\,\xi + (a_3 b_2 - a_2 b_3)\,\eta \tag{2.44}$$

where

$$\begin{cases} a_1 = \dfrac{1}{4}(-r_1 + r_2 + r_3 - r_4) \\ a_2 = \dfrac{1}{4}(-r_1 - r_2 + r_3 + r_4) \\ a_3 = \dfrac{1}{4}(\ \ r_1 - r_2 + r_3 - r_4) \end{cases}, \qquad \begin{cases} b_1 = \dfrac{1}{4}(-z_1 + z_2 + z_3 - z_4) \\ b_2 = \dfrac{1}{4}(-z_1 - z_2 + z_3 + z_4) \\ b_3 = \dfrac{1}{4}(\ \ z_1 - z_2 + z_3 - z_4) \end{cases}. \tag{2.45}$$

As far as the shape functions N_i are concerned, they are assumed to have exactly the same form as the transformation functions (2.38), that is

$$N_i(\xi, \eta) = f_i(\xi, \eta). \tag{2.46}$$

2.4 COMPUTER PROGRAMS

The mechanical and numerical models described in the previous sections have been implemented in two computer programs called `WHEELE` and `FOURIER`. Taking into account the goal of the work, both programs have been especially tailored for the analysis of elastic stresses in railroad car wheels subject to contact loads. However, their structures have been chosen so that they can be modified quite easily in order to include other types of loading. This section contains only some basic information about the programs.

The program `WHEELE` is a finite element code that allows one to solve the problem of analysis of elastic stresses in an axisymmetric body subject to external loads represented by means of the Fourier series. It is executed in the batch mode i.e., both the input and output data have the form of external files and no interaction between the program and its user is required. The input data consist of six files of ASCII type that contain the information about the topology of the finite element mesh, material properties and loading. The last item of information is prepared by means of the program `FOURIER`. The output data consist of three files of ASCII type that contain the solution to the problem, i.e., the stresses and displacements for the earlier user-specified radial planes.

The program `FOURIER` is an auxiliary program that computes the coefficients of the Fourier series for external loads. It has been assumed that a wheel may be subject to any number of loads of contact type. In order to define each of the loads, the systems of global (r, φ, z) and local (X, Y, Z) coordinates have to be established (figure 2.2). The system of global coordinates is a cylindrical system in which (r, z) is the profile plane containing the center of the contact zone. The way the system of local coordinates is defined is very flexible. In the simplest case (figure 2.2), the origin C of the system coincides with the center of the contact zone, the X axis is normal to the plane (r, z) and has the direction of the φ axis, the Y axis has the direction of the z axis, and the Z axis is defined so that the system (X, Y, Z) is a right-handed, rectangular cartesian system. In the most general case

(figure 2.3), the location of the origin does not have to coincide with the center of the contact zone and, additionally, the slope of the (X,Y) plane may be specified by giving the value of the angle α. In this case, the center of the contact zone C' is defined as the projection of the point C onto the wheel surface in the Z direction.

The dimensions of the contact zone and the surface tractions are defined in the system of local coordinates. According to experimental observations, it has been assumed that the contact zone can be approximated by a rectangle with sides $2a$ and $2b$ which are parallel to the X and Y axes, respectively (figure 2.4), and the surface tractions can be described by means of bi-parabolic functions

$$t_i(X,Y) = t_{0i}\left[1-\left(\frac{X}{a}\right)^2\right]\left[1-\left(\frac{Y}{b}\right)^2\right], \qquad i = X,\, Y,\, Z \tag{2.47}$$

in which

$$t_{0i} = \frac{9}{16}\frac{T_i}{ab}, \qquad a = A\sqrt{\frac{3\pi}{8}}, \qquad b = B\sqrt{\frac{3\pi}{8}} \tag{2.48}$$

where t_i denotes the surface tractions caused by the force T_i acting in the ith local direction; the parameters A and B are the semi-major and semi-minor axes of the ellipse computed using the Hertz formulae. It should be stressed that such a definition does not correspond to the definition of the surface tractions in (2.16), where the system of global coordinates was used, but the appropriate transformation has been included in the program.

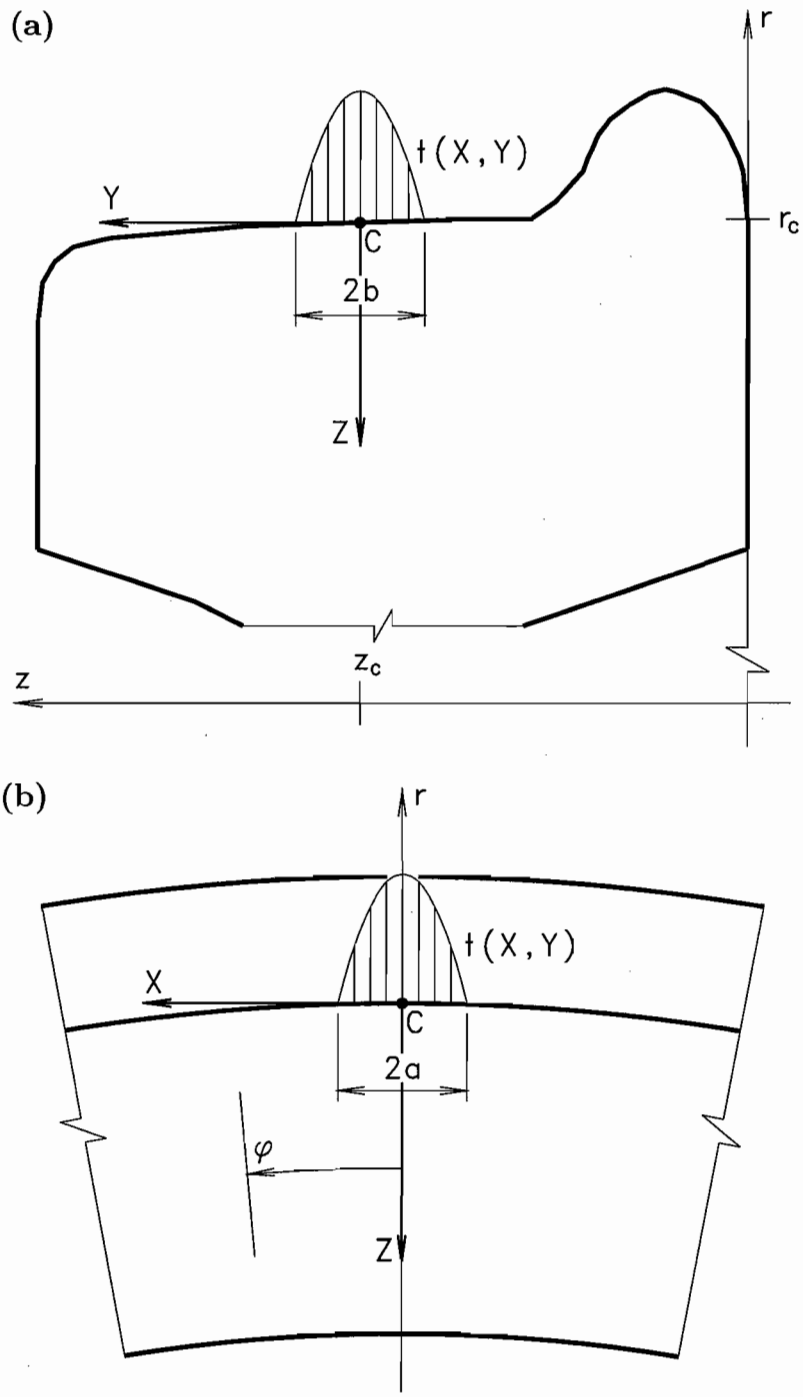

Figure 2.2 Conventions for the Global and Local Systems of Coordinates

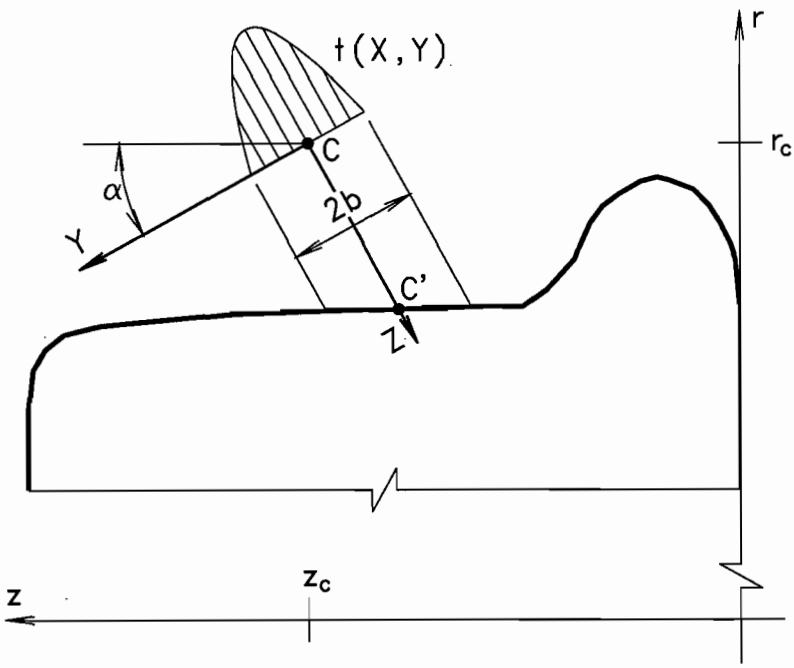

Figure 2.3 Conventions for the Local System of Coordinates – General Case

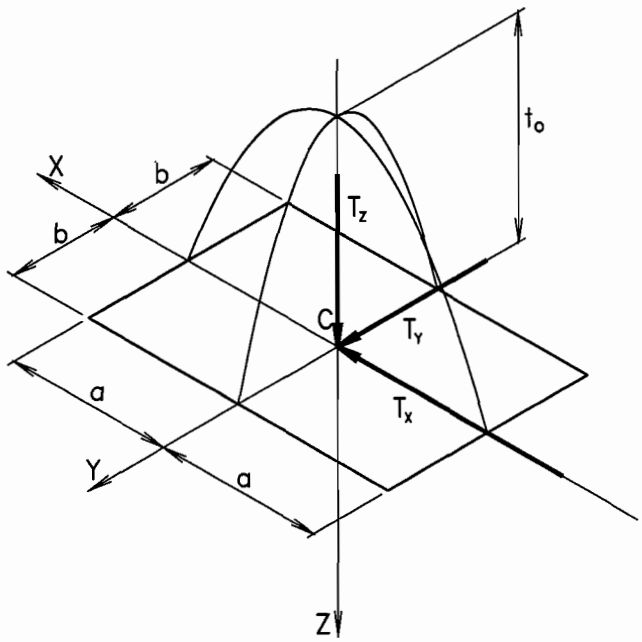

Figure 2.4 Conventions for a Rectangular Contact Zone with Bi-Parabolic Distribution of Surface Tractions

2.5 NUMERICAL TESTS

A wide variety of numerical tests has been carried out in order to validate the approach applied to the analysis of elastic stresses, especially the computer programs described in the previous section. All the tests performed can be divided into two groups.

The first one consists of relatively simple benchmark problems with known analytical solutions. Unfortunately, these tests are one-dimensional and they did not allow one to draw many conclusions that could be useful for real three-dimensional problems. A thick-walled cylinder subject to internal pressure may be given as an example. These tests were performed in the initial stage of testing and their results are not presented here. There also exist more combined two- and three-dimensional problems with known analytical solutions but the simplifying assumptions made in order to formulate them are so restrictive that their usefulness can also be questioned.

The second group of tests consists of more complex problems with unknown analytical solutions. The most important examples are a circular disk subject to contact loading and a thick-walled cylinder under internal loading varying along the longitudinal axis. The solutions to these problems have been compared with solutions obtained by means of `ABAQUS, v.5.3-2` [12]. It should be stressed that such comparisons were possible because all the problems were two-dimensional. If they had been formulated as three-dimensional problems, a special approach would have had to be applied while using `ABAQUS`. It also could have turned out that much more powerful computer equipment would have been necessary.

2.5.1 Circular Disk

In this test, a circular disk of inner radius r_i, outer radius r_o, and thickness $2b$ was subjected to the concentrated surface tractions $t(X)$ of parabolic distribution (figure 2.5). The width of the contact zone $2a$ was chosen so that it corresponded to the angle $2\varphi_o$. It was assumed that the disk was in plane stress conditions and all the points on the surface $r = r_i$ were subject to the following constraints: $u_r = 0$, $u_\varphi = 0$. Two cases of loading were considered (figure 2.6) in which the disk was subject to the vertical $t_Z(X)$ and horizontal $t_X(X)$ surface tractions. The corresponding Fourier series included only symmetric and antisymmetric modes, respectively.

Some selected results are shown in figures 2.7 through 2.14. They were obtained assuming the following non-dimensional data: inner radius $r_i = 1$, outer radius $r_o = 8$, Young's modulus $E = 1$, and Poisson's ratio $\nu = 0.3$; the intensity of the surface tractions (peak value) was equal to 1.0; the width of the contact zone $2a \approx 2.088$ corresponded to the angle $2\varphi_o = 15°$.

The problem was solved using four finite element meshes. In each case the number of elements in the z direction was constant and equal to two elements. In theory, the solution to the problem does not depend on this direction, so any number of elements could have been used, particularly only one row of elements could have been considered. In practice, the solution may be z-dependent because the static boundary conditions on the surfaces $z = b$ and $z = -b$ are not satisfied precisely. The influence of this effect on the quality of the solution may be exposed if two or more rows of finite elements are used. The number of elements in the radial direction was equal to 8, 16, 32, and 64 elements. The width of the disk $2b$ was equal to 2.0, 1.0, 0.5, and 0.25, respectively, so a constant aspect ratio for all the meshes was kept.

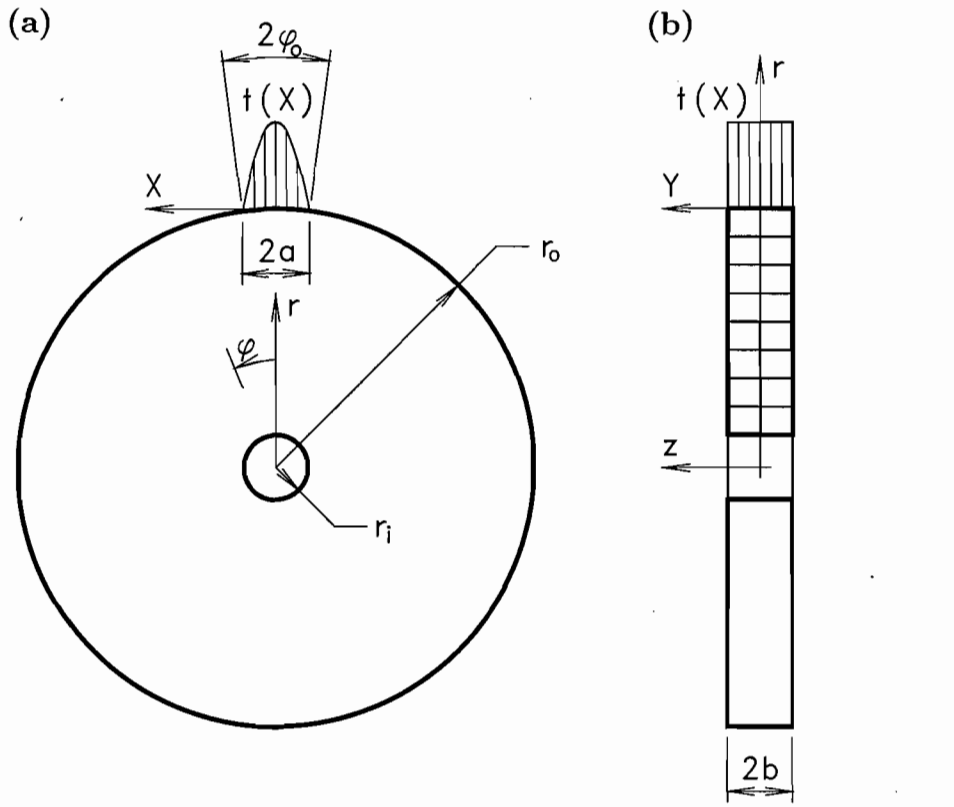

Figure 2.5 Circular Disk under Concentrated Surface Tractions

As far as the number of Fourier modes (harmonics) is concerned, it was assumed to be equal to 250 modes. Such a number seems to be too excessive for the problem under consideration but it allowed checking the influence of higher harmonics on the solution. In general, it is not possible to determine in advance how many harmonics have to be taken into account in order to obtain a high quality solution. On the one hand, the number of harmonics should be chosen so that the load is described precisely. For surface tractions of parabolic distribution, the wavelength for the highest harmonic should be at least from 4 to 6 times smaller than the angular width of the contact zone $2\varphi_o$, i.e., in the case considered from 96 to 144 harmonics should be included. On the other hand, the quality of the solution also depends on the mesh density and that is why it cannot be improved by the increase in the number of harmonics if the mesh is too coarse.

For comparison, the problem was also solved using ABAQUS. In this case, it was treated as a two-dimensional plane stress problem. Only half the disk was considered and it was discretized using two irregular meshes of 8-node finite elements.

The results for the case of vertical loading are shown in figures 2.7 through 2.10. The radial σ_{rr} and hoop $\sigma_{\varphi\varphi}$ stresses are plotted for two selected rays $\varphi = 0°$ and $\varphi = \varphi_o = 7.5°$ that contain the center and the end point of the contact zone, respectively. The shear stresses $\sigma_{r\varphi}$ are also plotted for two rays, but instead of the ray $\varphi = 0°$, where these stresses are equal to zero, an additional ray $\varphi = 2\varphi_o = 15°$ was chosen. The influence of the number

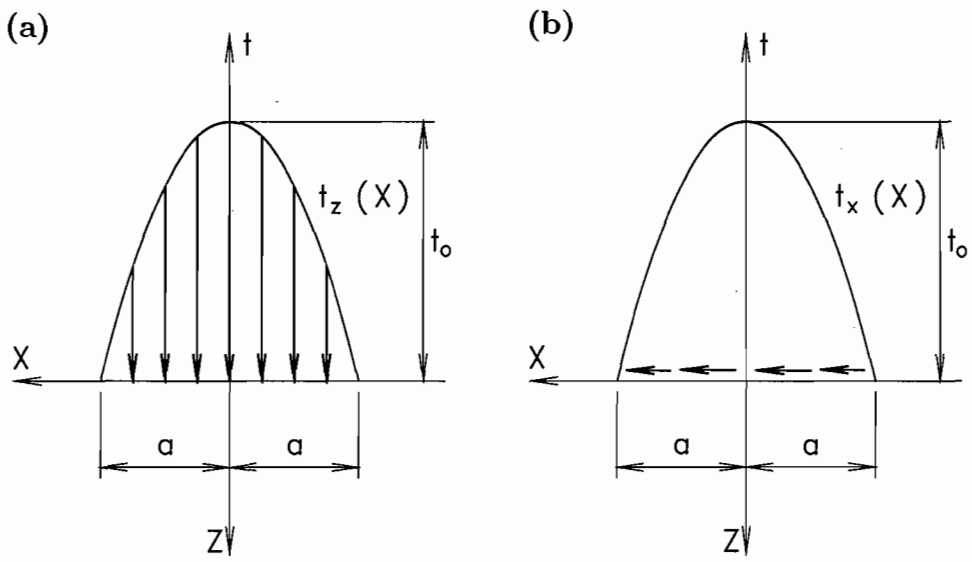

Figure 2.6 Vertical and Horizontal Surface Tractions in the Circular Disk Problem

of harmonics and the mesh density on the quality of the solution is shown in figure 2.7 for the most representative stresses σ_{rr} at two points on the outer surface.

The results for the case of horizontal loading are shown in figures 2.11 through 2.14. The stress tensor components are plotted for the same rays as before, i.e., containing the center of the contact zone and either the end point of the zone or the point of the coordinate $\varphi = 2\varphi_o = 15°$, depending on where non-zero values exist. This time, the shear stresses $\sigma_{r\varphi}$ have been chosen as the most representative stresses to visualize the influence of the number of harmonics and the mesh density on the quality of the solution.

In both cases of the vertical and horizontal loads, high quality solutions have been obtained. The biggest errors occur on both the inner and outer surfaces (a consequence of the bilinear interpolation of the displacement field). However, the values at the centroids of the elements, which are used in the analysis of residual stresses, are subject to much smaller errors, even in the vicinity of the contact zone. With regard to the number of harmonics necessary to obtain a good solution, the estimate based on the wavelength seems to be correct, though in real problems an excess is still recommended. As for the minimal mesh density, it should be determined for each specific problem separately and an attempt to draw general conclusions from the above test seemed to be aimless.

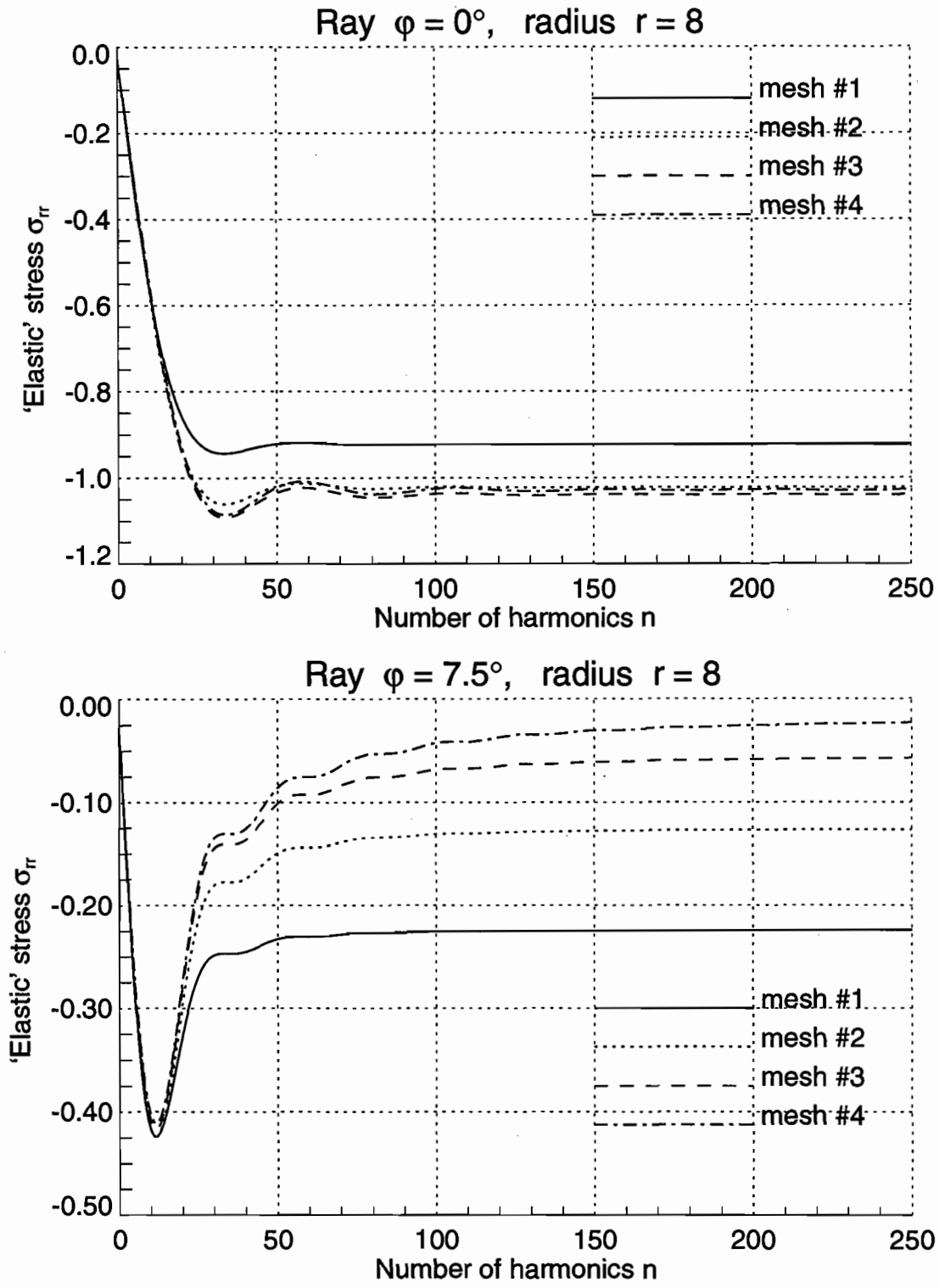

Figure 2.7 Radial 'Elastic' Stresses σ_{rr} as a Function of the Number of Fourier Modes in the Circular Disk under Concentrated Vertical Surface Tractions

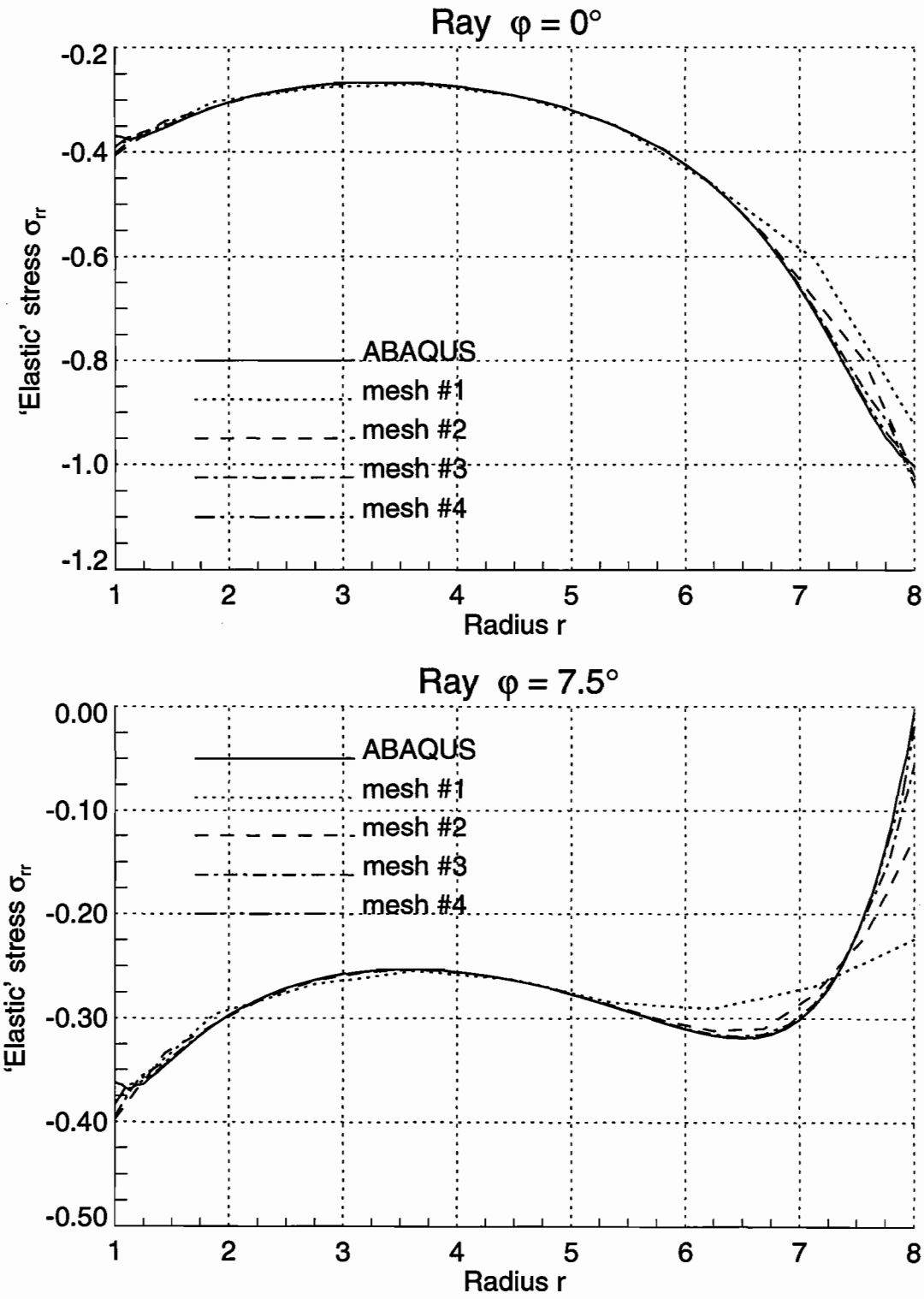

Figure 2.8 Radial 'Elastic' Stresses σ_{rr} in the Circular Disk under Concentrated Vertical Surface Tractions

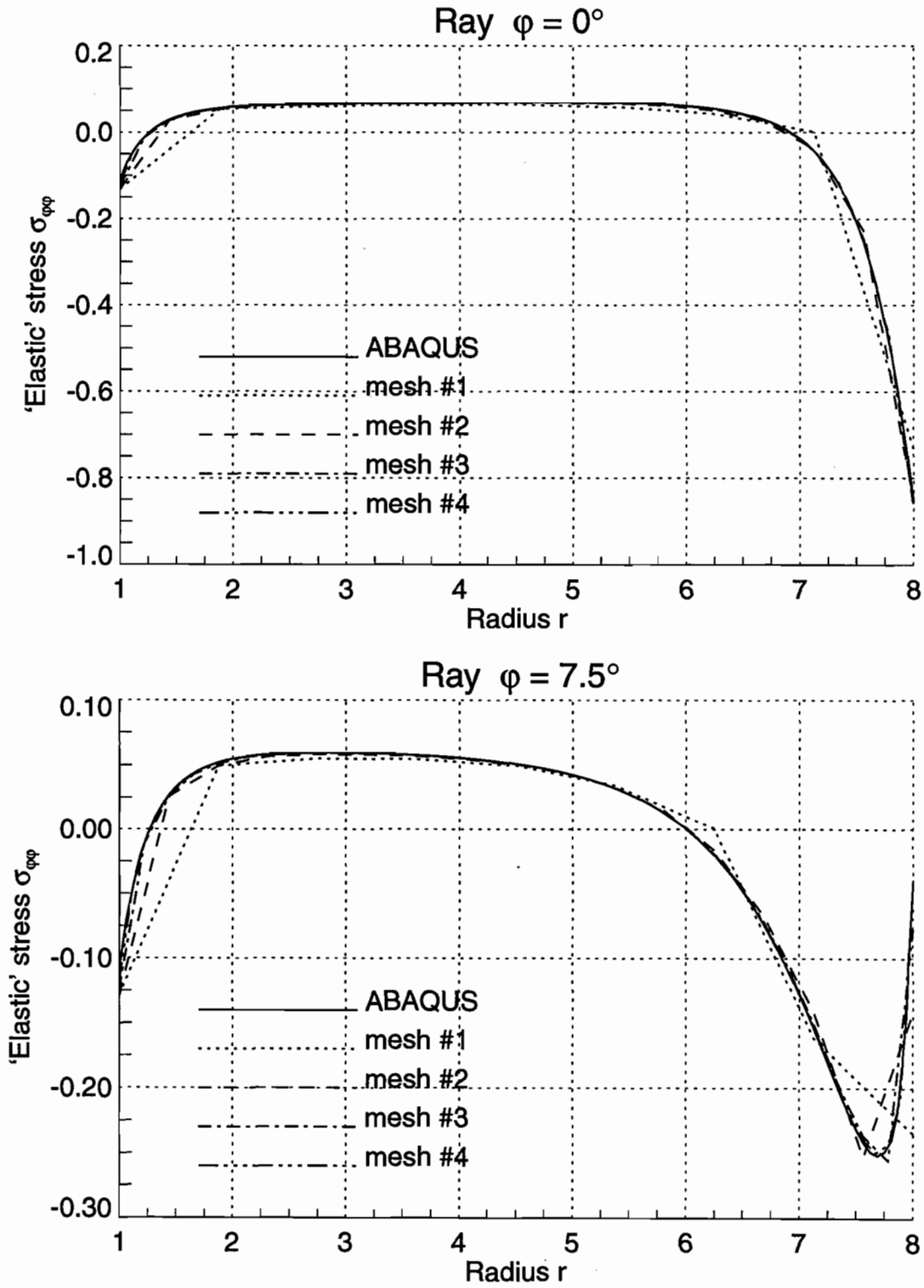

Figure 2.9 Hoop 'Elastic' Stresses $\sigma_{\varphi\varphi}$ in the Circular Disk under Concentrated Vertical Surface Tractions

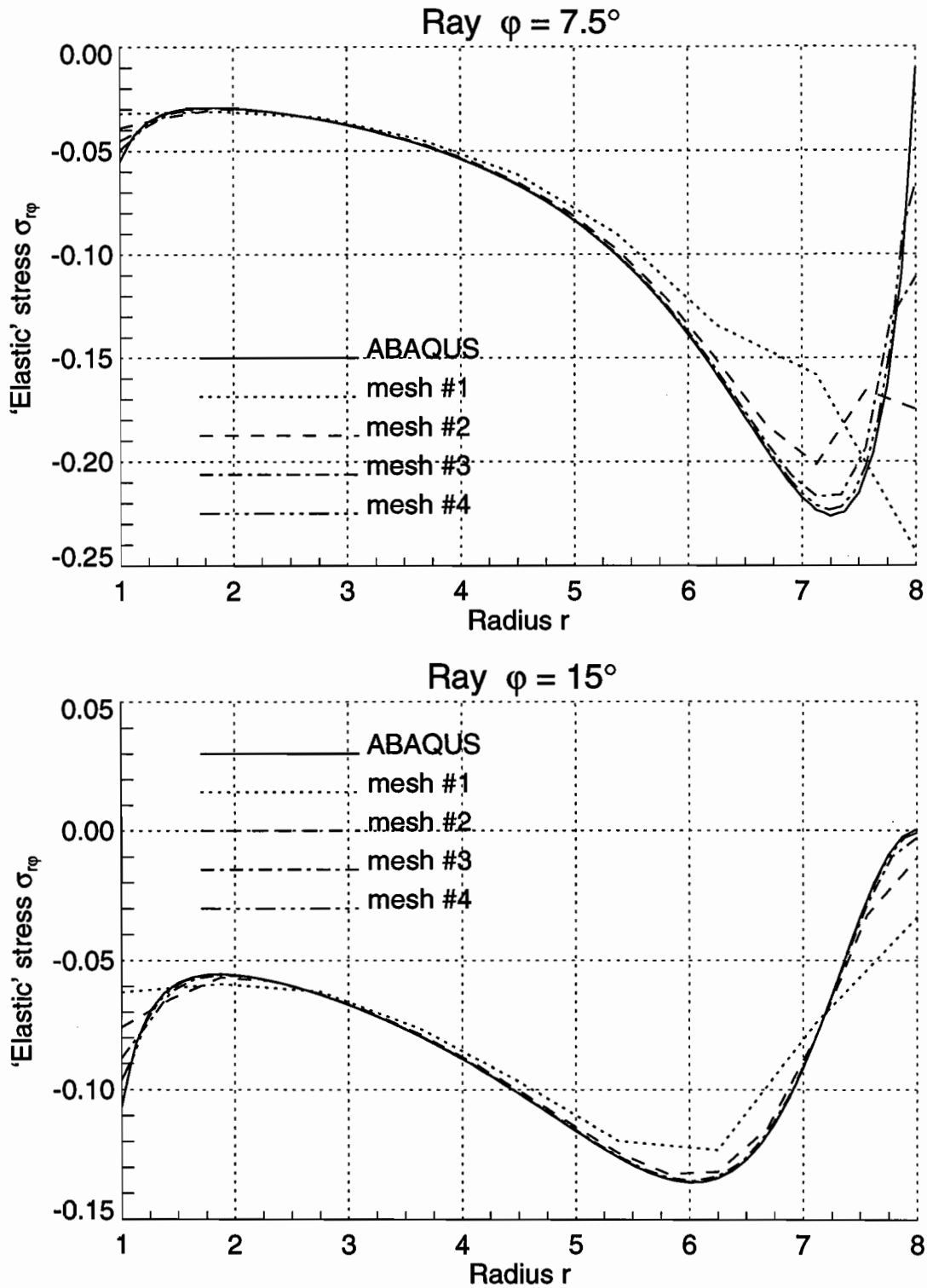

Figure 2.10 Shear 'Elastic' Stresses $\sigma_{r\varphi}$ in the Circular Disk under Concentrated Vertical Surface Tractions

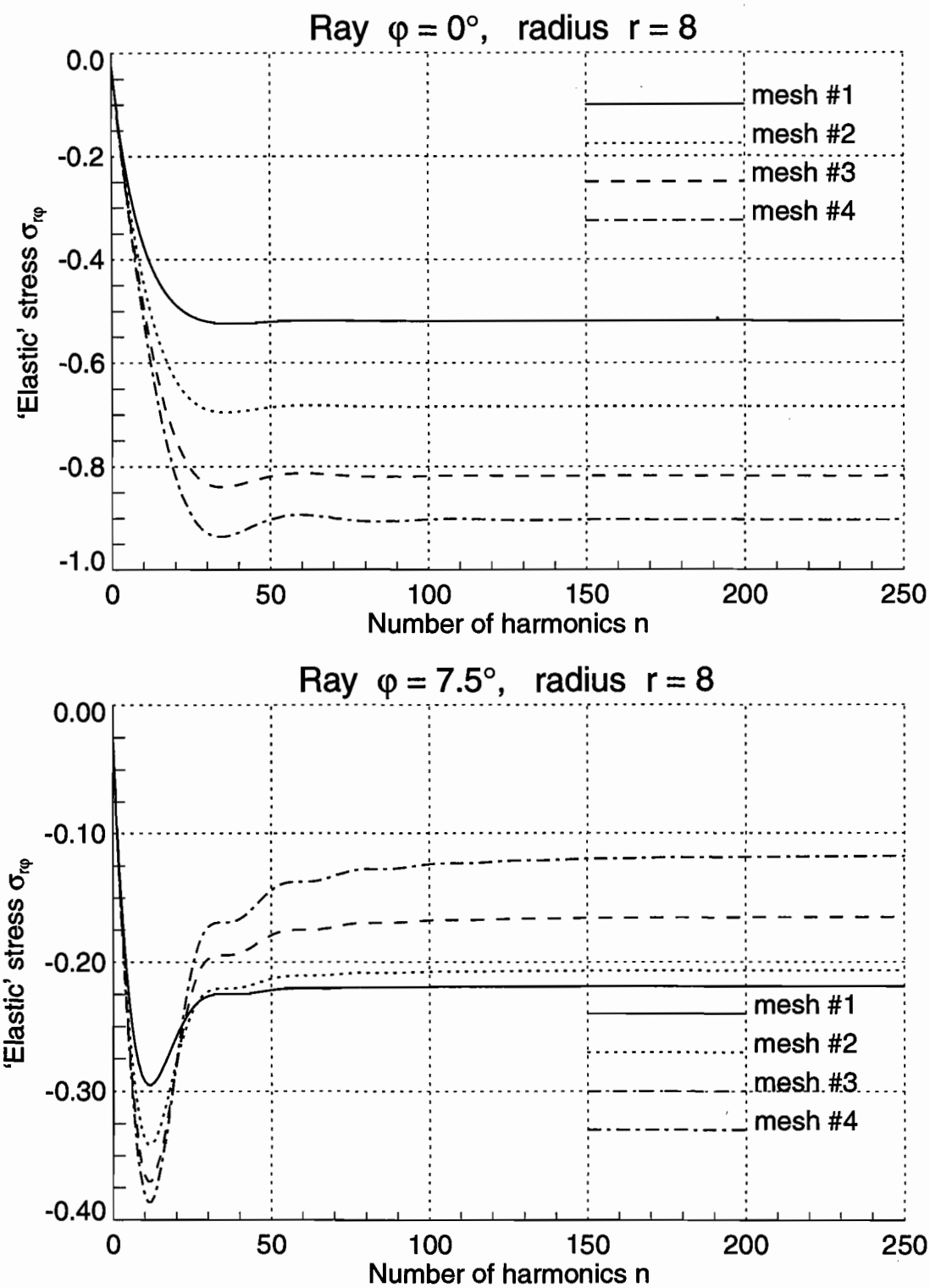

Figure 2.11 Shear 'Elastic' Stresses $\sigma_{r\varphi}$ as a Function of the Number of Fourier Modes in the Circular Disk under Concentrated Horizontal Surface Tractions

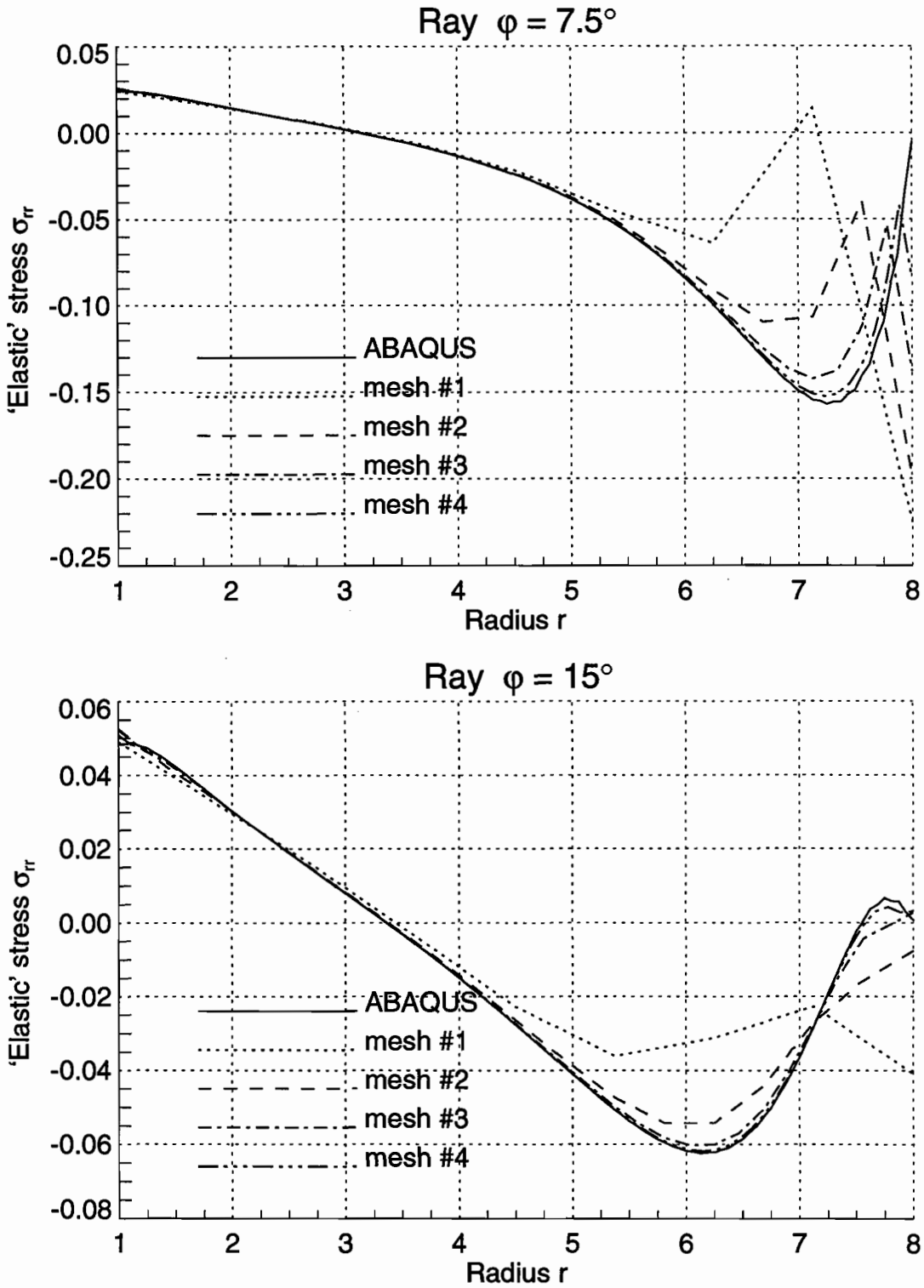

Figure 2.12 Radial 'Elastic' Stresses σ_{rr} in the Circular Disk under Concentrated Horizontal Surface Tractions

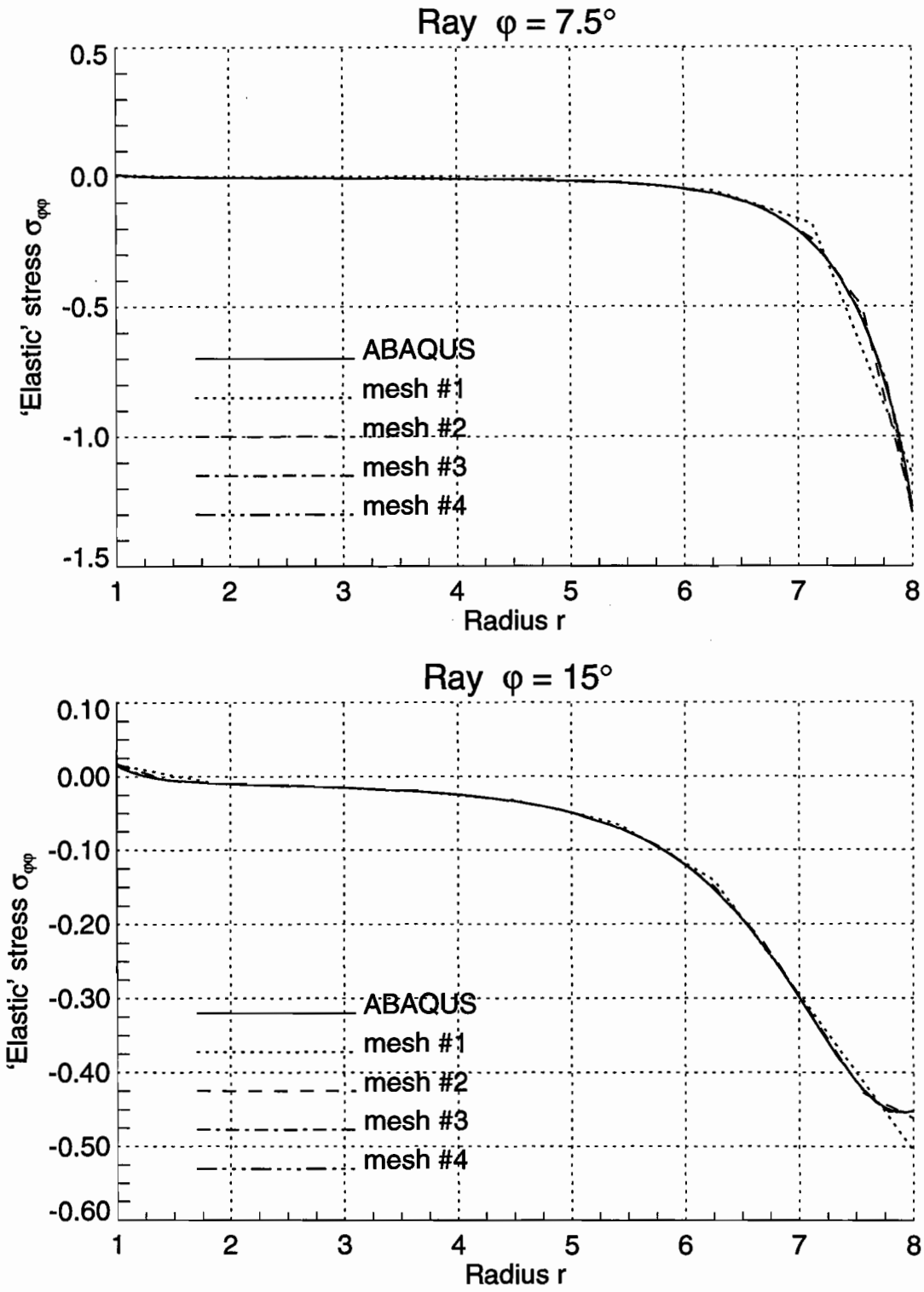

Figure 2.13 Hoop 'Elastic' Stresses $\sigma_{\varphi\varphi}$ in the Circular Disk under Concentrated Horizontal Surface Tractions

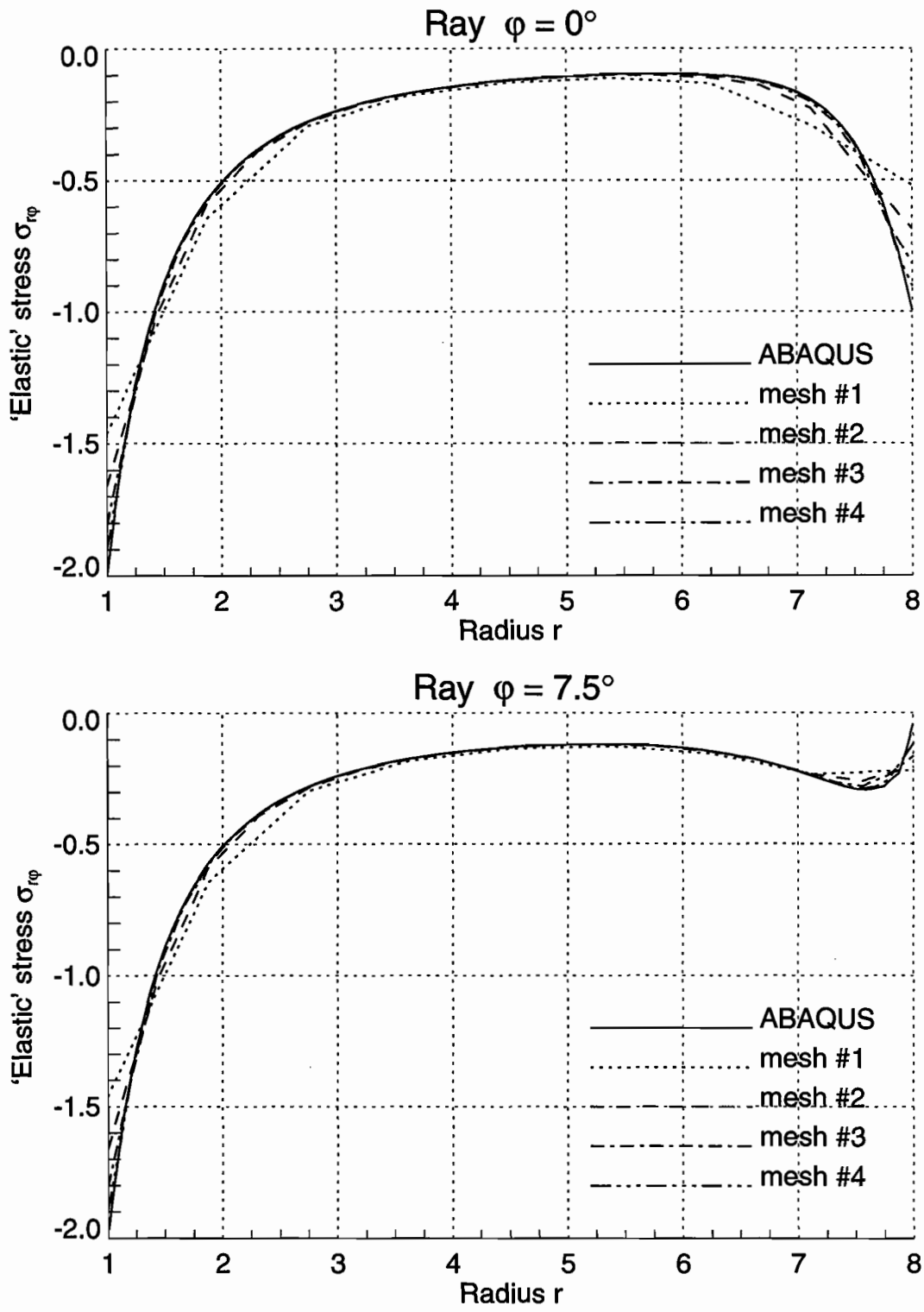

Figure 2.14 Shear 'Elastic' Stresses $\sigma_{r\varphi}$ in the Circular Disk under Concentrated Horizontal Surface Tractions

2.5.2 Thick-Walled Cylinder

In this test, a thick-walled cylinder of inner radius r_i, outer radius r_o, and thickness $2d$ was subject to internal pressure $p(z)$ (figure 2.15). The width of the loading zone was equal to d. It was assumed that the distribution of the load in the longitudinal direction was parabolic. In the circumferential direction the load was axisymmetric, so the corresponding Fourier series included only the zeroth mode. With regard to the boundary conditions, the plane stress state was considered.

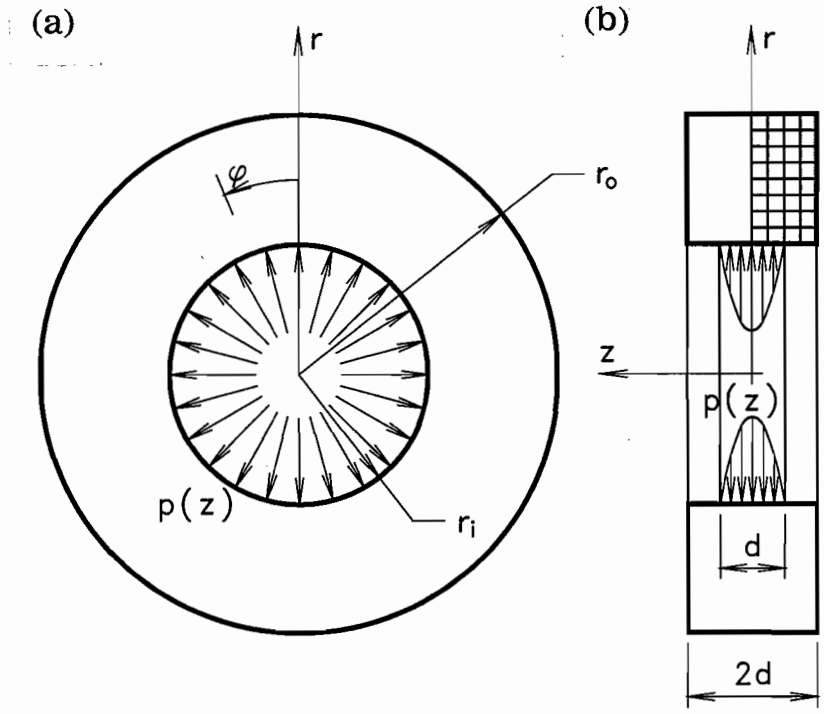

Figure 2.15 Thick-Walled Cylinder under Internal Loading

Some selected results are shown in figures 2.16 through 2.24. They were obtained assuming the following non-dimensional data: inner radius $r_i = 2$, outer radius $r_o = 4$, cylinder thickness $2d = 2$, Young's modulus $E = 1$, and Poisson's ratio $\nu = 0.3$; the intensity of the internal load (peak pressure value) was equal to 1.0. Taking into account the symmetry of the problem, only half the cylinder was considered with the appropriate boundary conditions $u_z = 0$ on the plane of symmetry $z = 0$.

The problem was solved using four finite element meshes of square elements that consisted of 8, 16, 32, and 64 elements in the radial direction, and 4, 8, 16, and 32 elements in the longitudinal direction, respectively. The coarsest and finest meshes are shown in figure 2.16.

For comparison, the problem was also solved by means of ABAQUS, using the same finite element meshes. In this case, 8-node axisymmetric elements were applied.

The convergence of the solution is presented in figures 2.17 through 2.20. The radial σ_{rr}, hoop $\sigma_{\varphi\varphi}$, and axial σ_{zz} stresses are plotted for two selected cross sections $z = 0$ and $z = 0.5$ that contain the center and the end point of the loading zone, respectively. The shear stresses σ_{rz} are also plotted for two cross sections, but instead of the cross section $z = 0$, where these stresses are equal to zero, an additional cross section $z = 0.25$ was chosen. In figures 2.21 through 2.24, the above stress tensor components are presented in the form of contour line plots. This time, only the best solution obtained for the mesh #4 together with the ABAQUS solution are shown.

The results obtained for the problem of the thick-walled cylinder as well as the ones for the problem of the circular disk validate both of the programs worked out for the analysis of elastic stresses. Also in this case the biggest errors can be observed in the zone where the highest concentration of stresses occurs. This fact should be taken into consideration during the process of mesh generation and appropriate mesh refinement in both the radial and longitudinal directions should be applied.

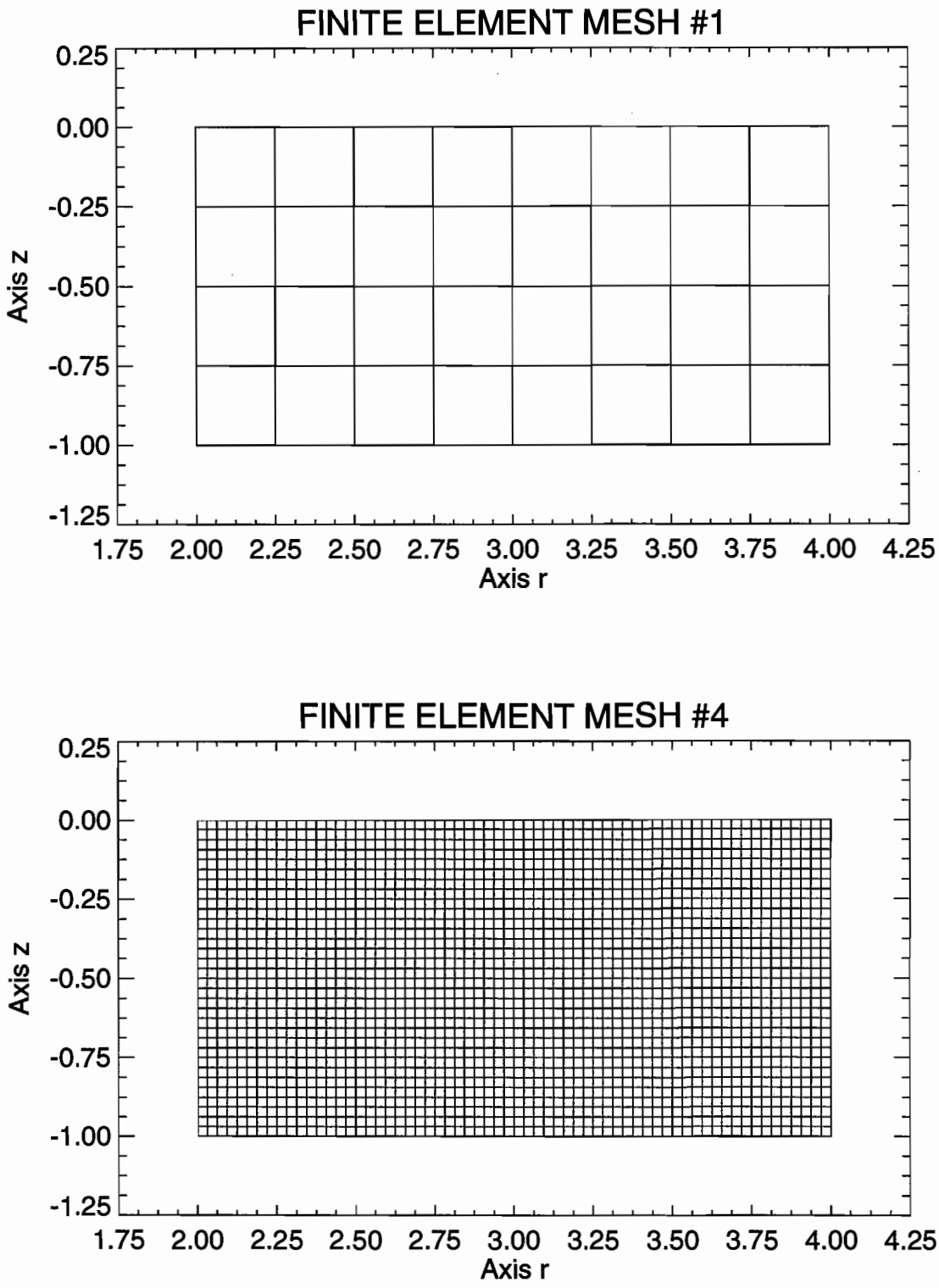

Figure 2.16 Finite Element Meshes #1 and #4 in the Problem of a Thick-Walled Cylinder under Internal Loading

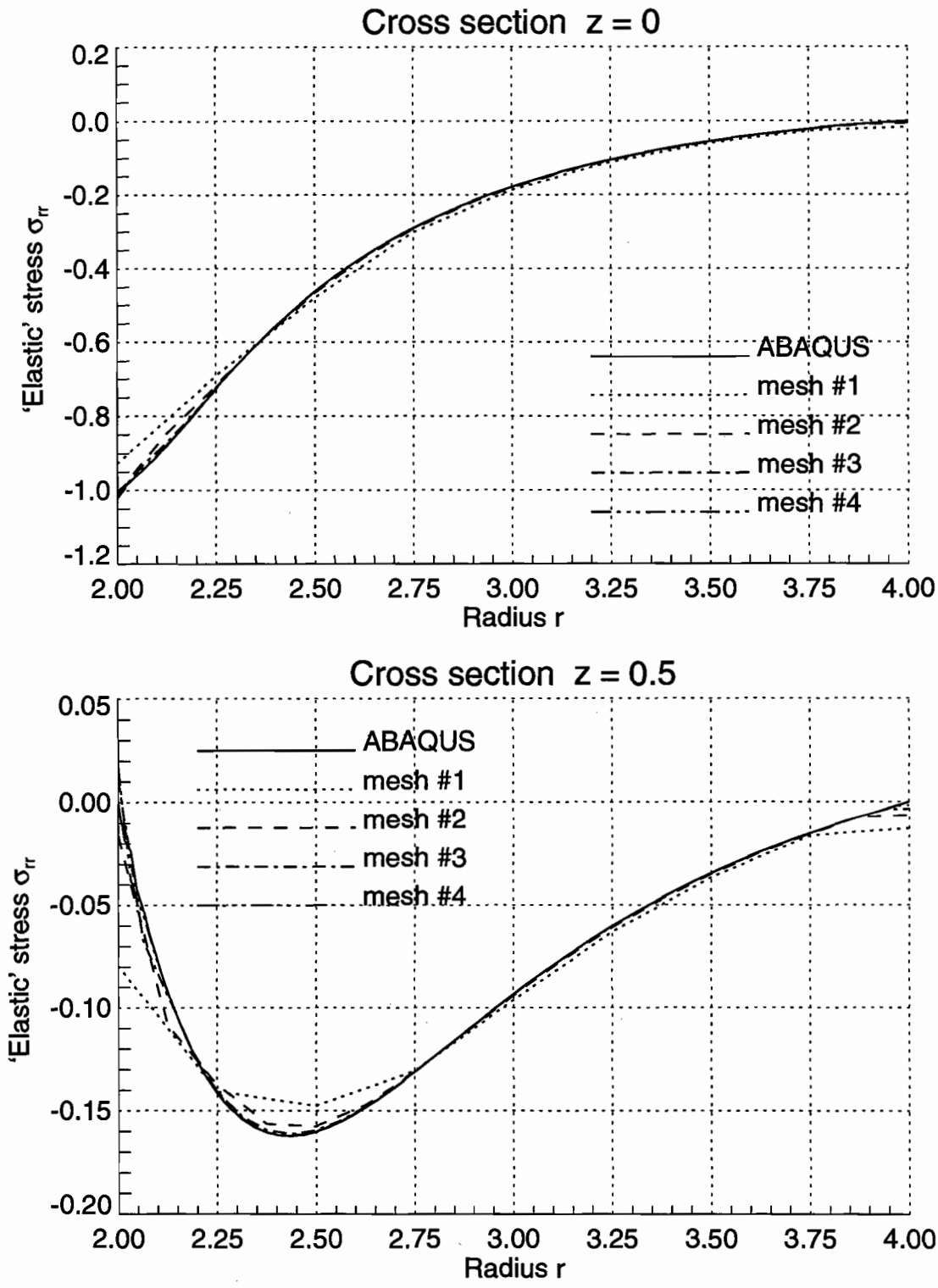

Figure 2.17 Radial 'Elastic' Stresses σ_{rr} in the Thick-Walled Cylinder under Internal Loading

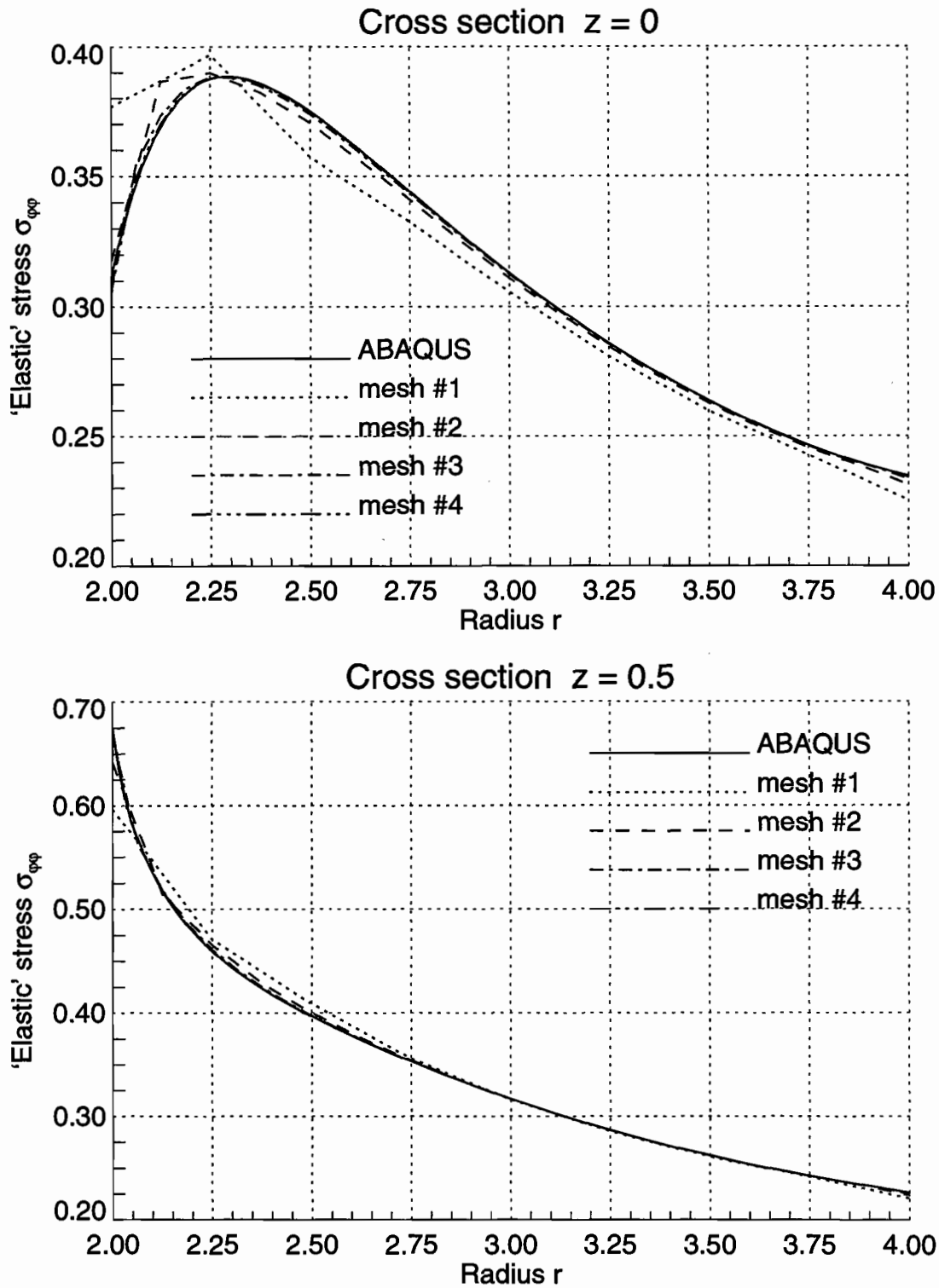

Figure 2.18 Hoop 'Elastic' Stresses $\sigma_{\varphi\varphi}$ in the Thick-Walled Cylinder under Internal Loading

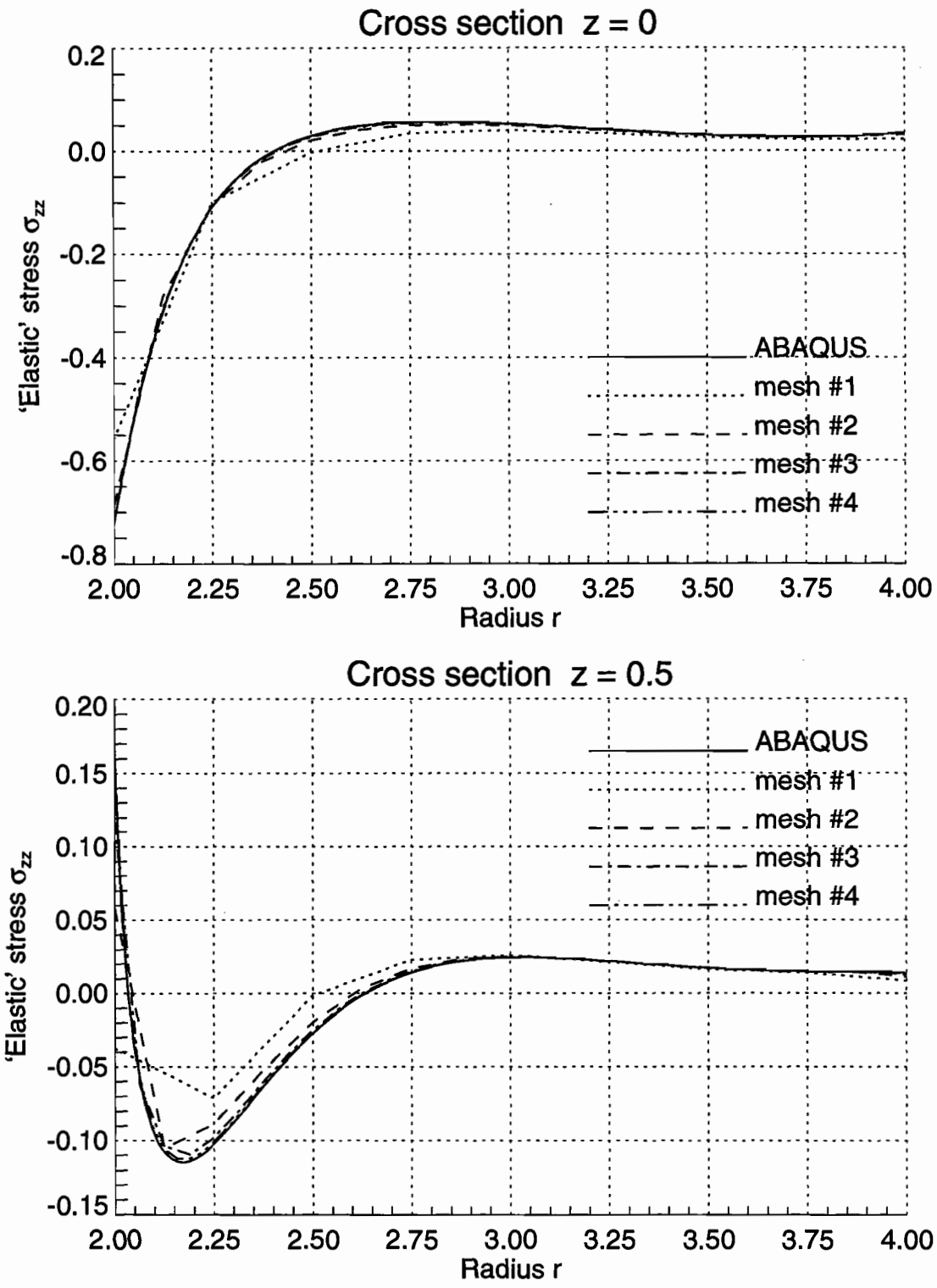

Figure 2.19 Axial 'Elastic' Stresses σ_{zz} in the Thick-Walled Cylinder under Internal Loading

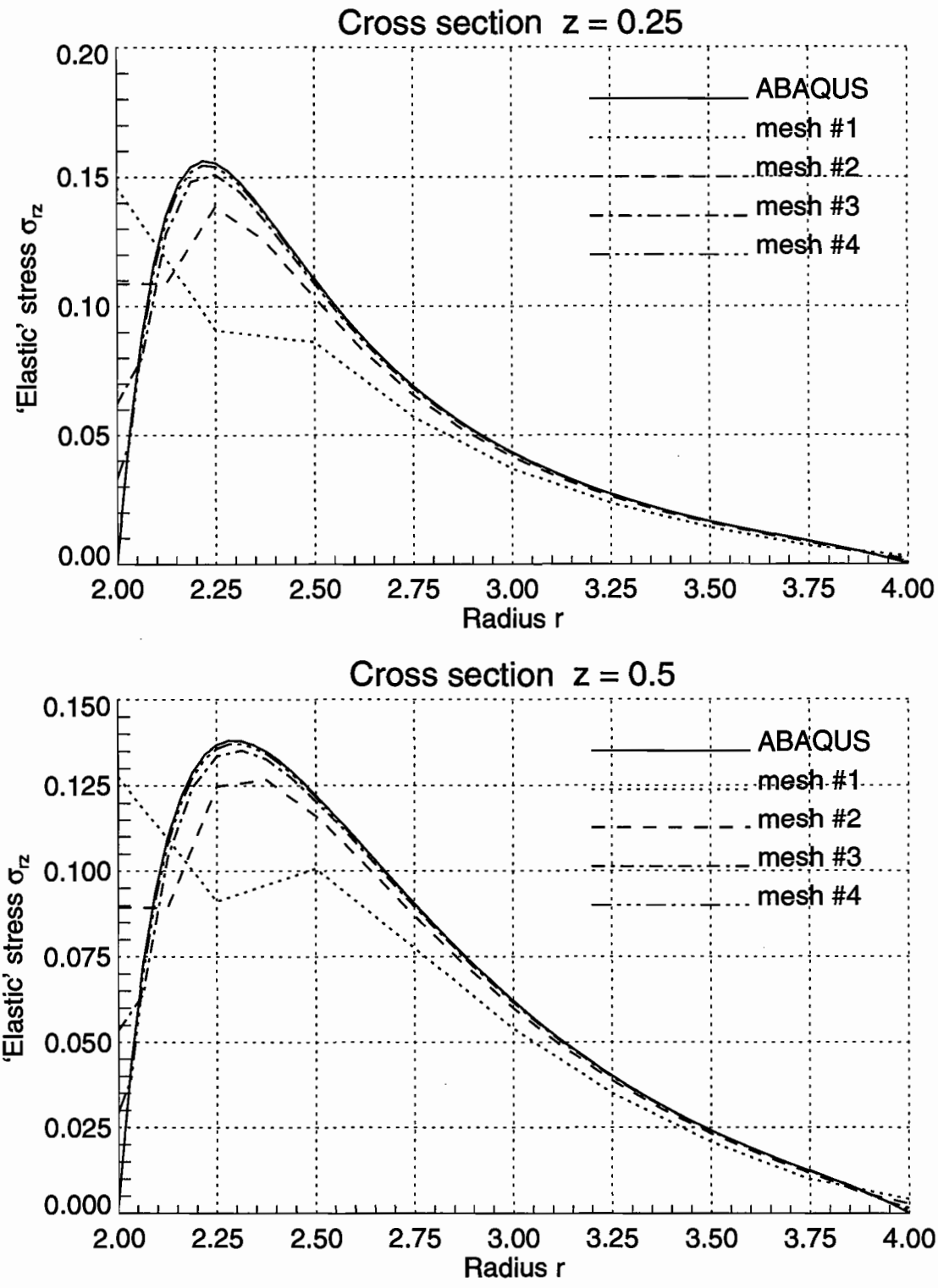

Figure 2.20 Shear 'Elastic' Stresses σ_{rz} in the Thick-Walled Cylinder under Internal Loading

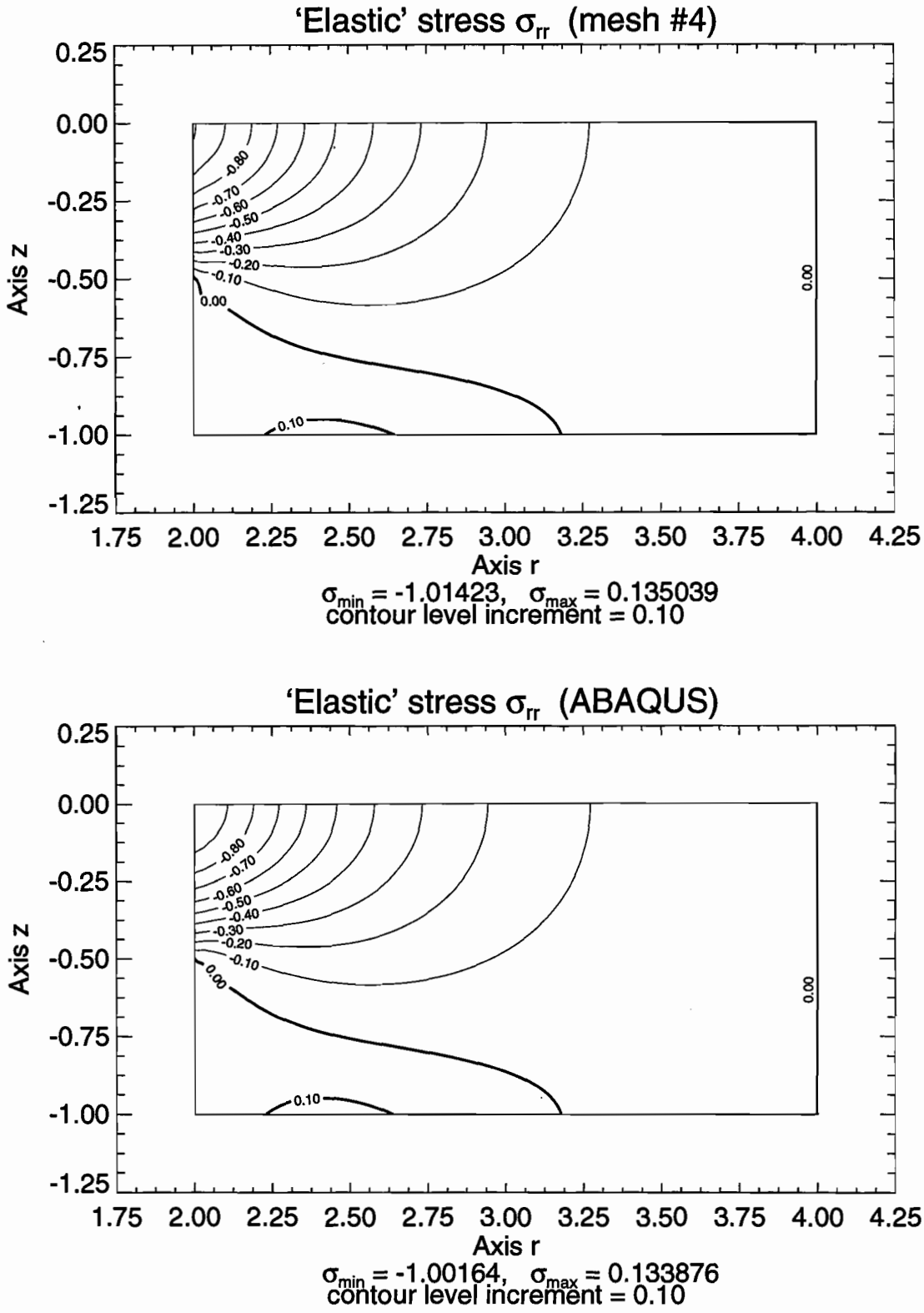

Figure 2.21 Contour Lines of Radial 'Elastic' Stresses σ_{rr} in the Thick-Walled Cylinder under Internal Loading

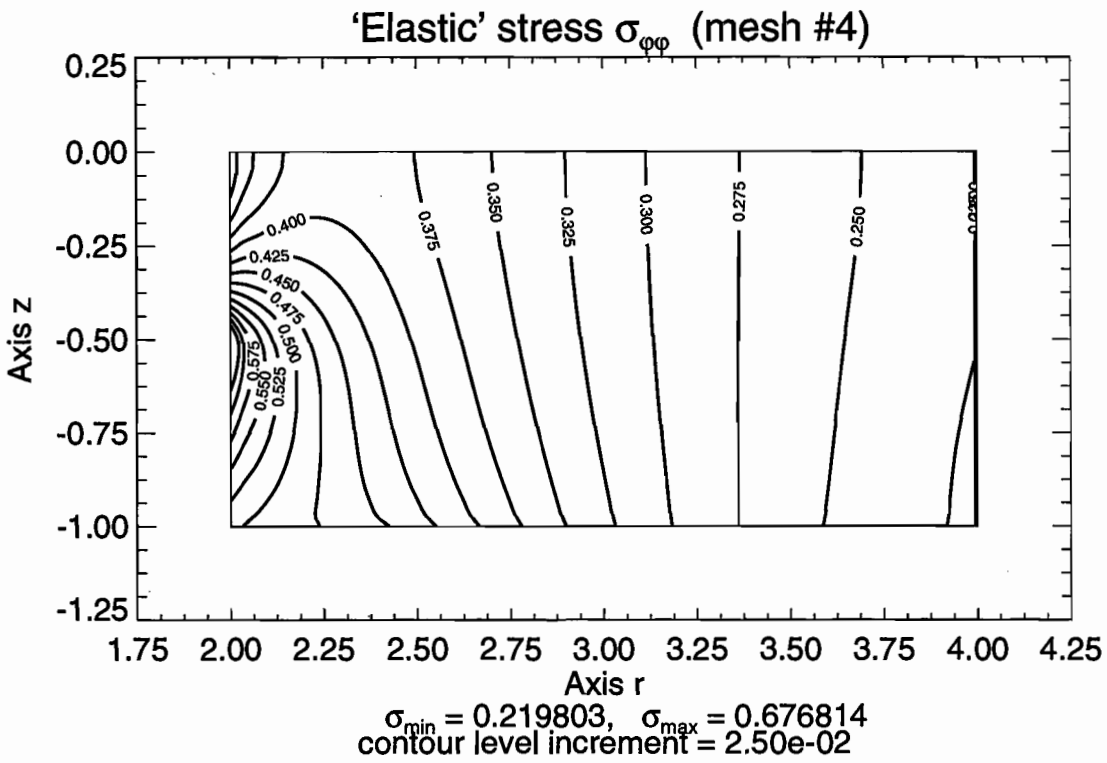

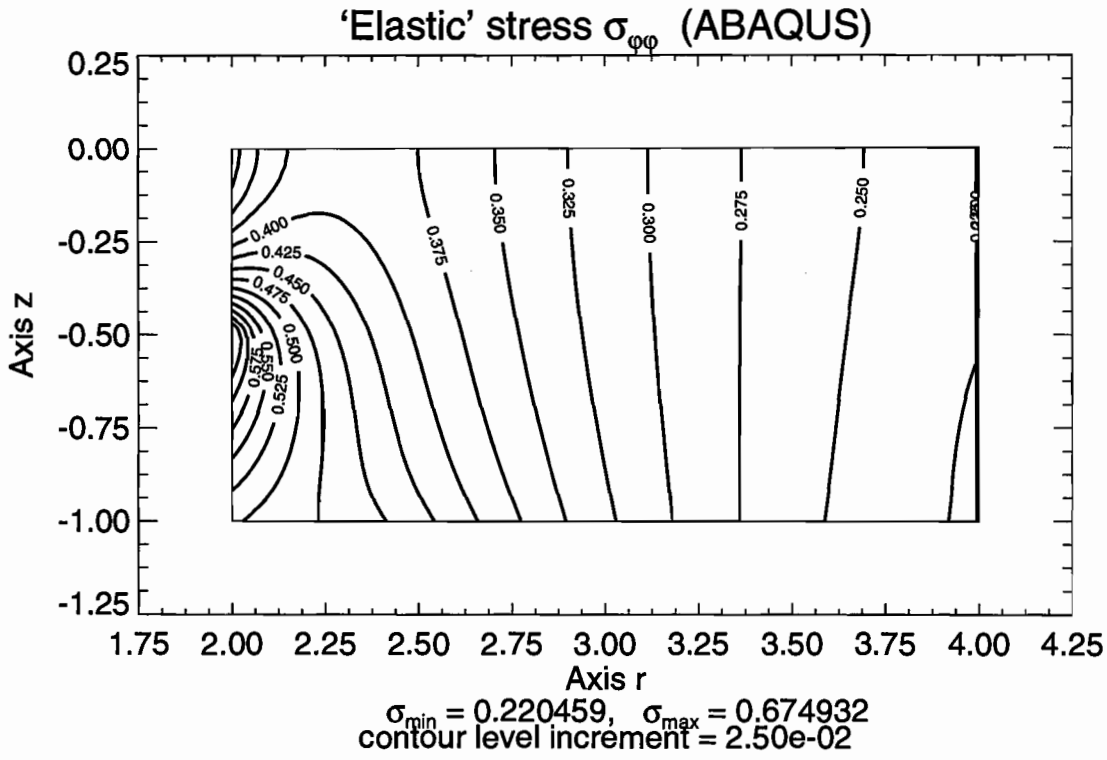

Figure 2.22 Contour Lines of Hoop 'Elastic' Stresses $\sigma_{\varphi\varphi}$ in the Thick-Walled Cylinder under Internal Loading

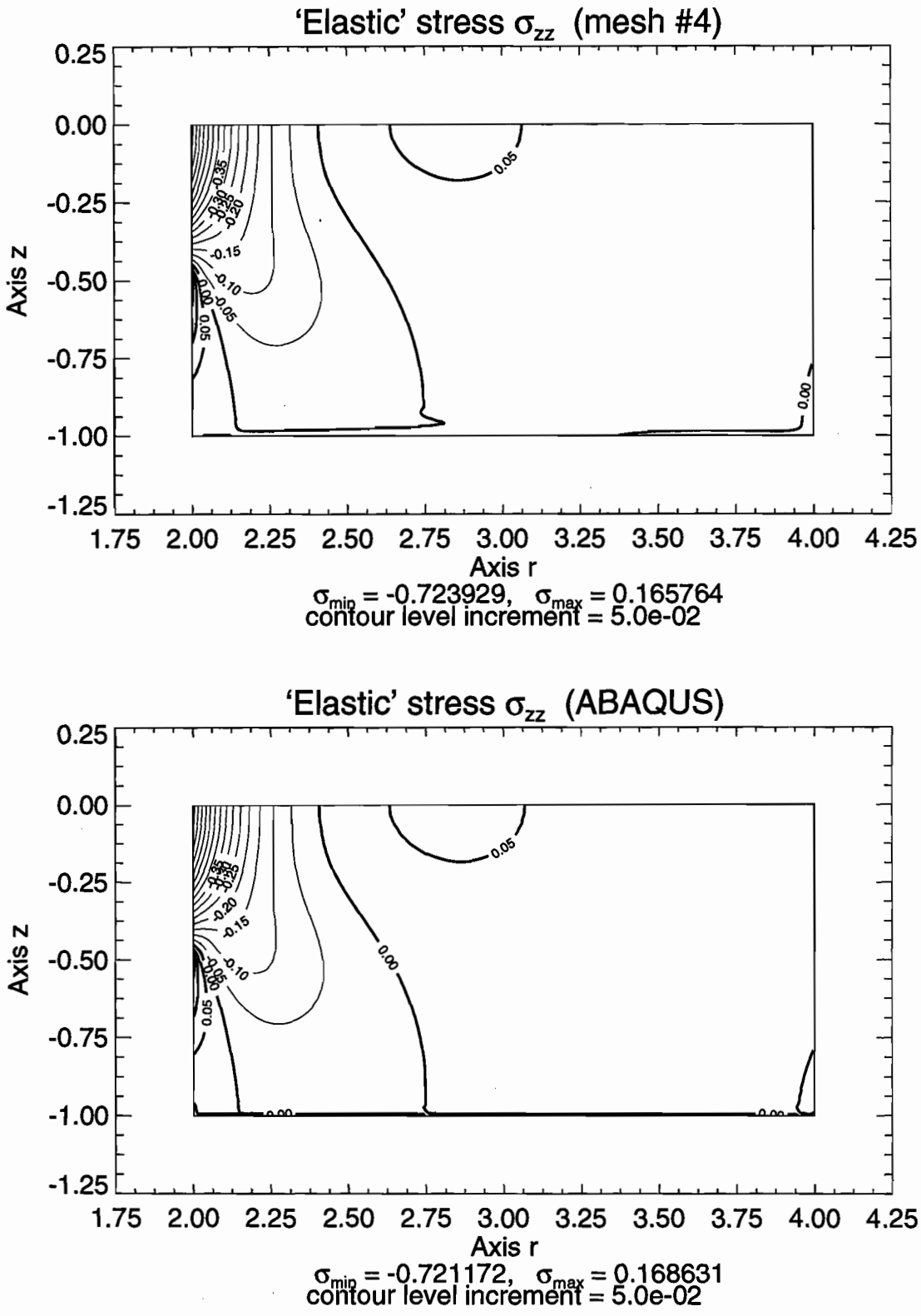

Figure 2.23 Contour Lines of Axial 'Elastic' Stresses σ_{zz} in the Thick-Walled Cylinder under Internal Loading

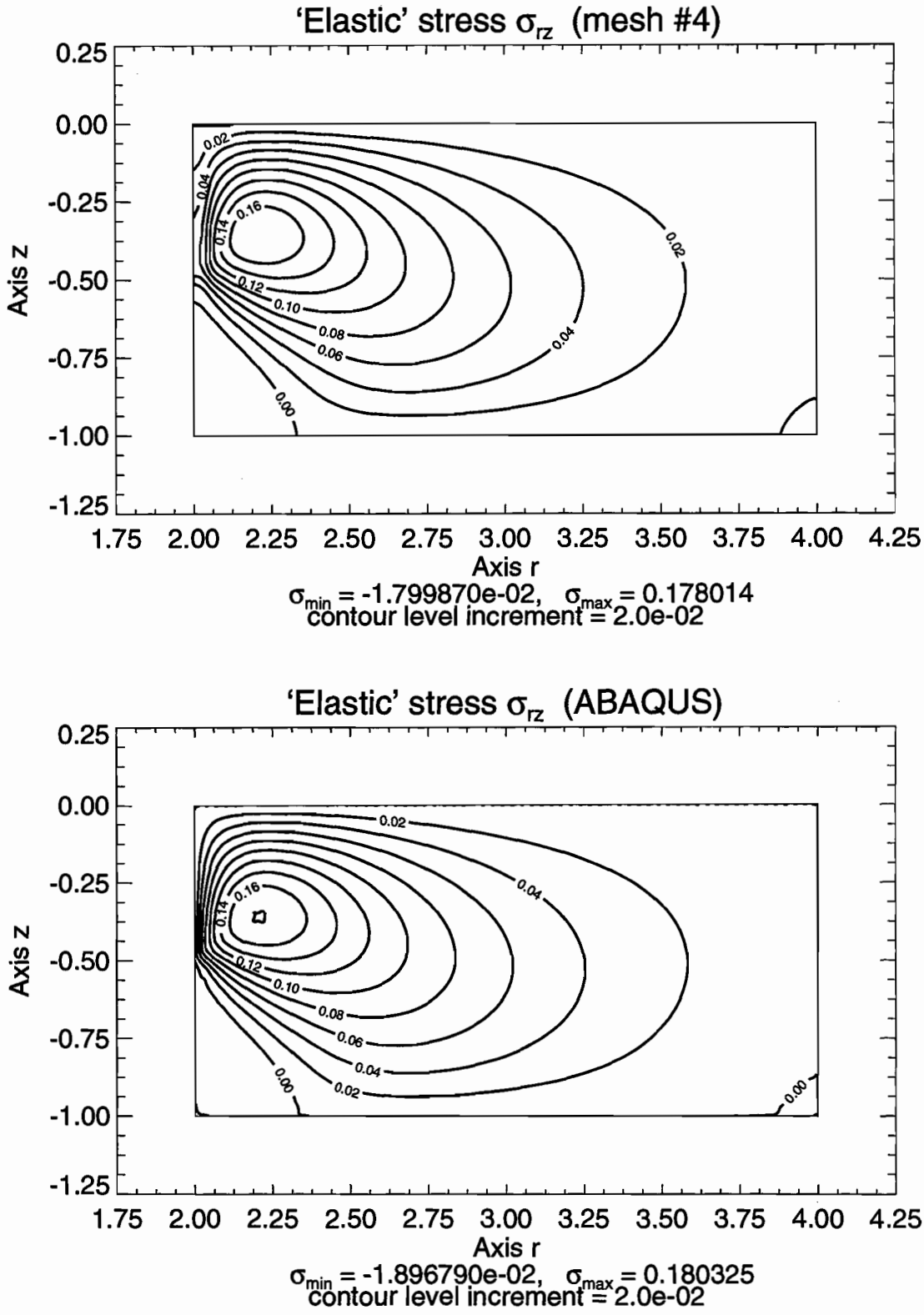

Figure 2.24 Contour Lines of Shear 'Elastic' Stresses σ_{rz} in the Thick-Walled Cylinder under Internal Loading

2.6 EXAMPLE ANALYSES FOR A RAILROAD CAR WHEEL

After the computer programs had been successfully validated using the test problems described in the previous section, they were applied to the evaluation of elastic stresses in a railroad car wheel subject to contact loading. The profile plane geometry used in these analyses was limited to that of a 32-inch diameter MU commuter vehicle wheel with 'S'-design flexible plate.

Two cases of loading were considered. In the first one, the wheel was subject only to the vertical surface tractions $t_Z(X,Y)$ of intensity $t_{0Z} = 1239.98\,\mathrm{MPa}$ acting over the rectangular contact area of dimensions $a = 6.947\,\mathrm{mm}$ and $b = 5.083\,\mathrm{mm}$, with the center C of coordinates $r = 0.405655\,\mathrm{m}$ and $z = 0.084882\,\mathrm{m}$ and the slope $\alpha = 0°$ (for the notation and conventions see section 2.4). The parameters t_{0Z}, a and b were calculated using the formulae (2.48) where the vertical force T_Z was equal to $77.84\,\mathrm{kN}$ and the dimensions of the elliptical contact area $A = 6.4\,\mathrm{mm}$ and $B = 4.683\,\mathrm{mm}$ were obtained by means of the Hertz formulae assuming the following data: radius of the wheel $R_2 = 0.4064\,\mathrm{m}$, radius of the wheel profile $R_2' = \infty$, and radius of the rail profile $R_1 = 0.254\,\mathrm{m}$; the rail was assumed to be flat in the longitudinal direction, i.e., $R_1' = \infty$.

In the second case of loading, the wheel was subject to the vertical surface tractions $t_Z(X,Y)$ of intensity $t_{0Z} = 1239.98\,\mathrm{MPa}$ and the horizontal surface tractions $t_X(X,Y)$ of intensity $t_{0X} = 0.2t_{0Z} = 247.996\,\mathrm{MPa}$. For simplicity, the influence of the horizontal loading on the dimensions of the contact zone was neglected.

The number of the Fourier modes (harmonics) was assumed to be equal to 1189 modes for both of the cases considered (in fact, in the second case this number was doubled because the load had to be described by means of both the symmetric and anti-symmetric Fourier modes). The above value was determined in two steps. In the first one, it was chosen so that the wavelength for the highest harmonic was 6 times smaller than the angular width of the contact zone (see discussion in section 2.5), resulting in 1103 modes. In the second step, the dependence of the Fourier coefficients on the number of modes was drawn, the half-wave with the 1103rd mode was identified, and all the modes belonging to this half-wave (up to 1189) were taken into account.

As far as the material properties are concerned, Young's modulus E and Poisson's ratio ν were assumed to be temperature-independent and equal to $206.832\,\mathrm{GPa}$ and 0.3, respectively. Additionally, the dimensions of the Hertz ellipse were calculated assuming that both the rail and the wheel were made of material with the same elastic constants.

The problem was solved using five finite element meshes that consisted of 399, 559, 907, 1495, and 1621 elements, respectively. The first mesh, shown in figures 2.25 and 2.26, is based on one of the meshes supplied by the Volpe National Transportation Systems Center (see report no. 2 in this series); the original mesh was slightly modified, so that the generation of denser meshes could be performed partly automatically. The mesh refinement was restricted to the rim where the highest concentration of stresses was expected, particularly to the area below the tread surface (figures 2.27 through 2.30).

The results for the case of vertical loading are shown in figures 2.31 through 2.42. The convergence of the solution with respect to the mesh density is presented in figures 2.31 through 2.36 where the stress tensor components are plotted along the line $\alpha - \alpha$ shown in figures 2.26 through 2.30. The radial σ_{rr}, hoop $\sigma_{\varphi\varphi}$, axial σ_{zz}, and shear σ_{rz} stresses are plotted for two selected radial planes $\varphi = 0°$ and $\varphi = 0.981°$ that contain the center and the end point of the contact zone, respectively. The shear stresses $\sigma_{r\varphi}$ and $\sigma_{\varphi z}$ are

also plotted for two radial planes, but instead of the plane $\varphi = 0°$, where these stresses are equal to zero, an additional plane $\varphi = 1.962°$ was chosen. These results indicate that the meshes #1 and #2 are definitely too coarse for the problem under consideration. It seems to be obvious when one takes into account the number of finite elements along the contact zone (2 and 4 elements, respectively). The results obtained for the mesh #3 are reasonable but the mesh is still too coarse to reflect the variation of stresses correctly. Both the meshes #4 and #5 may be recognized as appropriate for the problem considered.

The convergence of the solution with respect to the number of harmonics is presented in figures 2.37 and 2.38. Only one point of the wheel — the center of the contact zone — was chosen to investigate this problem and that is why the stresses $\sigma_{r\varphi}$ and $\sigma_{\varphi z}$ (which are equal to zero at this point) are not shown. The minimal number of harmonics based on the wavelength criterion seems to be too excessive, but, as for the problem of the circular disk, some excess is still recommended, especially when the elastic stresses are used as input data for the analysis of residual stresses where even small variations in the elastic stresses may result in different solutions.

Finally, in figures 2.39 through 2.42, the stress tensor components are shown in the form of contour line plots. This time only the solutions obtained for the meshes #4 and #5 and for the radial planes $\varphi = 0°$ are presented.

The results for the second case of loading where both the vertical and horizontal surface tractions were taken into account are shown in figures 2.43 through 2.45. Only the contour line plots for the radial plane $\varphi = 0°$ are presented because all the conclusions drawn for the first case of loading are still valid. The horizontal loading has significant influence only on the shear stresses $\sigma_{r\varphi}$ and $\sigma_{\varphi z}$, both qualitatively and quantitatively, and the other stress tensor components remain almost unchanged. In order to restrict the number of figures, it has been decided not to show the solution obtained for the mesh #5. First of all, the differences between this solution and the one obtained for the mesh #4 are quite small. Secondly, only the solutions used as input data in the analysis of residual stresses are presented and, unfortunately, the available computer equipment did not allow solution of the latter problem for the mesh #5.

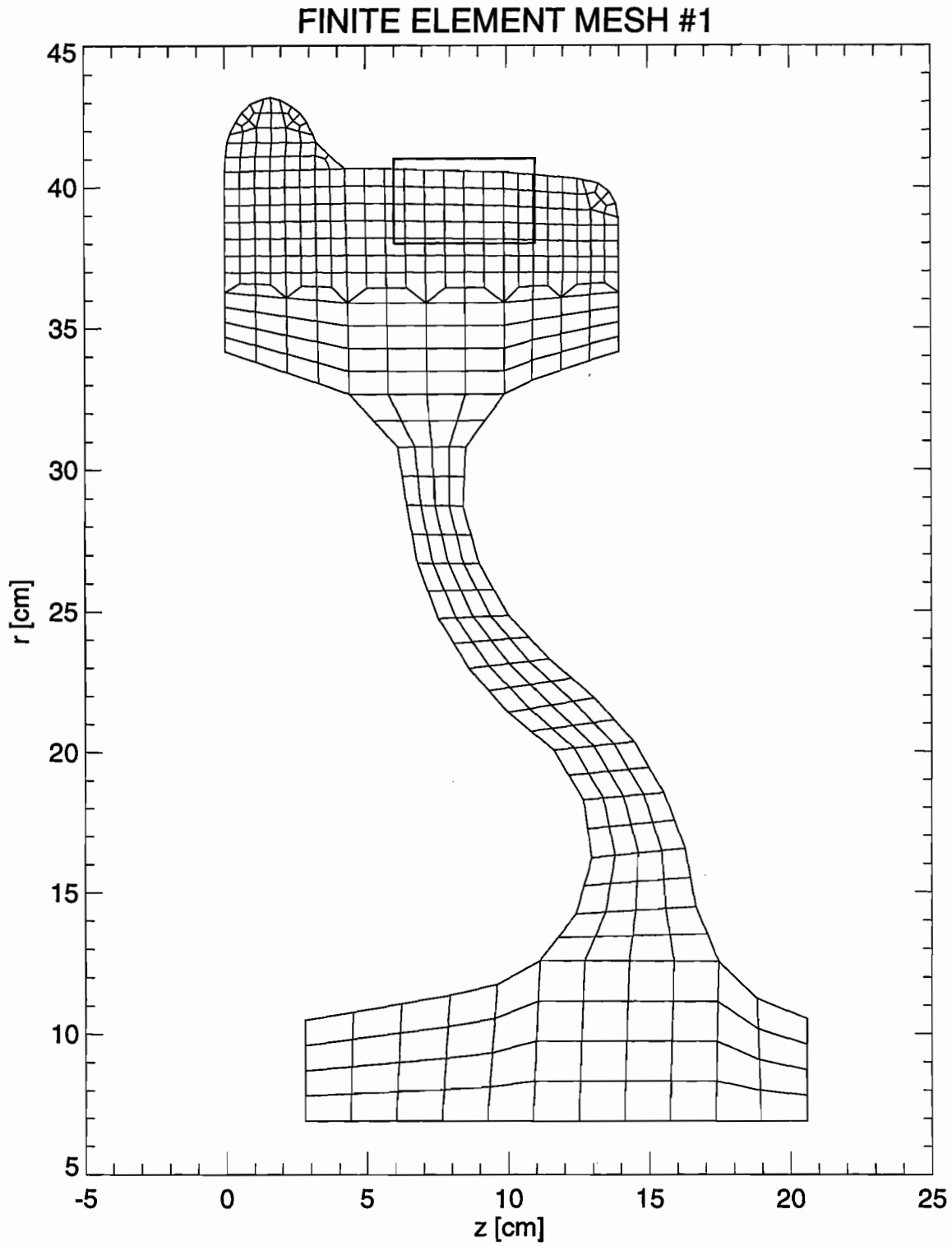

Figure 2.25 Finite Element Mesh #1 in the Problem of a Railroad Car Wheel under Contact Loading

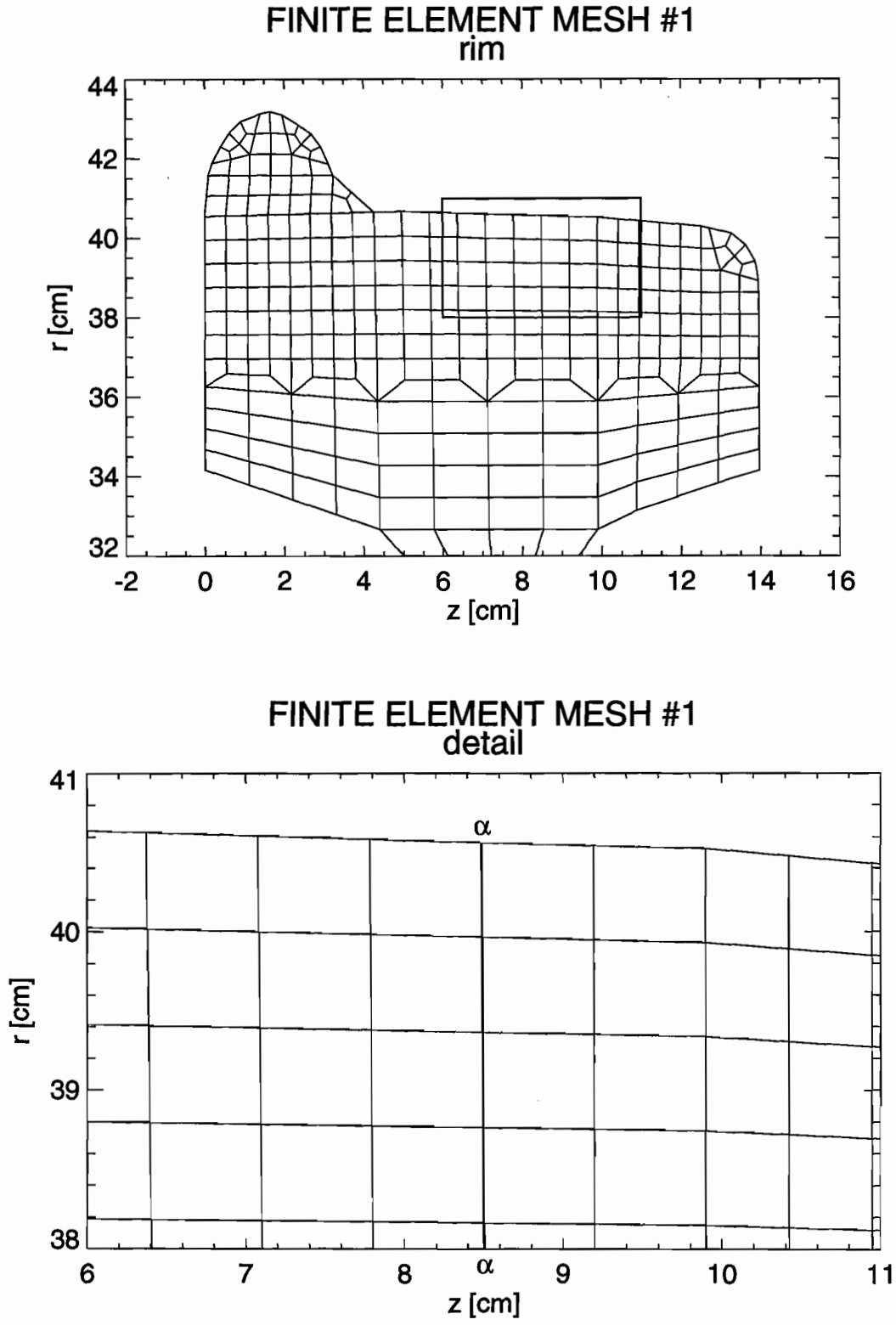

Figure 2.26 Finite Element Mesh #1 in the Problem of a Railroad Car Wheel under Contact Loading – Rim and Detail

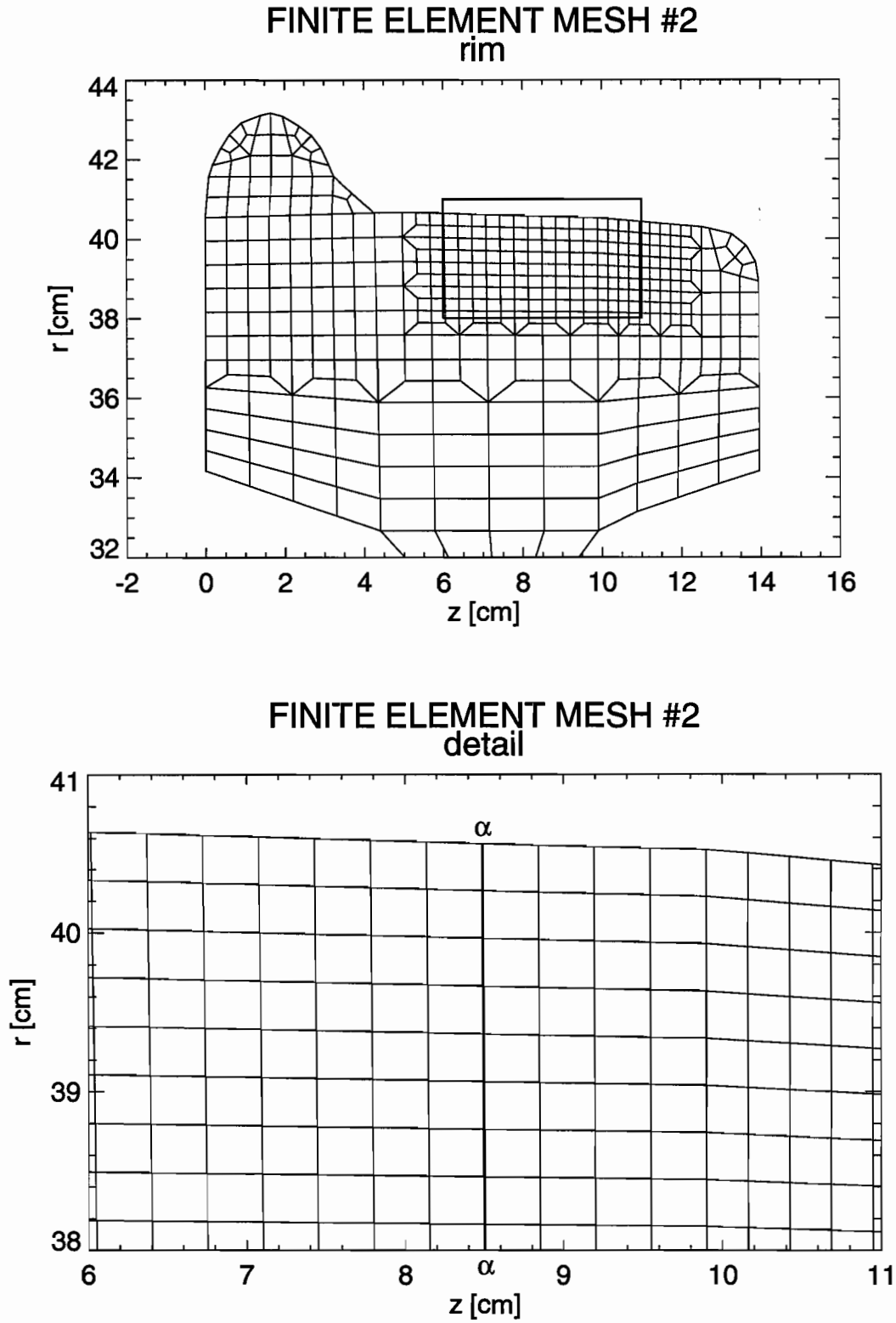

Figure 2.27 Finite Element Mesh #2 in the Problem of a Railroad Car Wheel under Contact Loading – Rim and Detail

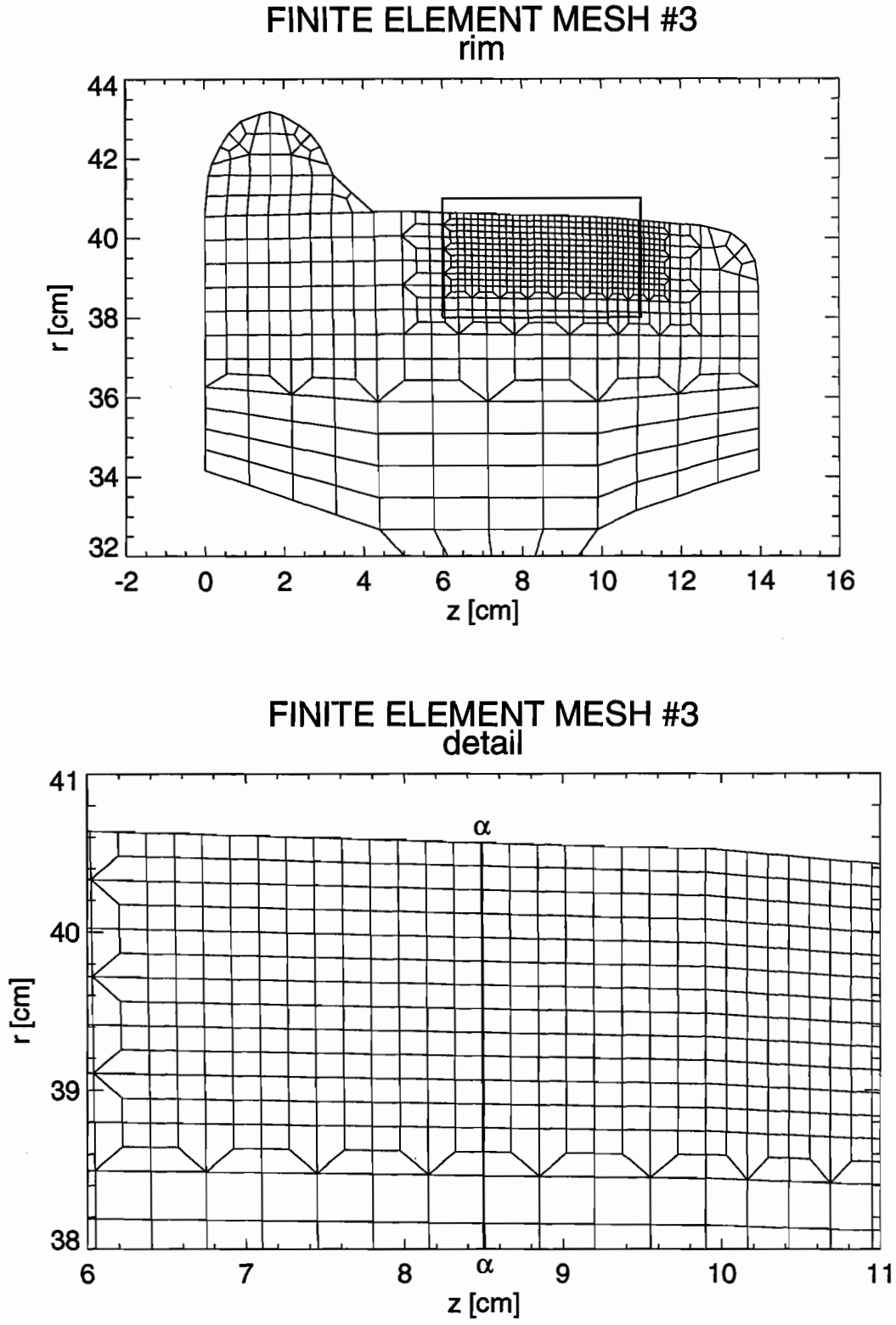

Figure 2.28 Finite Element Mesh #3 in the Problem of a Railroad Car Wheel under Contact Loading – Rim and Detail

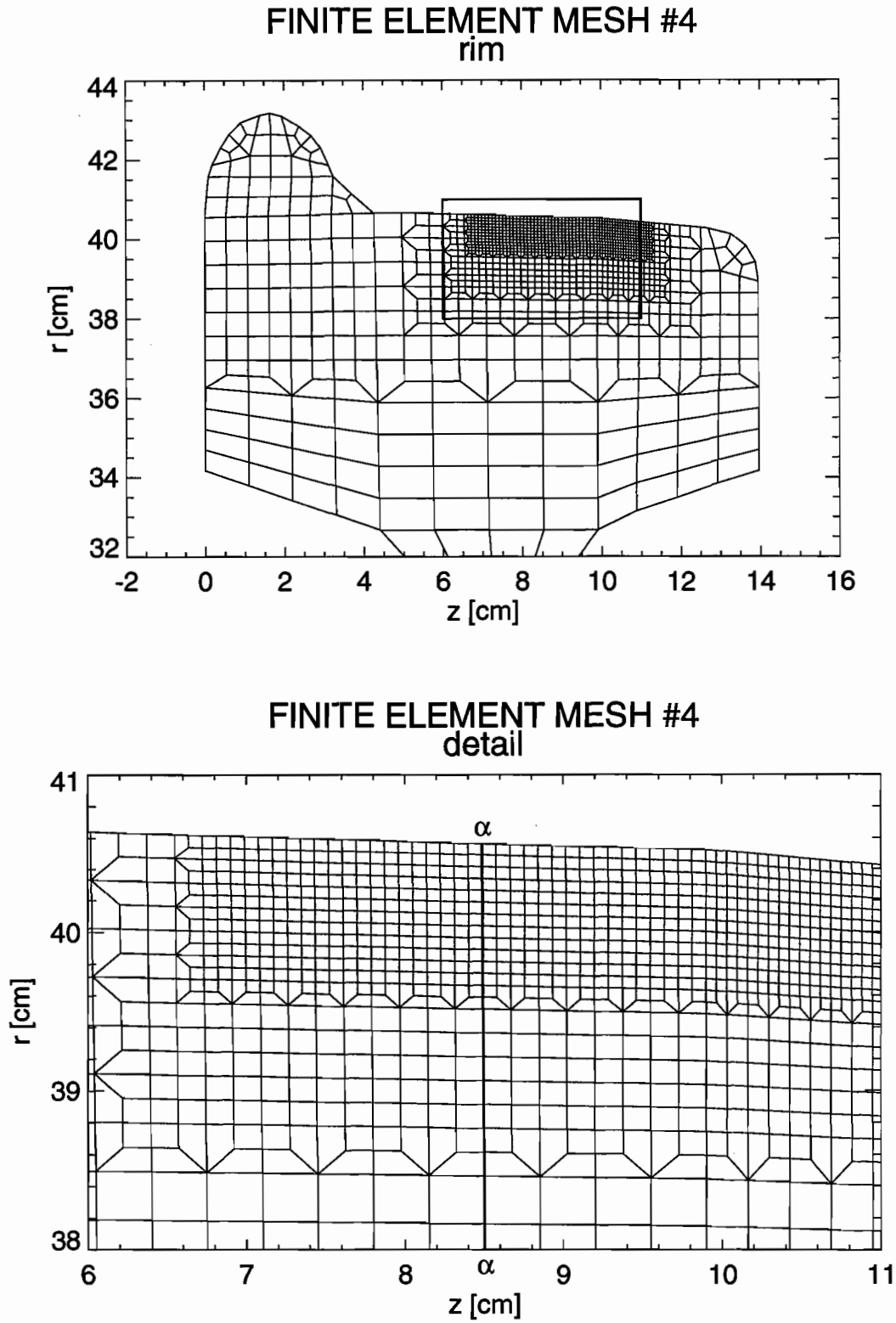

Figure 2.29 Finite Element Mesh #4 in the Problem of a Railroad Car Wheel under Contact Loading – Rim and Detail

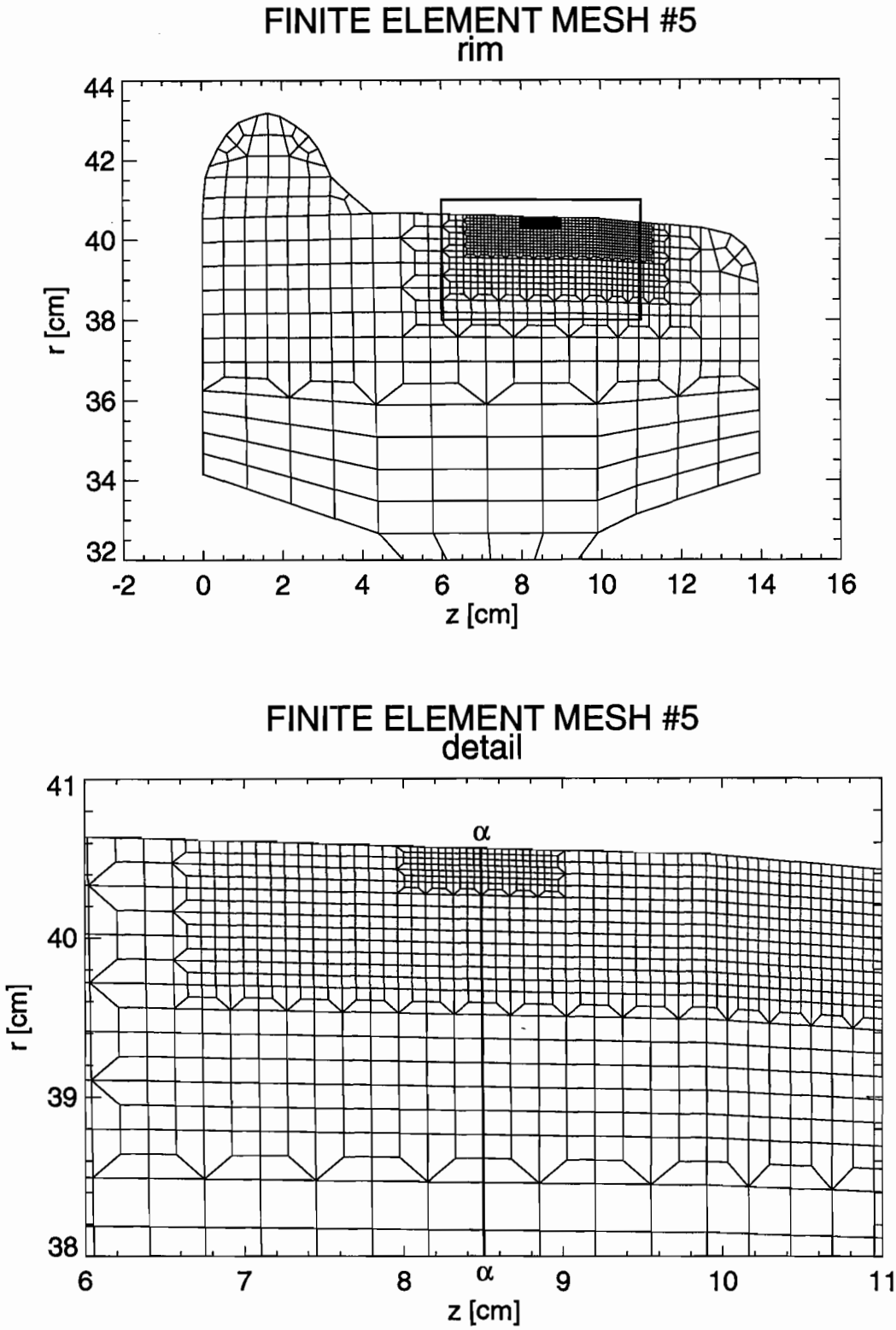

Figure 2.30 Finite Element Mesh #5 in the Problem of a Railroad Car Wheel under Contact Loading – Rim and Detail

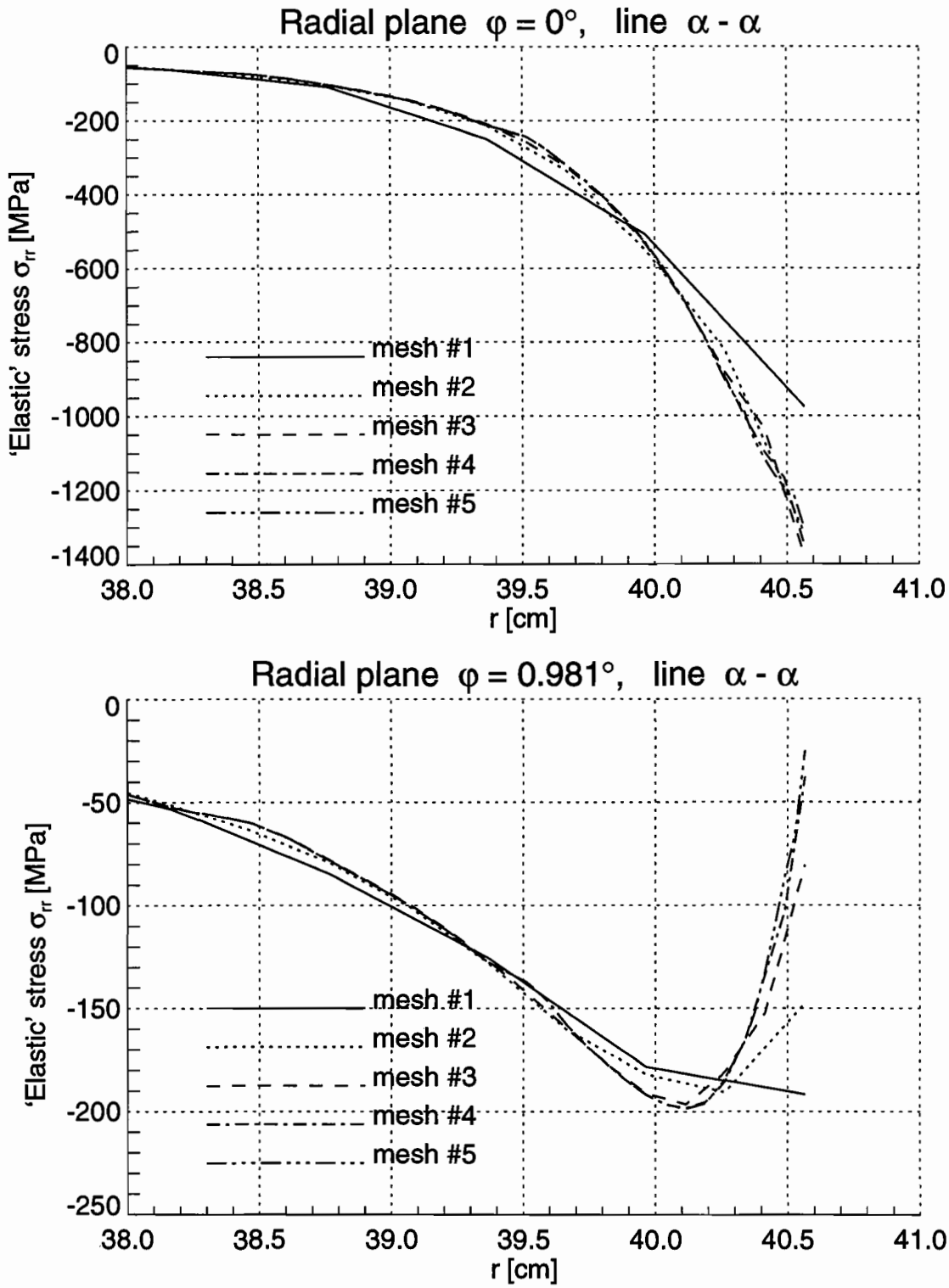

Figure 2.31 Radial 'Elastic' Stresses σ_{rr} in the Railroad Car Wheel under Vertical Loading

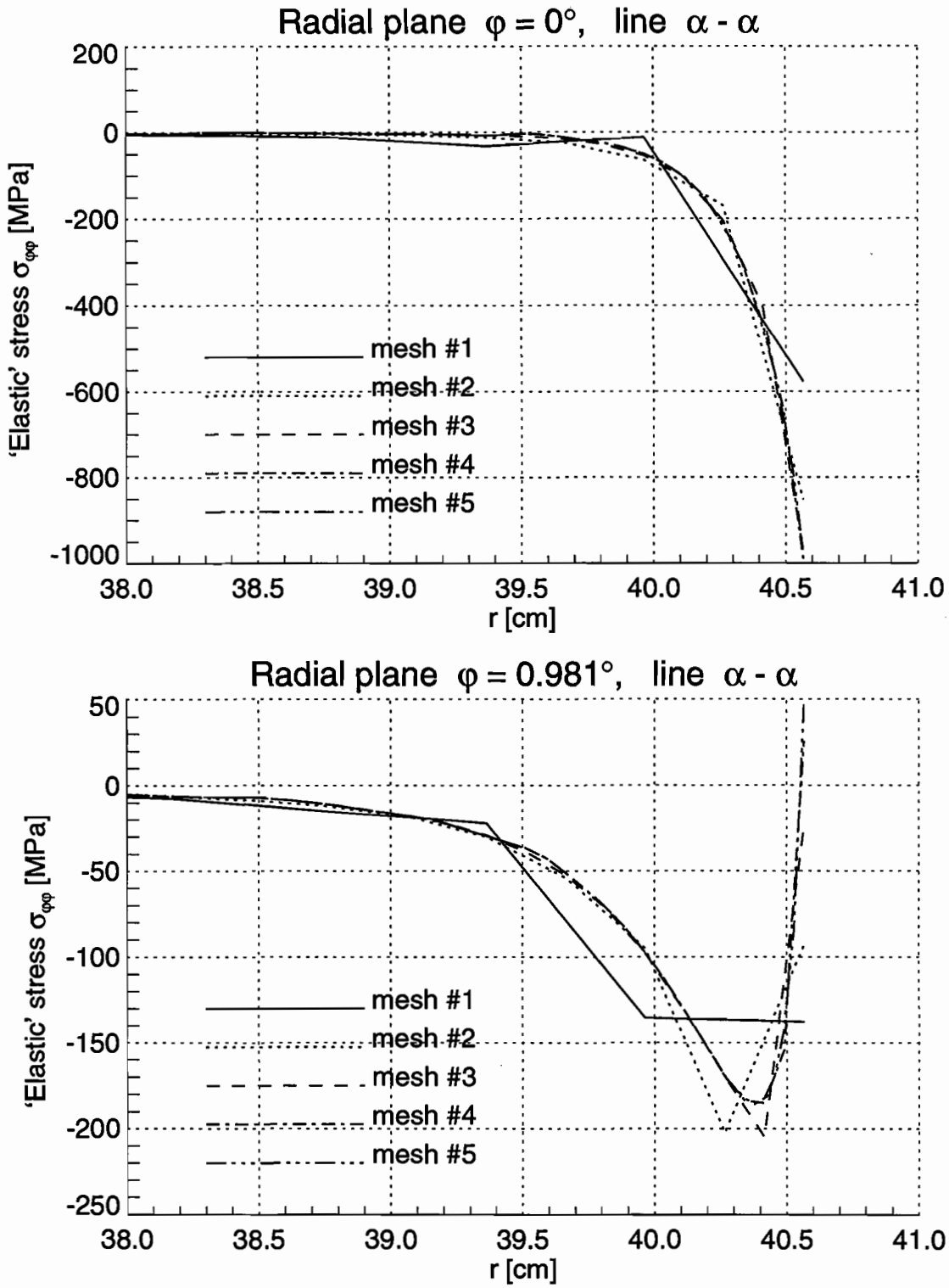

Figure 2.32 Hoop 'Elastic' Stresses $\sigma_{\varphi\varphi}$ in the Railroad Car Wheel under Vertical Loading

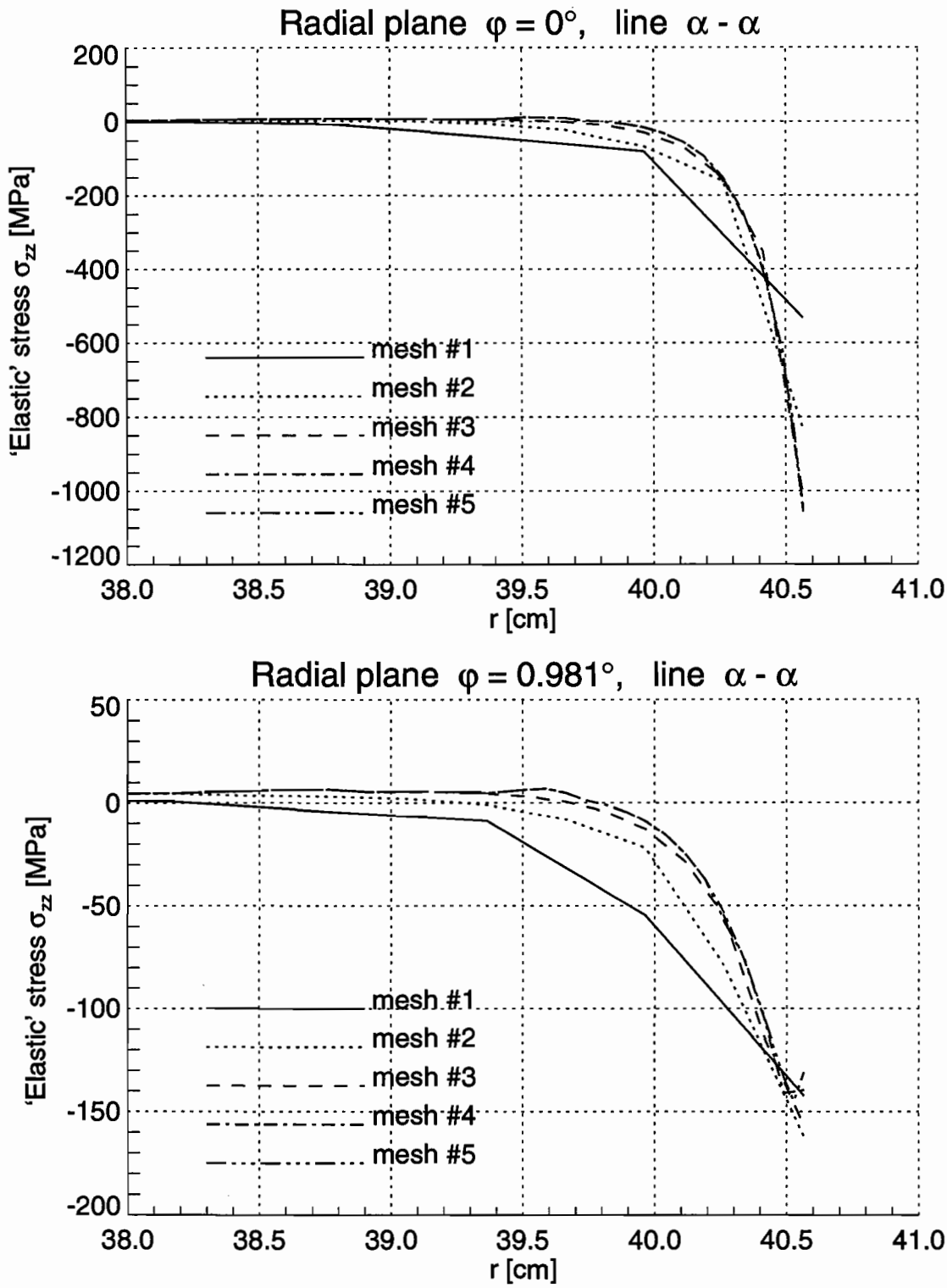

Figure 2.33 Axial 'Elastic' Stresses σ_{zz} in the Railroad Car Wheel under Vertical Loading

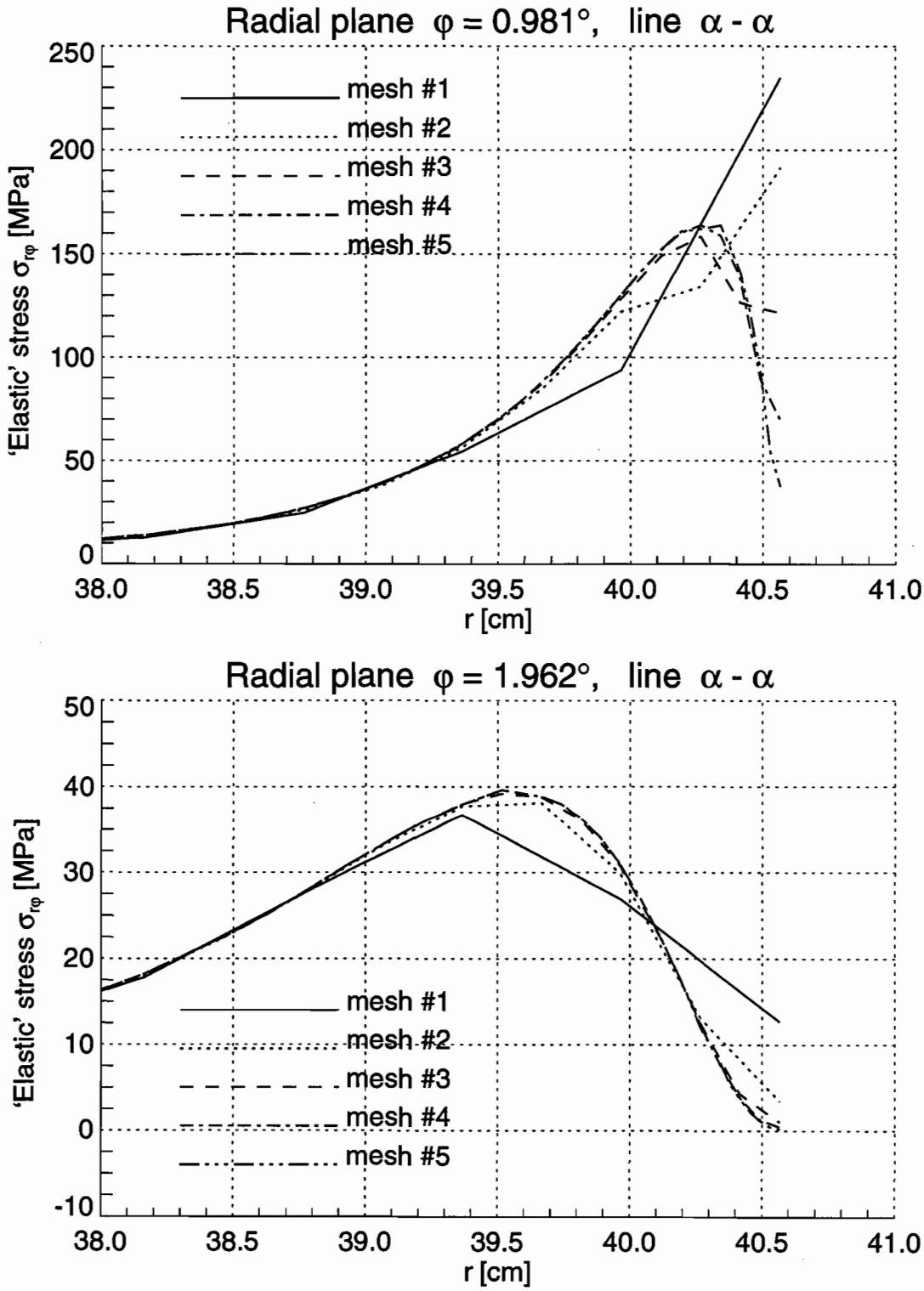

Figure 2.34 Shear 'Elastic' Stresses $\sigma_{r\varphi}$ in the Railroad Car Wheel under Vertical Loading

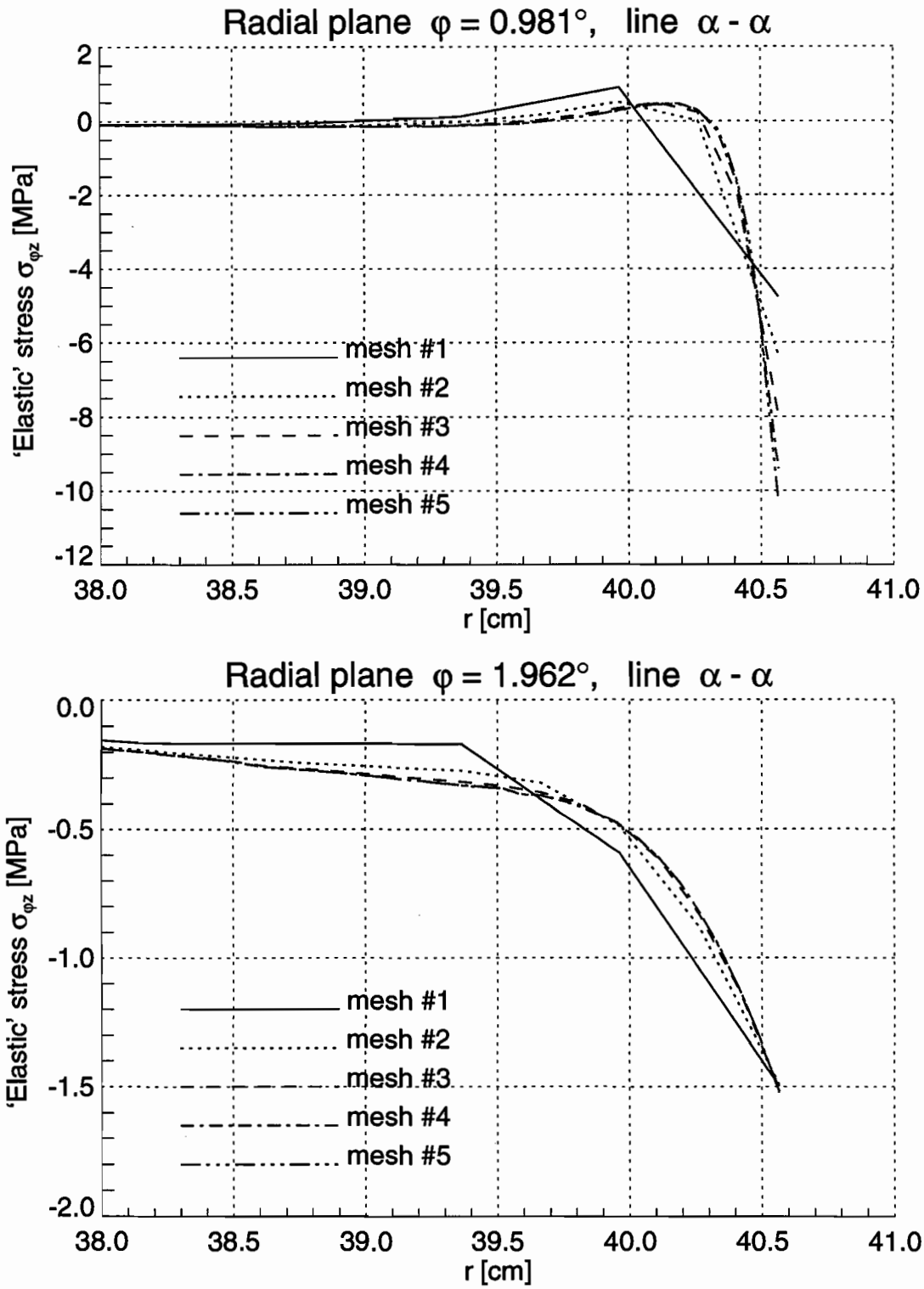

Figure 2.35 Shear 'Elastic' Stresses $\sigma_{\varphi z}$ in the Railroad Car Wheel under Vertical Loading

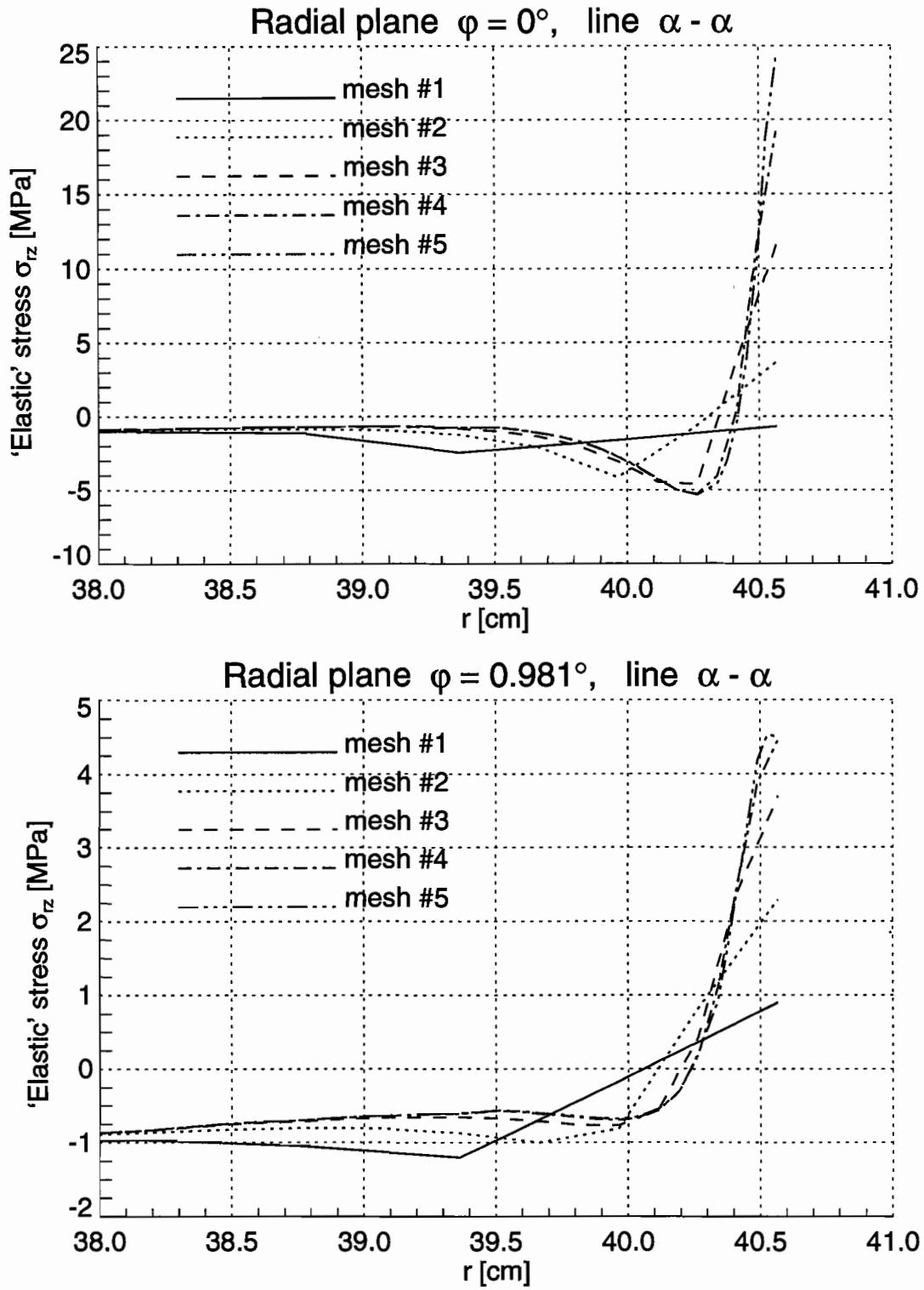

Figure 2.36 Shear 'Elastic' Stresses σ_{rz} in the Railroad Car Wheel under Vertical Loading

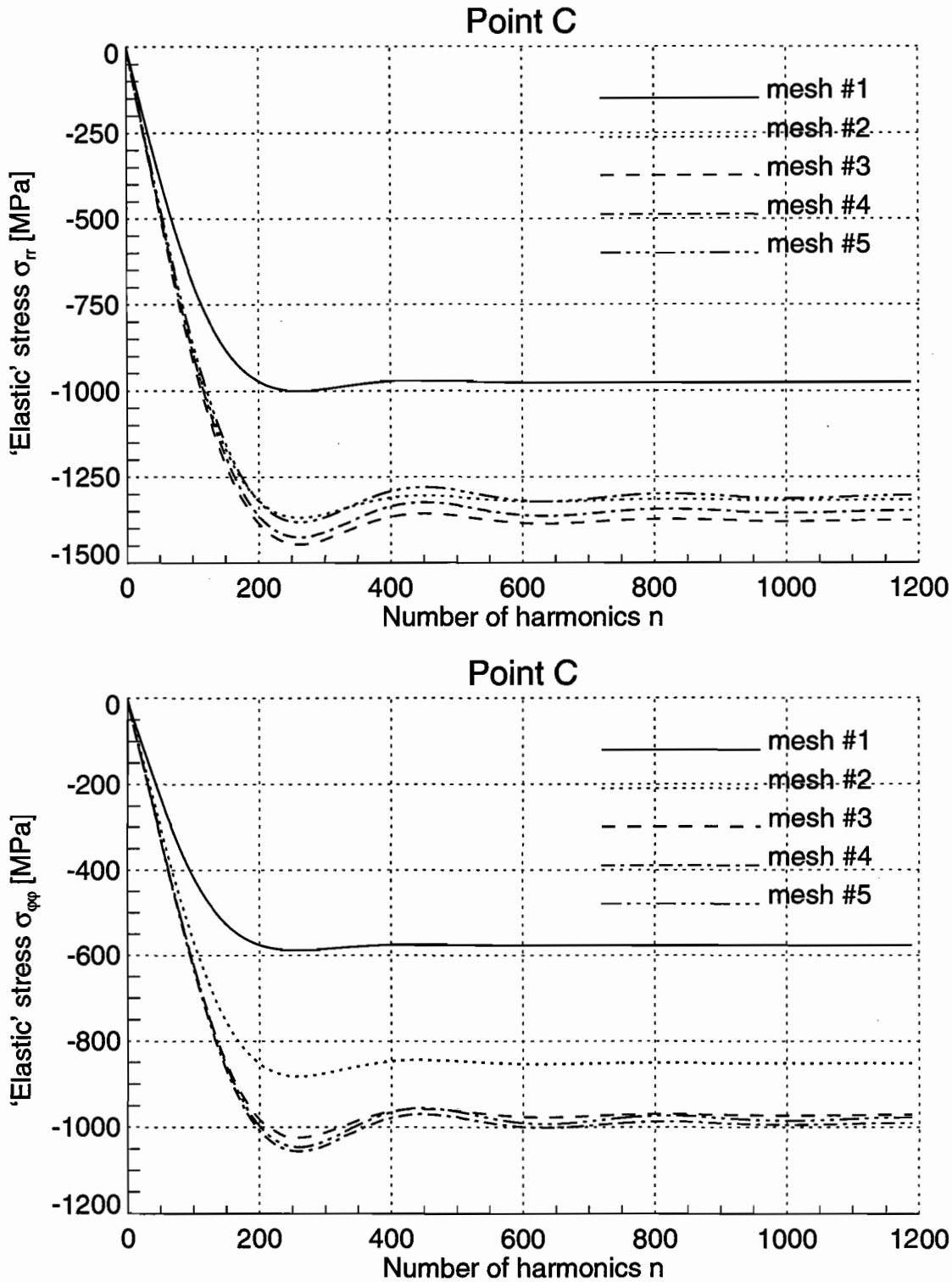

Figure 2.37 Radial σ_{rr} and Hoop $\sigma_{\varphi\varphi}$ 'Elastic' Stresses as a Function of the Number of Fourier Modes in the Railroad Car Wheel under Vertical Loading

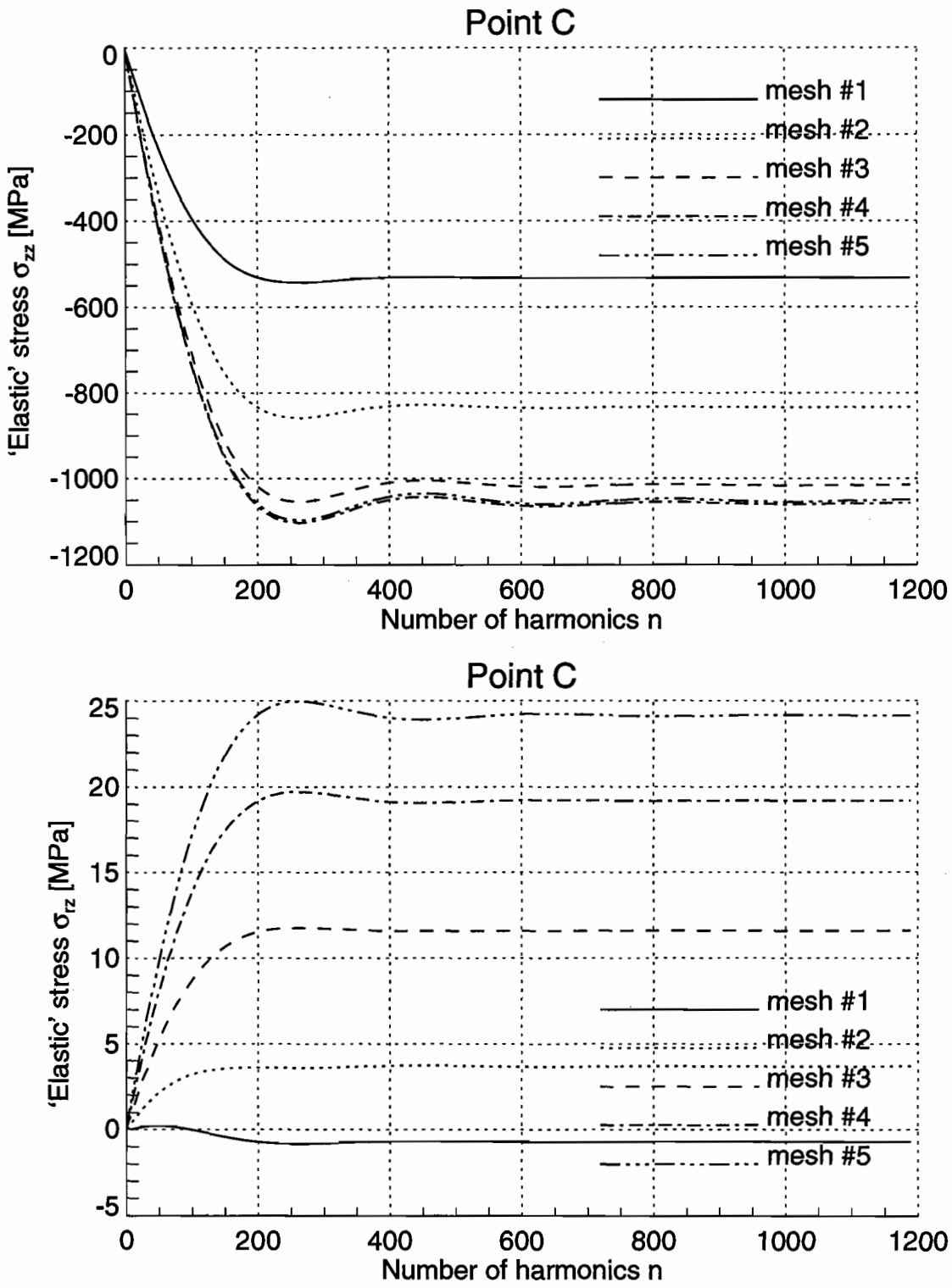

Figure 2.38 Axial σ_{zz} and Shear σ_{rz} 'Elastic' Stresses as a Function of the Number of Fourier Modes in the Railroad Car Wheel under Vertical Loading

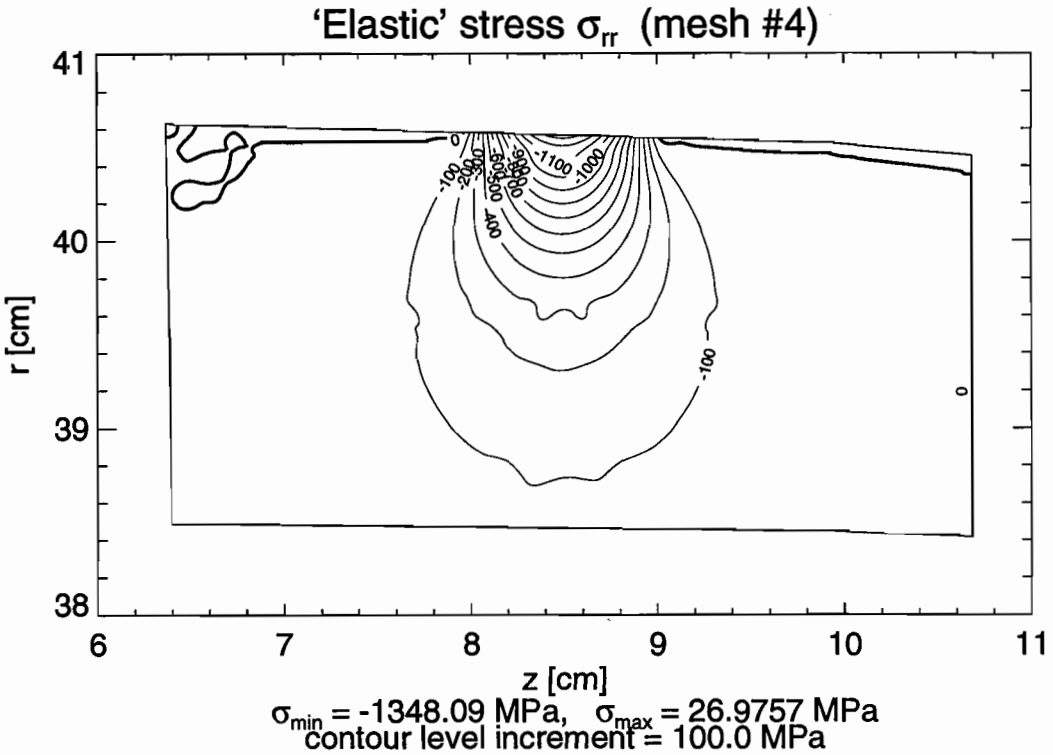

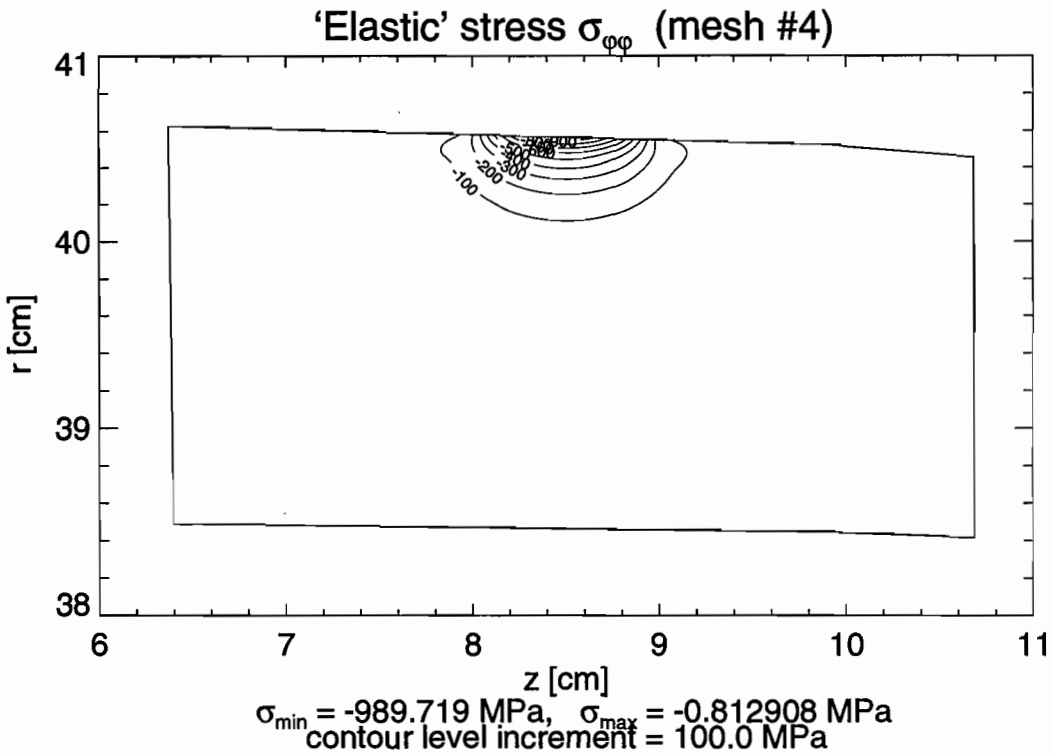

Figure 2.39 Contour Lines of Radial σ_{rr} and Hoop $\sigma_{\varphi\varphi}$ 'Elastic' Stresses in the Railroad Car Wheel under Vertical Loading – Solution for Mesh #4

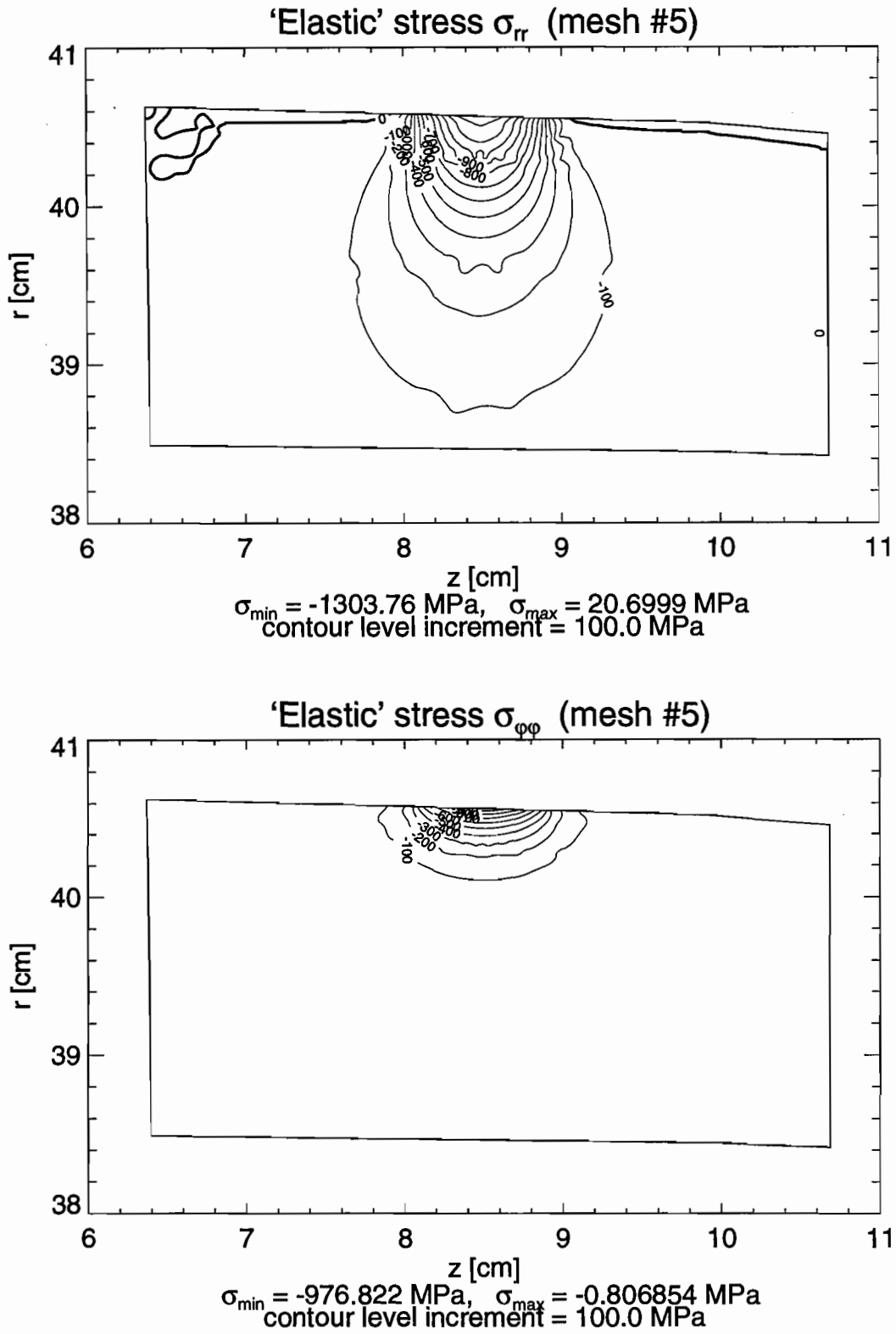

Figure 2.40 Contour Lines of Radial σ_{rr} and Hoop $\sigma_{\varphi\varphi}$ 'Elastic' Stresses in the Railroad Car Wheel under Vertical Loading – Solution for Mesh #5

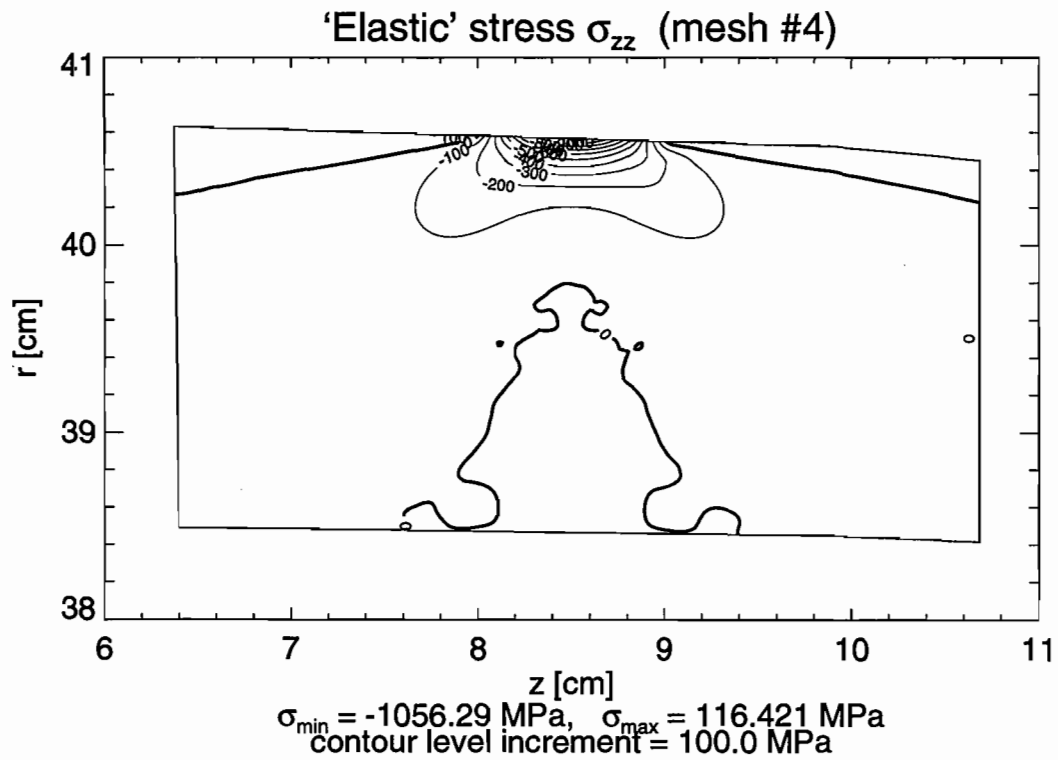

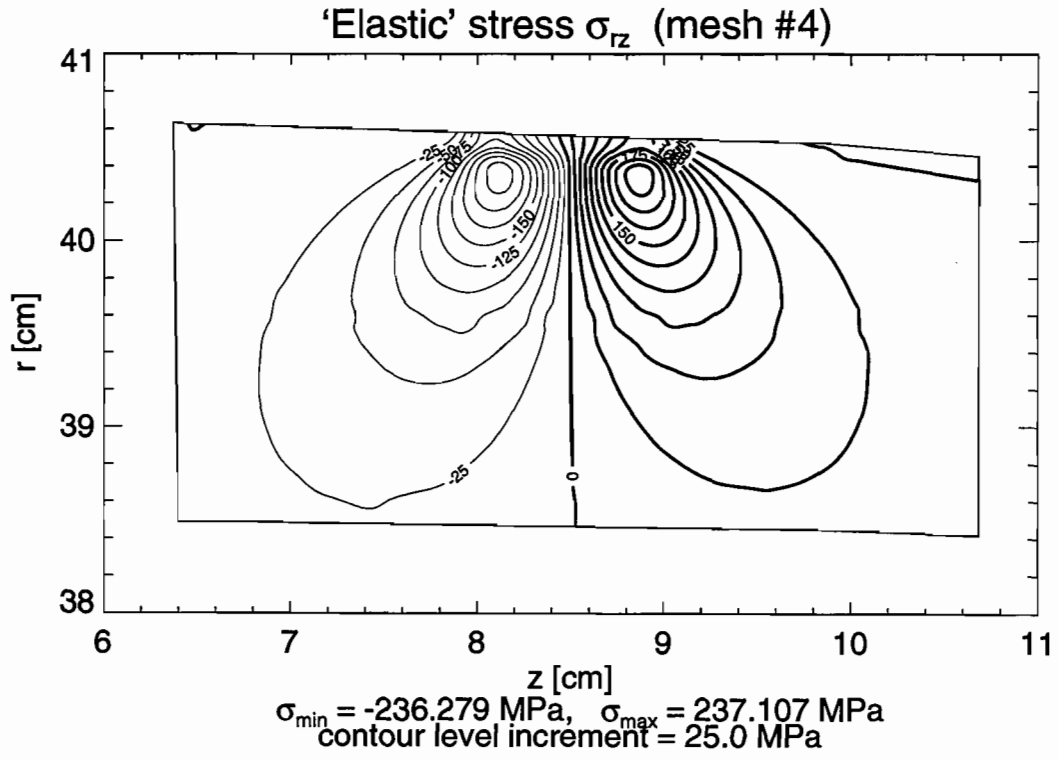

Figure 2.41 Contour Lines of Axial σ_{zz} and Shear σ_{rz} 'Elastic' Stresses in the Railroad Car Wheel under Vertical Loading – Solution for Mesh #4

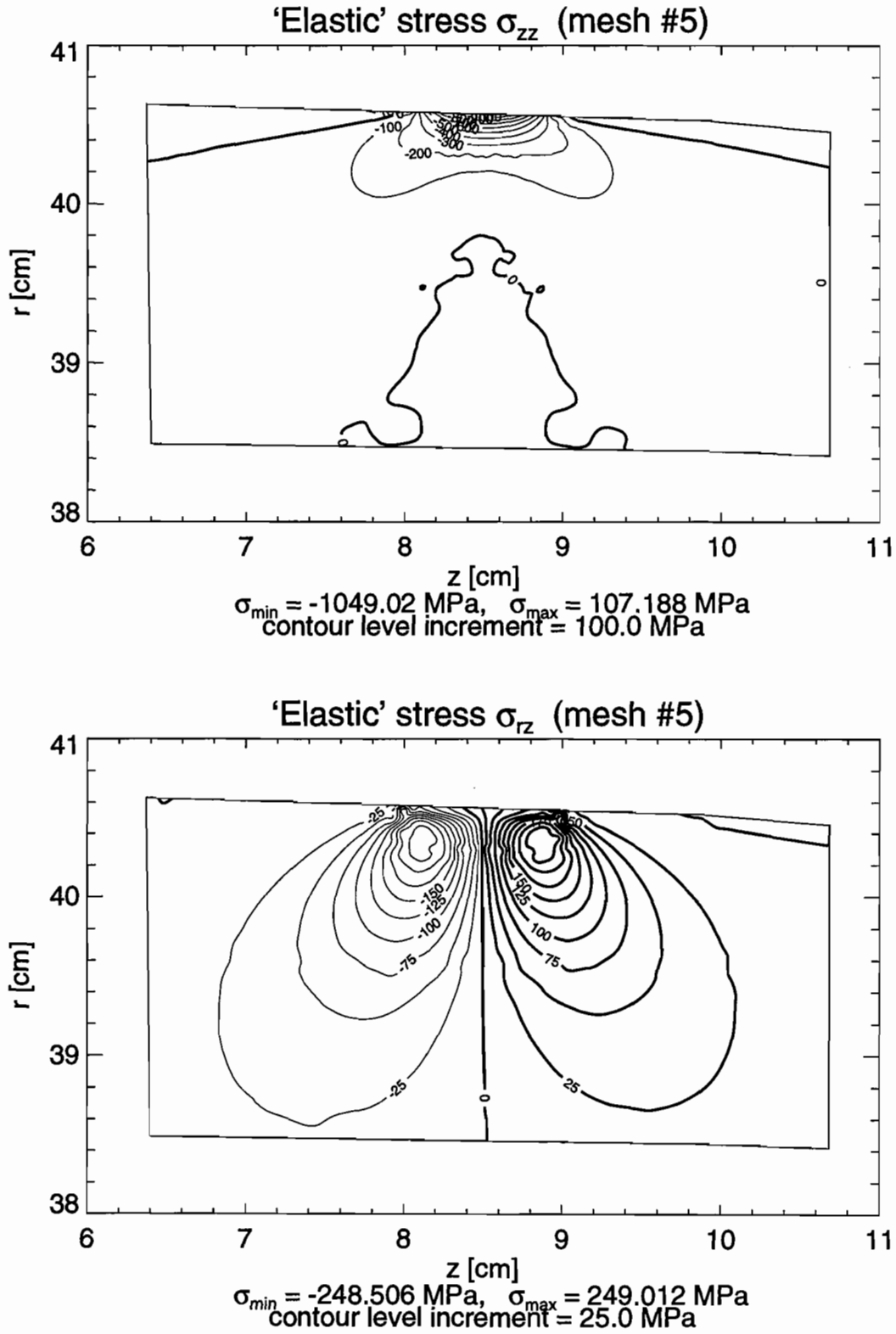

Figure 2.42 **Contour Lines of Axial σ_{zz} and Shear σ_{rz} 'Elastic' Stresses in the Railroad Car Wheel under Vertical Loading – Solution for Mesh #5**

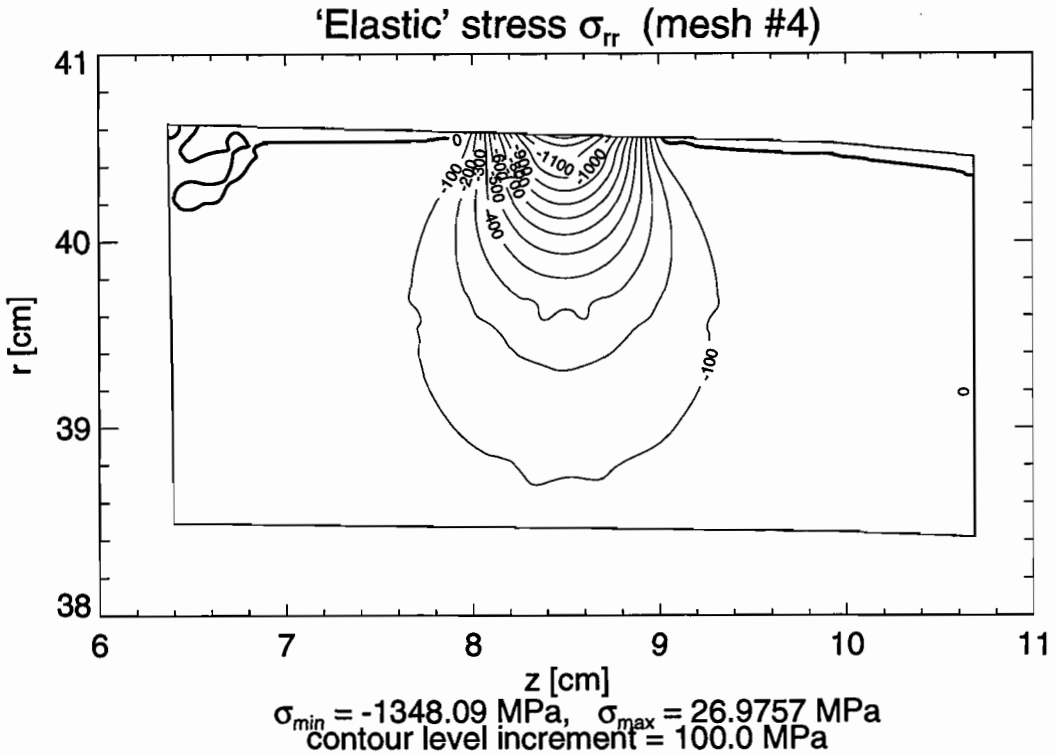

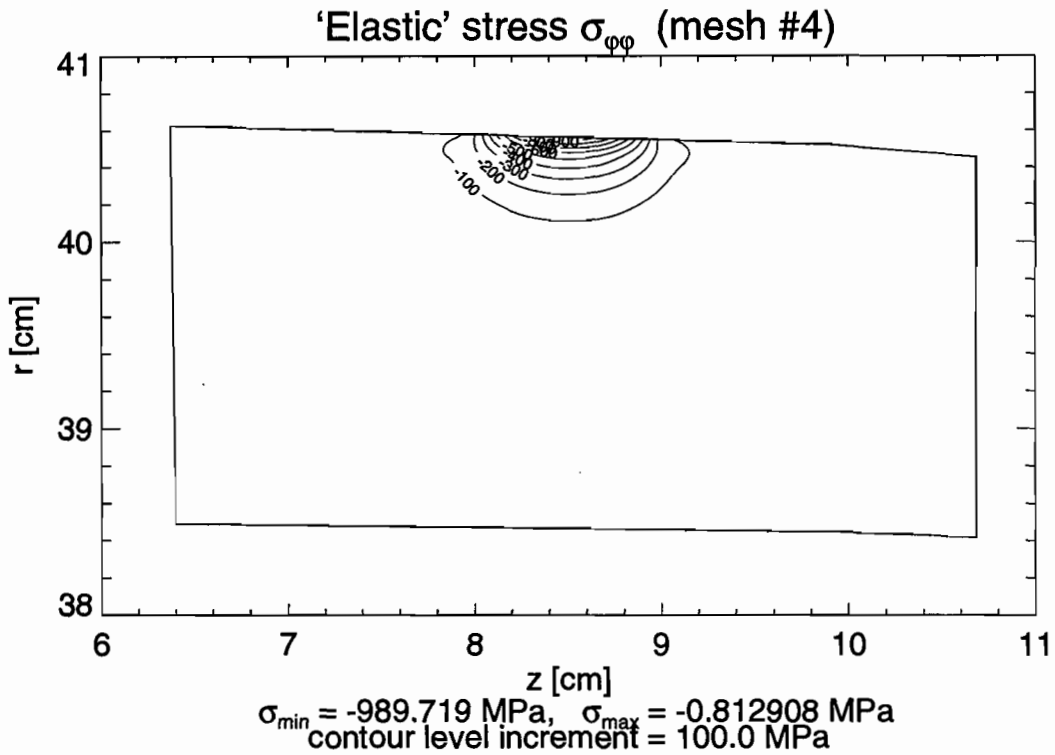

Figure 2.43 Contour Lines of Radial σ_{rr} and Hoop $\sigma_{\varphi\varphi}$ 'Elastic' Stresses in the Railroad Car Wheel under Vertical and Horizontal Loading – Solution for Mesh #4

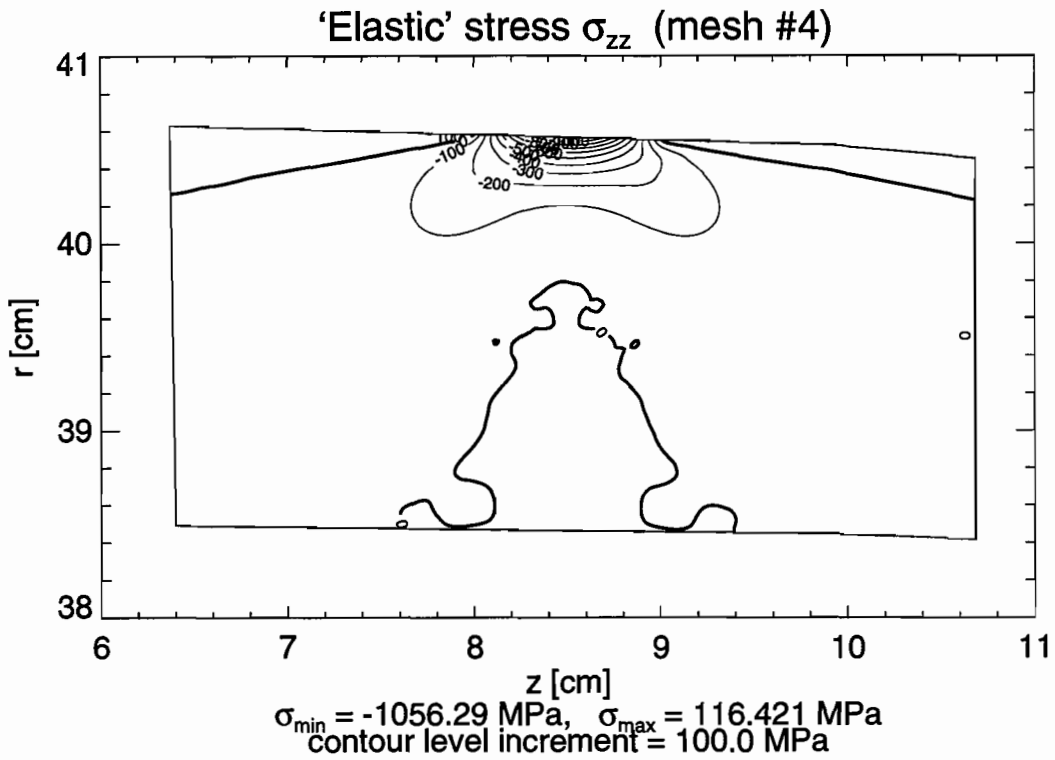

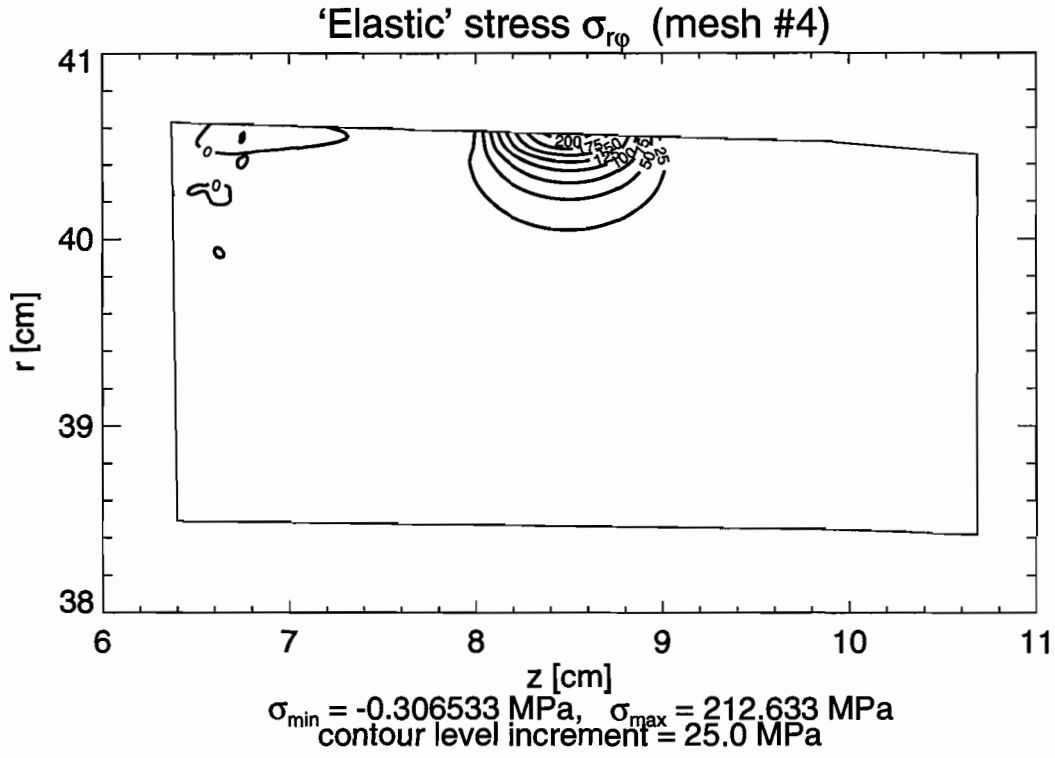

Figure 2.44 Contour Lines of Axial σ_{zz} and Shear $\sigma_{r\varphi}$ 'Elastic' Stresses in the Railroad Car Wheel under Vertical and Horizontal Loading – Solution for Mesh #4

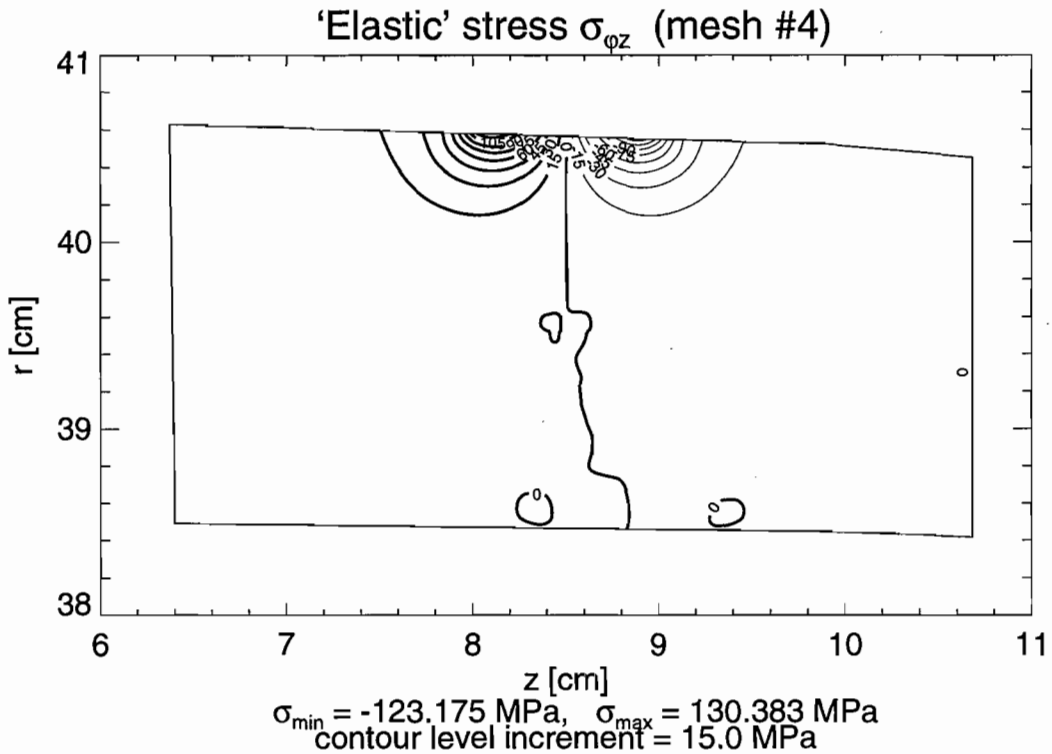

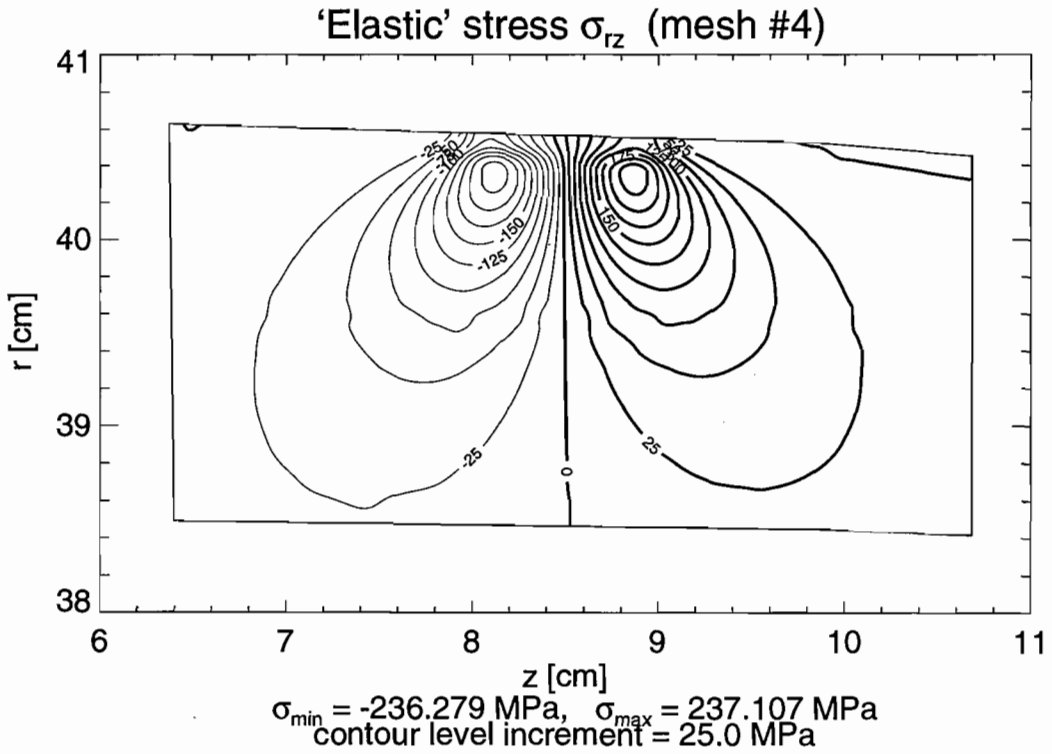

Figure 2.45 Contour Lines of Shear 'Elastic' Stresses $\sigma_{\varphi z}$ and σ_{rz} in the Railroad Car Wheel under Vertical and Horizontal Loading – Solution for Mesh #4

3. MODEL FOR ANALYSIS OF RESIDUAL STRESSES

This chapter covers all the matters associated with the development of an elastic-plastic model for analysis of residual stresses in railroad car wheels. Section 3.1 contains some introductory remarks dealing with possible ways of such analysis. Sections 3.2 and 3.3 describe the mechanical and numerical models, respectively. The above models have been implemented in a package of computer programs described in section 3.4. The approach has been extensively validated by means of test problems formulated for a thick-walled cylinder. Some selected results of these tests and their discussion are presented in section 3.5. Finally, the model has been applied to the evaluation of residual stresses in a railroad car wheel subject to both mechanical and thermal loading (section 3.6).

3.1 INTRODUCTORY REMARKS

The subject of this chapter is analysis of residual stresses in a selected class of axisymmetric bodies made of an elastic-perfectly plastic material and subject to both mechanical and thermal cyclic loads. The purpose of the work is to formulate a reliable method of analysis of such stresses in railroad car wheels working in service conditions.

In general, there are two methods of analysis of residual stresses in a body under a cyclic load. The first one is the classical incremental analysis [10], [11] oriented towards tracing the full process of loading of the body. It allows one to determine the behavior of the body at each moment of the loading process, and the information obtained this way is complete, i.e., both the statical and kinematical quantities are known. The main disadvantage of incremental analysis is the fact that in case of cyclic loads it is extremely time-consuming. An attempt to trace only one cycle of loading for a real railroad car wheel would probably require hundreds or thousands of increments. The number of cycles that should be taken into account in order to reach a state of shakedown may also be quite large. Moreover, the service load-time history required as input data is not known, so, such analysis should be performed several times assuming the most representative loading paths. Finally, the dimension of a problem that is solved using incremental analysis is determined by total stress or strain states and for a railroad car wheel has to be assumed equal to three. Thus, practical applications of this approach to the problem under consideration seem to be out of the question unless very powerful computer equipment is available.

The second method of analysis of residual stresses is the shakedown analysis. It allows one to determine whether the body under consideration is able to adapt to current cyclic loads. If the body shakes down, some additional information of either stress or displacement type may be obtained depending on the method used (the classical statical Melan and kinematical Koiter theorems [13]). The main advantage of this approach is the fact that only the final state of the body after adaptation is considered without tracing the whole service load-time history. The analysis requires only the enveloping load states to be known and they can be usually found quite easily. Moreover, the dimension of a problem that is solved using shakedown analysis is determined by residual stress or strain states. For railroad car wheels these states can be assumed to be two-dimensional, simplifying the analysis significantly. The main disadvantage of this approach in the classical sense is the fact that only some selected information may be obtained, and it corresponds to the maximal magnitude of the load for which shakedown is possible.

A novel approach to the problem of evaluation of residual stresses, the constrained energy minimization method [2], [14], [15], has been applied in this work. In contrast to the classical shakedown analysis, it allows one to compute residual stresses not only for the load of maximal magnitude but also for a load of any magnitude for which shakedown

is possible (so-called actual stresses). This approach has been successfully applied to the evaluation of residual stresses in railroad rails [4], [16], [17]. It has proven to be powerful and reliable and gives estimates of rail residual stress fields that seem to be in reasonable agreement with available experimental measurements.

The above method has been modified so that it can be used for the evaluation of residual stresses in railroad car wheels. First of all, the prismatic geometry used for rails has been replaced with axisymmetric toroidal geometry. Similarly, the assumption that a residual stress state in a rail does not depend on the rail's longitudinal direction has been replaced with the assumption that a residual stress state in a wheel is axisymmetric, even though some of the live-load stresses (e.g., due to rail/wheel contact) are not. Consequently, an appropriate hybrid finite element has been formulated and used to modify the numerical model for evaluation of residual stresses.

Significant changes have been made regarding the types of loads. They can be divided into two groups. The first one deals with traction loads. In the rail analyses to date, only normal tractions due to wheel/rail contact have been modelled because this appears to be a reasonable approximation for the unpowered wheels of freight cars, which constitute the major source of rail mechanical loading. Conversely, the wheels which most immediately require attention are powered and thus subject to significant tangent as well as normal tractions. Additionally, in this case the selection of an enveloping stress state that would represent external loads is not straightforward and usually more than one enveloping stress state should be considered. The above issues have been taken into account while formulating the new finite element (all the stress tensor components are included) and expanding the constraint flow logic in the computer programs (many enveloping stress states can be defined). The second group of modifications is connected with thermal loads. Thermal stresses in rails are limited to simple states of uniform axial tension or compression with low magnitudes, and have not been included so far in the shakedown analyses. In wheels, thermal stresses may constitute a significant part of total stresses and cannot be neglected. Additionally, they are accompanied by substantial variations in material properties, requiring the application of an appropriate algorithm for the evaluation of residual stresses. Such an algorithm has been proposed in [14] and implemented in the computer programs described in section 3.4.

3.2 MECHANICAL MODEL

The mechanical model applied to the analysis of residual stresses in railroad car wheels is based on the classical Melan theorem and the Haar-Karman principle [13]. It has been formulated for an elastic-perfectly plastic body that is subject to cyclic loading

– body forces

$$\overline{F}_i(\mathbf{x},t) = \overline{F}_i(\mathbf{x},t+nt_c) \qquad \text{in } V,$$

– surface tractions

$$\overline{T}_i(\mathbf{x},t) = \overline{T}_i(\mathbf{x},t+nt_c) \qquad \text{on } \partial V_\sigma, \tag{3.1}$$

– and displacements

$$\overline{u}_i(\mathbf{x},t) = \overline{u}_i(\mathbf{x},t+nt_c) \qquad \text{on } \partial V_u$$

where V is the volume occupied by the body, ∂V_σ and ∂V_u are parts of the boundary surface ∂V, $\mathbf{x}$ represents a point of the body, t the time, t_c the period of one cycle, n the number of cycles, and $i = 1, 2, 3$.

The problem of the evaluation of residual stresses takes the form of the following optimization problem

Find the minimum of the total complementary energy functional

$$\Pi_C = \int_V \frac{1}{2}(\sigma_{ij}^r - \sigma_{ij}^{R_0}) C_{ijkl} (\sigma_{kl}^r - \sigma_{kl}^{R_0})\, dV \tag{3.2}$$

with respect to the residual stress field $\sigma_{ij}^r(\mathbf{x})$ *satisfying*

– *the equilibrium equations*

$$\sigma_{ij,j}^r = 0 \qquad \text{in } V, \tag{3.3}$$

– *the statical boundary conditions*

$$\nu_j \sigma_{ij}^r = 0 \qquad \text{on } \partial V_\sigma, \tag{3.4}$$

– *and the yield conditions*

$$\Phi(\sigma_{ij}^r + \sigma_{ij}^E) \leq 0 \qquad \text{in } V \cup \partial V, \tag{3.5}$$

where $\sigma_{ij}^{R_0} = \sigma_{ij}^{R_0}(\mathbf{x})$ is an initial residual stress field, $\sigma_{ij}^E = \sigma_{ij}^E(\mathbf{x}, t)$ is an elastic stress field, $\Phi(\sigma_{ij})$ is a function which represents the yield conditions, ν_j is a unit normal vector to the surface ∂V_σ, and C_{ijkl} is the tensor of elastic compliances.

The solution σ_{ij}^r obtained this way is either the exact solution σ_{ij}^R or an upper bound in sense of the total complementary energy of the body, i.e.,

$$\Pi_C(\sigma_{ij}^R - \sigma_{ij}^{R_0}) \leq \Pi_C(\sigma_{ij}^r - \sigma_{ij}^{R_0}). \tag{3.6}$$

In this work, the above mechanical model has been applied to a selected class of axisymmetric bodies made of an elastic-perfectly plastic material with temperature-dependent properties. It has been assumed that the residual stress state does not depend on the circumferential direction. Consequently, the problem may be considered as a two-dimensional one. However, the total stress state is still three-dimensional and the yield conditions should be imposed on enveloping stress states that correspond to different radial planes. The number of such states depends on the type of loading applied to the body and cannot usually be determined in advance.

The elastic stress field $\sigma_{ij}^E(\mathbf{x}, t)$ is the solution to the given boundary value problem under the assumptions of the linear theory of elasticity. It represents both the stresses due to rail/wheel contact and the stresses associated with thermal effects. The latter stresses are

accompanied by substantial variation in material properties, and the optimization problem (3.2–3.5) has to be replaced by a sequence of subproblems corresponding to subsequent time parameter values $t = t_0, t_1, \ldots, t_k$. The ith subproblem is solved by applying the relevant thermal stresses and material properties and assuming that there exist initial residual stresses equal to the residual stresses obtained in the $(i-1)$th step, i.e., $\sigma_{ij}^{R_0}(t_i) = \sigma_{ij}^r(t_{i-1})$.

3.3 NUMERICAL MODEL

This section describes the numerical model applied to the analysis of residual stresses in railroad car wheels. It has been divided into two parts. The first one presents the general formulation of the model, its concepts and notation. The second part deals with detailed description of the finite element that has been implemented in the computer programs worked out for the problem under consideration.

3.3.1 Finite-Element Formulation

The numerical model applied to the analysis of residual stresses has been derived from the mechanical model presented in the previous section using the assumed stress model of the finite element method [9]. The region of the body V is divided into a finite number N_e of disjoint subregions V_n (finite elements). For each finite element, the following fields are assumed

(1) a self-equilibrated residual stress field σ_{ij}^r,

(2) a displacement field u_i that has to be continuous along the common boundary of two adjacent elements, and

(3) the corresponding strain field ε_{ij} related to the displacement field u_i by (2.4).

The stress field approximation in the assumed stress model is discontinuous along the interelement boundaries. In general, this is allowed in solid continuum mechanics provided that the corresponding surface tractions are in equilibrium. In order to satisfy this requirement, the total complementary energy functional (3.2) has to be modified by an additional term with the strain field playing the role of Lagrange multipliers. Taking into account the division of the region into finite elements, the mechanical model (3.2–3.5) may be written as follows

Find the minimum of the total complementary energy functional

$$\Pi_C = \sum_{n=1}^{N_e} \left(\int_{V_n} \frac{1}{2} \overline{\sigma}_{ij} C_{ijkl} \overline{\sigma}_{kl} \, dV - \int_{V_n} \overline{\sigma}_{ij} \varepsilon_{ij} \, dV \right) \tag{3.7}$$

with respect to the self-equilibrated residual stress field $\sigma_{ij}^r(\mathbf{x})$ satisfying the yield conditions

$$\Phi(\overline{\sigma}_{ij} + \sigma_{ij}^{R_0} + \sigma_{ij}^E) \leq 0 \qquad \text{in } V_n \cup (\partial V)_n, \tag{3.8}$$

where

$$\overline{\sigma}_{ij} = \sigma_{ij}^r - \sigma_{ij}^{R_0}. \tag{3.9}$$

It should be stressed that the statical boundary conditions (3.4) are satisfied automatically when the modified form (3.7) of the total complementary energy functional is used.

For each finite element, the stresses $\overline{\sigma}_{ij}$ and the displacements u_i are represented (using matrix notation) as follows

$$\overline{\boldsymbol{\sigma}} = \mathbf{Q}\boldsymbol{\beta}_n, \tag{3.10}$$

$$\mathbf{u} = \mathbf{N}\mathbf{q}_n \tag{3.11}$$

where $\mathbf{Q}$ is a stress interpolation matrix, $\boldsymbol{\beta}_n$ is a vector of stress parameters, $\mathbf{N}$ is a displacement interpolation matrix, and $\mathbf{q}_n$ is a vector of generalized displacements defined at a finite number of nodal points of the element. The corresponding strains $\boldsymbol{\varepsilon}$, related to the displacements $\mathbf{u}$ by (2.4), can also be expressed in terms of the generalized displacements $\mathbf{q}_n$, that is

$$\boldsymbol{\varepsilon} = \mathbf{L}\mathbf{u} = \mathbf{L}\mathbf{N}\mathbf{q}_n = \mathbf{B}\mathbf{q}_n \tag{3.12}$$

where $\mathbf{L}$ is the matrix of differential operators and $\mathbf{B}$ is a strain interpolation matrix.

The substitution of (3.10) and (3.12) into (3.7) and (3.8) results in the following numerical model for the evaluation of residual stresses

Find the minimum of the total complementary energy functional

$$\Pi_C = \sum_{n=1}^{N_e} \left(\frac{1}{2}\boldsymbol{\beta}_n^T \mathbf{H}_n \boldsymbol{\beta}_n - \boldsymbol{\beta}_n^T \mathbf{G}_n \mathbf{q}_n \right) \tag{3.13}$$

with respect to the generalized displacements $\mathbf{q}_n$ *and the stress parameters* $\boldsymbol{\beta}_n$ *satisfying the yield conditions*

$$\frac{1}{2}\boldsymbol{\beta}_n^T \mathbf{Y}_{1n} \boldsymbol{\beta}_n + \boldsymbol{\beta}_n^T \mathbf{Y}_{2n} + Y_{3n} \leq 0 \qquad \text{in } V_n \cup (\partial V)_n, \tag{3.14}$$

in which

$$\mathbf{H}_n = \int_{V_n} \mathbf{Q}^T \mathbf{C} \mathbf{Q} \, dV, \tag{3.15}$$

$$\mathbf{G}_n = \int_{V_n} \mathbf{Q}^T \mathbf{B} \, dV, \tag{3.16}$$

$$\mathbf{Y}_{1n} = \frac{3E}{1+\nu} \mathbf{Q}^T \mathbf{C}_d \mathbf{Q}, \tag{3.17}$$

$$\mathbf{Y}_{2n} = \frac{3E}{1+\nu} \mathbf{Q}^T \mathbf{C}_d (\boldsymbol{\sigma}^{R_0} + \boldsymbol{\sigma}^E), \tag{3.18}$$

$$Y_{3n} = \frac{3E}{2(1+\nu)} (\boldsymbol{\sigma}^{R_0} + \boldsymbol{\sigma}^E)^T \mathbf{C}_d (\boldsymbol{\sigma}^{R_0} + \boldsymbol{\sigma}^E) - \sigma_0^2, \tag{3.19}$$

where E is Young's modulus, ν is Poisson's ratio, $\mathbf{C}_d$ is the deviatoric part of the matrix of elastic compliances, and σ_0 is a flow stress, usually assumed to be 5 or 10% above the

specified average 0.2% offset yield strength. The forms of the yield conditions (3.14) and matrices (3.17–3.19) have been derived assuming the Mises-Hencky yield criterion.

The above description of the numerical model applied to the analysis of residual stresses is very concise. Its scope was to present the basics of the model, particularly the notation that is necessary to understand the detailed information about the finite element used in case of railroad car wheels. For more extensive description of the model and the techniques that are used in real implementations, the reader is referred to [15], [17].

3.3.2 Axisymmetric Quadrilateral Finite Element

The finite element applied to the analysis of residual stresses in railroad car wheels is an axisymmetric four-node element with linear approximation of the stress field and bilinear approximation of the displacement field. In the present case, all elements are described in the global system of cylindrical coordinates (r, z) defined on a selected radial plane. In general, they are irregular quadrilateral elements (figure 2.1a) and that is why it is usually convenient first to transform them into squares (figure 2.1b) and then to construct the interpolation functions and basic finite element matrices only for one typical element defined in the local system of rectangular cartesian coordinates (ξ, η). The transformation and the relations between integration and differentiation in both the systems of coordinates are described in section 2.3.3.

The vector of stresses $\overline{\boldsymbol{\sigma}}$, the vector of stress parameters $\boldsymbol{\beta}_n$, and the stress interpolation matrix $\mathbf{Q}$ defined in (3.10) can be written in the global system of cylindrical coordinates as follows

$$\overline{\boldsymbol{\sigma}}^T = \{\, \sigma_{rr} \quad \sigma_{\varphi\varphi} \quad \sigma_{zz} \quad \tau_{r\varphi} \quad \tau_{\varphi z} \quad \tau_{rz} \,\}, \tag{3.20}$$

$$\boldsymbol{\beta}_n^T = \{\, \beta_1 \quad \dots \quad \beta_9 \,\}, \tag{3.21}$$

$$\mathbf{Q} = \begin{bmatrix} 1 & r & z & 0 & 0 & 0 & 0 & 0 & 0 \\ 1 & 2r & z & 0 & 0 & 0 & 0 & 0 & 0 \\ 0 & 0 & 0 & 1 & r & 2z & 0 & 0 & 0 \\ 0 & 0 & 0 & 0 & 0 & 0 & r & 0 & 0 \\ 0 & 0 & 0 & 0 & 0 & 0 & -3z & 1 & r \\ 0 & 0 & 0 & 0 & 0 & -r & 0 & 0 & 0 \end{bmatrix} \tag{3.22}$$

where the matrix $\mathbf{Q}$ has been derived assuming the linear approximation of the stress tensor components and then satisfying the equilibrium equations.

Before the matrix $\mathbf{H}_n$ defined in (3.15) is derived, it is convenient to divide it into two parts that correspond to the deviatoric $\mathbf{C}_d$ and volumetric $\mathbf{C}_v$ parts of the matrix of elastic compliances $\mathbf{C}$, that is

$$\mathbf{H}_n = \mathbf{H}_{dn} + \mathbf{H}_{vn} \tag{3.23}$$

in which

$$\mathbf{H}_{dn} = \int_{V_n} \mathbf{Q}^T \mathbf{C}_d \mathbf{Q}\, dV, \tag{3.24}$$

$$\mathbf{H}_{vn} = \int_{V_n} \mathbf{Q}^T \mathbf{C}_v \mathbf{Q}\, dV, \tag{3.25}$$

where

$$\mathbf{C}_d = \frac{1+\nu}{3E}\begin{bmatrix} 2 & -1 & -1 & 0 & 0 & 0 \\ & 2 & -1 & 0 & 0 & 0 \\ & & 2 & 0 & 0 & 0 \\ & & & 6 & 0 & 0 \\ & \text{sym} & & & 6 & 0 \\ & & & & & 6 \end{bmatrix}, \tag{3.26}$$

$$\mathbf{C}_v = \frac{1-2\nu}{3E}\begin{bmatrix} 1 & 1 & 1 & 0 & 0 & 0 \\ & 1 & 1 & 0 & 0 & 0 \\ & & 1 & 0 & 0 & 0 \\ & & & 0 & 0 & 0 \\ & \text{sym} & & & 0 & 0 \\ & & & & & 0 \end{bmatrix}. \tag{3.27}$$

The substitution of (3.22), (3.26) and (3.27) into (3.24) and (3.25) results in the following form of both the integrands

$$\mathbf{Q}^T\mathbf{C}_d\mathbf{Q} = \frac{1+\nu}{3E}\times$$

$$\begin{bmatrix} 2 & 3r & 2z & -2 & -2r & -4z & 0 & 0 & 0 \\ & 6r^2 & 3rz & -3r & -3r^2 & -6rz & 0 & 0 & 0 \\ & & 2z^2 & -2z & -2rz & -4z^2 & 0 & 0 & 0 \\ & & & 2 & 2r & 4z & 0 & 0 & 0 \\ & & & & 2r^2 & 4rz & 0 & 0 & 0 \\ & & & & & 8z^2+6r^2 & 0 & 0 & 0 \\ & & \text{sym} & & & & 6r^2+54z^2 & -18z & -18rz \\ & & & & & & & 6 & 6r \\ & & & & & & & & 6r^2 \end{bmatrix}, \tag{3.28}$$

$$\mathbf{Q}^T\mathbf{C}_v\mathbf{Q} = \frac{1-2\nu}{3E}\begin{bmatrix} 4 & 6r & 4z & 2 & 2r & 4z & 0 & 0 & 0 \\ & 9r^2 & 6rz & 3r & 3r^2 & 6rz & 0 & 0 & 0 \\ & & 4z^2 & 2z & 2rz & 4z^2 & 0 & 0 & 0 \\ & & & 1 & r & 2z & 0 & 0 & 0 \\ & & & & r^2 & 2rz & 0 & 0 & 0 \\ & & & & & 4z^2 & 0 & 0 & 0 \\ & & \text{sym} & & & & 0 & 0 & 0 \\ & & & & & & & 0 & 0 \\ & & & & & & & & 0 \end{bmatrix}. \tag{3.29}$$

Finally, in order to compute the matrices $\mathbf{H}_{dn}$ and $\mathbf{H}_{vn}$, appropriate integration should be performed. Taking into account the fact that the problem is axisymmetric, such integration can be carried out over the area A_n of the nth element, that is

$$\int_{V_n} f(r,z)\,dV = 2\pi \int_{A_n} f(r,z)\,r\,dr\,dz. \tag{3.30}$$

Usually, it is much more convenient to use the local system of coordinates (ξ,η) instead of the global system (r,z), thus the formula (2.40) should be additionally applied.

The vector of displacements $\mathbf{u}$, the vector of generalized displacements $\mathbf{q}_n$, and the displacement interpolation matrix $\mathbf{N}$ defined in (3.11) can be written in the local system of coordinates as follows

$$\mathbf{u}^T(\xi,\eta) = \left\{ u_r(\xi,\eta) \quad u_\varphi(\xi,\eta) \quad u_z(\xi,\eta) \right\}, \tag{3.31}$$

$$\mathbf{q}_n^T = \left\{ \mathbf{q}_1^T \quad \dots \quad \mathbf{q}_4^T \right\}, \tag{3.32}$$

$$\mathbf{N}(\xi,\eta) = \left[\mathbf{N}_1(\xi,\eta) \quad \dots \quad \mathbf{N}_4(\xi,\eta) \right] \tag{3.33}$$

in which

$$\mathbf{q}_i^T = \left\{ q_{ri} \quad q_{\varphi i} \quad q_{zi} \right\}, \qquad i = 1, \dots, 4, \tag{3.34}$$

$$\mathbf{N}_i(\xi,\eta) = \begin{bmatrix} N_i(\xi,\eta) & 0 & 0 \\ 0 & N_i(\xi,\eta) & 0 \\ 0 & 0 & N_i(\xi,\eta) \end{bmatrix}, \tag{3.35}$$

where $\mathbf{q}_i$ is the vector of generalized nodal displacements at the ith node of the element, and N_i is the shape function associated with this node, that is

$$N_i(\xi,\eta) = \frac{1}{4}(1+\xi\xi_i)(1+\eta\eta_i). \tag{3.36}$$

Further analysis requires the relation (3.12) also to be specified in the local system of coordinates. The strain vector $\boldsymbol{\varepsilon}$ and the matrix of differential operators $\mathbf{L}$ can be written as follows

$$\boldsymbol{\varepsilon}^T = \left\{ \varepsilon_{rr} \quad \varepsilon_{\varphi\varphi} \quad \varepsilon_{zz} \quad \gamma_{r\varphi} \quad \gamma_{\varphi z} \quad \gamma_{rz} \right\}, \tag{3.37}$$

$$\mathbf{L} = \begin{bmatrix} \dfrac{\partial}{\partial r} & 0 & 0 \\ \dfrac{1}{r} & 0 & 0 \\ 0 & 0 & \dfrac{\partial}{\partial z} \\ 0 & \dfrac{\partial}{\partial r} - \dfrac{1}{r} & 0 \\ 0 & \dfrac{\partial}{\partial z} & 0 \\ \dfrac{\partial}{\partial z} & 0 & \dfrac{\partial}{\partial r} \end{bmatrix}. \tag{3.38}$$

Before the strain interpolation matrix $\mathbf{B}$ is derived, it is convenient, as it was done in (3.32) and (3.33), to divide it into submatrices that are associated with the nodal points of the element

$$\mathbf{B} = \left[\mathbf{B}_1 \quad \dots \quad \mathbf{B}_4 \right]. \tag{3.39}$$

The substitution of (3.39), (3.38), (3.33) and (3.35) into (3.12) results in

$$\mathbf{B}_i = \begin{bmatrix} \dfrac{\partial N_i}{\partial r} & 0 & 0 \\ \dfrac{N_i}{r} & 0 & 0 \\ 0 & 0 & \dfrac{\partial N_i}{\partial z} \\ 0 & \dfrac{\partial N_i}{\partial r} - \dfrac{N_i}{r} & 0 \\ 0 & \dfrac{\partial N_i}{\partial z} & 0 \\ \dfrac{\partial N_i}{\partial z} & 0 & \dfrac{\partial N_i}{\partial r} \end{bmatrix}. \tag{3.40}$$

Consequently, before the matrix $\mathbf{G}_n$ is computed, the integrand in (3.16) should be decomposed, that yields

$$\mathbf{Q}^T\mathbf{B} = \begin{bmatrix} \mathbf{Q}^T\mathbf{B}_1 & \dots & \mathbf{Q}^T\mathbf{B}_4 \end{bmatrix} \tag{3.41}$$

in which

$$\mathbf{Q}^T\mathbf{B}_i = \begin{bmatrix} \dfrac{\partial N_i}{\partial r} + \dfrac{N_i}{r} & 0 & 0 \\ \left(\dfrac{\partial N_i}{\partial r} + 2\dfrac{N_i}{r}\right) r & 0 & 0 \\ \left(\dfrac{\partial N_i}{\partial r} + \dfrac{N_i}{r}\right) z & 0 & 0 \\ 0 & 0 & \dfrac{\partial N_i}{\partial z} \\ 0 & 0 & \dfrac{\partial N_i}{\partial z} r \\ -\dfrac{\partial N_i}{\partial z} r & 0 & 2\dfrac{\partial N_i}{\partial z} z - \dfrac{\partial N_i}{\partial r} r \\ 0 & \left(\dfrac{\partial N_i}{\partial r} - \dfrac{N_i}{r}\right) r - 3\dfrac{\partial N_i}{\partial z} z & 0 \\ 0 & \dfrac{\partial N_i}{\partial z} & 0 \\ 0 & \dfrac{\partial N_i}{\partial z} r & 0 \end{bmatrix}. \tag{3.42}$$

The integration necessary to compute the matrix $\mathbf{G}_n$ should be carried out using the same technique as in case of the matrices $\mathbf{H}_{dn}$ and $\mathbf{H}_{vn}$.

With regard to the matrices (3.17–3.19), they can be computed quite easily. The form of the matrix $\mathbf{Y}_{1n}$ has been already derived and can be recognized on the right-hand side of (3.28). The substitution of (3.22) and (3.26) into (3.18) and (3.19) results in the following forms of the vector $\mathbf{Y}_{2n}$ and scalar Y_{3n}

$$\mathbf{Y}_{2n} = \left\{ \begin{array}{c} \sigma_{rr} + \sigma_{\varphi\varphi} - 2\sigma_{zz} \\ 3\left(\sigma_{\varphi\varphi} - \sigma_{zz}\right) r \\ \left(\sigma_{rr} + \sigma_{\varphi\varphi} - 2\sigma_{zz}\right) z \\ -\left(\sigma_{rr} + \sigma_{\varphi\varphi} - 2\sigma_{zz}\right) \\ -\left(\sigma_{rr} + \sigma_{\varphi\varphi} - 2\sigma_{zz}\right) r \\ -2\left(\sigma_{rr} + \sigma_{\varphi\varphi} - 2\sigma_{zz}\right) z - 6\tau_{rz} r \\ 6\tau_{r\varphi} r - 18\tau_{\varphi z} z \\ 6\tau_{\varphi z} \\ 6\tau_{\varphi z} r \end{array} \right\}, \tag{3.43}$$

$$Y_{3n} = \frac{1}{2}\left[\left(\sigma_{rr} - \sigma_{\varphi\varphi}\right)^2 + \left(\sigma_{\varphi\varphi} - \sigma_{zz}\right)^2 + \left(\sigma_{rr} - \sigma_{zz}\right)^2 + 6\left(\tau_{r\varphi}^2 + \tau_{\varphi z}^2 + \tau_{rz}^2\right)\right] - \sigma_0^2 \tag{3.44}$$

where the vector $\boldsymbol{\sigma}$ represents the sum $\boldsymbol{\sigma}^{R_0} + \boldsymbol{\sigma}^{E}$.

3.4 COMPUTER PROGRAMS

The mechanical and numerical models described in the previous sections have been implemented in a package of computer programs. The package consists of six programs that can be divided into two groups.

The first group contains four programs called `STRATEGY`, `STATCOND`, `OPTIM`, and `ELASTZON`. These programs constitute the most important part of the package. They allow one to solve the problem of the evaluation of residual stresses not only for railroad car wheels but also for rails [4], [16], [17]. As far as the type of finite elements is concerned, virtually any assumed stress finite element can be used. The second group consists of two auxiliary programs called `MATRIX` and `RESIDUAL`. These relatively simple programs are strictly connected with the problem to be solved (rail, wheel), with the type of finite elements (quadrilateral, triangular), and finally with the approximations of the stress and displacement fields.

The structure of the programs and the program flow logic are relatively straightforward, except that the user should be prepared to monitor the progress of the optimization and, if necessary, to adjust certain control parameters. The first program to be executed is `MATRIX` which computes the finite-element matrices defined in (3.15–3.19) for given input data. Based on this information and the current state of residual stresses, the control program `STRATEGY` examines the yield conditions (3.14) for all enveloping stress states and divides the whole body into two parts — elastic and plastic zones. If all the yield conditions are satisfied, the current residual stress state is the final one and the post-processing program `RESIDUAL` is executed. If it is not the case, a new residual stress state has to be found and the program `STATCOND` is called. This program allows one to formulate the optimization problem (3.13–3.14) in terms of unknown stress parameters associated only with the plastic zone. The influence of the elastic zone on the form of the total complementary functional (3.13) is found using a procedure of static condensation. The optimization problem is solved by means of the program `OPTIM` using the method of feasible directions [18]. It should be stressed that `OPTIM` is the only program which has to be run

interactively. In spite of the fact that a special procedure of automated optimization has been worked out, usually user's involvement is required, especially in case of very large optimization problems. After the optimization problem has been solved and the stress parameters in the plastic zone have been found, the program `ELASTZON` is executed and the solution in the elastic zone is computed. The latter program terminates the basic loop in the program flow logic and `STRATEGY` is called again.

The input data for the programs consist of seven files of ASCII type. Four of them contain the information about the topology of the finite element mesh and material properties. They have exactly the same format as the input files used in the program `WHEELE` described in section 2.4. The other three files contain the information about elastic, thermal and initial residual stresses. As for the elastic stresses, the number of enveloping stress states is defined by the user and limited only by available computer equipment. With regard to the thermal stresses, they have been assumed to be rotationally symmetric. In fact, these stresses are elastic stresses and an additional file has been created for user's convenience. Finally, the initial residual stresses have also been assumed to be rotationally symmetric (basic assumption in the numerical model) and self-equilibrated (obvious). It should be stressed that, if the initial residual stresses come from experiment, the latter requirement is usually not satisfied unless the measurements are post-processed.

The output data consist of five files of ASCII type. Four of them contain the solution to the problem, i.e., the residual and total stresses computed at the centroids and nodes of the finite elements. The fifth file contains some information about the optimization problems, elements in the plastic zone, and active constraints (yield conditions) for all enveloping stress states.

3.5 NUMERICAL TESTS

The approach applied to the analysis of residual stresses in railroad car wheels is analogous to that applied in case of railroad rails [4], [16], [17]. As far as the mechanical and numerical models are concerned, prismatic geometry used for rails has been replaced with axisymmetric toroidal geometry and additionally the dependence of material properties on temperature has been taken into account [14]. With regard to the computer programs, those worked out for the evaluation of residual stresses in rails [17] have been extended accordingly, including some additional changes associated with the fact that more than one enveloping stress state must be taken into consideration.

The approach applied to the analysis of residual stresses in rails has been verified thoroughly using various benchmark tests with both known and unknown analytical solutions. That is why the number of tests performed in this work have been reduced significantly to those concerning the new axisymmetric topology and temperature-dependent material properties.

The most important test is that carried out for a thick-walled cylinder subject to internal loading varying along the longitudinal axis. This test was performed assuming exactly the same data as in the case of analysis of elastic contact stresses (section 2.5.2) except for the material properties. This time the cylinder was assumed to be made of an elastic-perfectly plastic material with the non-dimensional flow stress $\sigma_0 = 0.8$.

The problem was solved using three finite element meshes of square elements that consisted of 16, 32, and 64 elements in the radial direction, and 8, 16, and 32 elements in the longitudinal direction, respectively. The coarsest mesh #1 was absolutely inappropriate for this problem and was not considered.

For comparison, the problem was also solved by means of ABAQUS, using the same finite element meshes. In this case, 8-node axisymmetric elements were applied. The analysis was performed applying ten cycles of loading and unloading in order to assure that the solution corresponds to the state after adaptation. In fact there were almost no differences between the residual stress states after the first and the second cycles and maybe they were caused only by that fact that the problem was solved using incremental analysis. The quality of the solution is lower than in the case of elastic analysis, as expected, but still good for the purpose of comparison.

Some selected results are shown in figures 3.1 through 3.8. The convergence of the solution is presented in figures 3.1 through 3.4. The radial σ_{rr}, hoop $\sigma_{\varphi\varphi}$, and axial σ_{zz} stresses are plotted for two selected cross sections $z = 0$ and $z = 0.5$ that contain the center and the end of the loading zone, respectively. The shear stresses σ_{rz} are also plotted for two cross sections, but instead of the cross section $z = 0$, where these stresses are equal to zero, an additional cross section $z = 0.25$ was chosen. In figures 3.5 through 3.8, the above stress components are presented in the form of contour line plots. This time, only the best solution obtained for the mesh #4 and the ABAQUS solution are shown.

The results obtained for the problem under consideration validate both the mechanical and numerical models and the computer programs worked out for the evaluation of residual stresses. The biggest errors occur in the plastic zone where the residual stresses change very rapidly. It should be stressed that the quality of the solution is influenced not only by the mesh density but also by the quality of the elastic solution which is used as input data. Comparative tests carried out for problems with known analytical solutions indicate that even small differences in the latter solution may result in different residual stress states, and that is why appropriate mesh refinement should not be neglected.

As for the test dealing with temperature-dependent material properties, thanks to axisymmetry it could be performed for a real railroad car wheel. This test is presented in section 3.6.

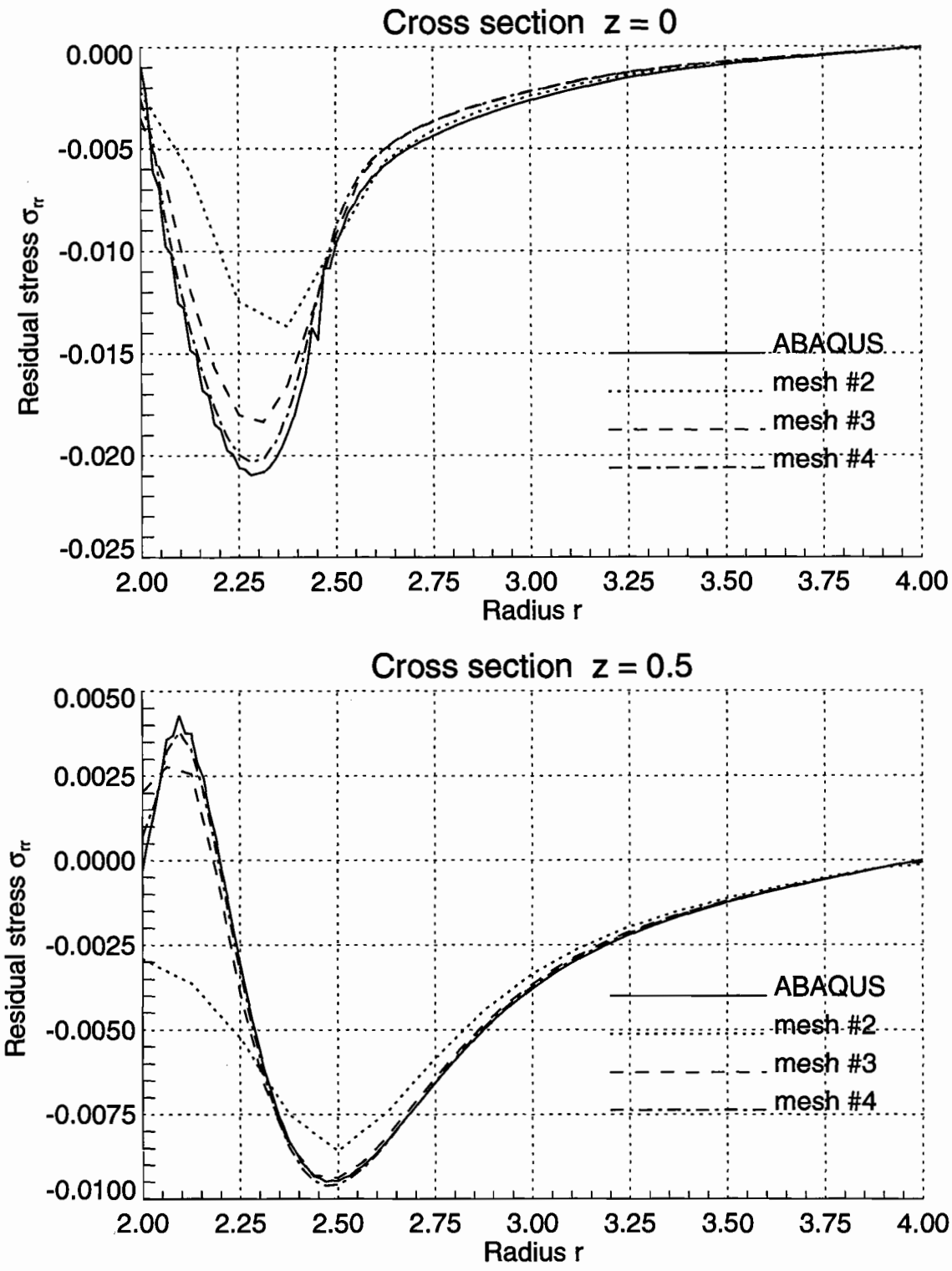

Figure 3.1 Radial Residual Stresses σ_{rr} in the Thick-Walled Cylinder under Internal Loading

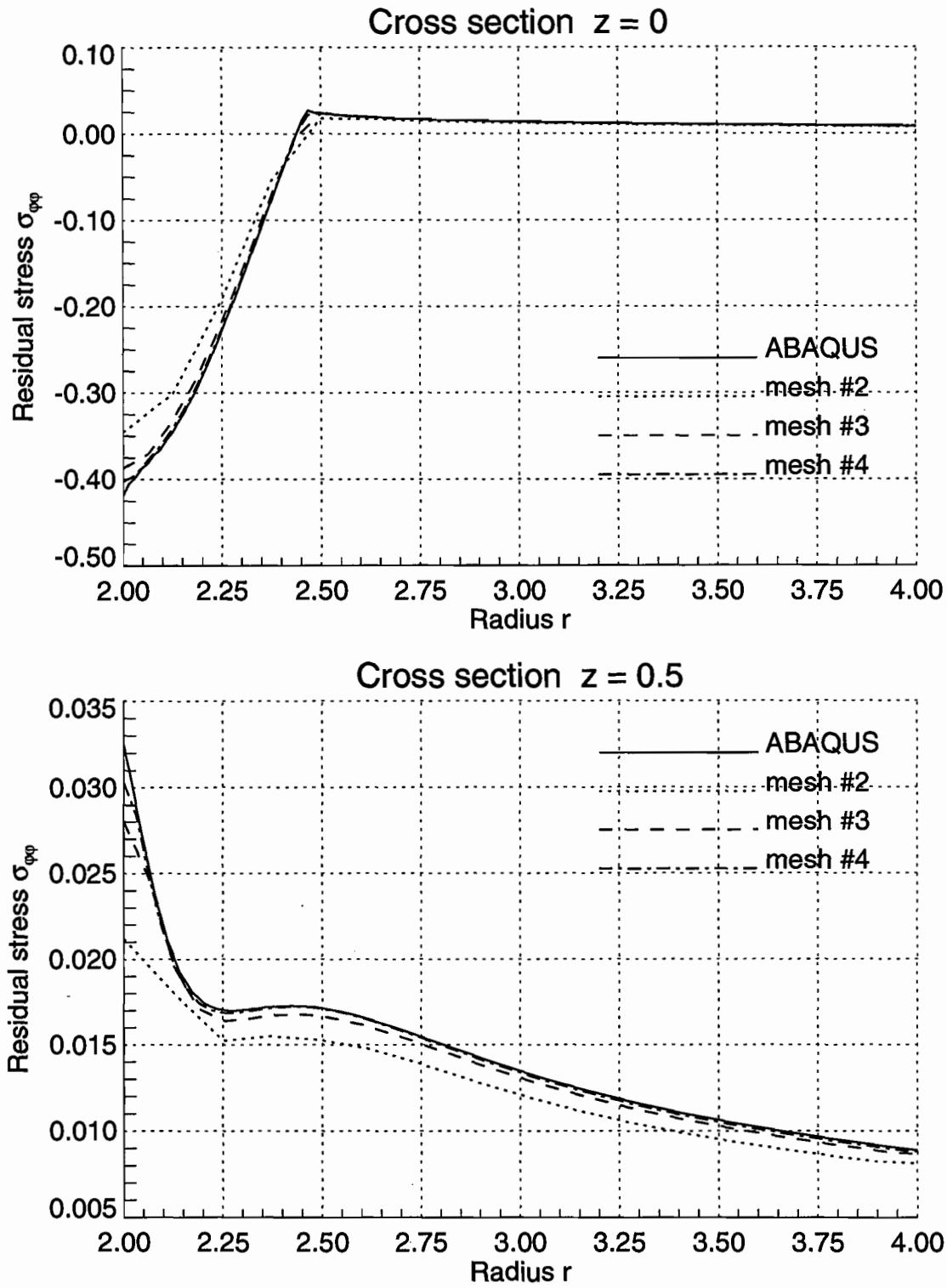

Figure 3.2 Hoop Residual Stresses $\sigma_{\varphi\varphi}$ in the Thick-Walled Cylinder under Internal Loading

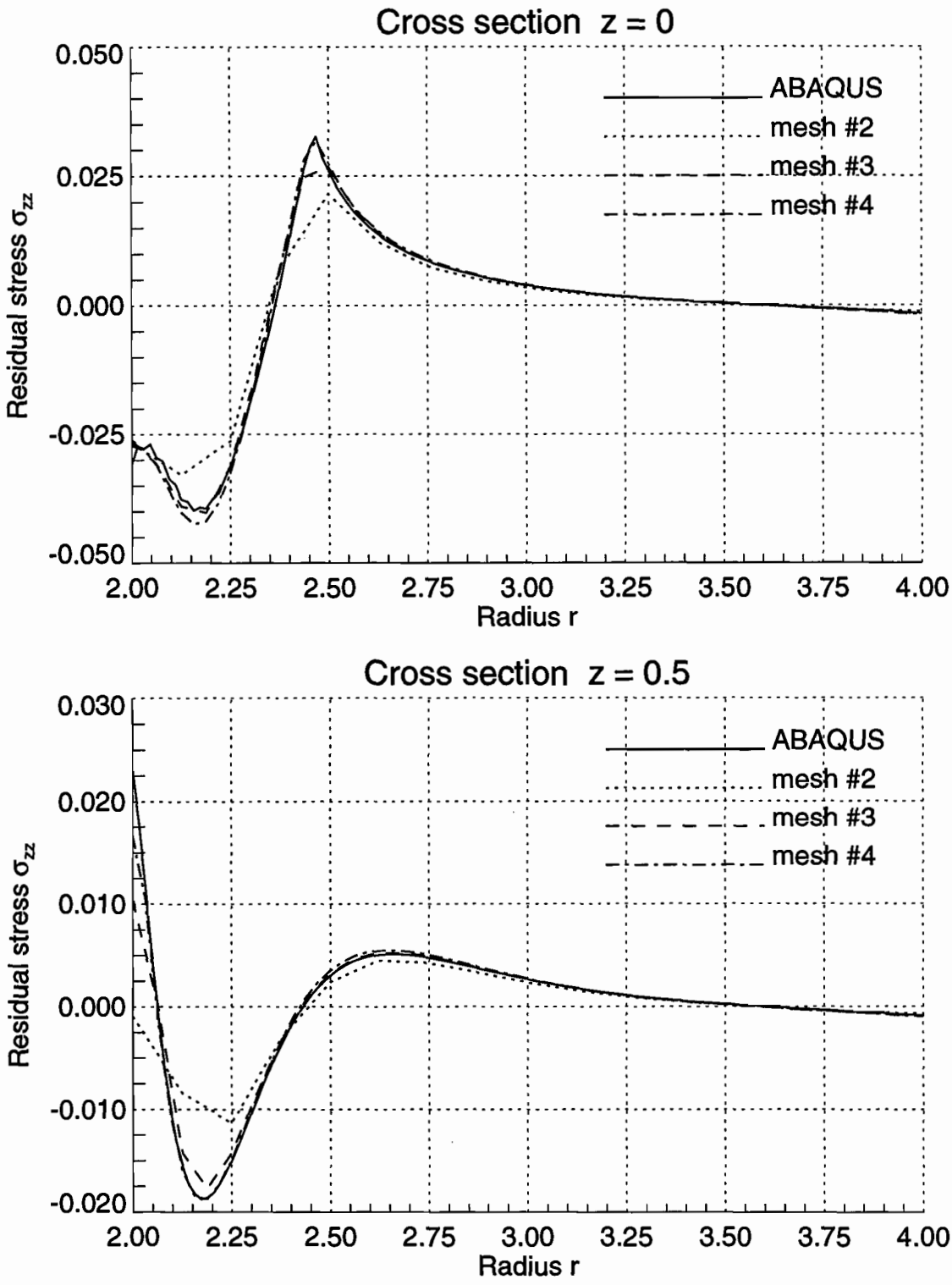

Figure 3.3 Axial Residual Stresses σ_{zz} in the Thick-Walled Cylinder under Internal Loading

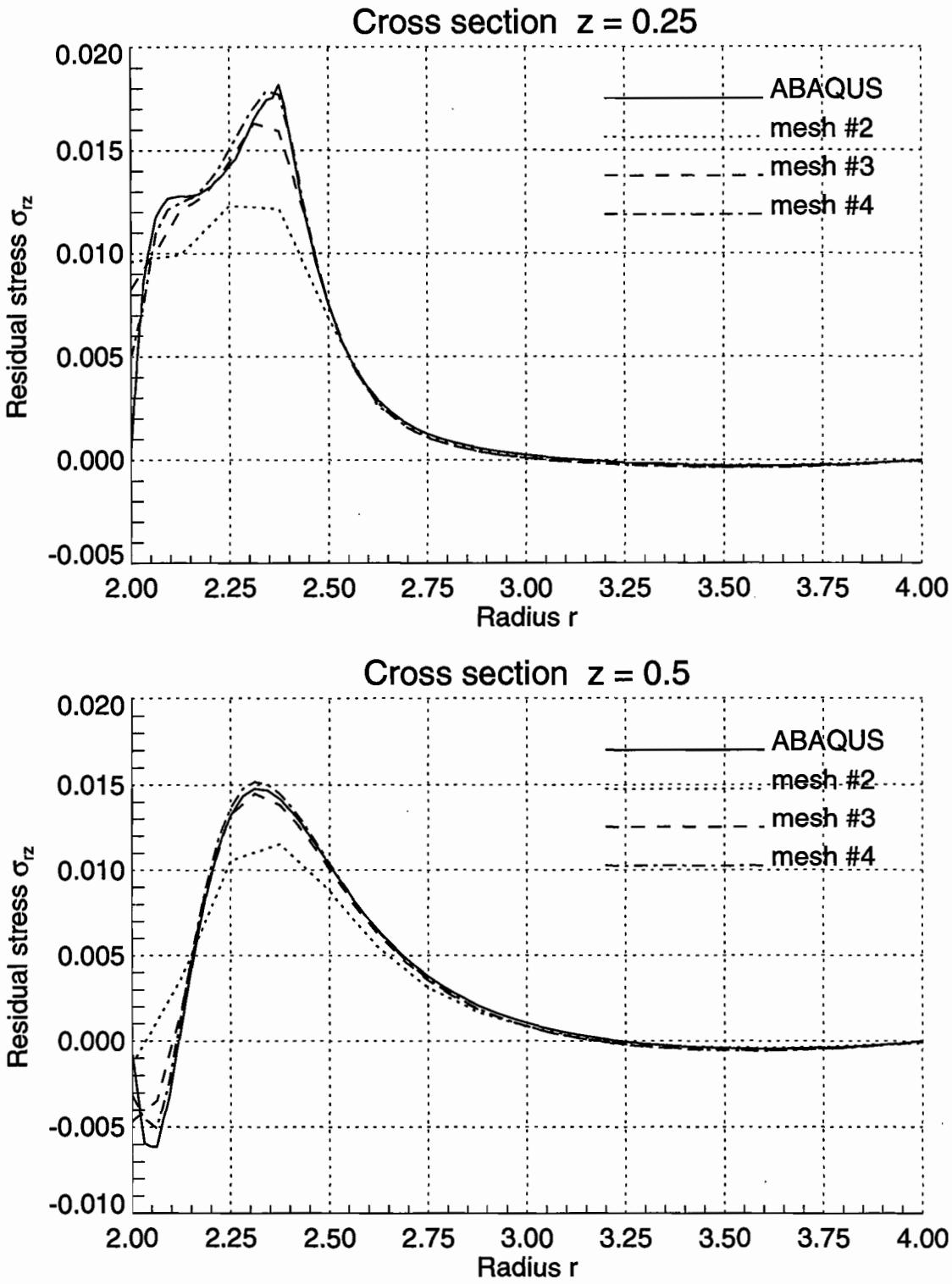

Figure 3.4 Shear Residual Stresses σ_{rz} in the Thick-Walled Cylinder under Internal Loading

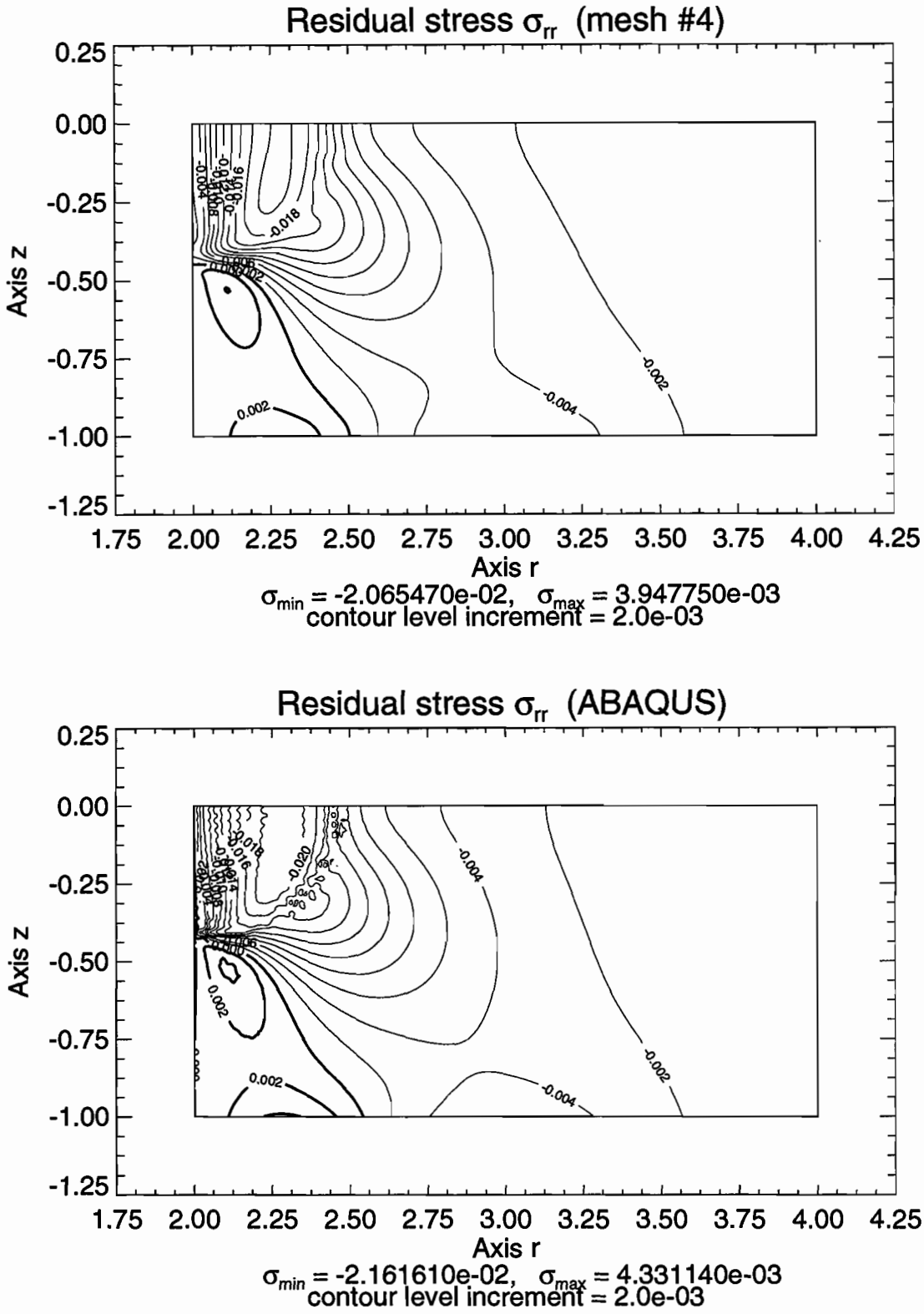

Figure 3.5 Contour Lines of Radial Residual Stresses σ_{rr} in the Thick-Walled Cylinder under Internal Loading

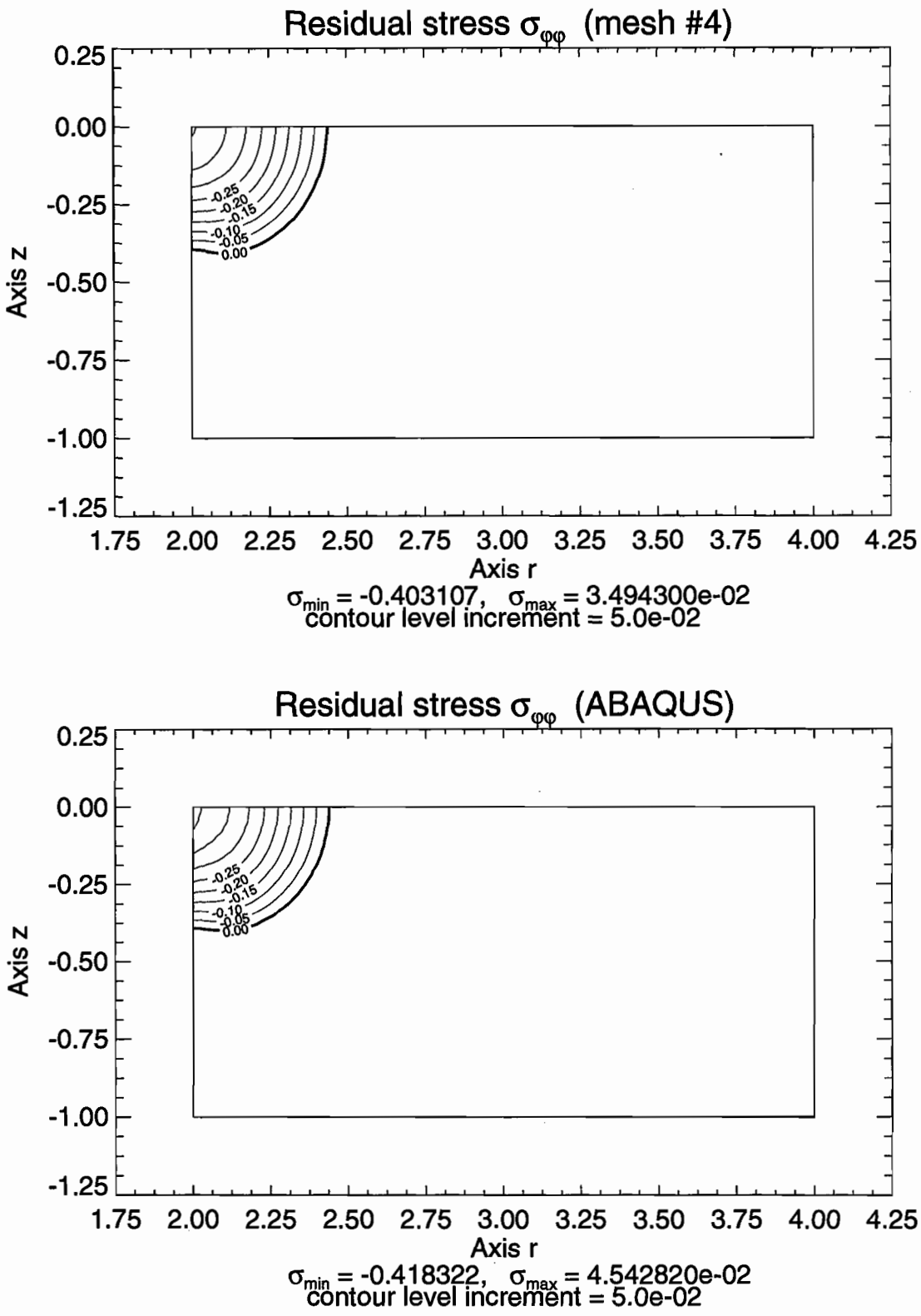

Figure 3.6 Contour Lines of Hoop Residual Stresses $\sigma_{\varphi\varphi}$ in the Thick-Walled Cylinder under Internal Loading

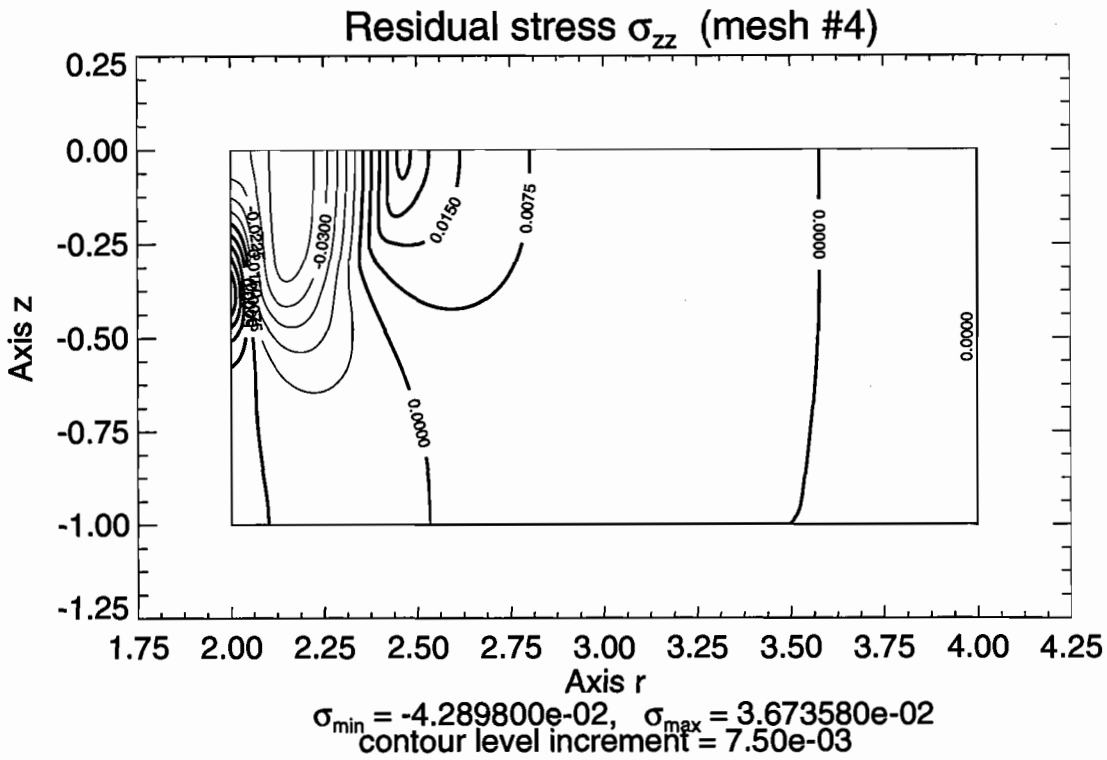

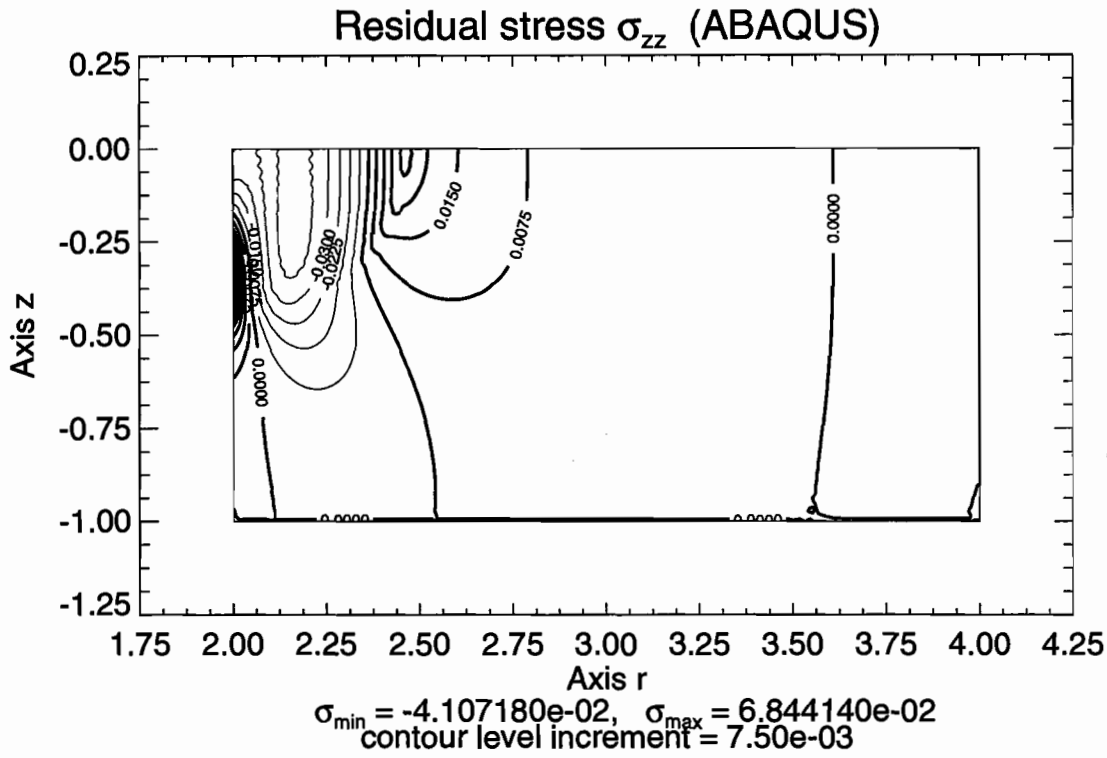

Figure 3.7 Contour Lines of Axial Residual Stresses σ_{zz} in the Thick-Walled Cylinder under Internal Loading

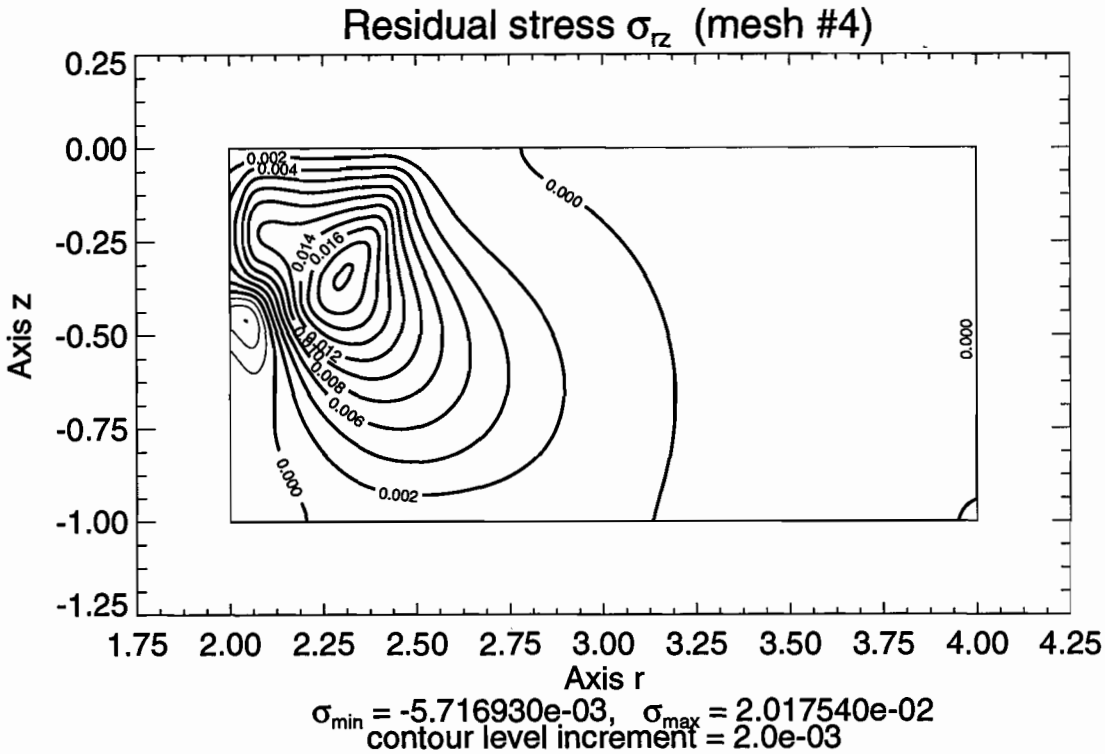

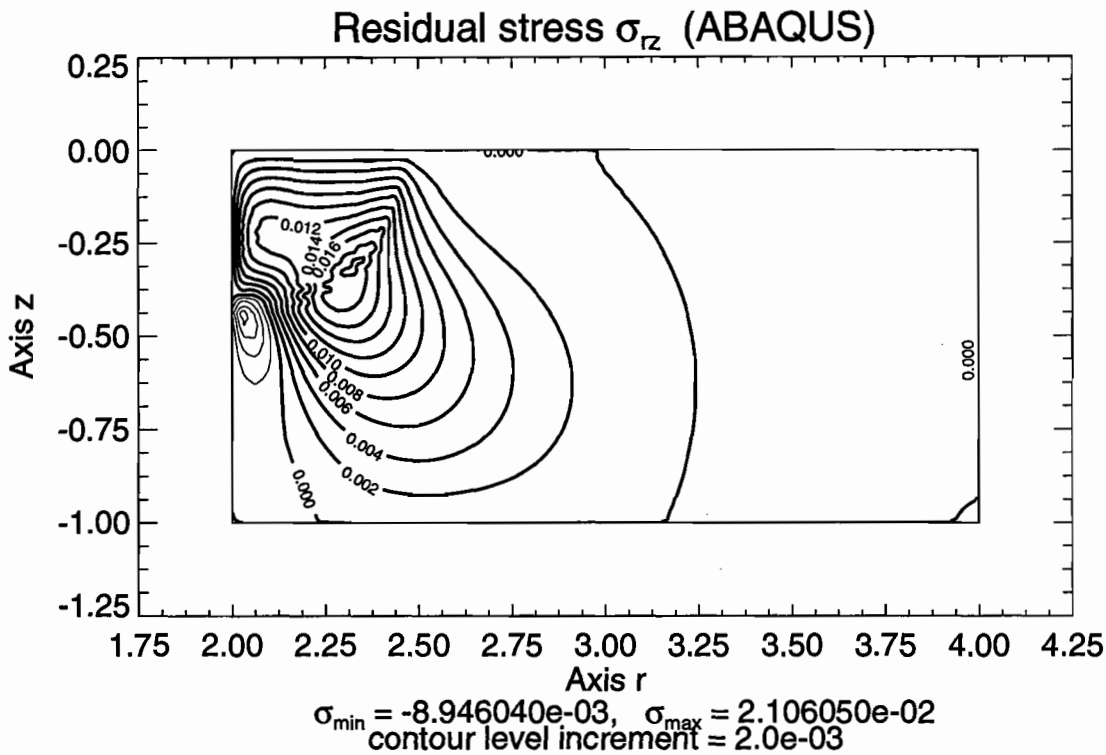

Figure 3.8 Contour Lines of Shear Residual Stresses σ_{rz} in the Thick-Walled Cylinder under Internal Loading

3.6 EXAMPLE ANALYSES FOR A RAILROAD CAR WHEEL

The computer programs worked out for the evaluation of residual stresses have been applied to estimate wheel shakedown stress states in a series of analyses. The profile geometry used in these analyses has been limited to that of a 32-inch diameter MU commuter vehicle wheel with 'S'-design flexible plate. Seven cases of loading have been considered and they can be divided into two groups. The first one consists of four cases in which the wheel has been subjected only to mechanical loading due to rail/wheel contact. Both vertical and horizontal surface tractions, and multiple running paths as well have been taken into account. The second group consists of three cases in which the influence of thermal loading on the residual stress state has been tested. All the cases considered are summarized in table 3.1.

Table 3.1 Case Matrix for Shakedown Stress State Analyses in Railroad Car Wheels

Case Number	1	2	3	4	5	6	7
Vertical Force	YES	YES	YES	YES	NO	YES	NO
Horizontal Force	NO	YES	NO	YES	NO	YES	NO
Running Paths	1	1	MULTI	MULTI	—	1	—
Thermal Loading	NO	NO	NO	NO	YES	YES	YES
Initial Stresses	NO	NO	NO	NO	NO	NO	YES

3.6.1 Cases 1 through 4

In case #1, the wheel was subject only to the vertical surface tractions $t_Z(X,Y)$ of intensity $t_{0Z} = 1239.98\,\text{MPa}$ acting over a rectangular contact area of dimensions $a = 6.947\,\text{mm}$ and $b = 5.083\,\text{mm}$, with the center C of coordinates $r = 0.405655\,\text{m}$ and $z = 0.084882\,\text{m}$ and the slope $\alpha = 0°$ (for the notation and conventions see section 2.4). The parameters t_{0Z}, a and b were calculated using the formulae (2.48), where the vertical force T_Z was equal to $77.84\,\text{kN}$, and the dimensions of the elliptical contact area $A = 6.4\,\text{mm}$ and $B = 4.683\,\text{mm}$ were obtained by means of the Hertz formulae assuming the following data: radius of the wheel $R_2 = 0.4064\,\text{m}$, radius of the wheel profile $R_2' = \infty$, and radius of the rail profile $R_1 = 0.254\,\text{m}$; the rail was assumed to be flat in the longitudinal direction, i.e., $R_1' = \infty$.

As far as the material properties are concerned, Young's modulus E, Poisson's ratio ν, and the flow stress σ_0 were assumed to be temperature-independent and equal to $206.832\,\text{GPa}$, 0.3, and $448.137\,\text{MPa}$, respectively. Additionally, the dimensions of the Hertz ellipse were calculated assuming that both the rail and the wheel were made of material with the same elastic constants.

The problem was solved using the same finite element meshes that were used in the elastic analyses presented in section 2.6. The coarsest mesh #1 was absolutely inappropriate for this problem and was not considered. The elastic solution necessary as input data was found by means of the programs described is section 2.4. The contour line plots of elastic stresses for the meshes #4 and #5 and for the radial plane $\varphi = 0°$ are shown in figures 2.39 through 2.42.

The analysis of residual stresses was performed assuming only one enveloping elastic stress state for the radial plane that contained the center of the contact zone ($\varphi = 0°$). In spite of the fact that such selection seems to be straightforward, after the residual stress state

had been found, the yield conditions were additionally examined for neighboring radial planes.

Some selected results for case #1 are shown in figures 3.9 through 3.14. The convergence of the solution with respect to the mesh density is presented in figures 3.9 and 3.10, where the stress tensor components are plotted along the line $\alpha-\alpha$ shown in figures 2.27 through 2.30. The contour line plots of stresses for the meshes #4 and #5 are presented in figures 3.11 through 3.14.

These results indicate that meshes #2 and #3 are definitely too coarse. Mesh #4 seems to be acceptable, and mesh #5 may be recognized as appropriate for the problem under consideration. The solutions obtained for meshes #4 and #5 are in quite good agreement. Significant differences can be observed only for the maximal values of hoop $\sigma_{\varphi\varphi}$ and axial σ_{zz} stresses. These values correspond to points on the tread surface and they are not reliable because they were computed using a quite simple extrapolation technique implemented in the procedure for contour line plotting. With regard to mesh #5, the application of such dense meshes in real analyses that usually have to be carried out repeatedly seems to be unrealistic. The number of decision variables and the number of constraints in the biggest optimization problem that had to be solved for mesh #5 were equal to 856 and 205, respectively. The CPU time spent on this analysis was approximately equal to 26 hours on VAX Station 4000-90. Thus, in practical applications, coarser meshes have to be used unless a much more powerful computer is available.

In case #2, the wheel was subject to the vertical surface tractions $t_Z(X,Y)$ of intensity $t_{0Z} = 1239.98\,\mathrm{MPa}$ and the horizontal surface tractions $t_X(X,Y)$ of intensity $t_{0X} = 0.2t_{0Z} = 247.996\,\mathrm{MPa}$. The other data were assumed to be exactly the same as for case #1. The elastic solution was found using the programs described in section 2.4. The contour line plots of elastic stresses for mesh #4 and for the radial plane $\varphi = 0°$ are presented in figures 2.43 through 2.45.

The problem was solved using meshes #2, #3 and #4. Available computer equipment did not allow one to solve this problem for mesh #5. First, the plastic zone was bigger than in case #1, as should be explained from the addition of horizontal loading. Consequently, the number of decision variables and the number of constraints in the optimization problem were higher. Second, the latter number was increased dramatically due to the number of enveloping stress states to be taken into consideration. In the first step the number of such states was assumed to be equal to 9, corresponding to the division of the contact zone into 8 sectors in the circumferential direction. In the second step, the number of sectors was doubled, resulting in 17 enveloping stress states. The differences between the corresponding solutions were very small and further division was not considered.

The results in the form of contour line plots of residual stresses for mesh #4 are shown in figures 3.15 through 3.17. For comparison, the minimal and maximal values of residual stresses from mesh #4 for all four cases of loading considered in this section are summarized in table 3.2. In spite of the fact that the horizontal loading constitutes only 20% of the vertical loading, it has relatively significant influence on the results. Except for the compressive radial stresses σ_{rr}, all the other stress tensor components are higher in magnitude. As far as quantitative differences are concerned, the biggest changes may be observed at the tread surface, especially for the hoop $\sigma_{\varphi\varphi}$ and axial σ_{zz} stresses. Of course, the action of the horizontal load is accompanied by non-zero shear stresses $\sigma_{r\varphi}$ and $\sigma_{\varphi z}$.

In cases #3 and #4, the wheel was subject to the same loading as in cases #1 and #2, respectively, but the effect of wheel wandering was additionally taken into account. The

Table 3.2 Minimal and Maximal Residual Stresses (MPa) in Railroad Car Wheels (Cases 1 through 4)

Case Number		1	2	3	4
σ_{rr}	min	-61.6	-37.9	-56.2	-37.5
	max	50.7	72.3	46.6	68.0
$\sigma_{\varphi\varphi}$	min	-307.3	-319.5	-347.3	-325.4
	max	52.1	72.2	45.8	61.1
σ_{zz}	min	-209.3	-251.3	-279.4	-328.2
	max	163.1	174.0	132.4	149.9
$\sigma_{r\varphi}$	min	—	-45.8	—	-26.4
	max	—	34.0	—	33.7
$\sigma_{\varphi z}$	min	—	-90.5	—	-74.2
	max	—	76.4	—	96.3
σ_{rz}	min	-53.8	-64.0	-63.5	-79.4
	max	55.4	67.5	64.2	84.8

term 'wheel wandering' refers to the tendency of wheels with different worn profiles to contact the rail at different lateral locations, resulting in multiple running paths. Both cases were solved using a heuristic procedure proposed in [4]. In this procedure, a wheel is subject to a sequence of loads corresponding to different locations of the contact zone. For the ith location, the residual stress state is computed applying the existing cyclic loading program and assuming that there exist initial residual stresses equal to the residual stresses obtained for the $(i-1)$th location.

Cases #3 and #4 were solved with mesh #4 for two programs of loading. In the first one the load was applied at 8 different locations 1, 2, ..., 8, as shown in figure 3.18. In the second program, the return of the load to the starting location was additionally considered. For each location, the elastic and residual stress states were found assuming exactly the same data as in cases #1 and #2, except for the coordinates of the center of the contact zone. For simplicity, the variation of the wheel radius R_2 along the tread surface was neglected.

The results in the form of contour line plots are presented in figures 3.19 through 3.22 for case #3 and in figures 3.23 through 3.28 for case #4. Each figure consists of two plots, for the first and second programs of loading (top and bottom, respectively). The minimal and maximal values of stresses are summarized in table 3.2. These results resemble the results obtained in cases #1 and #2, both qualitatively and quantitatively. As far as the shapes of the contour lines are concerned, they look as if they were obtained by simple stretching of the contour lines corresponding to a fixed location of loading along the tread surface. The isles and peninsulas of low magnitudes that can be observed for the radial σ_{rr} and shear $\sigma_{r\varphi}$, $\sigma_{\varphi z}$ and σ_{rz} stresses are an artificial effect caused by the application of the load in a finite number of steps (the real process would be continuous). It should be noted that the return of the load to the staring position usually had no significant influence on the distribution of residual stresses. The relatively big difference between the maximal values of axial stresses σ_{zz} for the two programs of loading (figure 3.21) is probably again connected with the application of a quite simple extrapolation technique to contour line plotting.

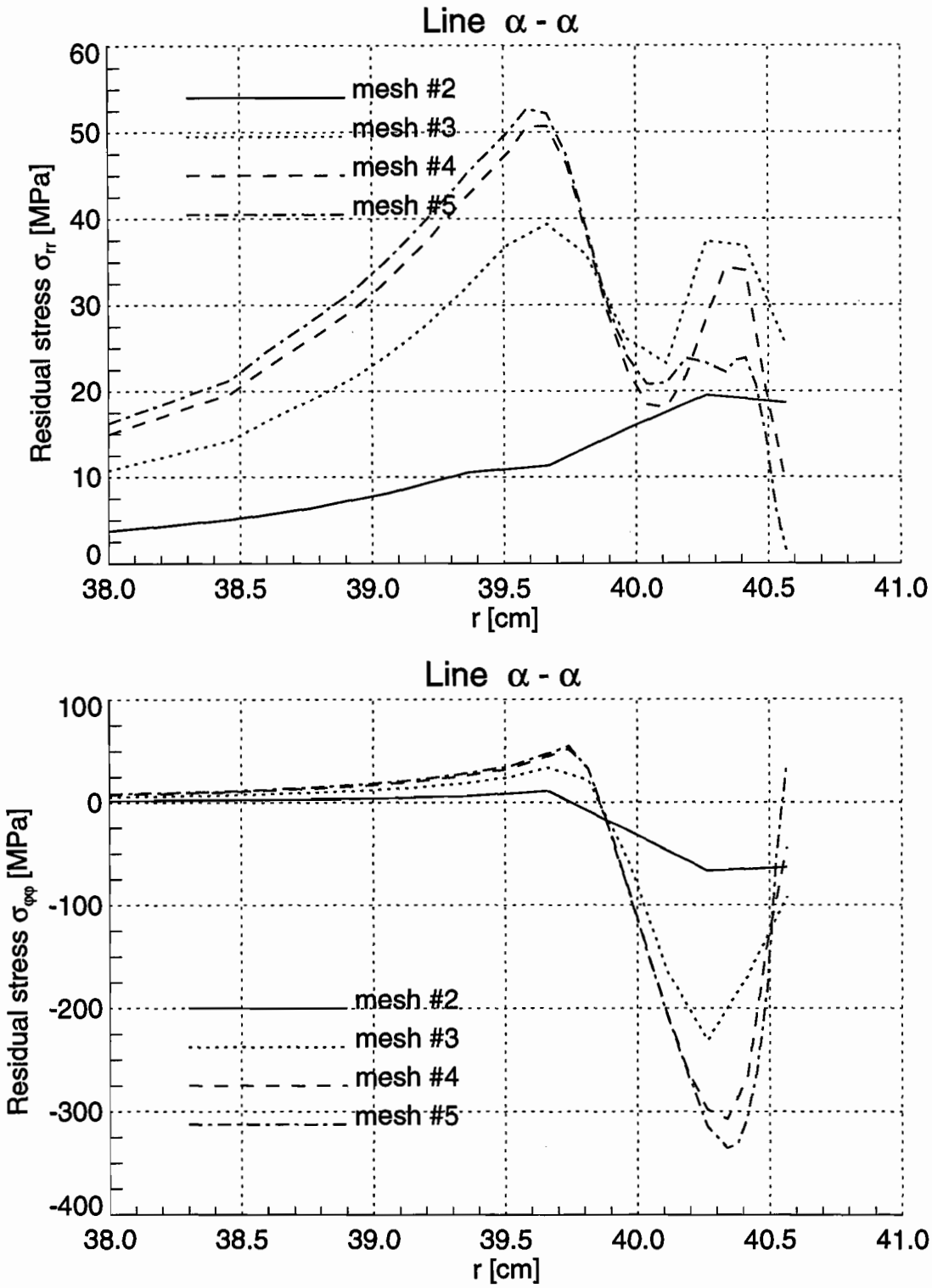

Figure 3.9 Radial σ_{rr} and Hoop $\sigma_{\varphi\varphi}$ Residual Stresses in the Railroad Car Wheel under Vertical Loading (Loading Case #1)

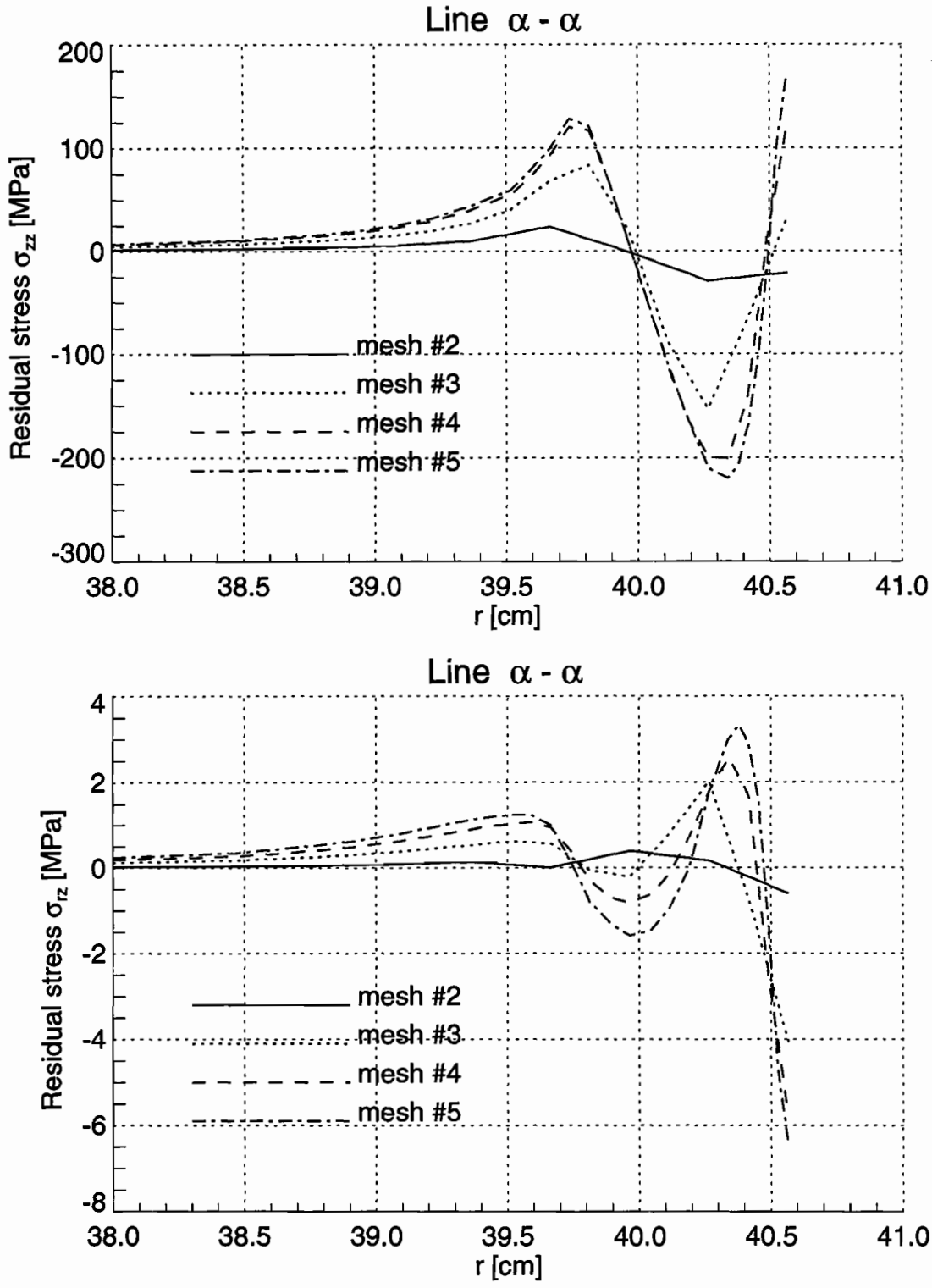

Figure 3.10 Axial σ_{zz} and Shear σ_{rz} Residual Stresses in the Railroad Car Wheel under Vertical Loading (Loading Case #1)

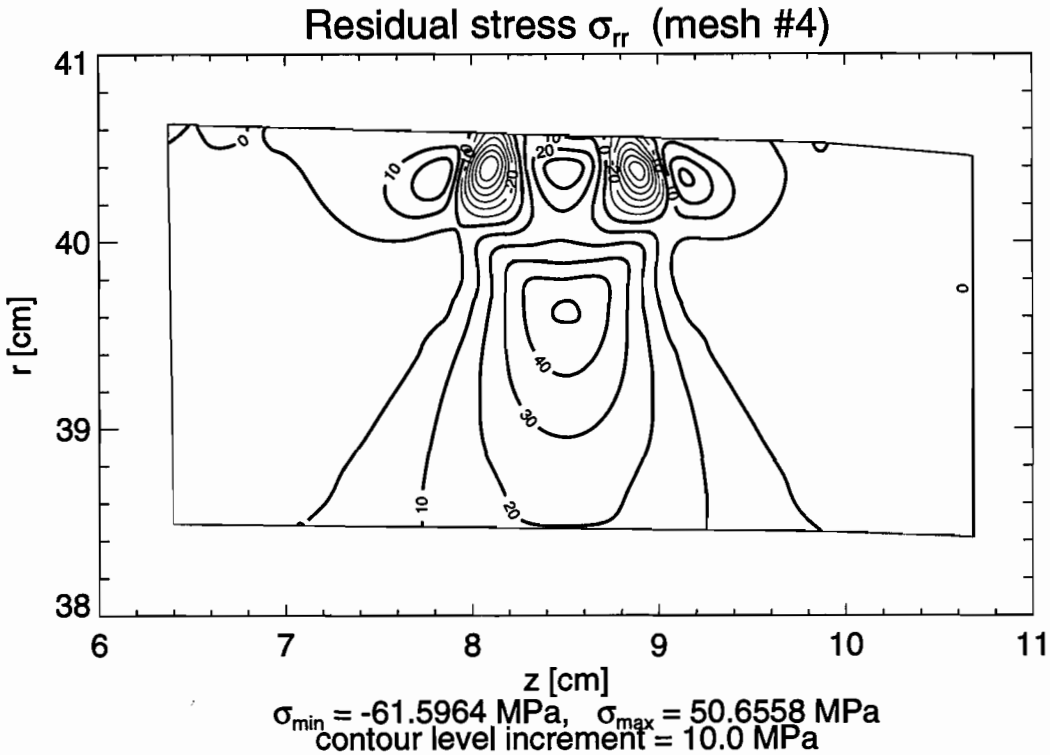

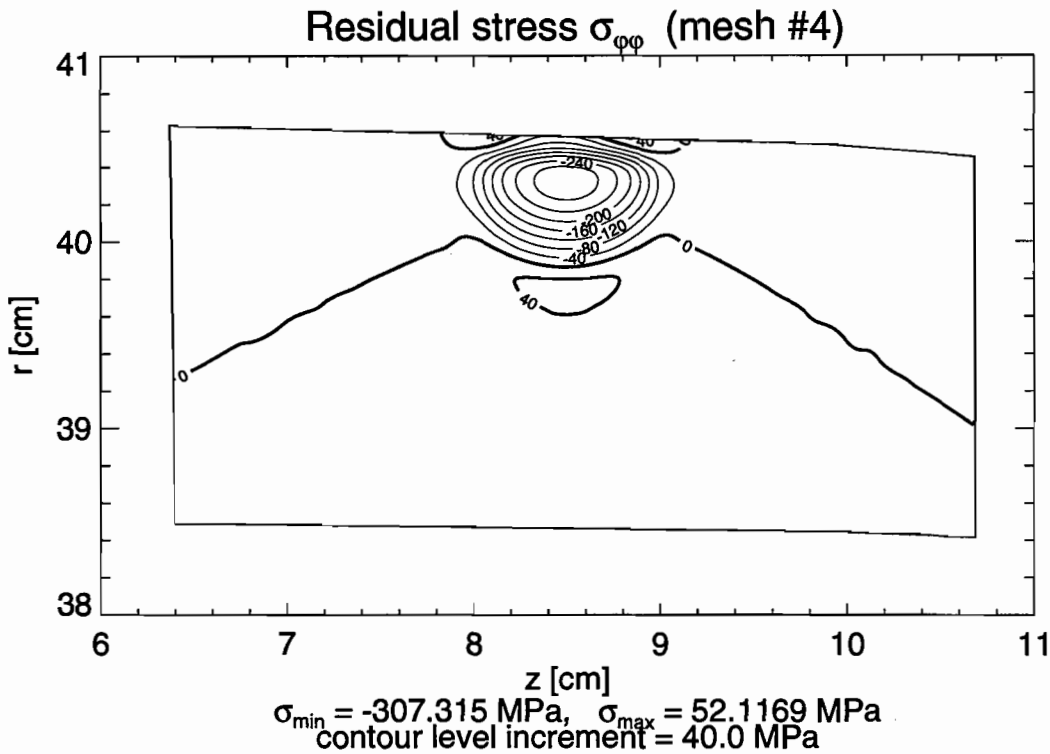

Figure 3.11 Contour Lines of Radial σ_{rr} and Hoop $\sigma_{\varphi\varphi}$ Residual Stresses in the Railroad Car Wheel under Vertical Loading (Loading Case #1) – Solution for Mesh #4

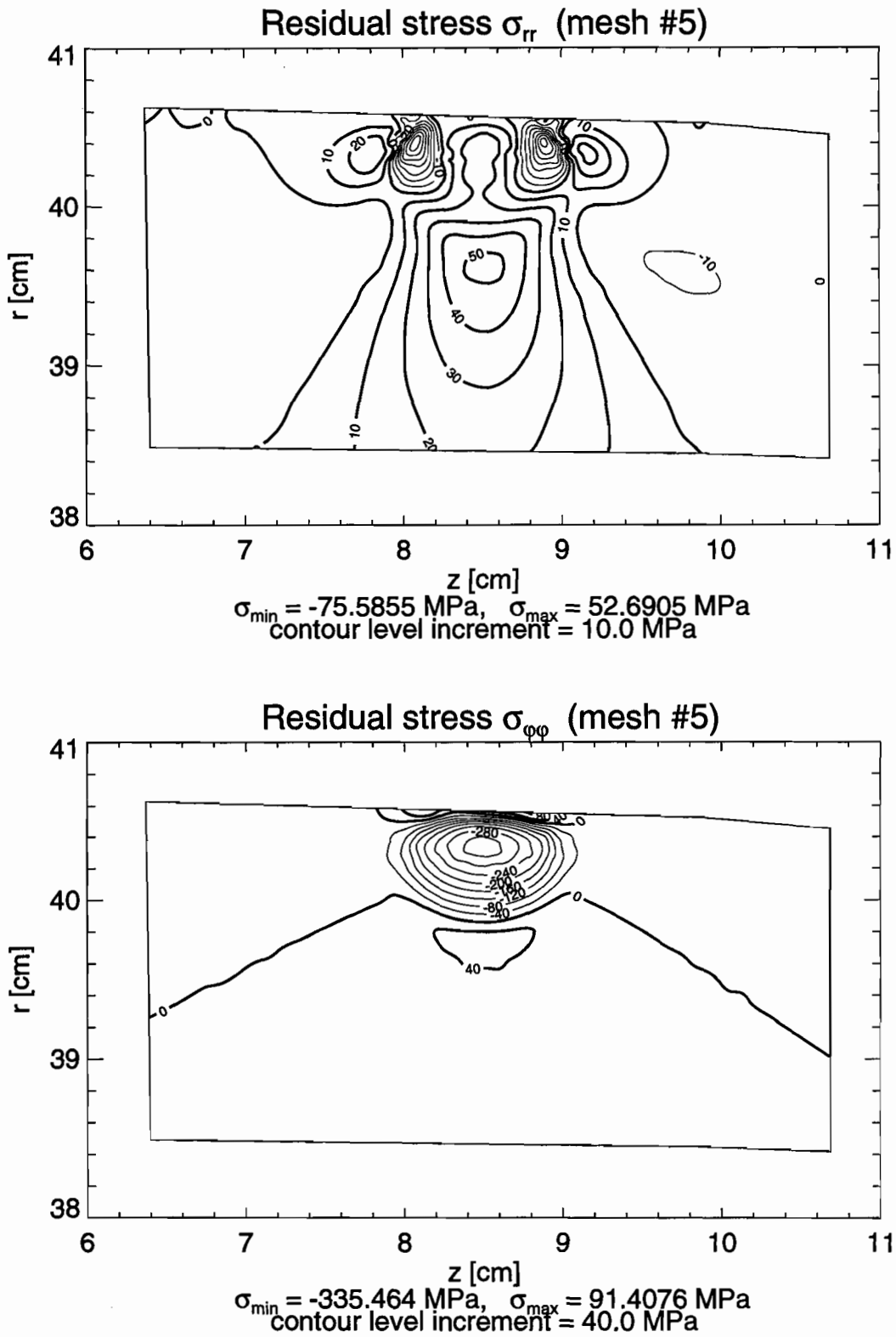

Figure 3.12 Contour Lines of Radial σ_{rr} and Hoop $\sigma_{\varphi\varphi}$ Residual Stresses in the Railroad Car Wheel under Vertical Loading (Loading Case #1) – Solution for Mesh #5

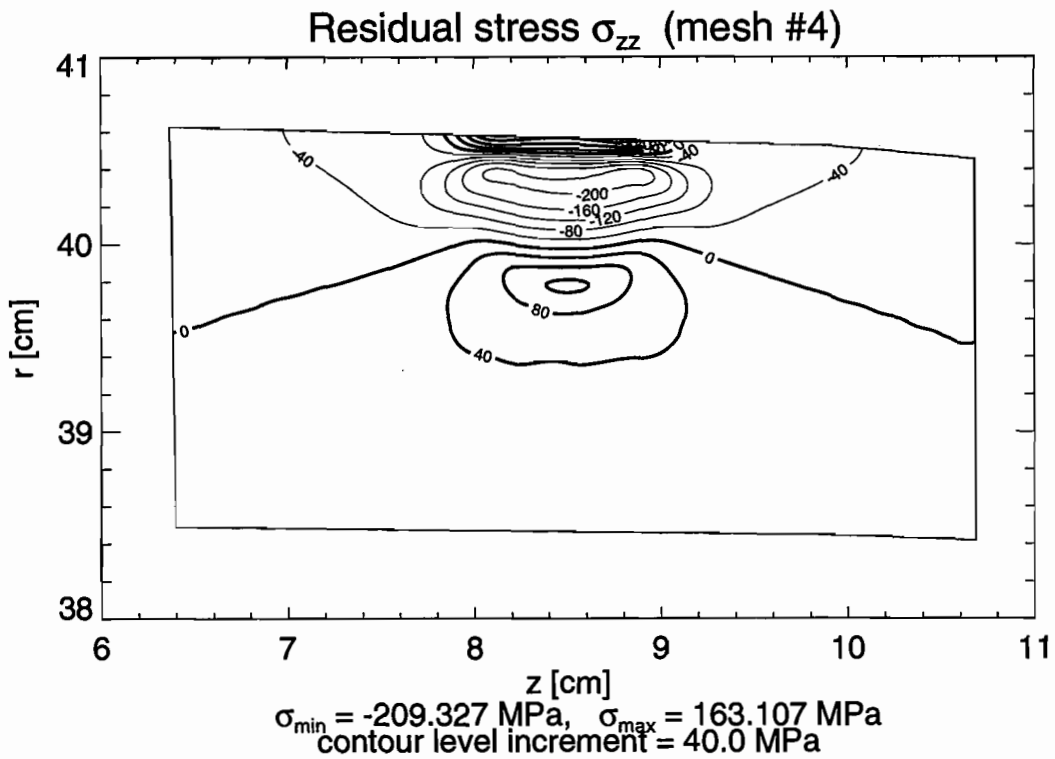

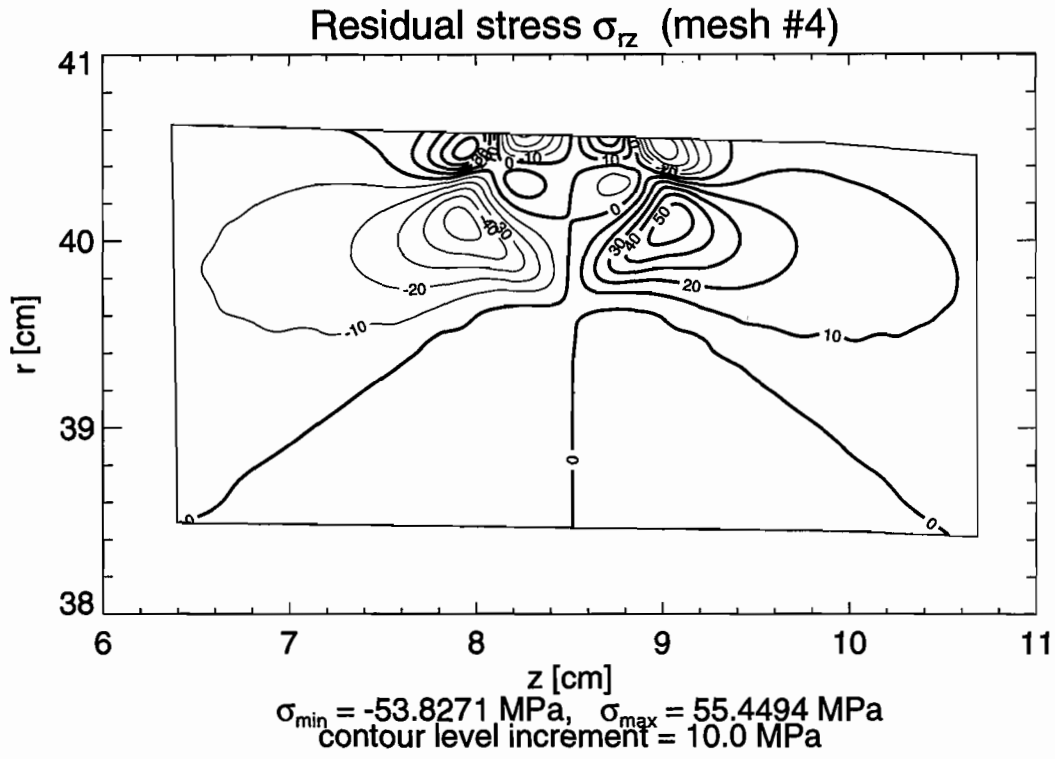

Figure 3.13 Contour Lines of Axial σ_{zz} and Shear σ_{rz} Residual Stresses in the Railroad Car Wheel under Vertical Loading (Loading Case #1) – Solution for Mesh #4

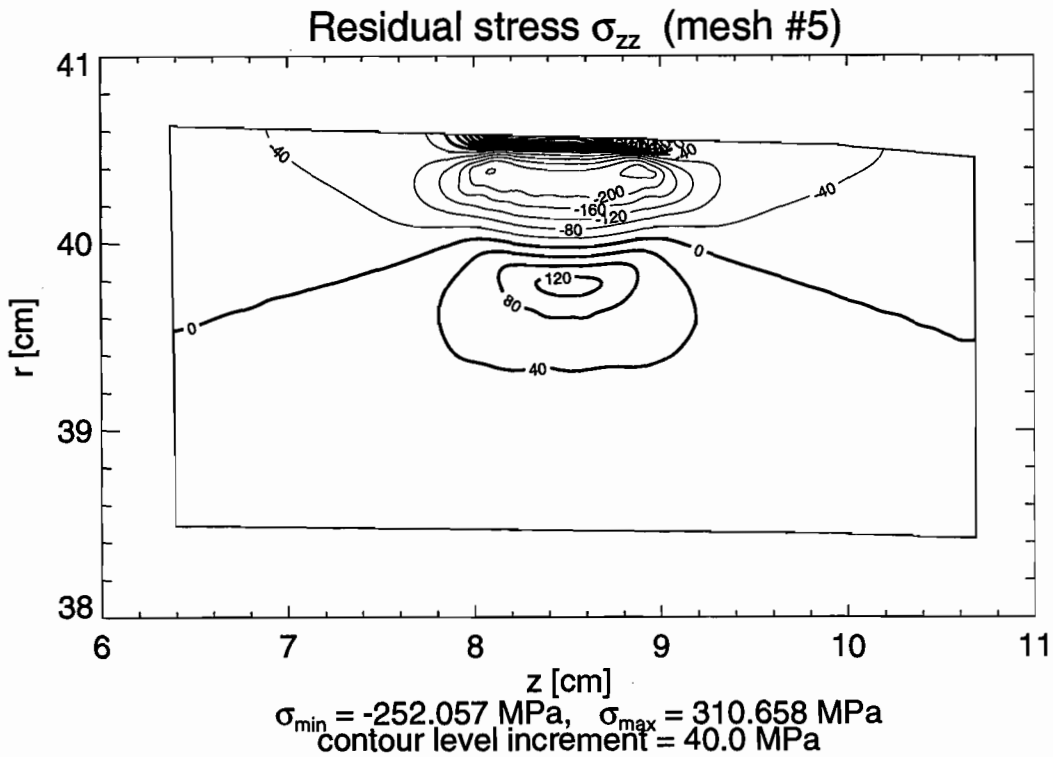

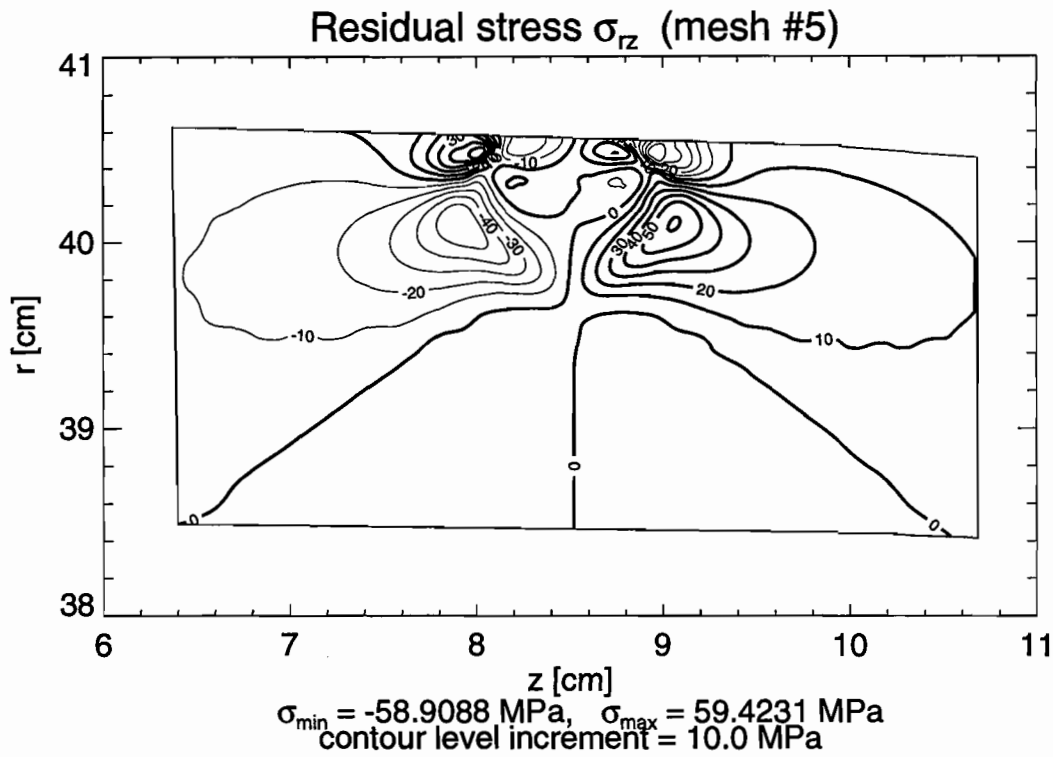

Figure 3.14 Contour Lines of Axial σ_{zz} and Shear σ_{rz} Residual Stresses in the Railroad Car Wheel under Vertical Loading (Loading Case #1) – Solution for Mesh #5

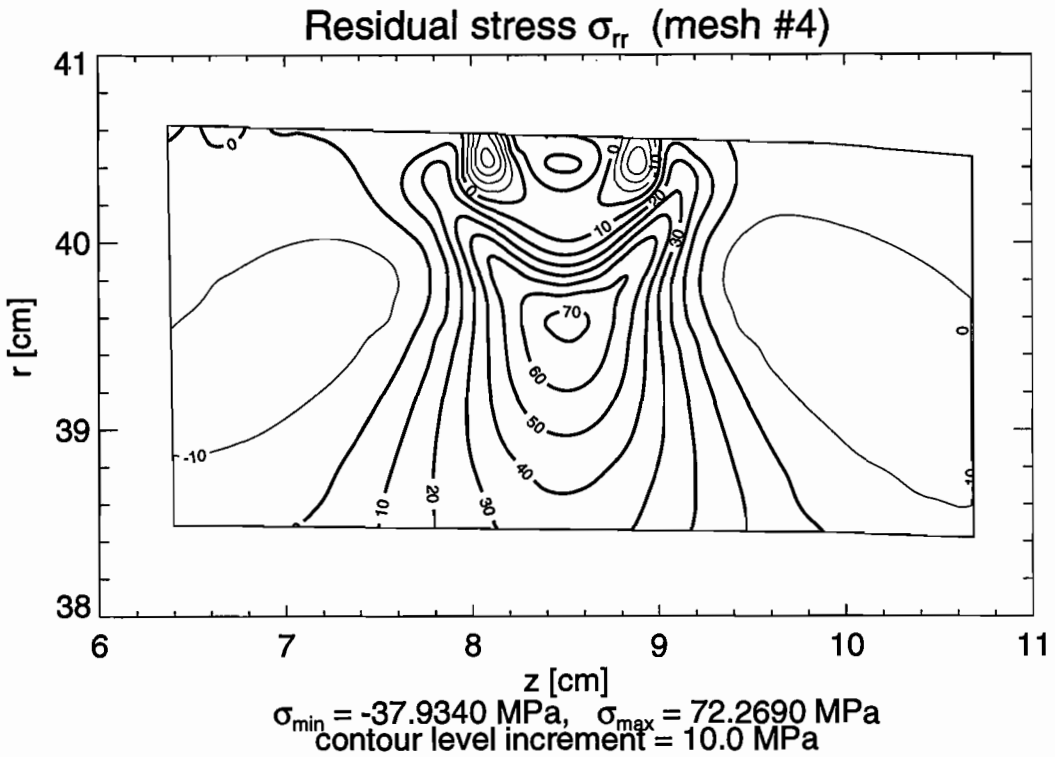

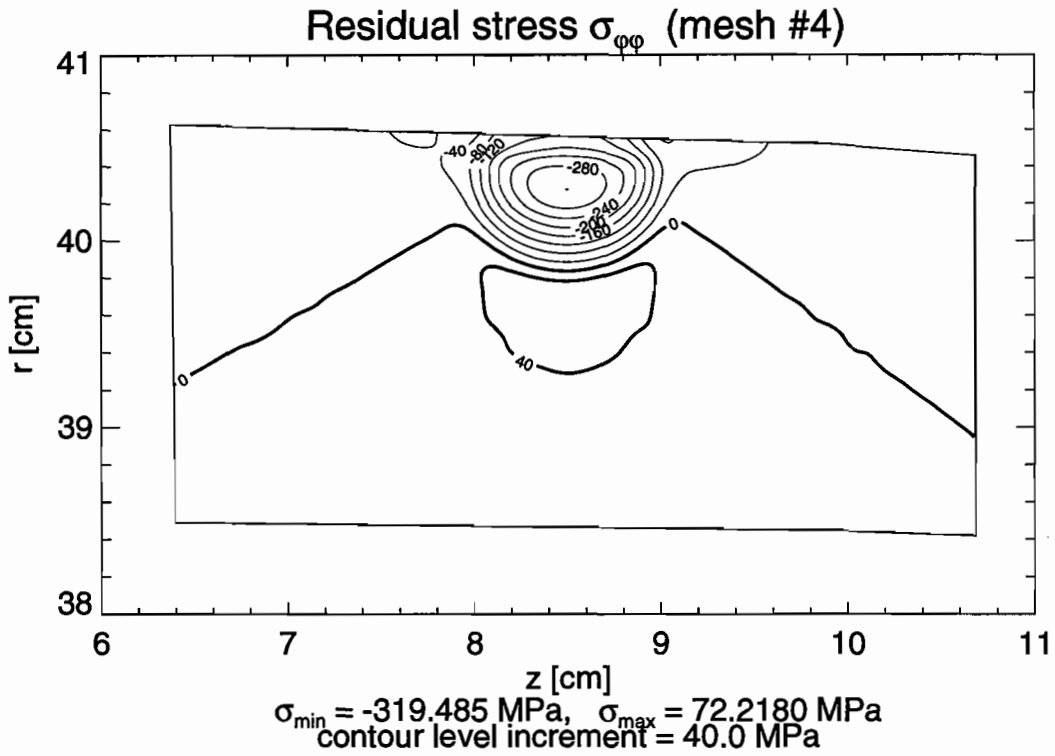

Figure 3.15 Contour Lines of Radial σ_{rr} and Hoop $\sigma_{\varphi\varphi}$ Residual Stresses in the Railroad Car Wheel under Vertical and Horizontal Loading (Loading Case #2) – Solution for Mesh #4

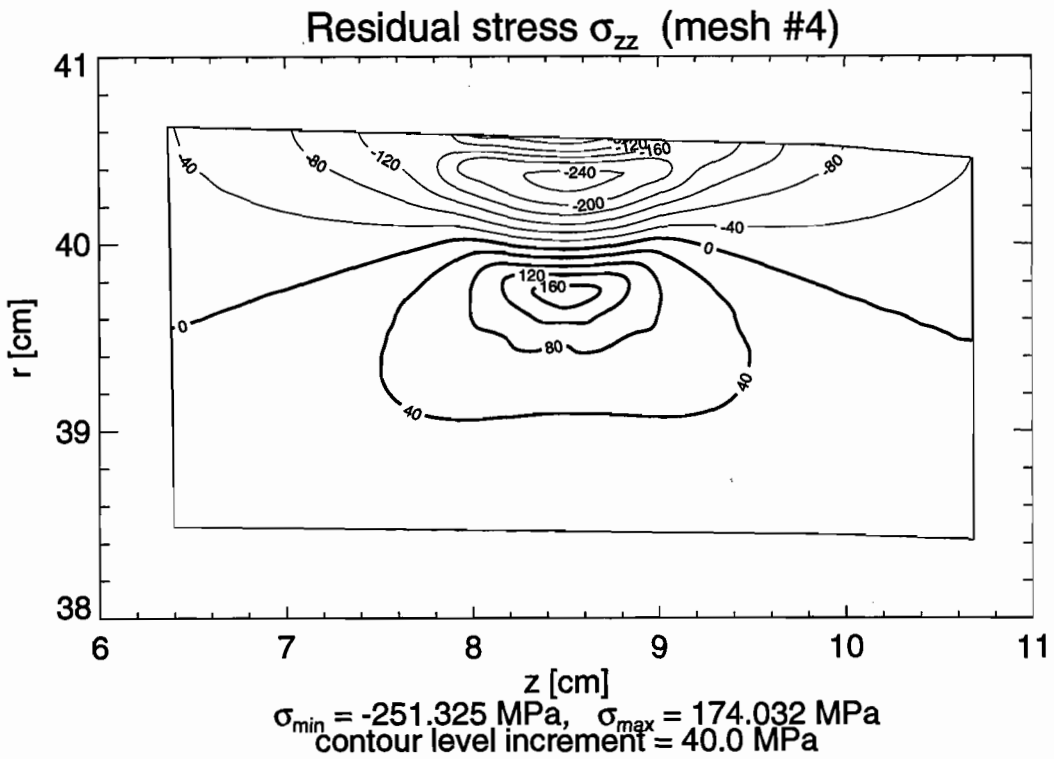

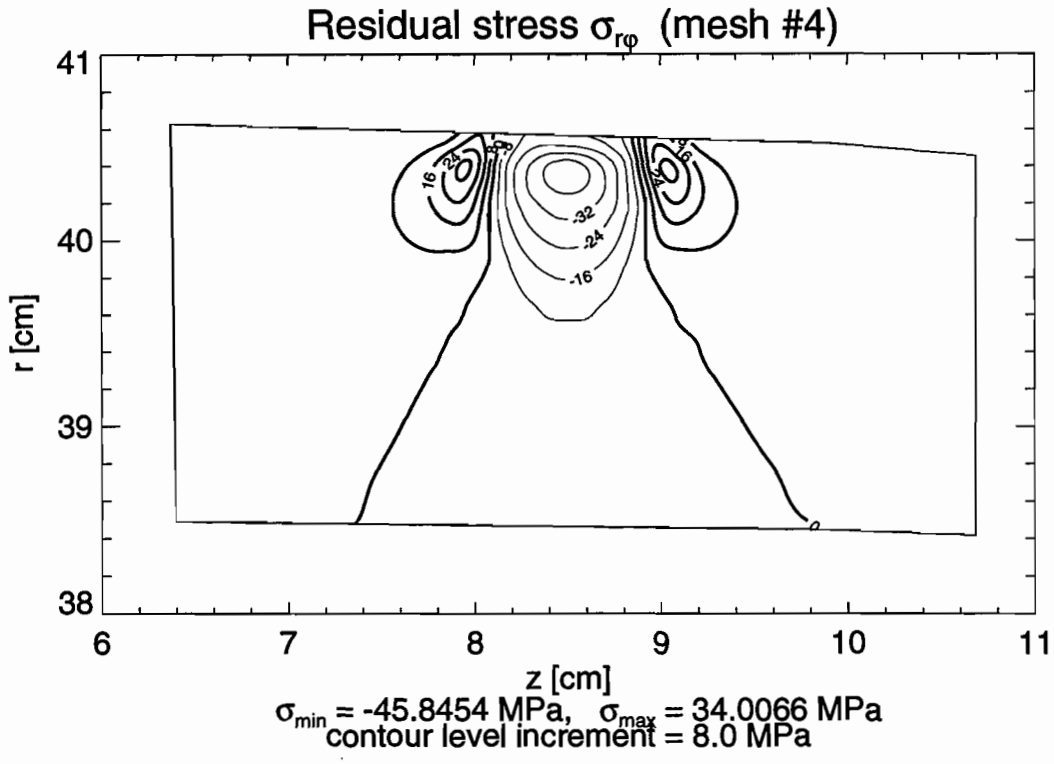

Figure 3.16 Contour Lines of Axial σ_{zz} and Shear $\sigma_{r\varphi}$ Residual Stresses in the Railroad Car Wheel under Vertical and Horizontal Loading (Loading Case #2) – Solution for Mesh #4

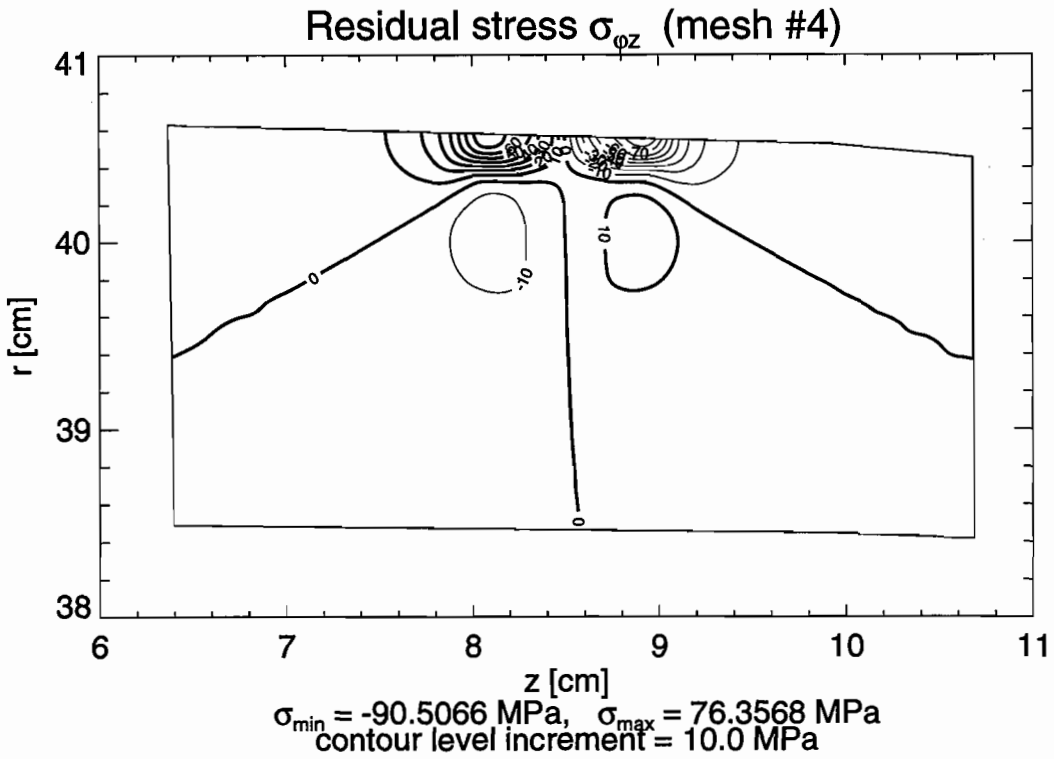

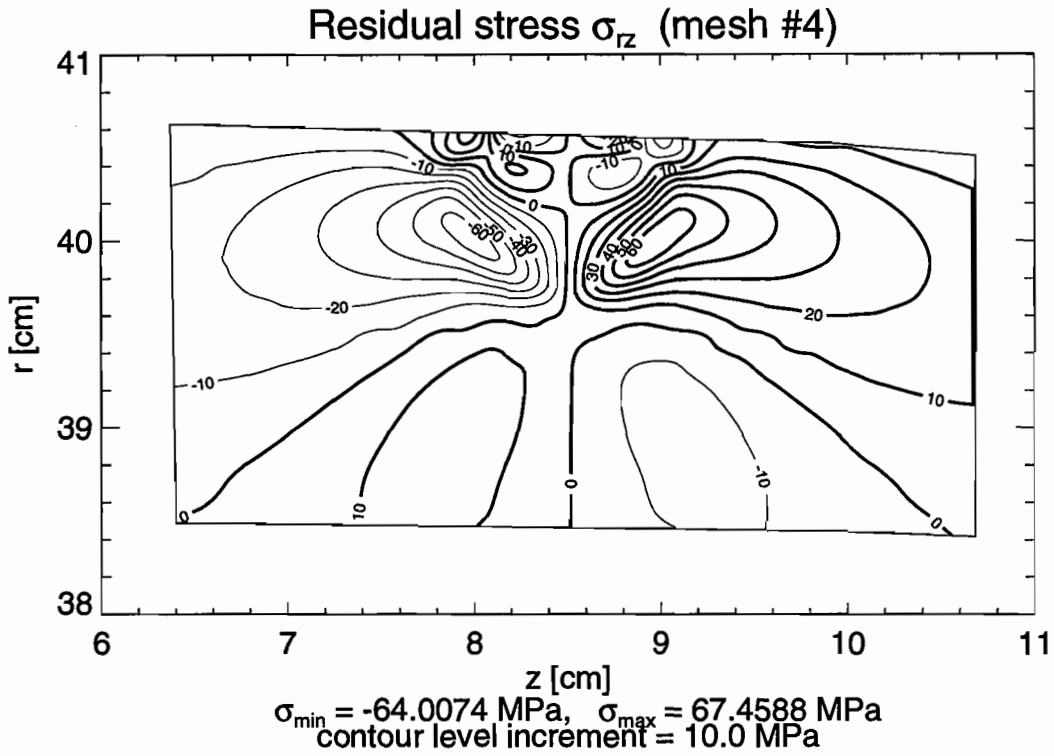

Figure 3.17 Contour Lines of Shear Residual Stresses $\sigma_{\varphi z}$ and σ_{rz} in the Railroad Car Wheel under Vertical and Horizontal Loading (Loading Case #2) – Solution for Mesh #4

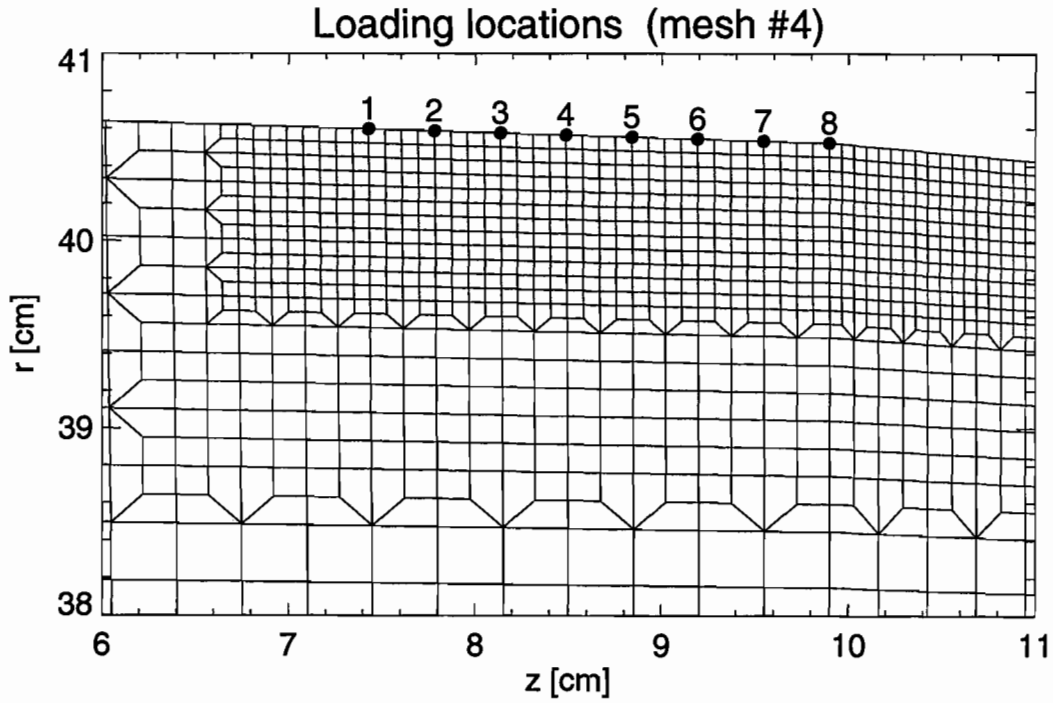

Figure 3.18 Loading Locations Assumed for Cases of Multiple Running Paths (Loading Cases #3 and #4)

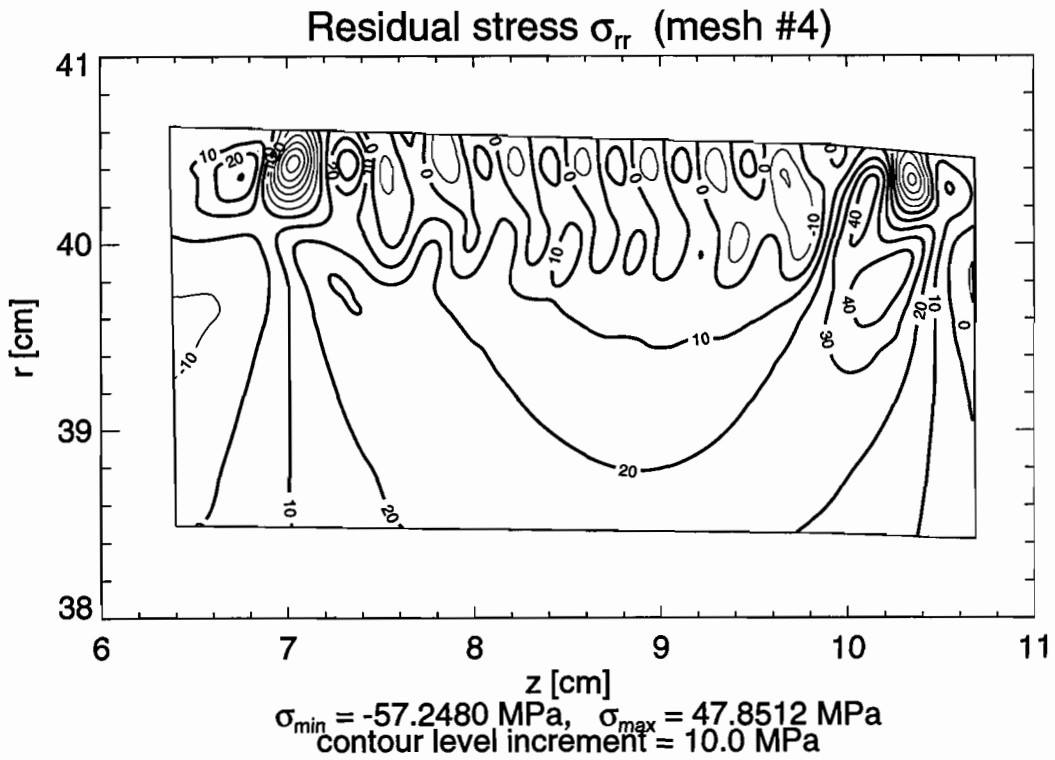

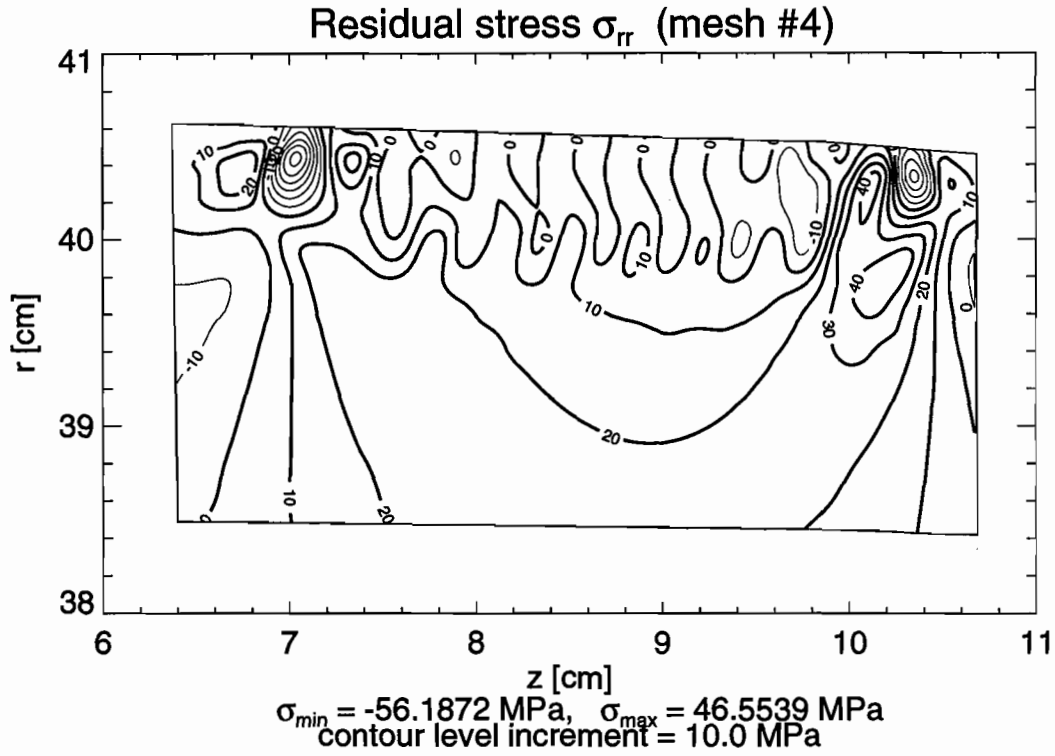

Figure 3.19 Contour Lines of Radial Residual Stresses σ_{rr} in the Railroad Car Wheel under Vertical Loading with Multiple Running Paths (Loading Case #3)

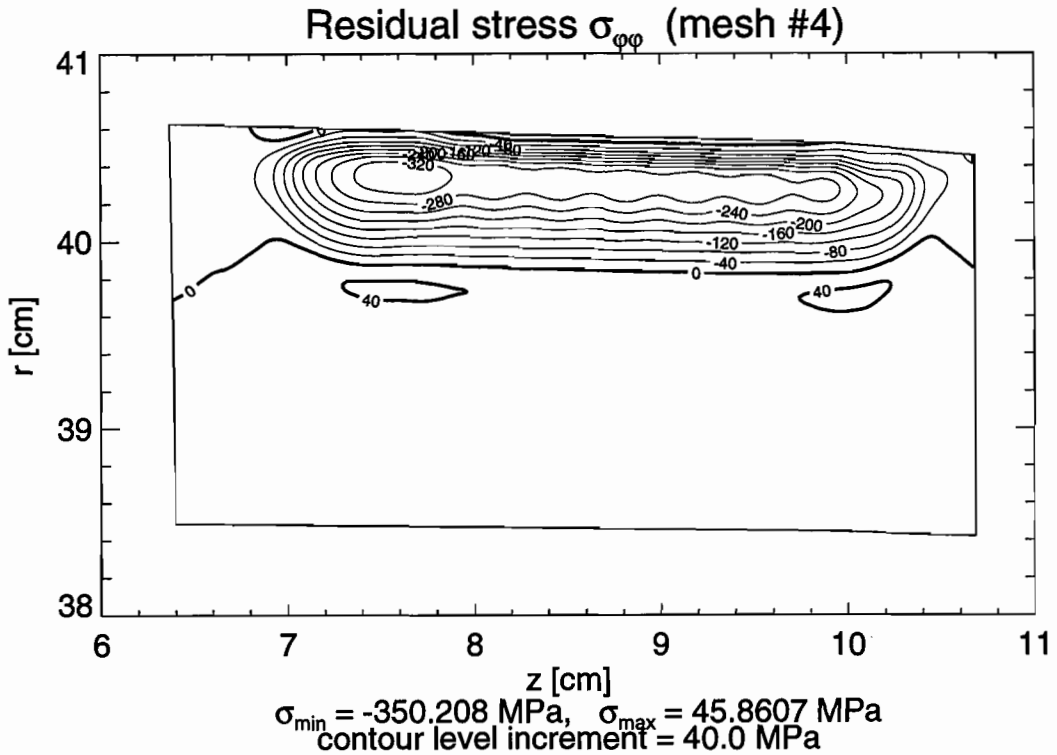

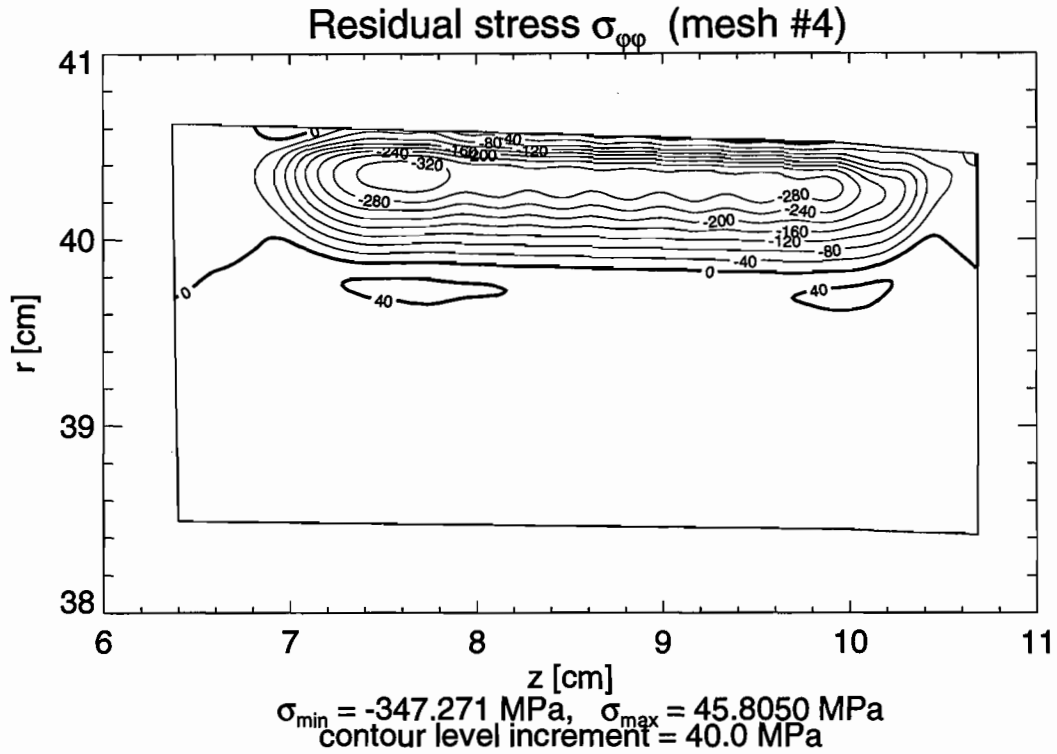

Figure 3.20 **Contour Lines of Hoop Residual Stresses $\sigma_{\varphi\varphi}$ in the Railroad Car Wheel under Vertical Loading with Multiple Running Paths (Loading Case #3)**

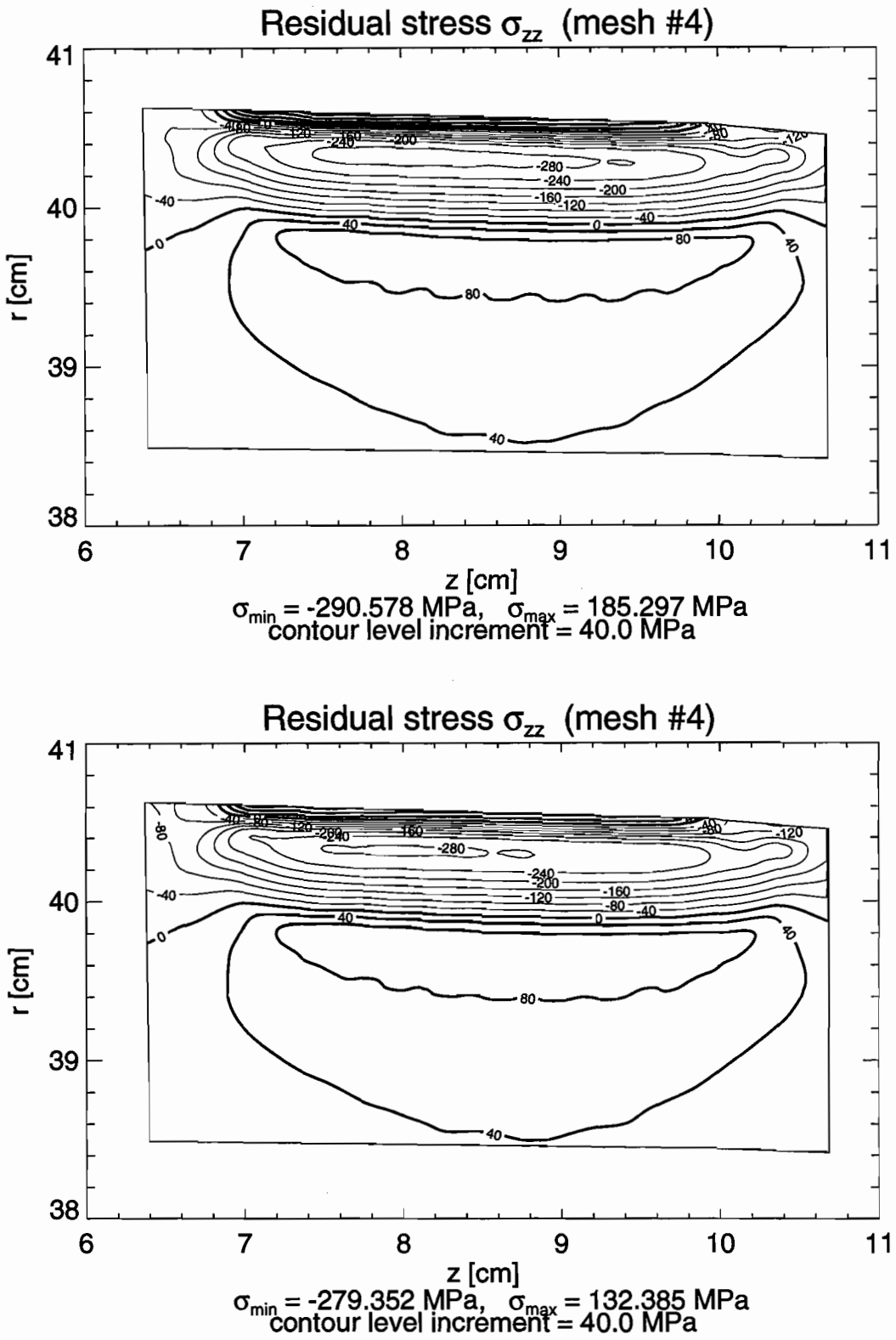

Figure 3.21 Contour Lines of Axial Residual Stresses σ_{zz} in the Railroad Car Wheel under Vertical Loading with Multiple Running Paths (Loading Case #3)

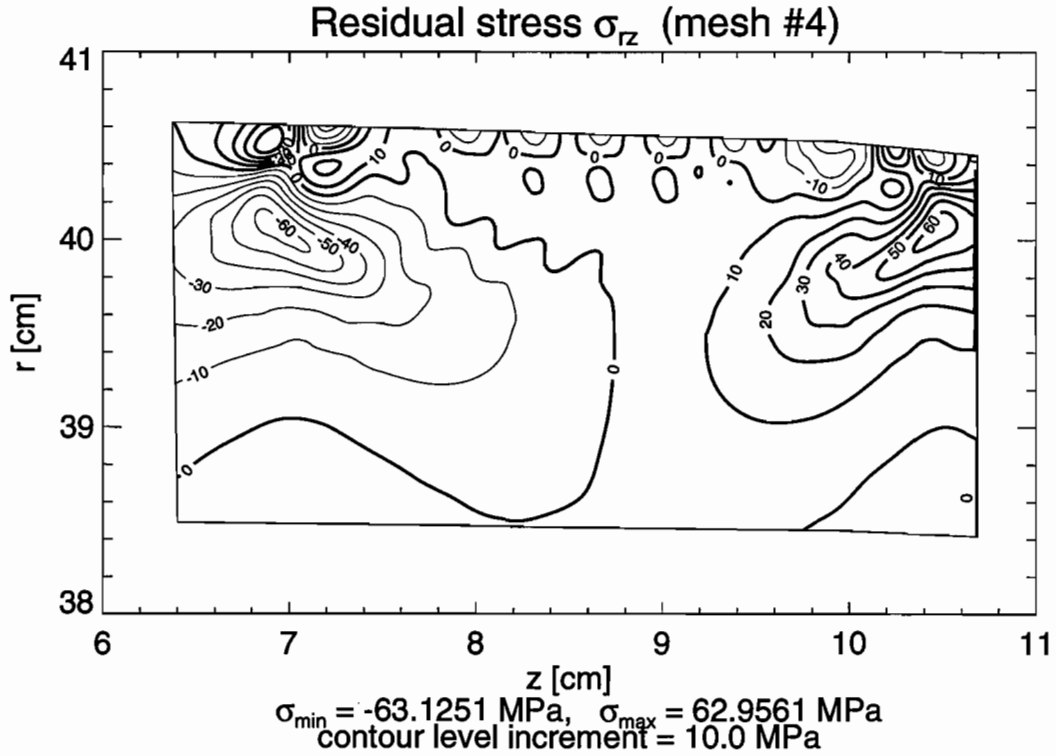

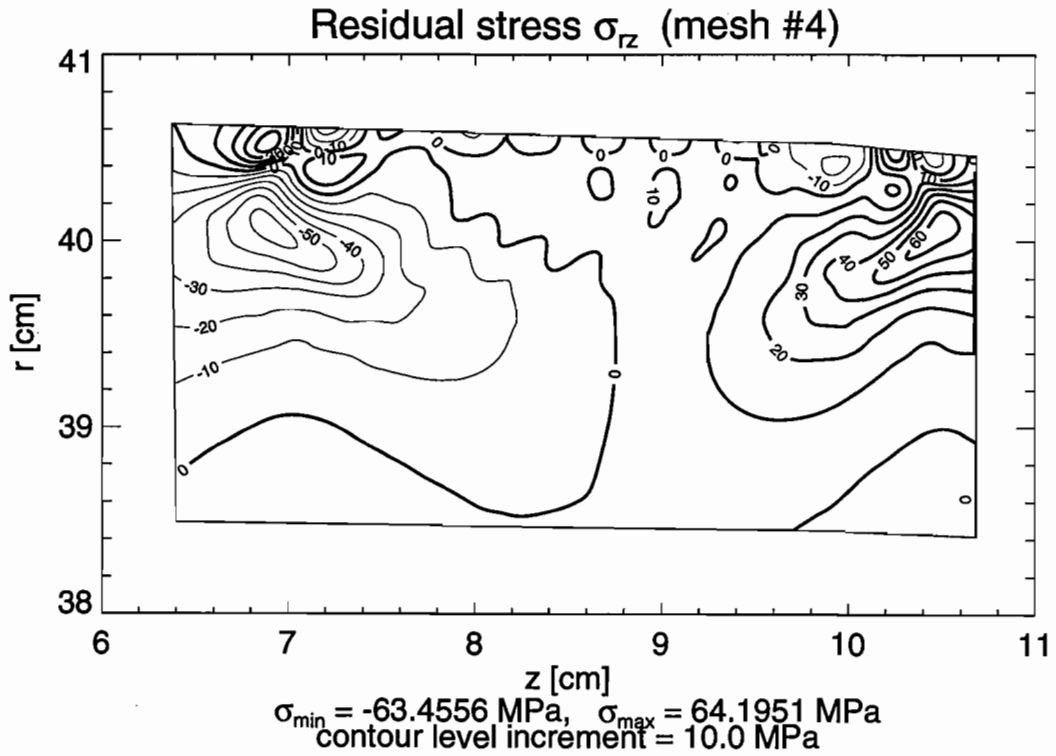

Figure 3.22 Contour Lines of Shear Residual Stresses σ_{rz} in the Railroad Car Wheel under Vertical Loading with Multiple Running Paths (Loading Case #3)

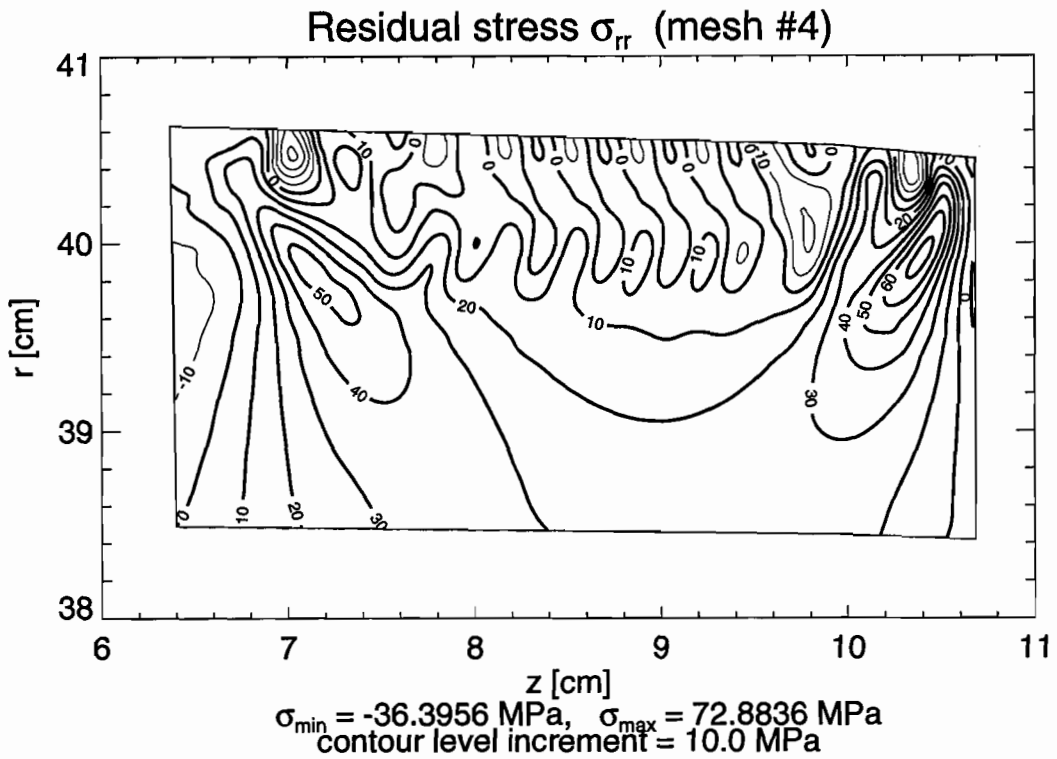

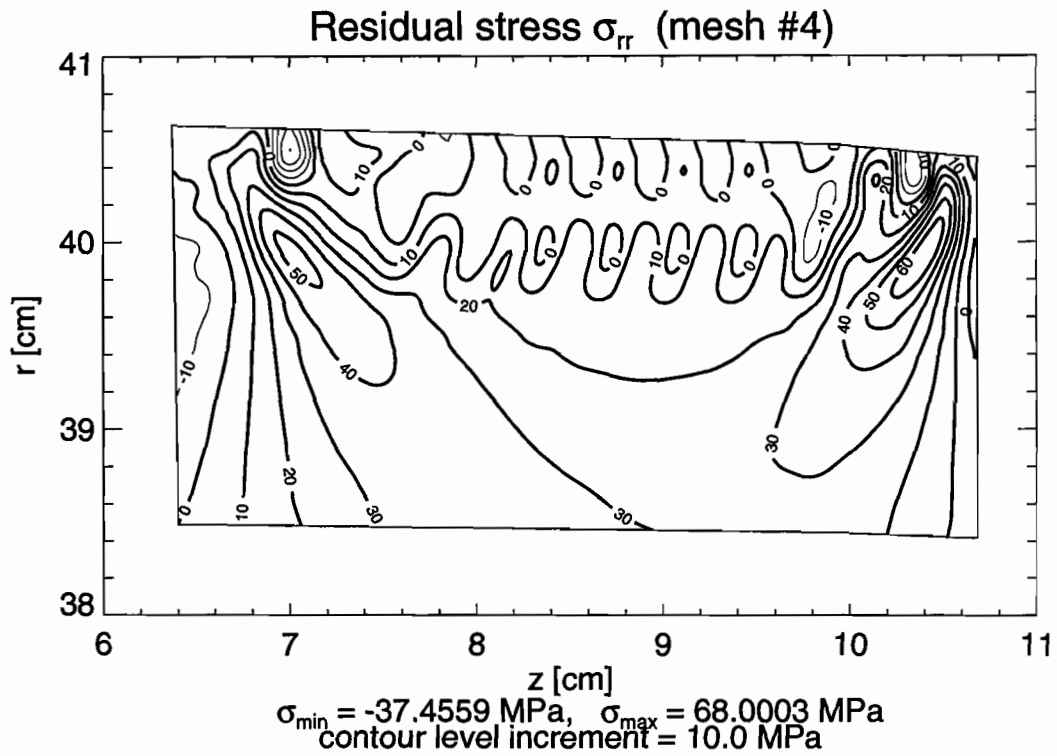

Figure 3.23 **Contour Lines of Radial Residual Stresses σ_{rr} in the Railroad Car Wheel under Vertical and Horizontal Loading with Multiple Running Paths (Loading Case #4)**

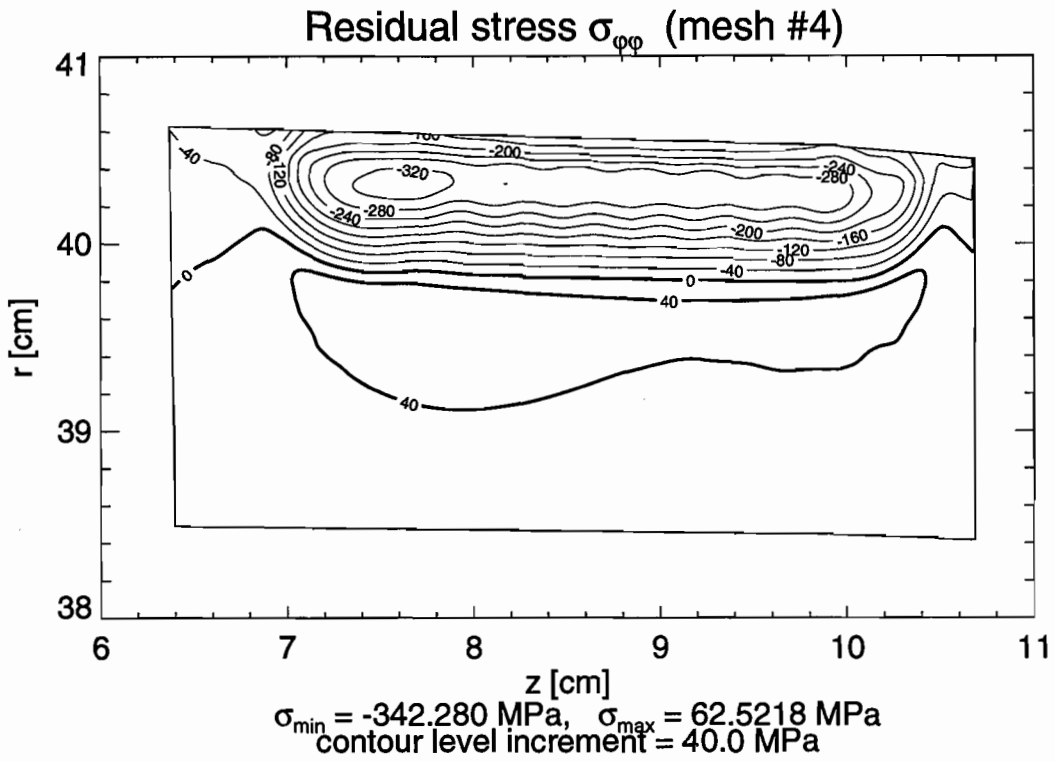

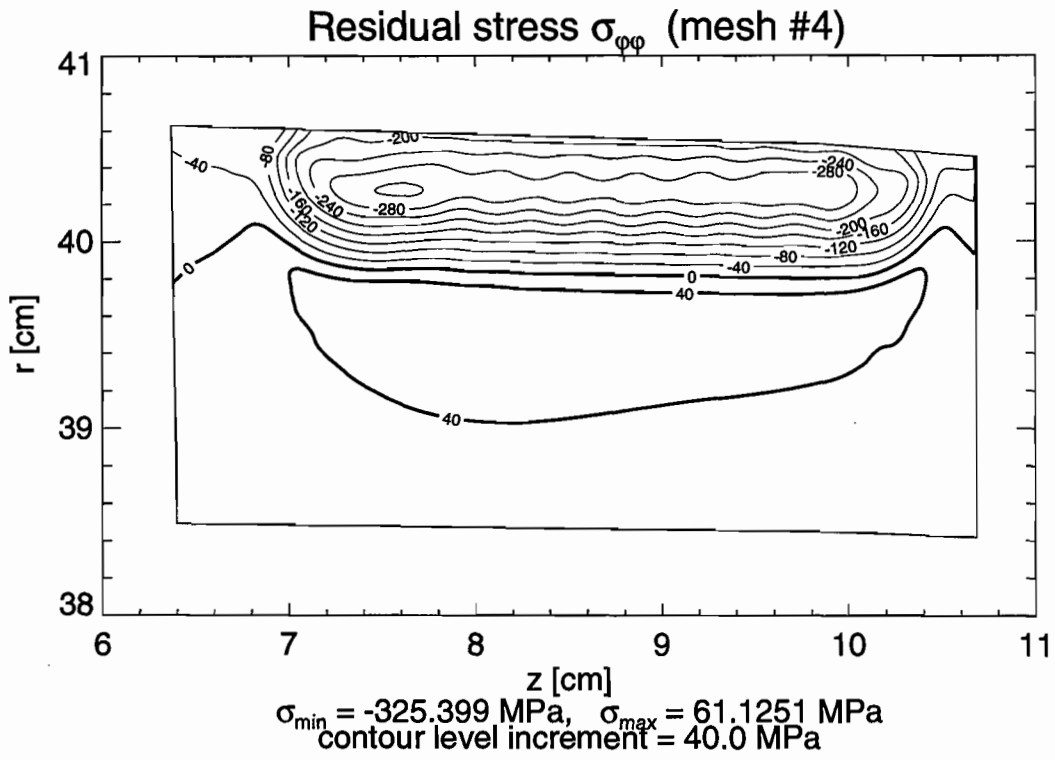

Figure 3.24 Contour Lines of Hoop Residual Stresses $\sigma_{\varphi\varphi}$ in the Railroad Car Wheel under Vertical and Horizontal Loading with Multiple Running Paths (Loading Case #4)

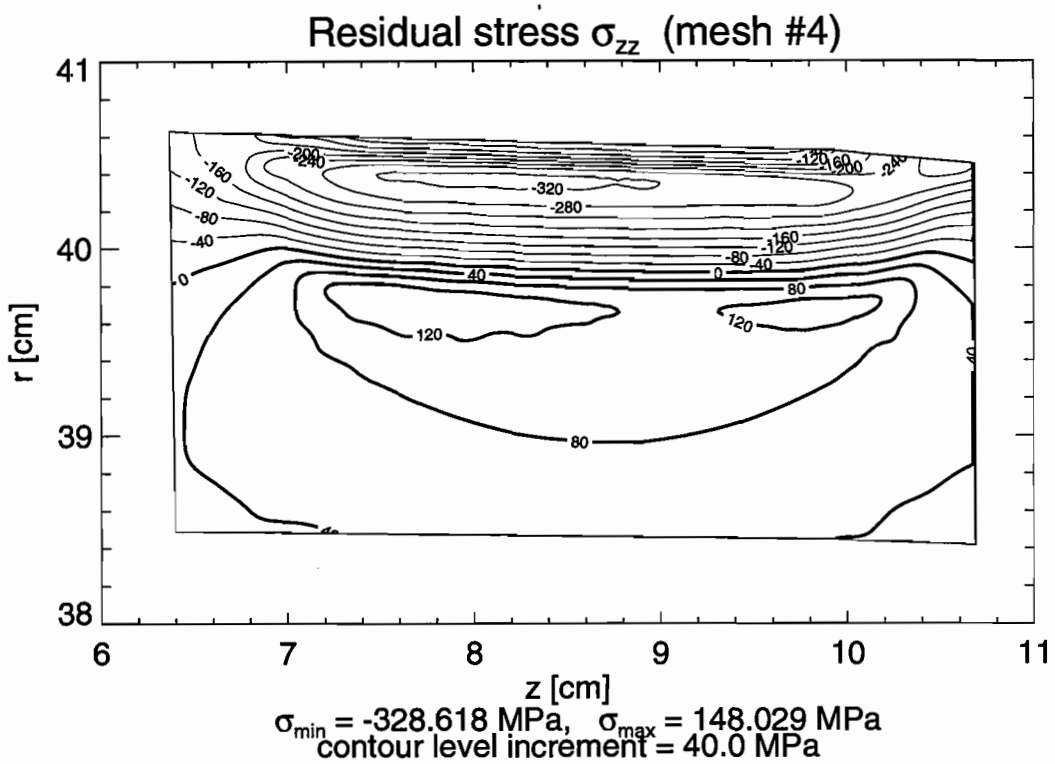

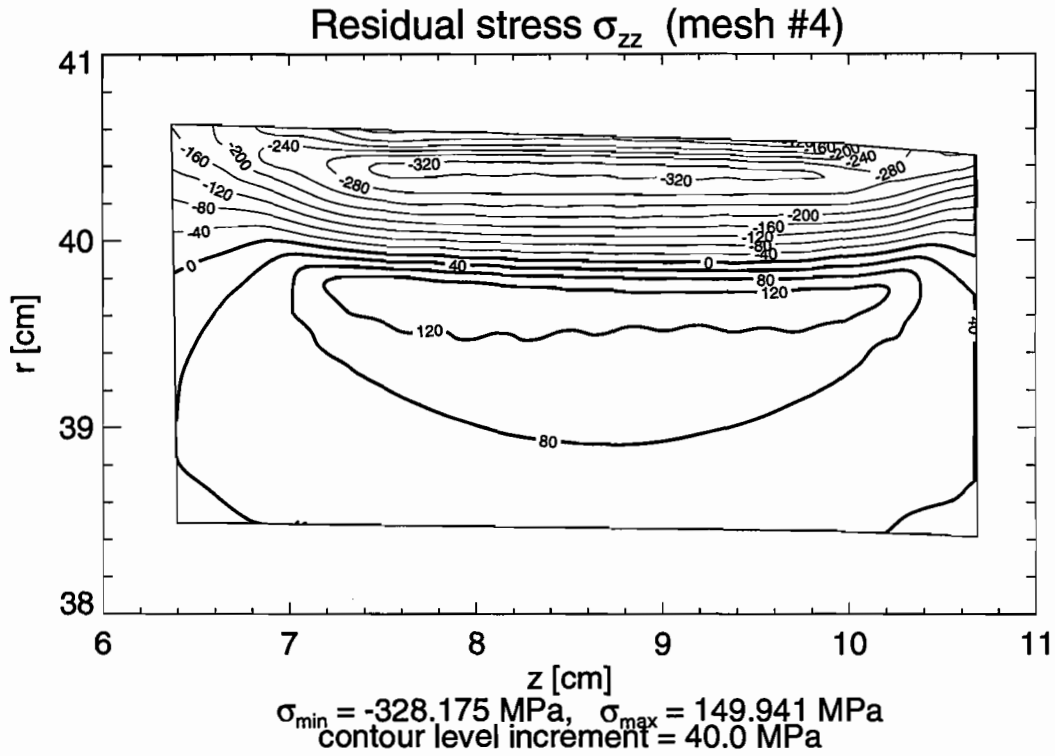

Figure 3.25 Contour Lines of Axial Residual Stresses σ_{zz} in the Railroad Car Wheel under Vertical and Horizontal Loading with Multiple Running Paths (Loading Case #4)

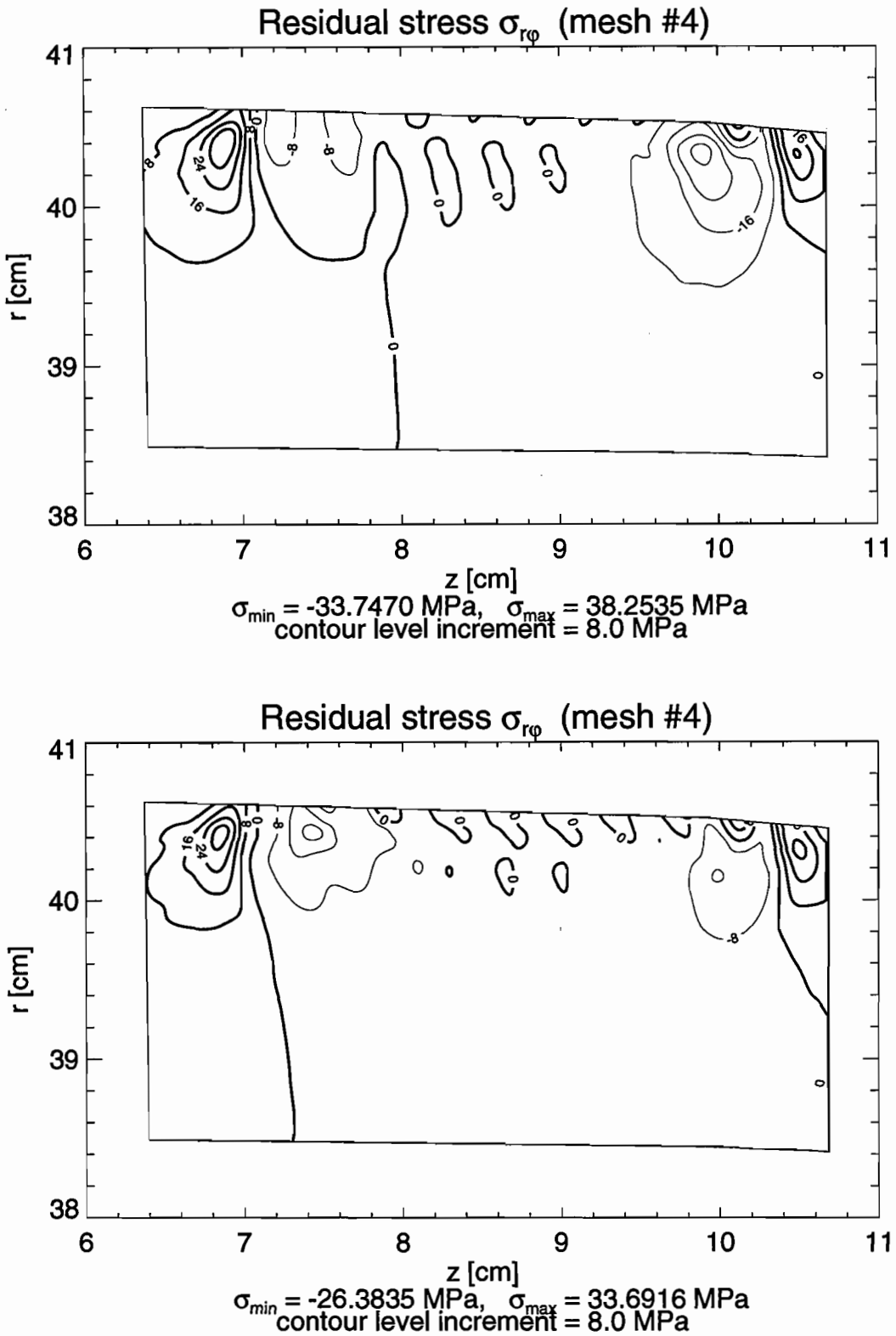

Figure 3.26 **Contour Lines of Shear Residual Stresses $\sigma_{r\varphi}$ in the Railroad Car Wheel under Vertical and Horizontal Loading with Multiple Running Paths (Loading Case #4)**

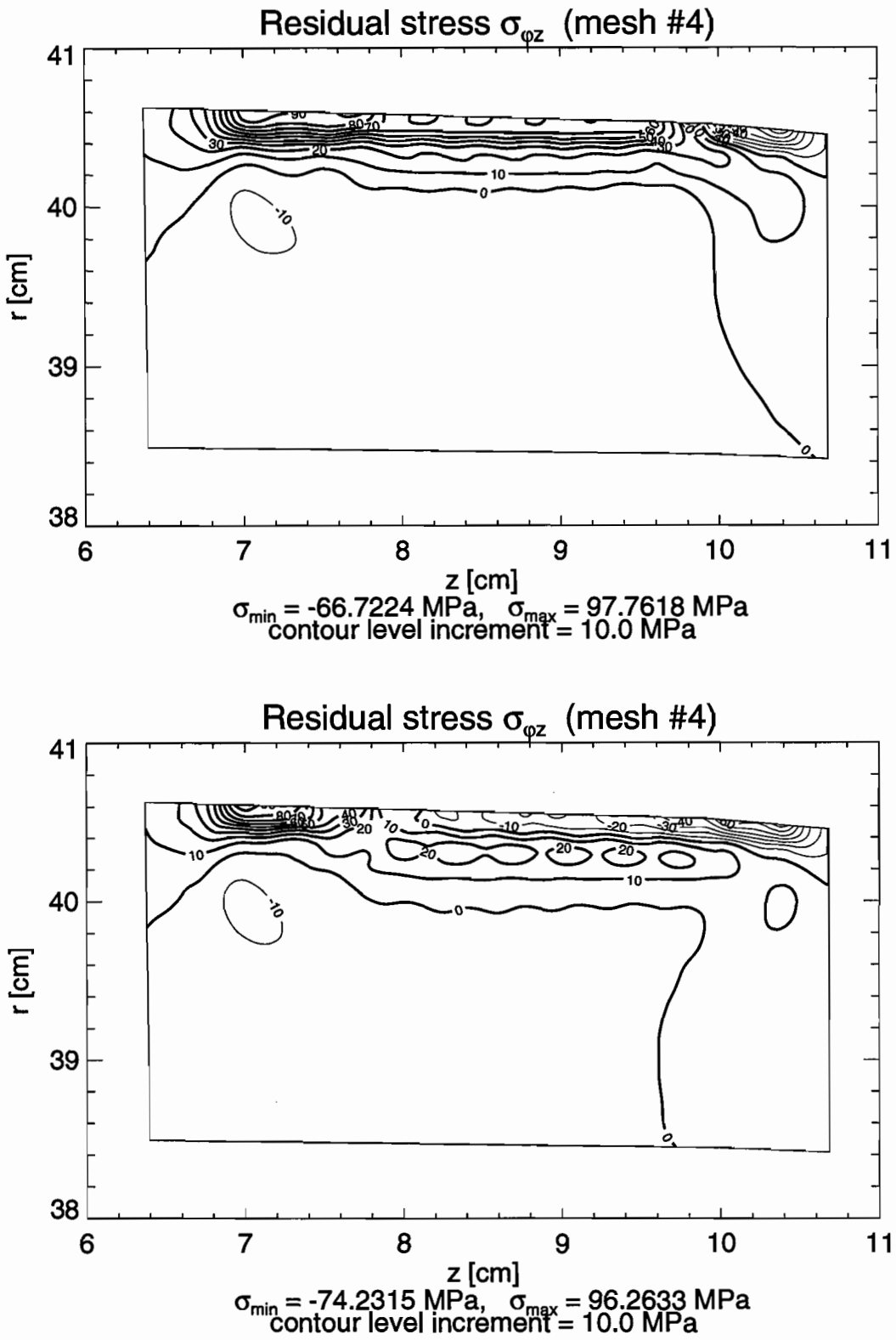

Figure 3.27 Contour Lines of Shear Residual Stresses $\sigma_{\varphi z}$ in the Railroad Car Wheel under Vertical and Horizontal Loading with Multiple Running Paths (Loading Case #4)

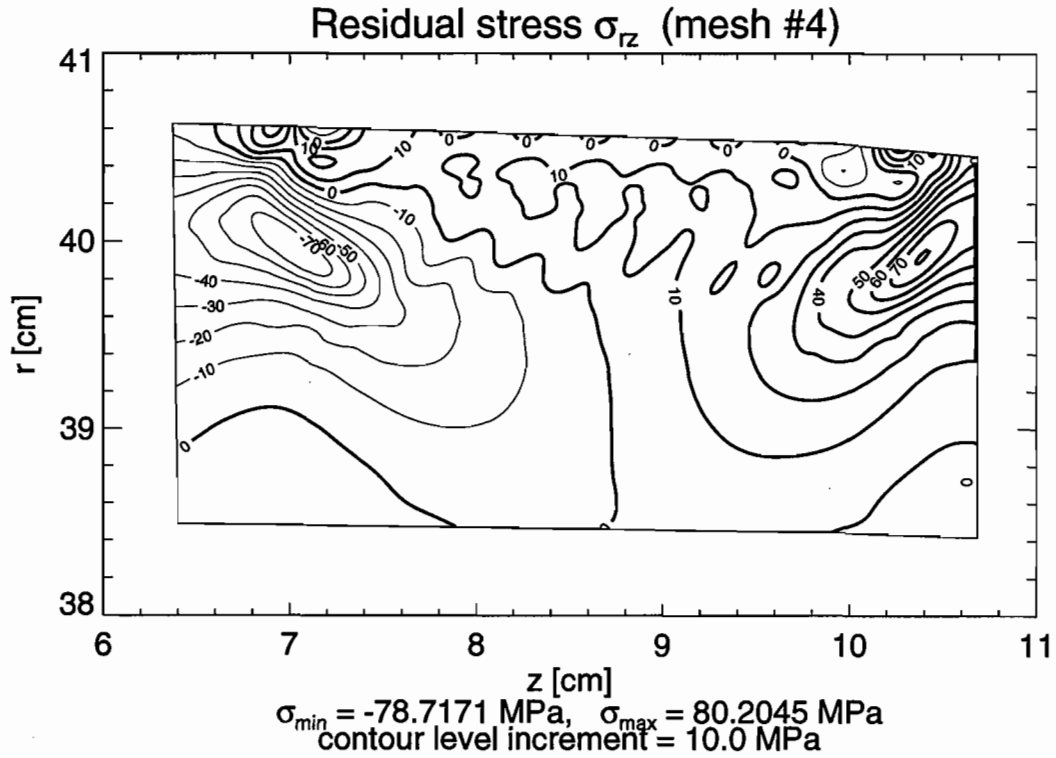

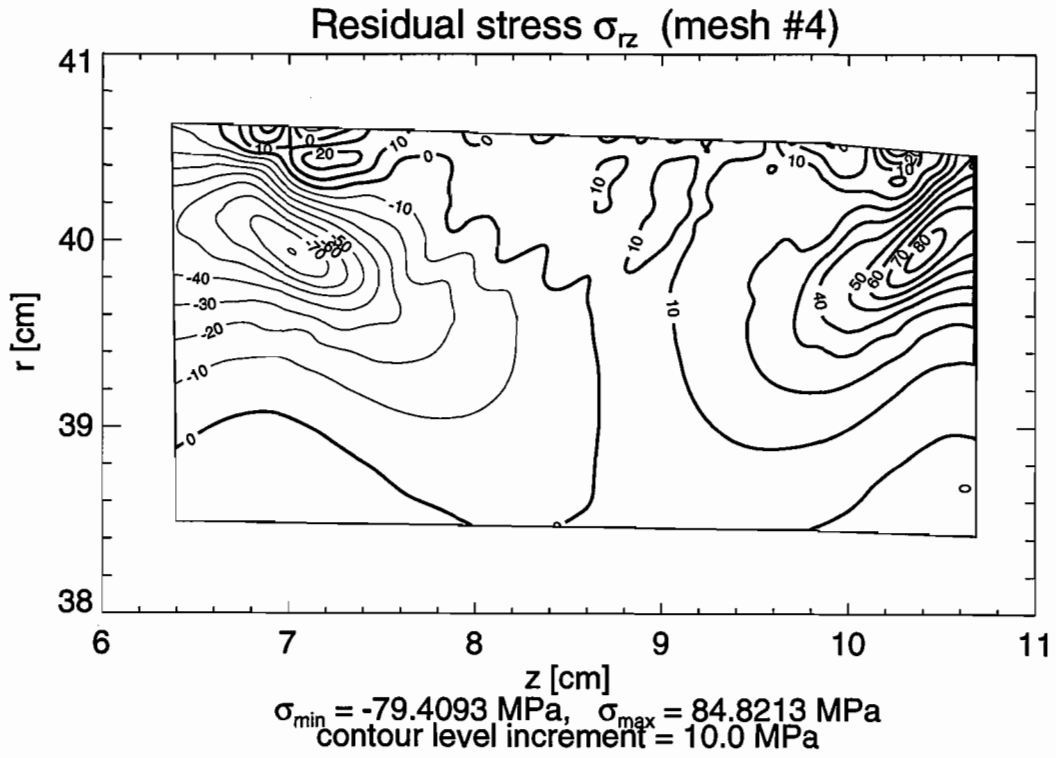

Figure 3.28 Contour Lines of Shear Residual Stresses σ_{rz} in the Railroad Car Wheel under Vertical and Horizontal Loading with Multiple Running Paths (Loading Case #4)

3.6.2 Cases 5 through 7

In case #5, the wheel was subject only to thermal loading due to stop-braking. No mechanical effects were included. Despite the fact that such a case of loading is purely hypothetical, thanks to its axisymmetry the problem could be reduced to a two-dimensional one and solved using incremental analysis implemented in one of available commercial finite element codes. This way the procedure proposed for the case of temperature-dependent material properties could be numerically verified.

In the preliminary analyses dealing with thermal loading, the thermal stresses (the elastic solution to the problem of thermal conductivity) were supplied by the Volpe National Transportation Systems Center (see report no. 2 in this series). They were obtained using finite element program `NIKE2D`. In further analyses, including those presented here, such solutions were obtained by means of `ABAQUS`, `v.5.3-2` [12]. There were two reasons for such replacement. First, intensive testing required the thermal stresses to be found repeatedly, and `ABAQUS` was the only appropriate program accessible to the authors. Second, for the purpose of verification, it was necessary to find another numerical solution to the problem of the evaluation of residual stresses. `ABAQUS` turned out to be a convenient program for this type of analysis, and the elastic solution could be obtained as a byproduct, without any additional effort.

The thermal analysis was performed for one typical stop-braking maneuver from 80 mph at 2 mph/s. It was assumed that the wheel was made of material with the temperature-dependent properties shown in figure 3.29. The thermal loading due to braking was simulated by applying a uniform heat flux along the tread surface. The heat flux versus time function is shown in figure 3.30. With regard to all the input data, they strictly corresponded to those given by the Volpe Center. The elastic analysis was carried out using fully coupled heat transfer/stress analysis. In fact it was not needed, as the stress analysis was dependent on the temperature distribution but there was no inverse dependency. In such cases, it is usually recommended that the heat analysis be done first with the temperatures being saved on the `ABAQUS` results file, and the stress analysis be done afterwards. However, such an approach would be extremely time-consuming because a great many elastic stress states corresponding to consecutive stages of the process were required. The elastic-plastic analysis was performed assuming identical input data except for the material properties and the cyclical character of the process. One cycle was defined as a period of ten hours with the heat flux being applied during the first forty seconds and was long enough to obtain a stable temperature distribution. The analysis was carried out applying ten cycles in order to assure that the solution corresponded to the state after adaptation. In fact, the difference between the residual stress states after the first and second cycles was negligible.

The problem was solved using the same finite element meshes as those used in the elastic analyses presented in section 2.6. The first goal was to examine the convergence of the solution with respect to mesh density. For simplicity, the residual stress state was found in one step, i.e., assuming the input data that corresponded to the maximal intensity of the thermal stresses at the center C of the heat flux zone. In order to determine the appropriate moment during the application of the heat flux, the curve shown in figure 3.30 was used. Taking into account further results, where the analysis was performed using the multistep procedure, such an arbitrary selection appeared to be very reasonable.

The results of this test are shown in figures 3.31 through 3.34 (top graphs), where the stress tensor components are drawn along the line $\alpha-\alpha$ shown in figures 2.26 through 2.28. These results indicate that mesh #3 is dense enough for the problem under consideration. Such

a conclusion may be surprising in the light of the results presented in section 3.6.1 unless one takes into account the fact that the plastic zone in this case is much bigger than the one caused by contact loading. That is why meshes #4 and #5 were not considered here. They were accompanied by huge optimization problems that could not have been solved using the available computer equipment.

The multistep procedure proposed for the case of temperature-dependent material properties was verified using only mesh #3. Two cases were considered. In the first one, the analysis was performed in 8 steps. The first step corresponded to the first appearance of plastic strains. It was found by testing the elastic stress intensity for consecutive increments in the elastic analysis. Then, it was assumed that significant changes in the temperature distribution and consequently in the material properties and elastic stresses occurred every ten increments. The last, eighth step was the one in which there was no further plastic deformation. In the second case, each time interval (ten increments) was divided into two subintervals, resulting in 15 steps. The corresponding temperature and elastic stress intensity at the center of the heat flux zone are shown in figure 3.30 as small points.

The results of this test are presented in figures 3.31 through 3.34 (bottom graphs) and in figures 3.35 through 3.38 in the form of contour line plots. They indicate that there is almost no difference between the solutions obtained using 8- and 15-step procedures. Both of these solutions are in very good agreement with the ABAQUS solution. The biggest differences may be observed in the plastic zone, particularly at the tread surface. It should be noticed that the static boundary conditions in the ABAQUS solution are not fully satisfied. The radial residual stresses σ_{rr} should be approximately equal to zero on the tread surface but they are not (see figure 3.35), a factor that influences the quality of the whole solution in this region. The one-step solution is subject to some errors but seems to be quite reasonable and may be used in preliminary analyses, e.g., when an appropriate finite element mesh has to be chosen.

In case #6, the wheel was subject to the thermal loading due to one stop-braking maneuver from 80 mph at 2 mph/s, the vertical surface tractions $t_Z(X,Y)$ of intensity $t_{0Z} = 1239.98$ MPa and the horizontal surface tractions $t_X(X,Y)$ of intensity $t_{0X} = 0.2t_{0Z} = 247.996$ MPa. This type of residual stress analysis appeared to be extremely time-consuming. First, the multistep procedure connected with temperature-dependent material properties had to be applied. Second, there were a great many active constraints in each optimization problem. The number of enveloping stress states was exactly the same as before but this time the stress field intensity was very high not only near the center of the contact zone but also at distant points due to the thermal loading.

This problem was solved using mesh #3, and its results are presented in figures 3.39 through 3.41. To the best of the authors' knowledge, these are the first results of the evaluation of residual stresses in a railroad car wheel where both mechanical and thermal effects are taken into account. Thus, their quality can be judged only by the quality of the other results presented in this report. The comparison with the results obtained in cases #2 and #5, where the wheel was subject to the components of the loading considered here, indicates that the solution is correct. It looks as if the solutions for the cases of contact (#2) and thermal (#6) loads were superimposed. Of course, such superimposition can be considered only qualitatively because the analysis was nonlinear.

In case #7, the wheel was subject to the thermal loading due to one stop-braking maneuver from 80 mph at 2 mph/s. It was assumed that there existed initial residual stresses representing the original as-manufactured stress state. The appropriate data had been

obtained at the Volpe National Transportation Systems Center by means of the stress reconstruction procedure described in report no. 3 in this series.

This problem was solved using mesh #3, and its results are presented in figures 3.42 through 3.45. The comparison with the results obtained in case #5 (figures 3.35 through 3.38), where the presence of the as-manufactured stresses was not taken into consideration, indicates that the solution is correct. The contour lines at the tread surface and its vicinity are very similar to those obtained in case #5. The influence of the initial residual stresses in this area is relatively small, which is not surprising if one takes into account the fact that the thermal loading is accompanied here by plastic strains of high intensity. Conversely, the distribution of the final residual stresses at points that are distant from the tread surface is mainly influenced by the initial residual stresses, both qualitatively and quantitatively. It should be stressed that the magnitudes of the initial residual stresses are relatively high, resulting in a much bigger plastic zone than in case #5 and, consequently, in much bigger optimization problems to be solved.

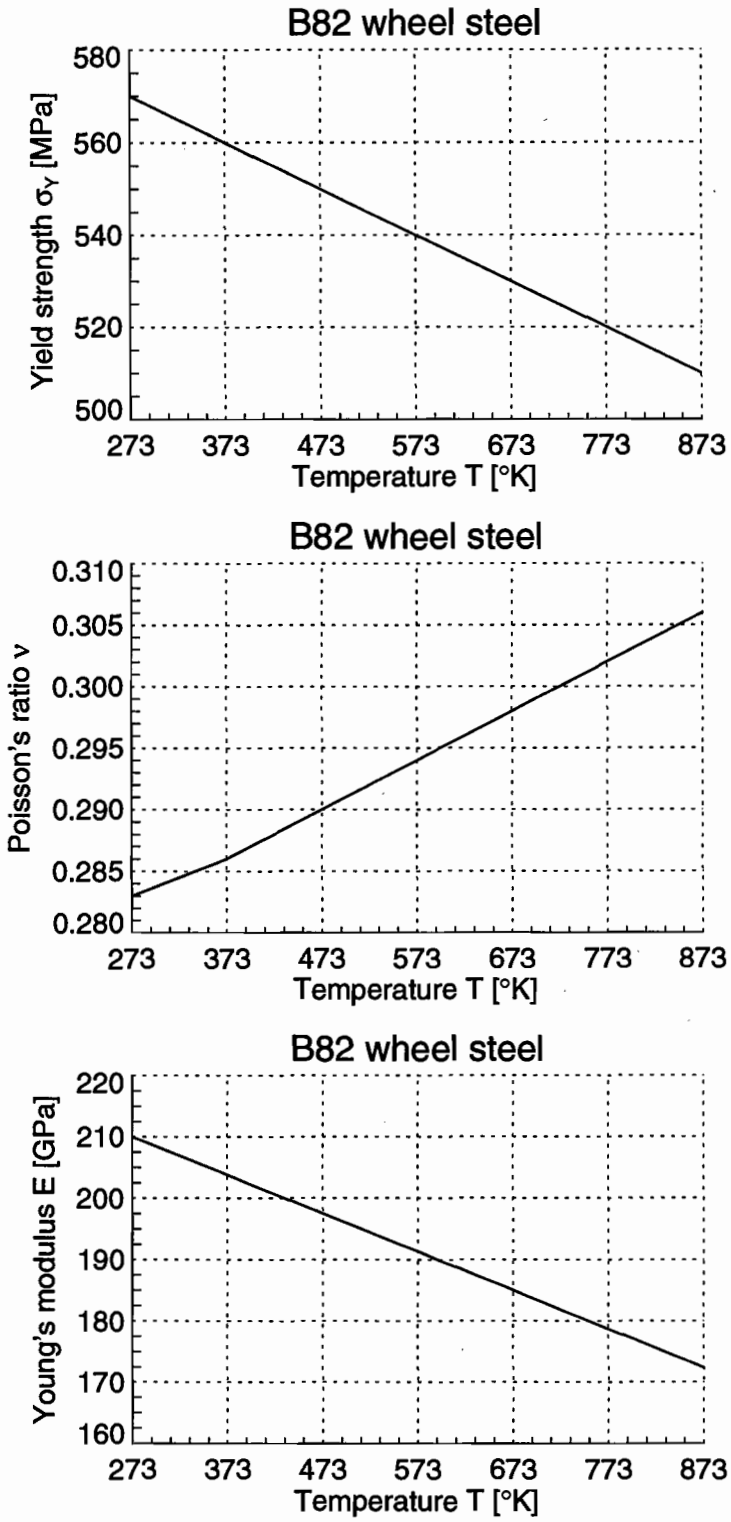

Figure 3.29 Material Properties Used to Represent Wheel Steel in Cases of Thermal Loading (Loading Cases #5, #6 and #7)

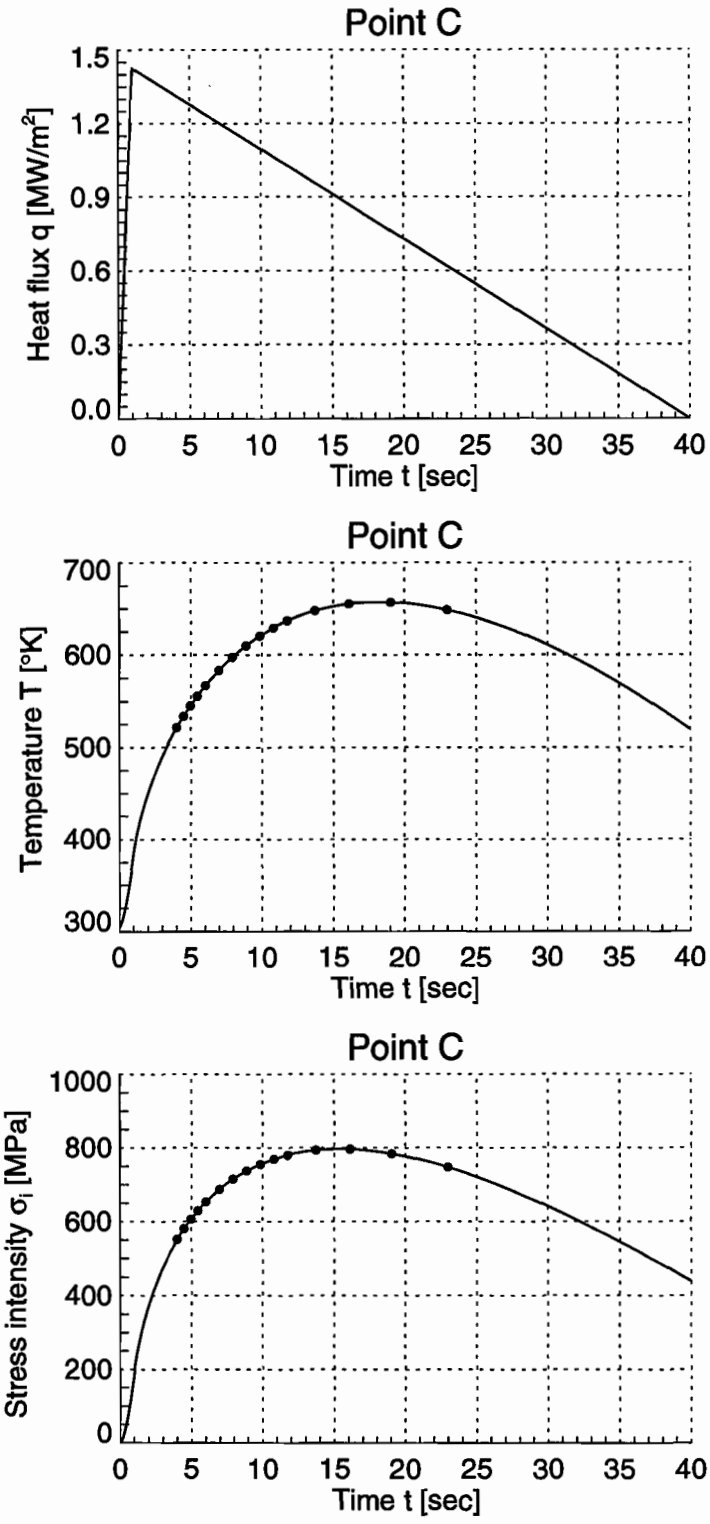

Figure 3.30 Heat Flux, Temperature and Elastic Stress Intensity at Point C in Cases of Thermal Loading (Loading Cases #5, #6 and #7)

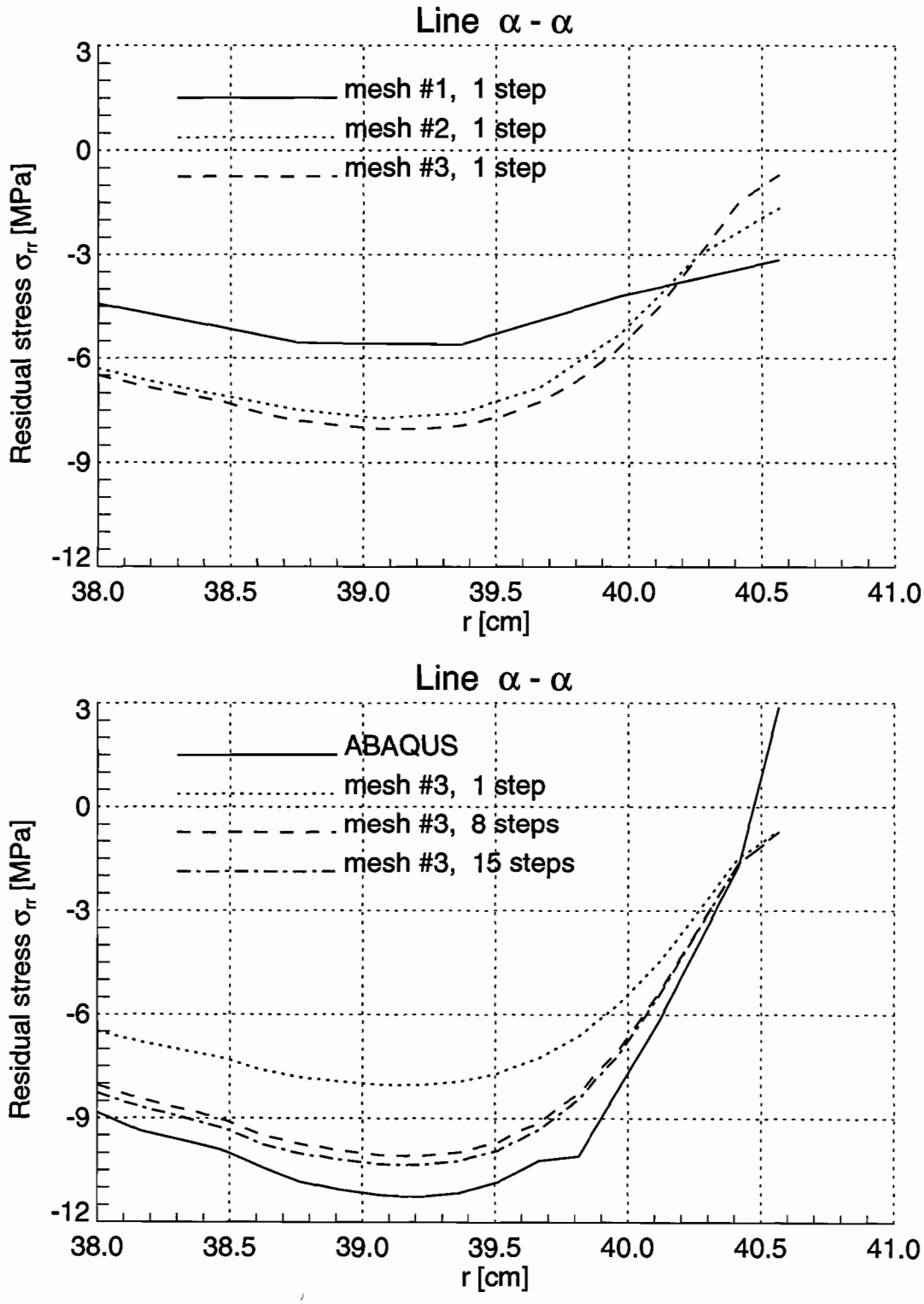

Figure 3.31 Radial Residual Stresses σ_{rr} in the Railroad Car Wheel under Thermal Loading (Loading Case #5)

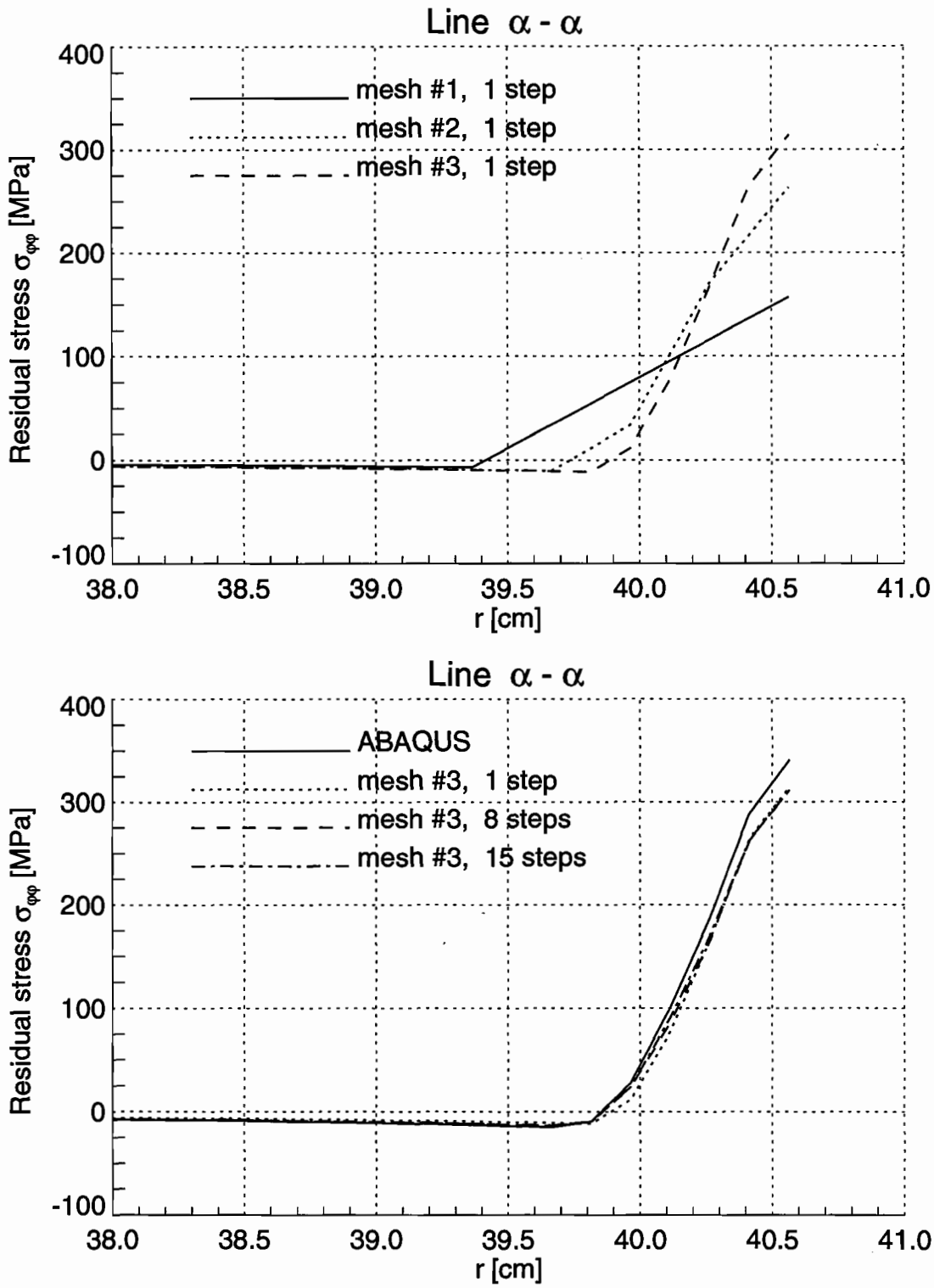

Figure 3.32 Hoop Residual Stresses $\sigma_{\varphi\varphi}$ in the Railroad Car Wheel under Thermal Loading (Loading Case #5)

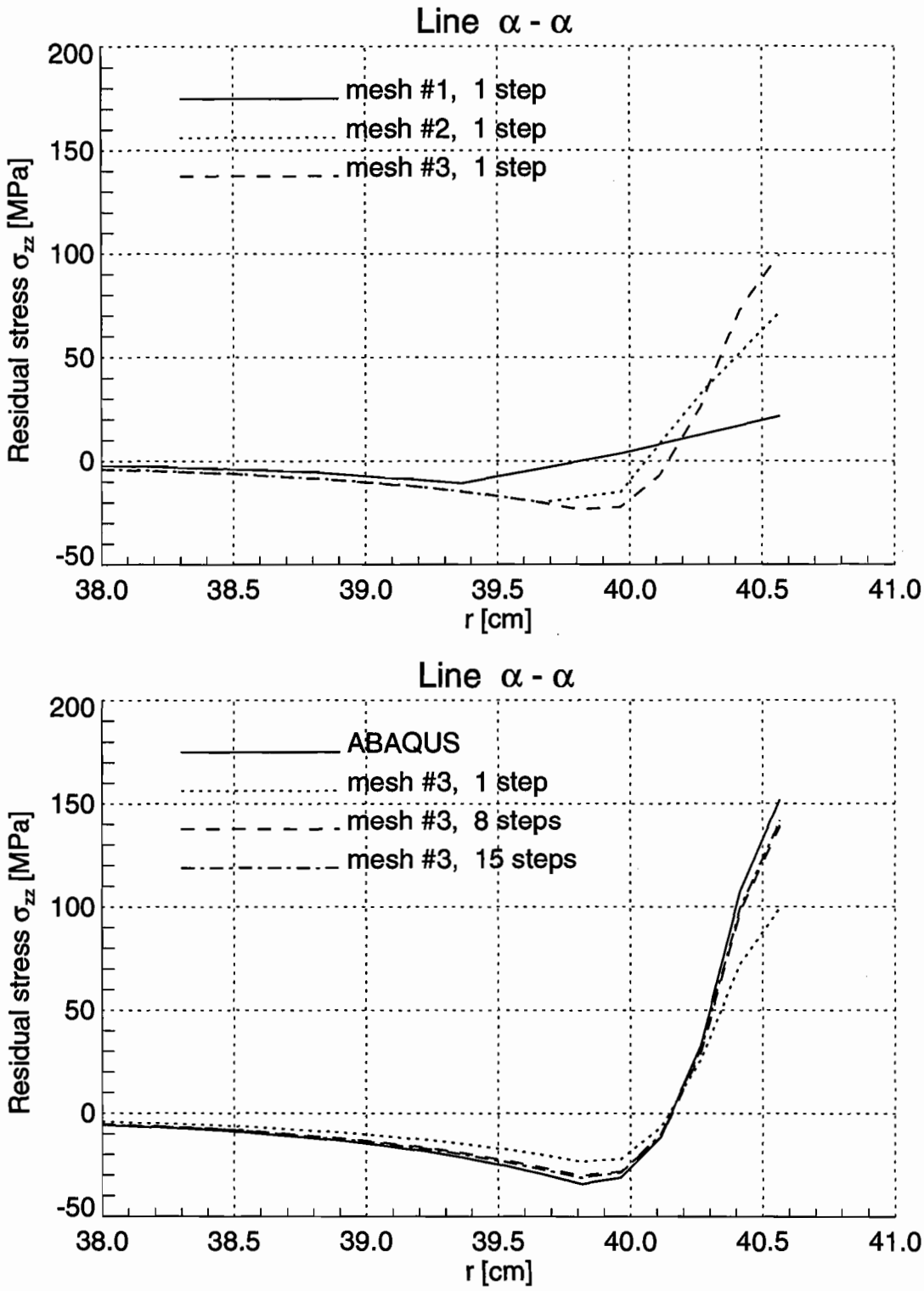

Figure 3.33 Axial Residual Stresses σ_{zz} in the Railroad Car Wheel under Thermal Loading (Loading Case #5)

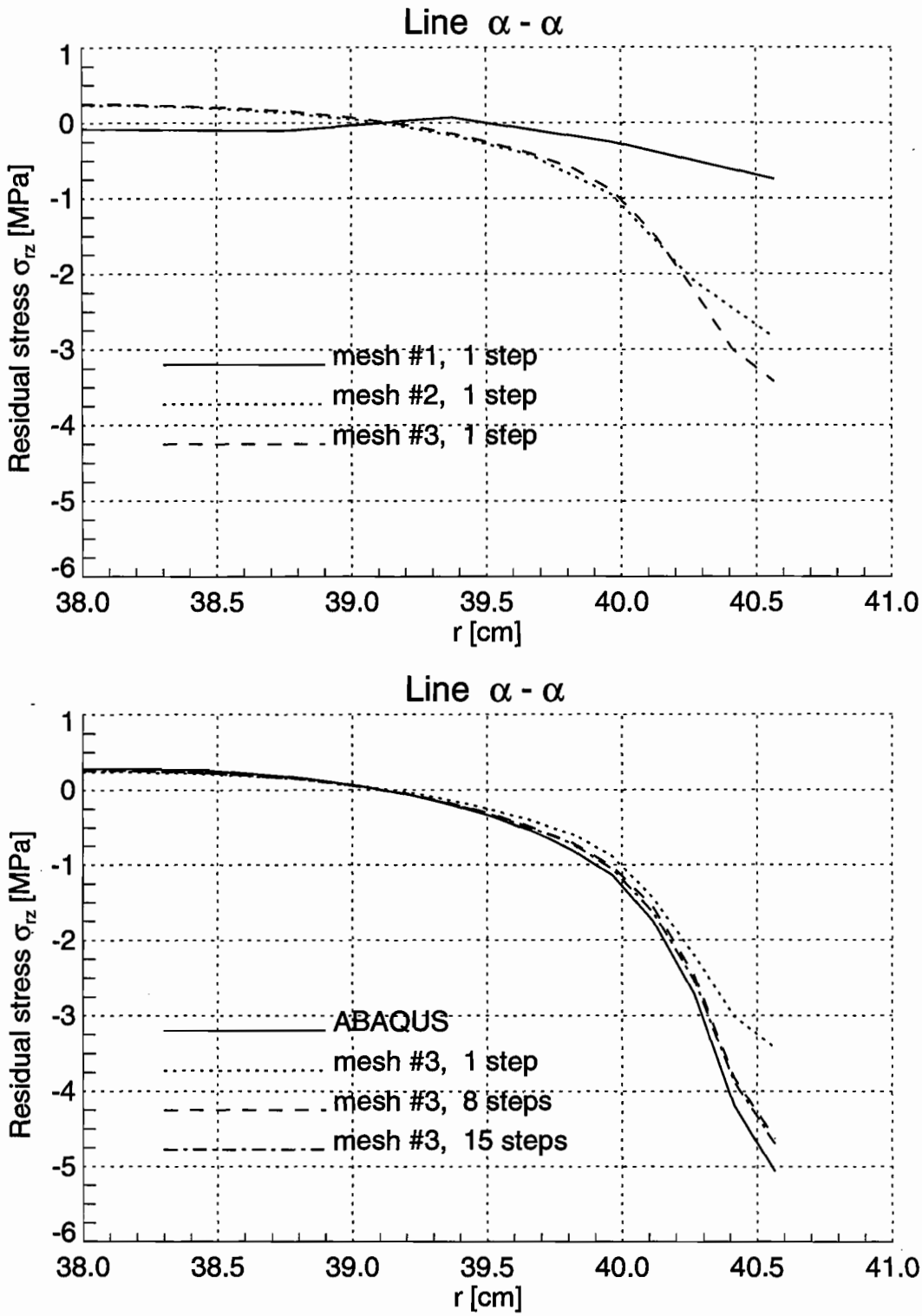

Figure 3.34 Shear Residual Stresses σ_{rz} in the Railroad Car Wheel under Thermal Loading (Loading Case #5)

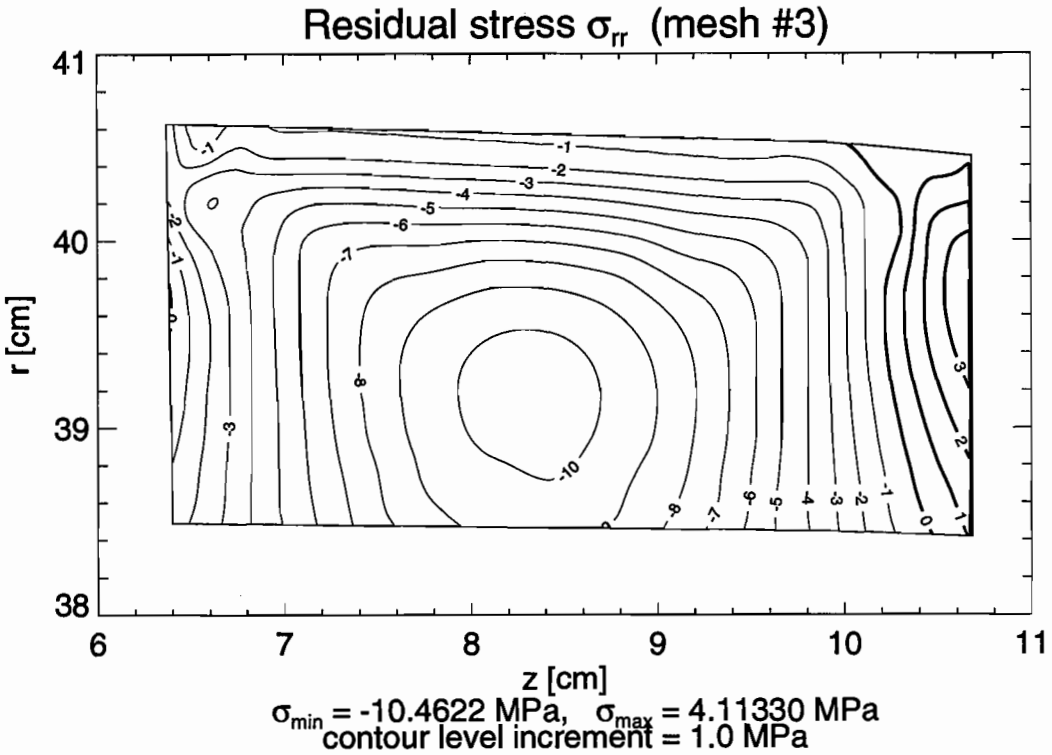

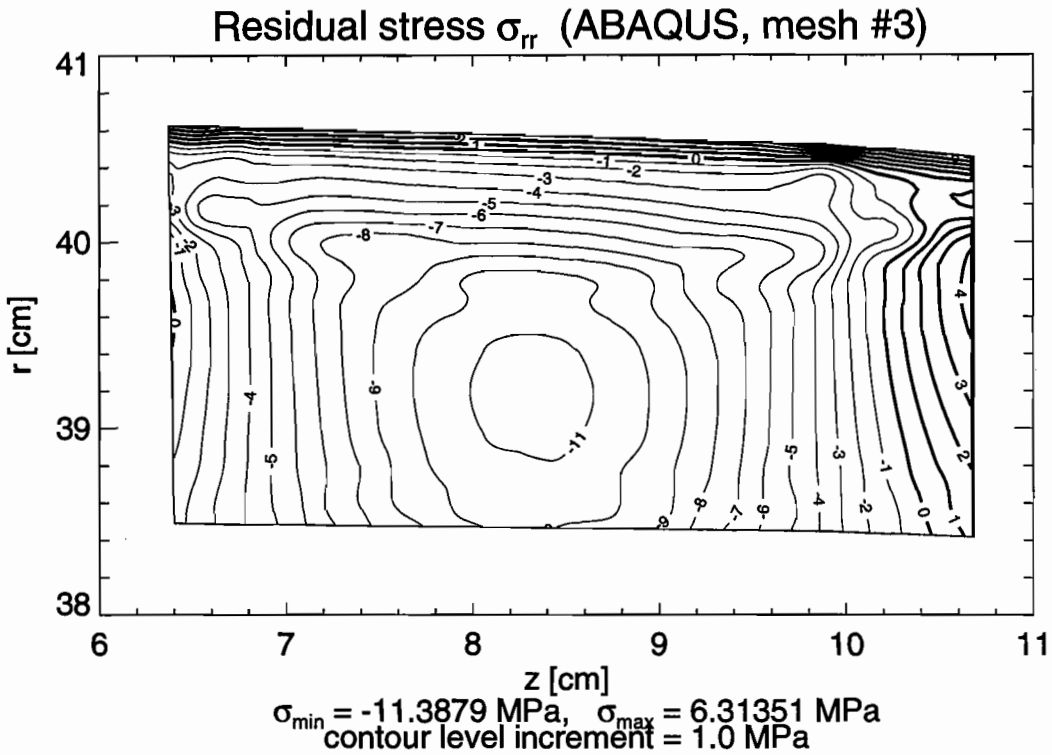

Figure 3.35 **Contour Lines of Radial Residual Stresses σ_{rr} in the Railroad Car Wheel under Thermal Loading (Loading Case #5) – Solution for Mesh #3**

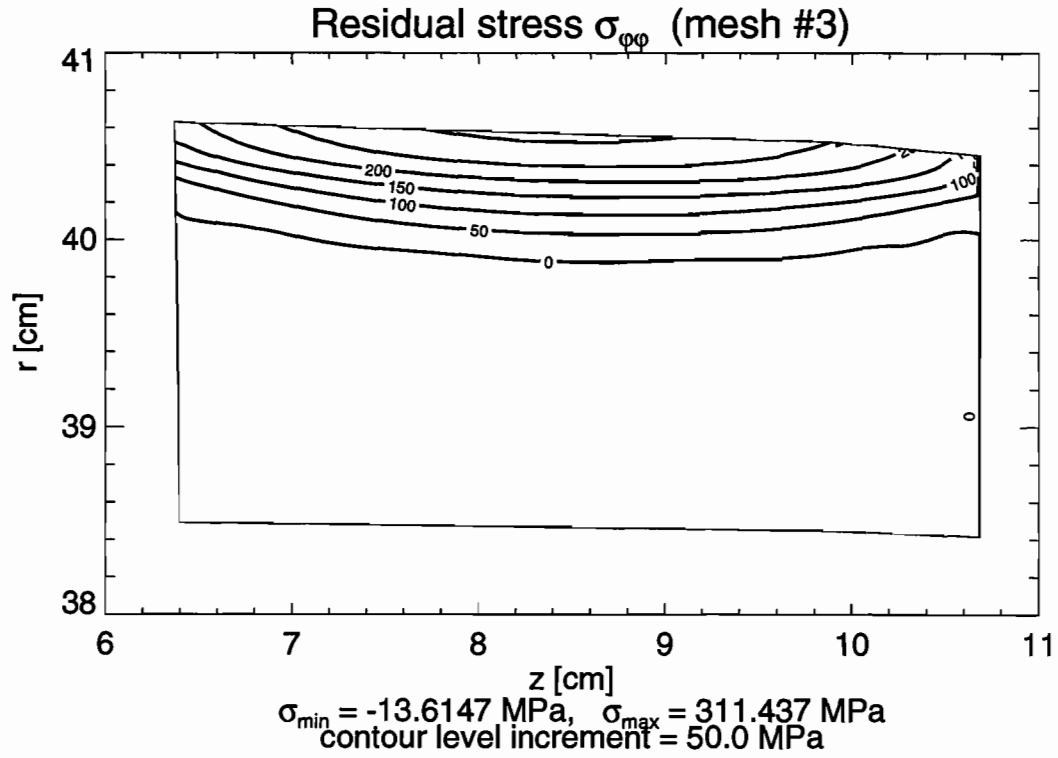

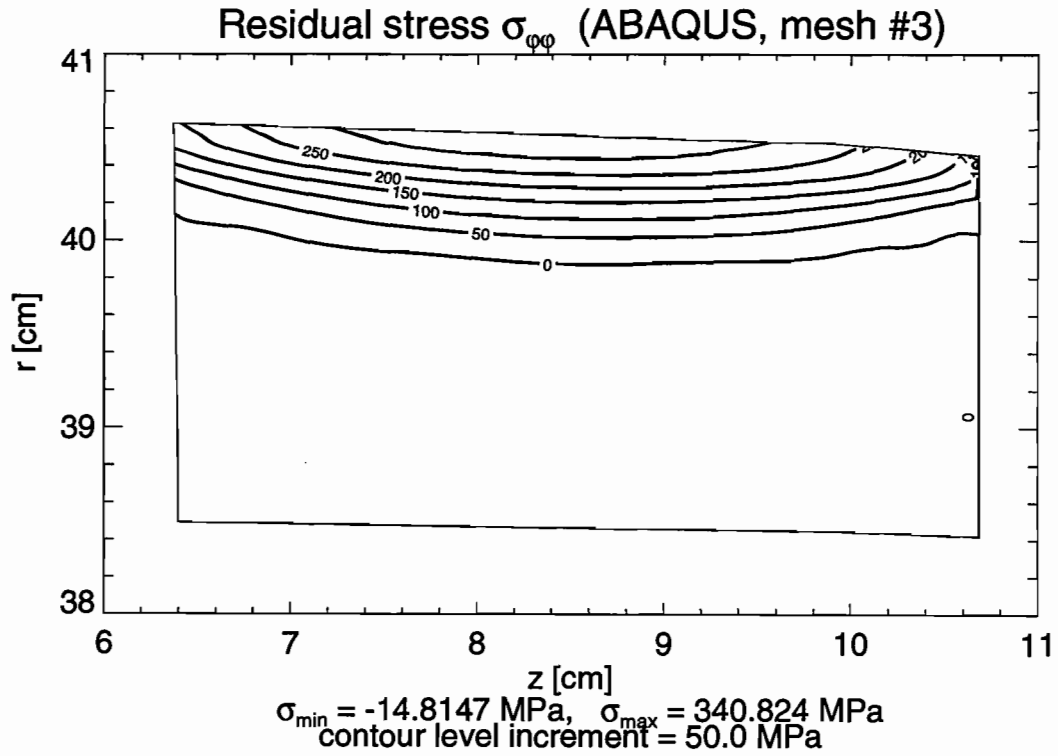

Figure 3.36 Contour Lines of Hoop Residual Stresses $\sigma_{\varphi\varphi}$ in the Railroad Car Wheel under Thermal Loading (Loading Case #5) – Solution for Mesh #3

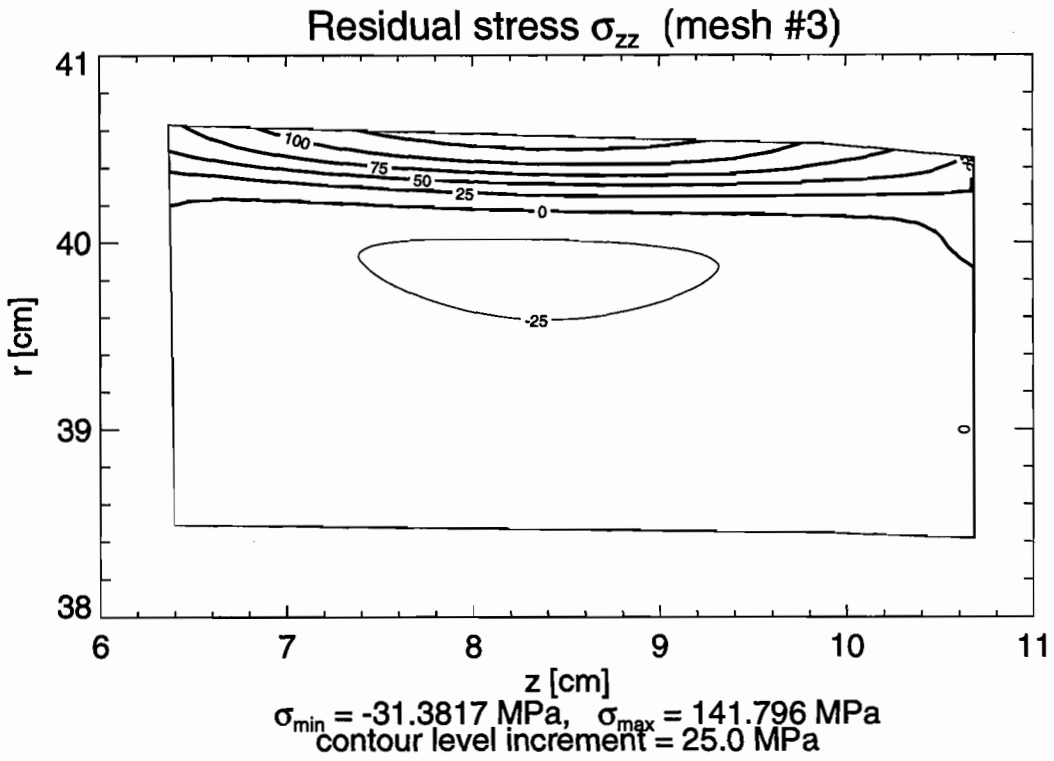

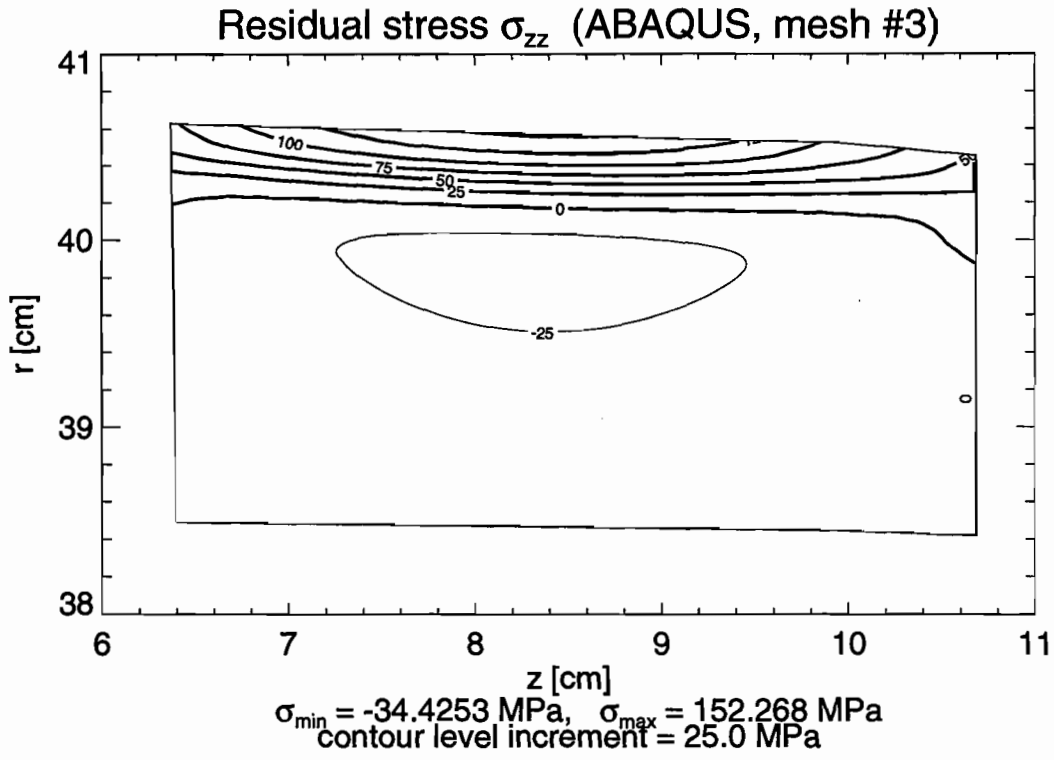

Figure 3.37 Contour Lines of Axial Residual Stresses σ_{zz} in the Railroad Car Wheel under Thermal Loading (Loading Case #5) – Solution for Mesh #3

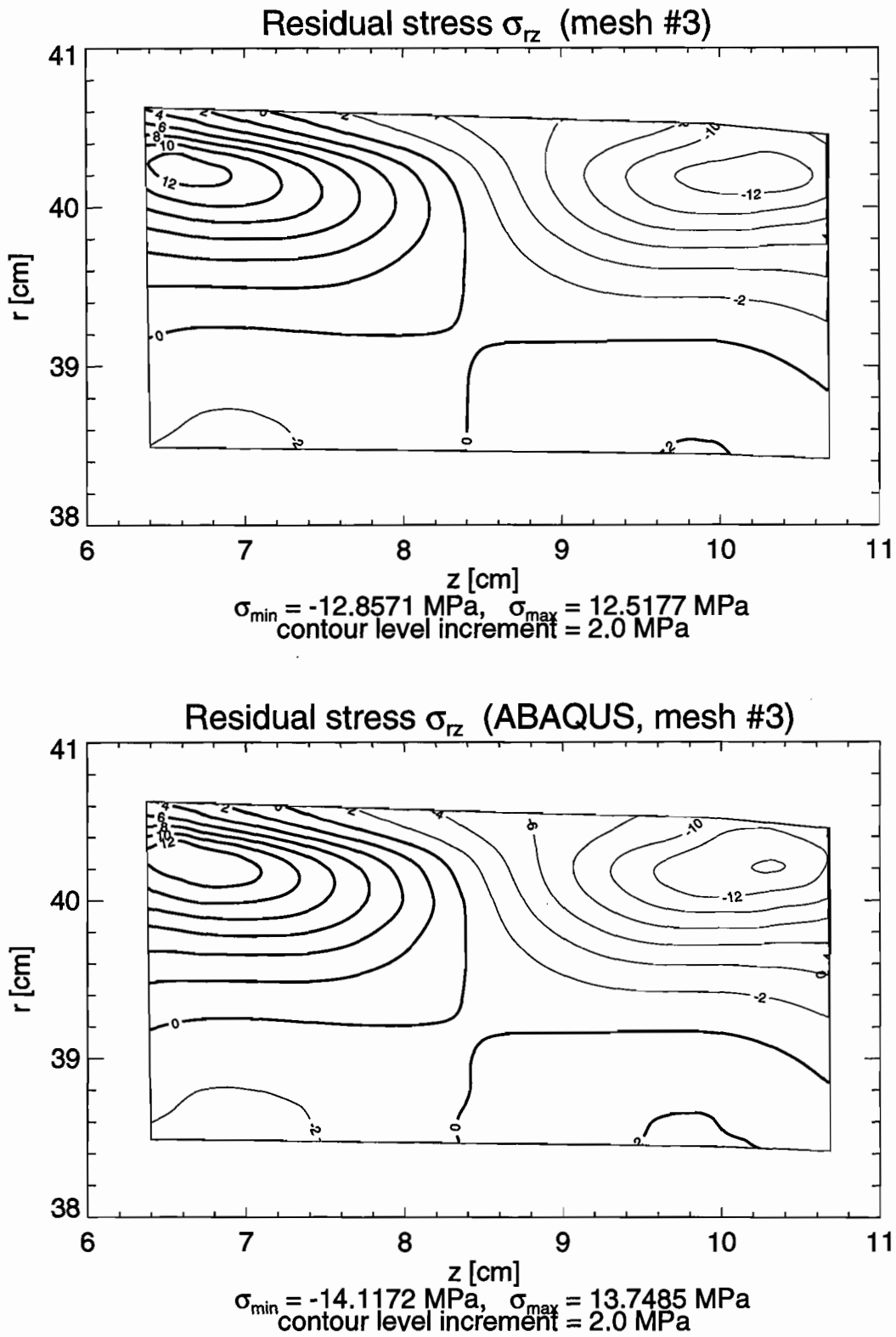

Figure 3.38 Contour Lines of Shear Residual Stresses σ_{rz} in the Railroad Car Wheel under Thermal Loading (Loading Case #5) – Solution for Mesh #3

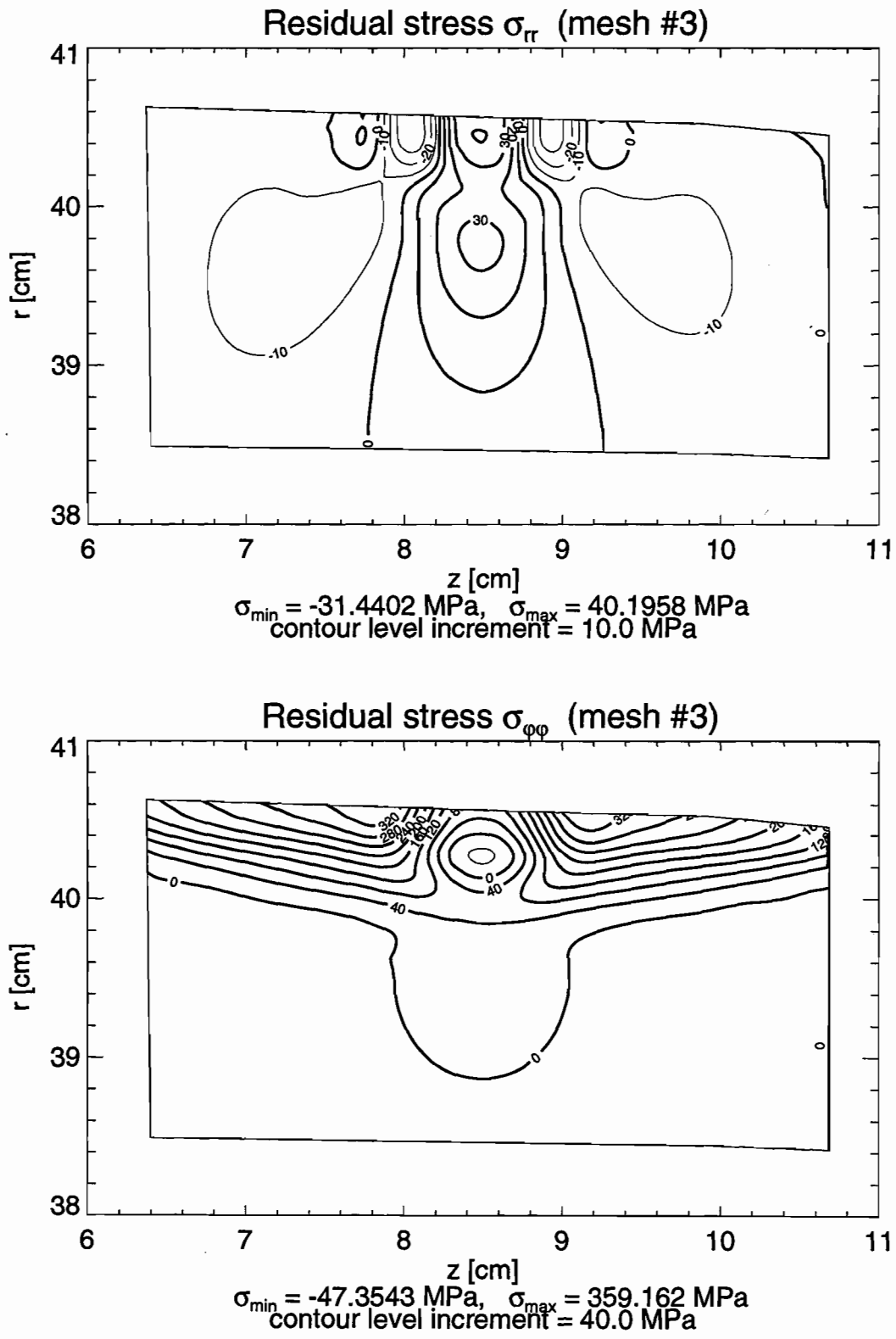

Figure 3.39 Contour Lines of Radial σ_{rr} and Hoop $\sigma_{\varphi\varphi}$ Residual Stresses in the Railroad Car Wheel under Thermal and Mechanical Loading (Loading Case #6)

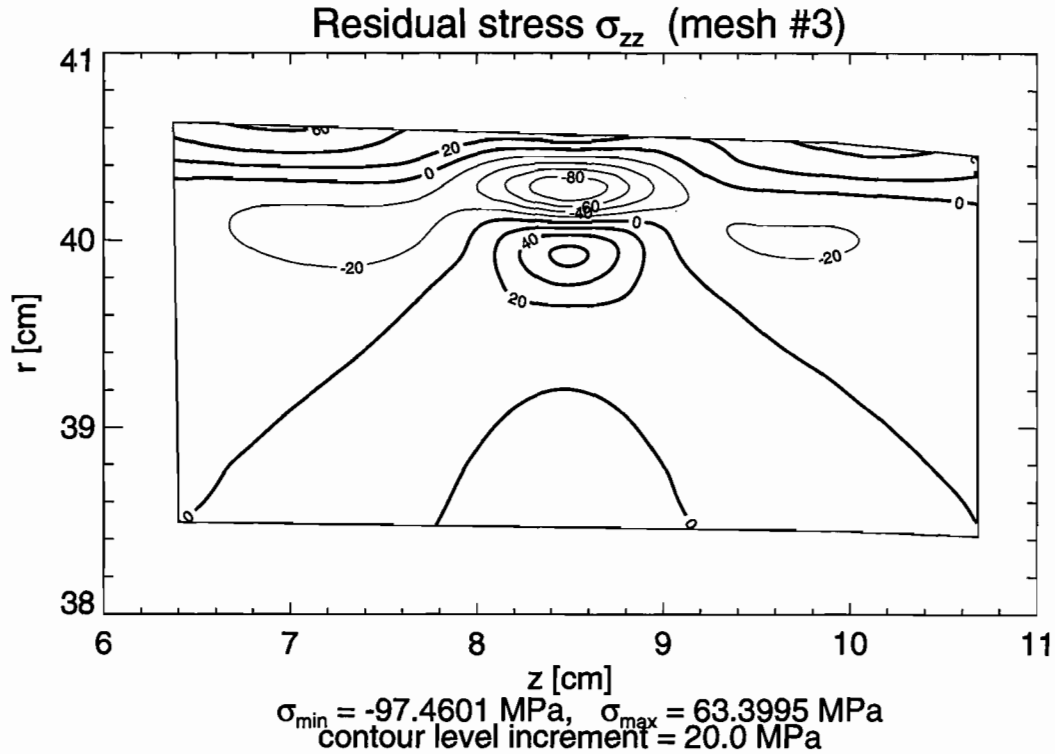

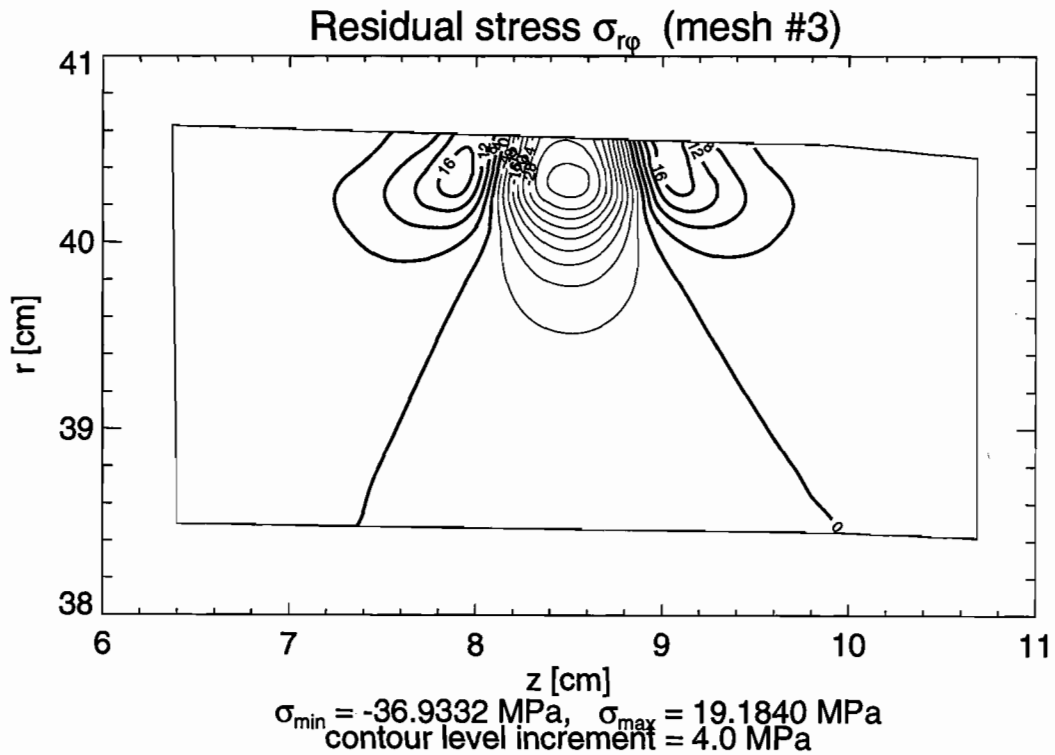

Figure 3.40 Contour Lines of Axial σ_{zz} and Shear $\sigma_{r\varphi}$ Residual Stresses in the Railroad Car Wheel under Thermal and Mechanical Loading (Loading Case #6)

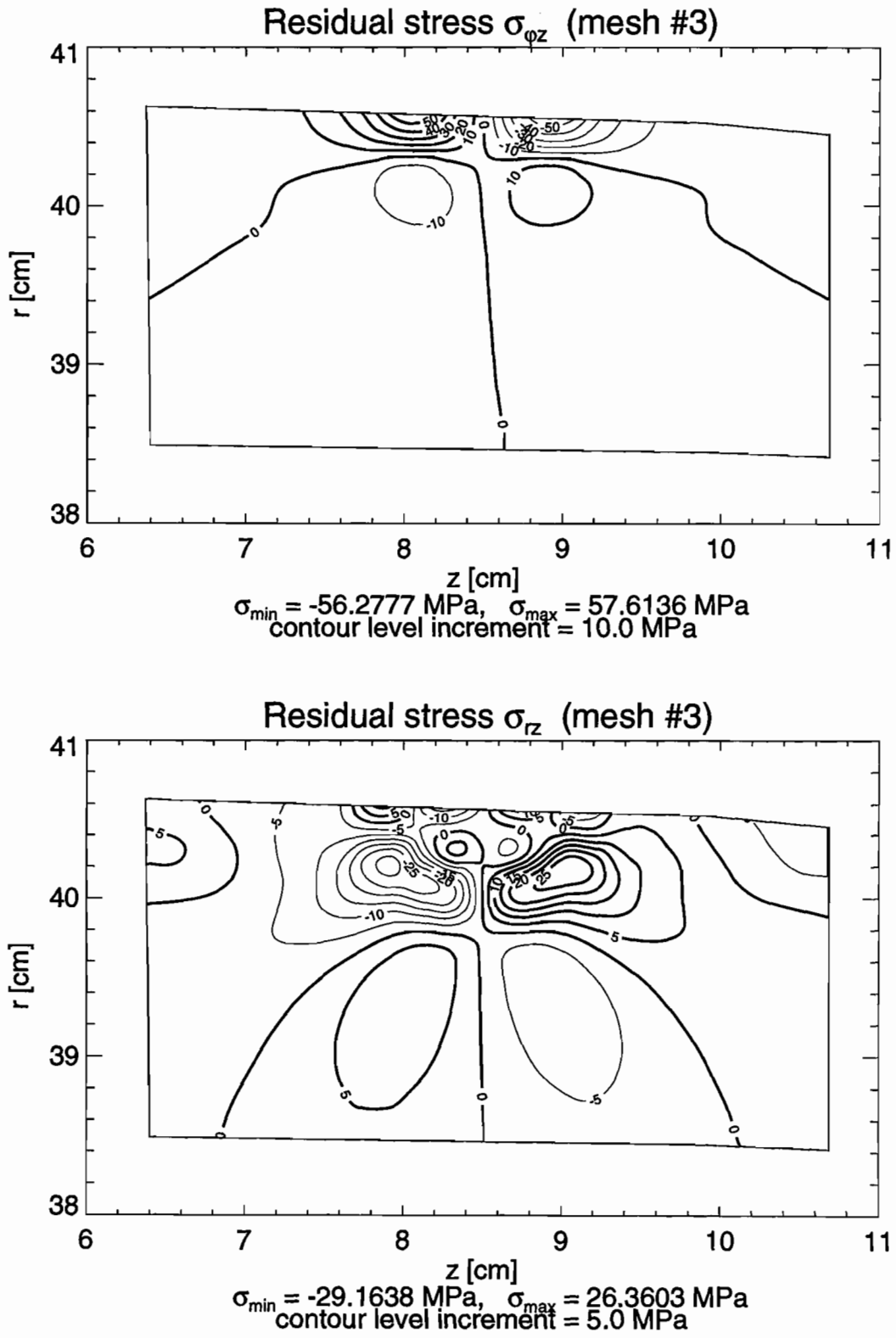

Figure 3.41 Contour Lines of Shear Residual Stresses $\sigma_{\varphi z}$ and σ_{rz} in the Railroad Car Wheel under Thermal and Mechanical Loading (Loading Case #6)

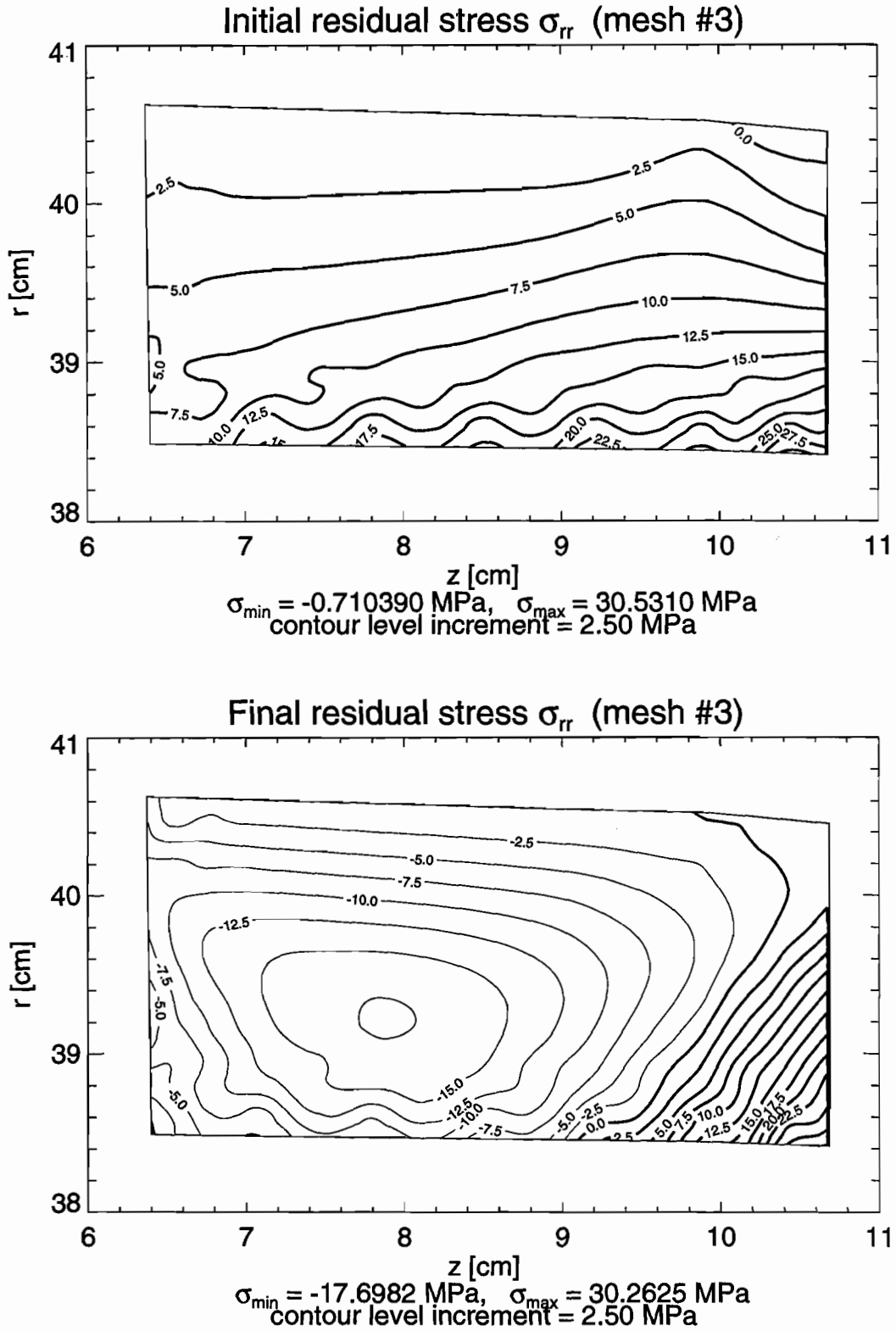

Figure 3.42 Contour Lines of Radial Residual Stresses σ_{rr} in the Railroad Car Wheel under Thermal Loading (Loading Case #7)

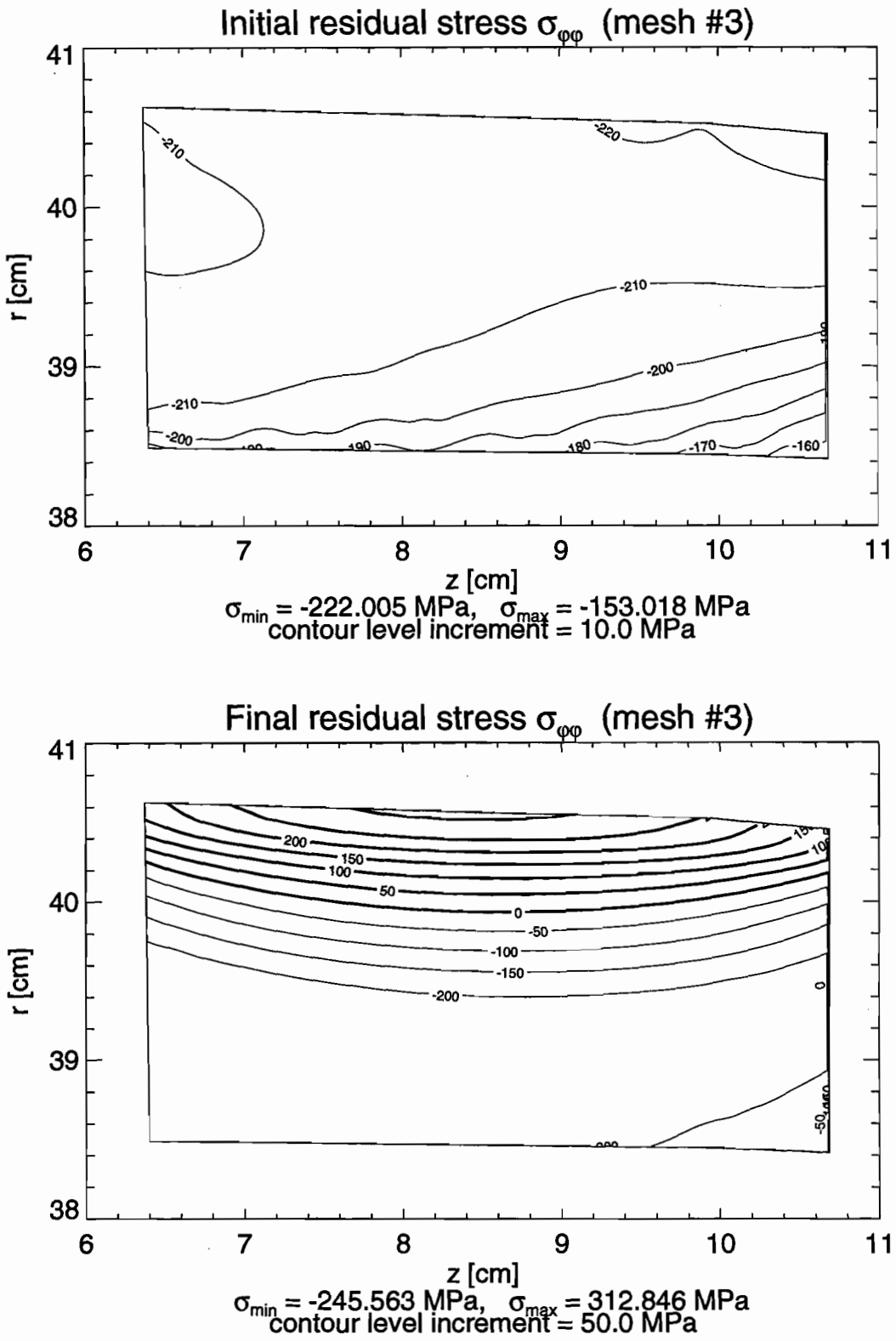

Figure 3.43 Contour Lines of Hoop Residual Stresses $\sigma_{\varphi\varphi}$ in the Railroad Car Wheel under Thermal Loading (Loading Case #7)

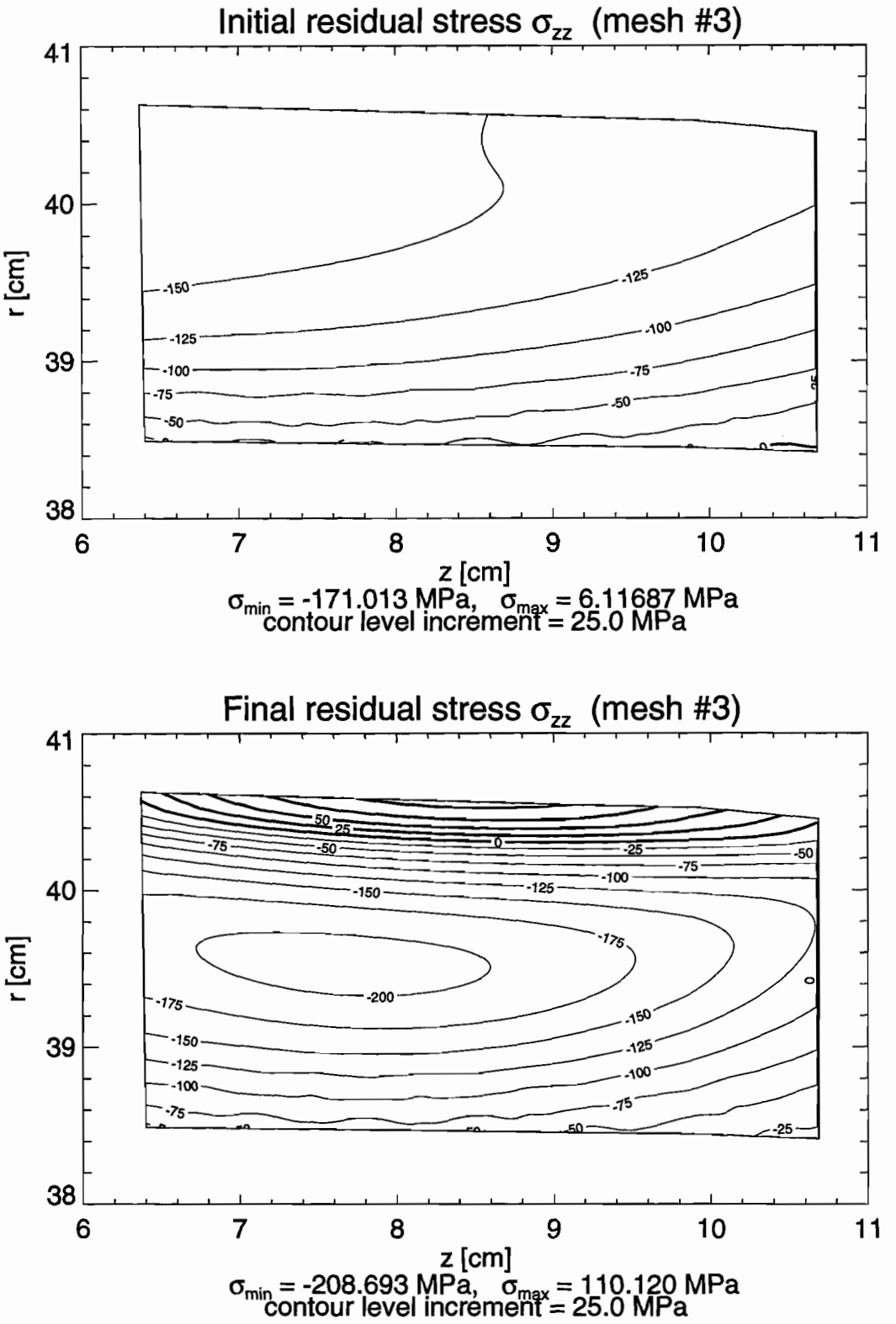

Figure 3.44 Contour Lines of Axial Residual Stresses σ_{zz} in the Railroad Car Wheel under Thermal Loading (Loading Case #7)

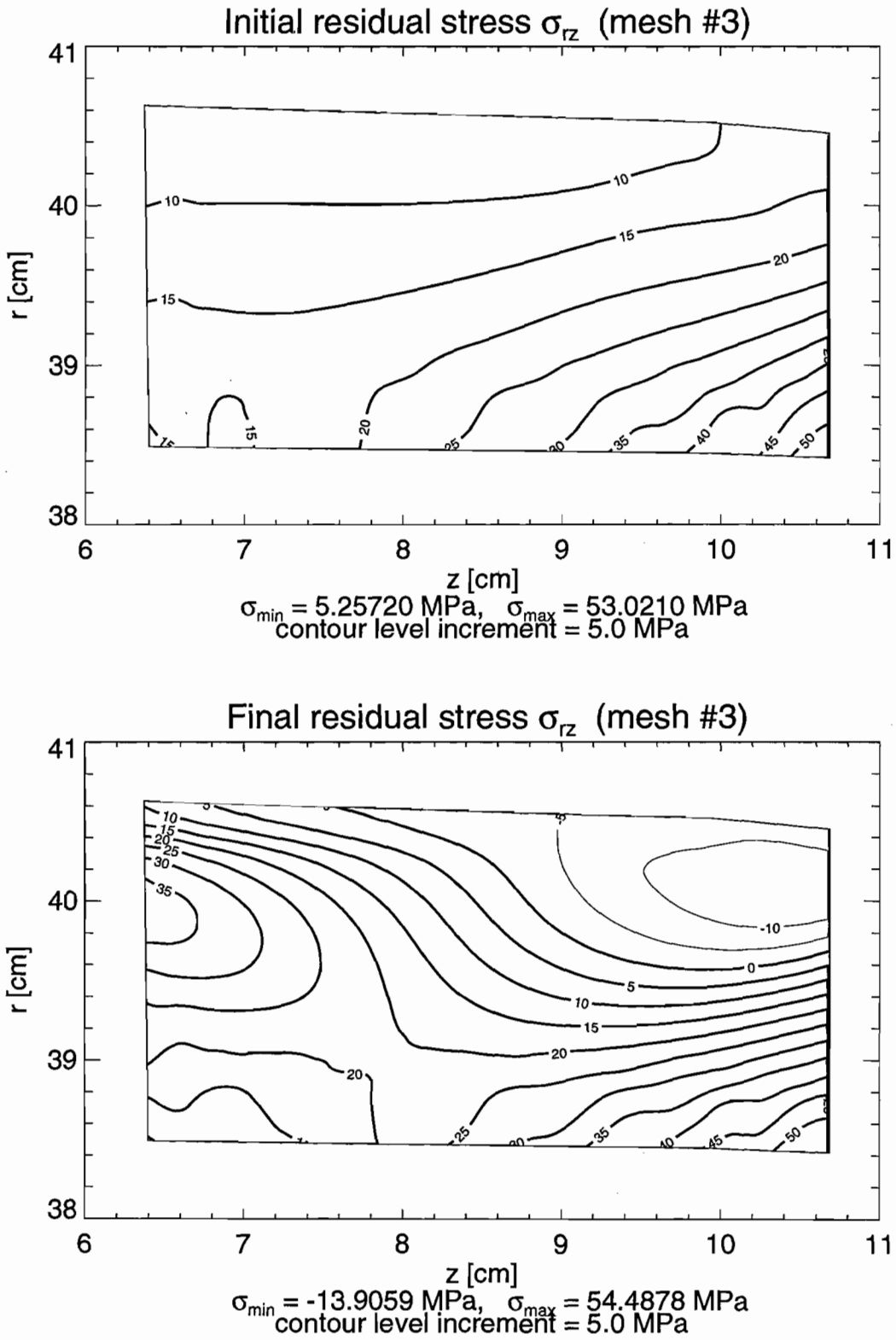

Figure 3.45 Contour Lines of Shear Residual Stresses σ_{rz} in the Railroad Car Wheel under Thermal Loading (Loading Case #7)

4. FINAL REMARKS

The numerical tests and the example analyses for railroad car wheels presented in this report validate the computer programs worked out for the analysis of elastic contact stresses and the evaluation of residual stresses in a selected class of axisymmetric bodies. High quality agreement with other numerical solutions has been obtained and the convergence of the solution as a function of mesh density has been demonstrated. The example analyses performed for real railroad car wheels have shown that the computer programs are a very useful and effective tool, especially for the analysis of residual stresses in shakedown conditions. In spite of the fact that the assumptions underlying the mechanical and numerical models, and consequently the computer programs, may be considered as quite restrictive, all the major phenomena typical for railroad car wheels can be taken into account in real analyses. Thus, not only surface tractions due to rail/wheel contact but also thermal stresses associated with braking maneuvers can be taken into consideration. The material of the wheel may be assumed to be temperature-dependent. Additionally, such phenomena as initial residual stresses coming from different sources, multiple running paths and more than one contact zone can also be included. Finally, it is worth stressing that almost all the examples presented here were solved using less than 16 MB of computer memory. Bigger memory, up to 24 MB, was required only when the finest mesh #5 was considered.

REPORTS IN THIS SERIES

1. Orringer, O., D.E. Gray, and R.J. McCown. 1993. *Evaluation of Immediate Actions Taken to Deal with Cracking Problems in Wheels of Rail Commuter Cars.* Volpe National Transportation Systems Center. Report no. DOT/FRA/ORD-93/15.
2. Tang, Y.H., J.E. Gordon, A.B. Perlman, and O. Orringer. 1993. *Finite Element Models, Validation, and Results for Wheel Temperature and Elastic Thermal Stress Distributions.* Volpe National Transportation Systems Center. Report no. DOT/-FRA/ORD-93/17.
3. Tang, Y.H., J.E. Gordon, O. Orringer, and A.B. Perlman. 1993. *Stress Reconstruction Analysis of Wheel Saw Cut Tests and Evaluation of Reconstruction Procedure.* Volpe National Transportation Systems Center. Report no. DOT/FRA/ORD-93/18.
4. Stuart, C. 1993. *Thermal Measurements of Commuter Rail Wheels Under Revenue Service Conditions.* ENSCO, Inc. Report no. DOT/FRA/ORD-93/19.
5. Pelloux, R.M. and D.C. Grundy. 1994. *Thermomechanical Testing and Microstructural Development of Class L Steel Wheel Alloy.* Department of Materials Science and Engineering, MIT. Report no. DOT/FRA/ORD-94/01.
6. Gordon, J.E. and O. Orringer. 1996. *Investigation of the Effects of Braking System Configurations on Thermal Input to Commuter Car Wheels.* Volpe National Transportation Systems Center. Report no. DOT/FRA/ORD-96/01.

REFERENCES

[1] Orringer, O. and D.E. Gray, in press. Thermal cracking in railroad vehicle wheels subjected to high performance stop braking. In *Theoretical and Applied Fracture Mechanics.*

[2] Orkisz, J., O. Orringer, M. Holowinski, M. Pazdanowski, and W. Cecot. 1990. Discrete analysis of actual residual stresses resulting from cyclic loadings. In *Computers & Structures 35(4).*

[3] Orringer, O., J. Orkisz, and Z. Swiderski (ed.). 1992. *Residual Stress in Rails: Effects on Rail Integrity and Railroad Economics.* Kluwer Academic Publishers, Dordrecht, The Netherlands.

[4] Orkisz, J. and M. Holowinski. 1992. Prediction of residual stresses in rails: practical benefits from theoretical approach. In *Rail Quality and Maintenance for Modern Railway Operation.* Edited by J.J. Kalker, D.F. Cannon, and O. Orringer. Kluwer Academic Publishers, Dordrecht, The Netherlands.

[5] Perlman, A.B., J.E. Gordon, and O. Orringer. 1992. Effect of grinding strategy on residual stress in the rail head. In *Rail Quality and Maintenance for Modern Railway Operation (op.cit.).*

[6] Gordon, J.E., in press. Simulation of the quenching process of railroad wheels. In *Proc. 11th International Wheelset Congress.*

[7] Johnson, K.L. 1985. *Contact Mechanics.* Cambridge University Press.

[8] Maugin, G.A. 1992. *The Thermomechanics of Plasticity and Fracture.* Cambridge University Press.

[9] Tong, P. and J.N. Rossetos. 1977. *Finite Element Method: Basic Technique and Implementation.* MIT Press.

[10] Bathe, K.J. 1982. *Finite Element Procedures in Engineering Analysis.* Prentice-Hall.

[11] Zienkiewicz, O.C. and R.L. Taylor. 1991. *The Finite Element Method.* McGraw-Hill.

[12] *ABAQUS User's Manual, version 5.3-2.* Hibbitt, Karlsson & Sorenson, Inc.

[13] Martin, J.B. 1975. *Plasticity: Fundamentals and General Results.* MIT Press.

[14] Orkisz, J. 1990. Residual stress analysis in railroad car wheels working in service conditions. In *Mechanika Teoretyczna i Stosowana 1-2(28).*

[15] Orkisz, J. 1992. Prediction of actual residual stresses by constrained minimization of energy. In *Residual Stress in Rails Effects on Rail Integrity and Railroad Economics (op.cit.).*

[16] Holowinski, M. 1992. *Hybrid FEM Analysis of Residual Stresses under Cyclic Loading.* Ph.D. thesis, Cracow University of Technology, Poland (in Polish).

[17] Holowinski, M. and J. Orkisz. 1992. Hybrid finite element method for estimation of actual residual stresses. In *Residual Stress in Rails (op.cit.).*

[18] Vanderplaats, G.N. 1984. *Numerical Optimization Techniques for Engineering Design: with Applications.* McGraw-Hill.

•U.S. GOVERNMENT PRINTING OFFICE:1996-720-703/83053